TECHNISCHE UNIVERSITÄT DARMSTADT

Investigating and Modeling the Impact of Moisture on the Reliability of Mid-Power Light-Emitting Diodes

DISSERTATION

Vom Fachbereich Elektro- und Informationstechnik
der Technischen Universität Darmstadt

zur Erlangung des akademischen Grades
eines Doktors der Ingenieurwissenschaften
(Dr.-Ing.)

genehmigte Dissertation

von

Simon Benkner, M.Sc.
aus Siegen

Referent:	Prof. Dr.-Ing. habil. Tran Quoc Khanh
Korreferent:	Prof. Dr.-Ing. Klaus Hofmann
Tag der Einreichung:	12.09.2023
Tag der mündlichen Prüfung:	29.11.2023

Darmstadt 2023

Simon Benkner: *Investigating and Modeling the Impact of Moisture on the Reliability of Mid-Power Light-Emitting Diodes*

Darmstadt, Technische Universität Darmstadt
Jahr der Veröffentlichung auf TUprints: 2024
URN: urn:nbn:de:tuda-tuprints-264936
Tag der mündlichen Prüfung: 29.11.2023

Zusammenfassung

In den letzten Jahrzehnten haben Licht-emittierende Dioden (LED) aufgrund ihrer flexiblen Steuerungsmöglichkeiten, ihrer hohen elektrooptischen Effizienz und ihrer außergewöhnlich hohen Lebensdauer den Markt für Allgemeinbeleuchtung weitestgehend besetzt. Mit der fortlaufenden Entwicklung neuer anwendungsspezifischer Leuchtstoffmaterialien werden auch zunehmend Nischenanwendungen besetzt. In einigen Anwendungsfällen ist die LED mehreren, oft erhöhten Umweltbelastungen wie Temperatur und Feuchtigkeit zugleich ausgesetzt. Ein Beispiel für eine solche Anwendung sind Beleuchtungszenarien im industriellen Agrar-Sektor jenseits der traditionellen Feldbewirtschaftung wie Gewächshäuser.
Die Auswirkung von Feuchtigkeit auf die LED als solche wurde in bisherigen Studien jedoch nur spärlich untersucht, da überwiegend thermische und elektrische Stressbedingungen im Vordergrund standen. Insbesondere wurden nur sehr wenige Studien zu Licht-emittierenden Dioden der Mid-Power Leistungsklasse in PLCC-Gehäusebauform (Plastic-Leaded Chip Carrier) mit Hinblick auf den Einfluss von Luftfeuchtigkeit auf deren Zuverlässigkeit durchgeführt. Diese Situation spiegelt sich auch in den gängigen Normen und Methoden zum Testen und Berechnen der Bauteilzuverlässigkeit wieder. Daher ist die Untersuchung des Einflusses von Feuchtigkeit auf die Zuverlässigkeit von Mid-Power LEDs sowie die Modellierung dieses Einflusses der Hauptgegenstand dieser Arbeit.
Im Verlauf dieser Arbeit wurde ein Experiment zur beschleunigten Degradation konzipiert und durchgeführt um tiefgehendere Erkenntnisse über die Rolle der Kombination von Umgebungstemperatur, Betriebsstrom und Luftfeuchtigkeit als Stressparameter auf die Degradation der LED zu gewinnen. Dieses Experiment umfasst vier aktuelle, im Handel erhältliche LEDs, die jeweils 24 verschiedenen Temperatur-, Luftfeuchtigkeits- und Strombedingungen ausgesetzt wurden. Der aktuelle Zustand jeder LED wurde fortlaufend im Hinblick auf deren optische, elektrische und thermische Eigenschaften gemessen.
Basierend auf den beobachteten Ergebnissen wird der Schluss gezogen, dass insbesondere das Eindringen von Feuchtigkeit die Zuverlässigkeit der Bauelemente stark beeinträchtigt, da sich die Verkapselung aufgrund von Scherkräften, welche durch hygroskopisches Aufquellen der Silikonverkapselung entstehen, von angrenzenden Teilen des Gehäuses löst. Dadurch können weiterführende Effekte wie das Anlaufen der reflektierenden Lead-Frame-Beschichtung oder die beschleunigte Auflösung beigemischter Leuchtstoffpartikel begünstigt auftreten.
Hinsichtlich der Modellierung der beobachteten Degradationsverläufe wurden verschiedene kontinuierliche Degradationsfunktionen und ein segmentierter Degradationsansatz untersucht. Letzterer zeigte vielversprechende Ergebnisse, insbesondere, wenn die anschließende Modellierung der Beschleunigungsparemter durch die Eyrings-Gleichung berücksichtigt wird. Darüber hinaus wurden eine Gaußsche Prozessregression als Modellierungsansatz für die Degradationstrajektorie sowie die Survival-Analyse als Ansatz für die Modellierung der Lebensdauer untersucht. Insbesondere für nicht-monotone Beschleunigungsfunktionen konnten beide Methoden eine erhöhte Genauigkeit gegenüber gängigen physikalisch-basierten Modellierungsansätzen erzielen.

Abstract

Over the past decades Light-emitting Diode (LED) devices have not only entered but occupied large segments of the general lighting market due to their flexible control features, high power conversion efficiency and exceptional long lifetime when operated at the recommended conditions. With the constant emergence of new application specific phosphor-materials niche applications are targeted. In some use cases the LED device is exposed to multiple, often elevated environmental stress conditions, such as temperature and humidity. An example of such an application is horticulture lighting in vertical or greenhouse farming scenarios.
However, especially the impact of moisture on the LED device as a whole is only sparsely investigated in past studies since mostly thermal and electrical stress conditions were targeted. In particular, only very few studies have been conducted on plastic-leaded chip carrier (PLCC) Mid-Power LED devices with respect to moisture. These situation is also reflected in common standards and methodologies for reliability testing and lifetime calculation. Therefore, the investigation of moisture ingress on performance of a LED and modeling this very is the main scope of this work.
Over the course of this work an Accelerated Degradation Test (ADT) experiment was designed and conducted to gain further insights on the role of the combination of temperature, current and humidity on the devices degradation. This experiment included four state-of-the-art, commercially available Mid-Power LED devices recommended for the use in horticulture applications that were each subjected to 24 different temperature, humidity and current conditions. The current state of each device was measured continuously with respect to its optical, electrical and thermal characteristics.
Based on the observed results it is concluded that especially moisture ingress severely impacts the devices performance by causing the encapsulant to detach from adjacent parts of the package due to shear forces introduced by hygroscopic swelling of the silicone encapsulant. Accompanying effects, such as tarnishing of the reflective lead-frame coating or accelerated dissolution admixed phosphor particles can also be reported.
Regarding the modeling of the observed degradation trajectories various continuous decay functions and a segmented decay approach were investigated. Latter showed promising results especially when considering the subsequent modeling of its decay parameters according to Eyrings equation. In addition, a Gaussian Process Regression as a decay modeling approach as well as Survival Analysis as a time-to-failure approach were explored. Especially for case of non-monotonous acceleration functions both yielded an increased accuracy compared to typical physics-based modeling approaches.

Acknowledgments

This thesis and its scientific achievements were written and accomplished during my time as a research associate in 2017-2023 at the Laboratory of Adaptive Lighting Systems and Visual Processing to obtain the Doctoral degree in Electrical Engineering and Information Technology from the Technical University of Darmstadt.

Firstly, I would like to express my deepest appreciation to my supervisor Prof. Dr.-Ing. habil. Tran Quoc Khanh for supporting and encouraging me during my research period while giving me the liberty to pursue my research interests. Further, I have to address my most gratitude to Prof. Dr.-Ing. Klaus Hofmann participating as a second referee for my doctoral examination and for reviewing my thesis.

I would like to extend my sincere thanks to my colleagues at the Laboratory of Adaptive Lighting Systems and Visual Processing for all the fruitful discussions, new ideas and insights into various lighting technology related research aspects. In this regard, I have to express my deeply gratitude to Stefan Klir and Alexander Herzog for our enriching and insightful conversations and successful research projects. Additionally, my thank goes to all my students who supported my research as student assistants or who have written a thesis under my supervision. Special thanks in this regards I have to dedicate to K. van Beek and T. Luan for their great work and support. Beyond that, I am very grateful to my good friend Max for our fruitful discussions on the topic and beyond.

Finally, I could not have taken this journey without the support of my beloved girlfriend Sandra, to whom I have to express my deepest gratitude. Alongside, I have to deeply thank my family for always supporting and encouraging me to pursue my interests and passion.

Contents

List of Figures

List of Tables

Acronyms

ADT	Accelerated Degradation Test
AEC	Automotive Electronics Council
ALT	Accelerated Life Test
AST	Accelerated Stress Test
BIC	Bayesian Information Criterion
BPA-PC	Bisphenol-A Polycarbonate
CPH	Cox Proportional Hazard
CTE	Coefficient of Thermal Expansion
DD	Data-driven
DoE	Design of Experiment
DOS	Density of States
DUT	Device Unter Test
EBL	Electron Blocking Layer
EDX	Energy dispersive X-ray spectroscopy
EMC	Epoxy Molding Compounds
ESD	Electrostatic Discharge
FWHM	Full Width Half Mid
GPR	Gaussian Process Regression
HAST	Highly Acclerated Stress Test
HP	High-Power
HTOL	High Temperature Operating Life
IES	Illuminating Engineering Society
JEDEC	Joint Electron Device Engineering Council Solid State Technology Assiciation
LASER	Light Amplification by Stimulated Emission of Radiation
LED	Light-emitting Diode
LP	Low-Power
MD	Model-Driven
ML	Machine Learning
MP	Mid-Power
MQW	Multi Quantum Well
NN	Neural Network

PC	Pre Conditioning
PCB	Printed Ciruit Board
pcLED	phosphor-converted Light-emitting Diode
PDE	Partial Differential Equation
PDMS	Polydimethylsiloxane
PL	Photo-Luminescence
PLCC	Plastic Leaded Chip Carrier
PMMA	Poly(methyl methacrylate)
PMPS	Polymethylphenylsiloxane
PTC	Power Temperature Cycling
QCSE	Quantum-confined Stark Effect
SEM	Scanning Electron Microscope
QW	Quantum Well
RBF	Radial Basis Function
RTD	Resistance Temperature Detector
RUL	Remaining Useful Life
SMT	Surface Mount Device
SMU	Source Measure Unit
SPD	Spectral Power Distribution
SRH	Shockley-Read-Hall
TC	Temperature Cycling
UV	Ultraviolet Spetrum
VIS	Visible Spectrum
WHTOL	Wet High Temperature Operating Life

Symbols

Symbol	Unit	Denotation
α	-	Acceleration factor
α_V	$\mathrm{mV\,K^{-1}}$	Forward voltage temperature coefficient
Δt	h	Measurement interval
$\Delta u'v'$	-	Euclidean distance between two chromaticity coordinates
Φ	W	Radiant flux
λ	nm	Wavelength
λ_p	nm	Peak wavelength
κ_c	$\mathrm{W\,m^{-1}\,K^{-1}}$	Thermal conductivity
μ	-	Mean value
μ_n, μ_p	$\mathrm{cm^2\,V^{-1}\,s^{-1}}$	Electron, hole mobility
η_{Droop}	-	Efficiency droop
η_{EQE}	-	External quantum efficiency
$\eta_{\mathrm{EQE,max}}$	-	Maximum external quantum efficiency
η_{IE}	-	Injection efficiency
η_{IQE}	-	Internal quantum efficiency
$\eta_{\mathrm{IQE,max}}$	-	Maximum internal quantum efficiency
η_{LE}	-	Phosphor luminous efficiency
η_{LEE}	-	Light extraction efficiency
η_{PCE}	-	Power conversion efficiency
η_{RE}	-	Recombination efficiency
η_{VfE}	-	Forward voltage efficiency
ρ	-	Reflectance
σ	-	Standard deviation
σ_e	$\mathrm{cm^2}$	Trap capture-cross-section
ψ_i	-	Segmented decay function breakpoint
$\Psi(\cdot)$	-	Wave function
τ_n, τ_e	s	Electron recombination lifetime
τ_p	s	Hole recombination lifetime
$\boldsymbol{\theta}$	-	Free parameters
Θ_D	K	Debye temperature
ξ	-	Phosphor to blue ratio

Symbol	Unit	Denotation
$\mathcal{GP}(\cdot)$	-	Gaussian process regression
$\mathcal{N}(\cdot)$	-	Normal distribution
$\mathcal{N}^+(\cdot)$	-	Positive half normal distribution
$\mathcal{U}(\cdot)$	-	Uniform distribution
a	Å	Lattice constant
A	s^{-1}	Shockley-Read-Hall coefficient
A	m^2	Area
A_q	-	Phosphor material constant
B	$cm^3\,s^{-1}$	Bimolecular recombination coefficient
B_H	GPa	Adiabatic bulk modulus
BIC	-	Bayesian information criterion
c	Å	Lattice constant
C	$cm^6 s^{-1}$	Auger coefficient
$\mathbf{C}$	$kg\,m^{-3}$	Concentration
C_i	F	Internal capacitance
d	m	Material thickness
D	$m^2\,s^{-1}$	Diffusion constant
D_n, D_p	$m^2\,s^{-1}$	Electron, hole diffusion constant
e^-	-	Electron
E	eV	Energy
E_a	eV	Activation energy
E_b	eV	Bowing parameter
E_c	eV	Conductance band energy level
E_e, E_h	eV	Electron, hole energy
E_F	eV	Fermi energy
E_g	eV	Bandgap energy
E_{Phonon}	eV	Energy of a phonon
E_{Photon}	eV	Energy of a photon
E_T	eV	Trap energy level
E_v	eV	Valence band energy level
$\vec{E}$	$N\,C^{-1}$	Electrical field
f	Hz	Frequency
$f_D(\cdot)$	-	Decay function
$f_L(\cdot)$	-	Linkage function
FWHM	nm	Full-width half-mid

Symbol	Unit	Denotation
G	$\mathrm{m^{-3}\,s^{-1}}$	Generation rate
$h(t)$	-	Hazard function
h^+	-	Hole
$H(\cdot)$	-	Heaviside Step Function
$H(t)$	-	Cumulative hazard function
i	-	Counting variable
I	A	Current
$I(T)$	$\mathrm{W\,m^{-2}}$	Intensity
I_F	A	Forward current
I_m	A	Measurement current
I_nom	A	Nominal measurement current
I_r	A	Reverse current
$I_\mathrm{r,leak}$	A	Reverse leakage current
I_s	A	Saturation current
j	-	Counting variable
$\mathbf{J}$	$\mathrm{kg\,m^{-2}\,s^{-1}}$	Diffusion flux
$\vec{k}$	$\mathrm{cm^{-1}}$	Wave vector
k_c	$\mathrm{cm^{-1}}$	Conduction band wave number
k_v	$\mathrm{cm^{-1}}$	Valence band wave number
$L_\mathrm{n}, L_\mathrm{p}$	µm	Electron, hole diffusion length
$m_\mathrm{e}^*, m_\mathrm{h}^*$	kg	Electron, hole effective mass
m_r^*	kg	Reduced effective mass
M	kg	Molecular mass
M_sat	kg	Saturated molecular mass
n	$\mathrm{cm^3}$	Electron concentration
n	-	Counting variable
n_0	$\mathrm{cm^{-3}}$	Equilibrium electron concentration
n_i	$\mathrm{cm^{-3}}$	Intrinsic charge carrier concentration
n_i	-	Refractive index
n_ideal	-	Ideality factor
N	-	Counts
N_ψ	-	Number of breakpoints
$N_\mathrm{A}, N_\mathrm{D}$	$\mathrm{cm^{-3}}$	Acceptor, donor concentration
N_T	$\mathrm{cm^{-3}}$	Trap concentration
NOP	-	Normalized output power

Symbol	Unit	Denotation
p	cm^{-3}	Hole concentration
p_0	cm^{-3}	Equilibrium hole concentration
$P(\cdot)$	-	Probability
P_{el}	W	Electrical power
$P_{\mathrm{el,typ}}$	W	Typical rated electrical power
P_{opt}	W	Optical power
P_{th}	W	Thermal power
Q	C	Charge
$\vec{Q}_c$	C	Directional charge
$\dot{Q}$	$\mathrm{J\,s}^{-1}$	Heat transfer rate
$r_{\mathrm{III}}, r_{\mathrm{V}}$	Å	Elements covalent radii
rH	%	Relative humidity
rH_{A}	%	Relative ambient humidity
R_{rad}	$\mathrm{cm}^{-3}\,\mathrm{s}^{-1}$	Radiative recombination rate
R_{p}	Ω	Parallel parasitic resistance
R_{s}	Ω	Series parasitic resistance
R_{th}	$\mathrm{W\,K}^{-1}$	Thermal resistance
R_{Auger}	$\mathrm{cm}^{-3}\,\mathrm{s}^{-1}$	Auger recombination rate
R_{SRH}	$\mathrm{cm}^{-3}\,\mathrm{s}^{-1}$	Shockley-Read-Hall recombination rate
S_i	-	Stress variable
$S(\lambda)$	$\mathrm{W\,nm}^{-1}$	Spectral power distribution
$S(t)$	-	Survival function
t	h	Time
t_{start}	h	Starting time of function interpolation
T	°C, K	Temperature
T_{a}	°C, K	Ambient temperature
T_{g}	K	Glass temperature
T_{j}	K	Junction temperature
T_{q}	K	Phosphor quenching temperature
u'	-	CIE 1976 UCS Chromaticity coordinate

Symbol	Unit	Denotation
v'	-	CIE 1976 UCS Chromaticity coordinate
v_{th}	$\mathrm{m\,s^{-1}}$	Thermal velocity
$\langle v \rangle$	$\mathrm{m\,s^{-1}}$	Mean phonon velocity
V_{active}	$\mathrm{cm^3}$	Volume of the active region
V_{ph}	$\mathrm{cm^3}$	Volume of phosphor compound
V_{D}	V	Diffusion voltage
V_{F}	V	Forward voltage
V_{T}	V	Thermal threshold voltage
W_{r}	$\mathrm{cm^{-3}\,s^{-1}}$	Radiative relaxation
W_{nr}	$\mathrm{cm^{-3}\,s^{-1}}$	Non-radiative relaxation
YI	-	Yellowing Index
c_0	$299\,792\,458\,\mathrm{m\,s^{-1}}$	Speed of light in vacuum
k_{B}	$8.617\,\mathrm{eV\,K^{-1}}$	Boltzmann constant
h	$6.626 \times 10^{-34}\,\mathrm{J\,s}$	Planck constant
$\hbar$	$1.054 \times 10^{-34}\,\mathrm{J\,s}$	Reduced Planck constant
q	$1.602 \times 10^{-19}\,\mathrm{C}$	Elementary charge

1 Introduction

From the discovery of semiconductor material's ability to emit light when subjected to an external voltage by Henry Round (1907), Oleg Losev (1921) and Georges Destriau (1935) [1, 2] to today's LED it has been a long journey. About four decades after the first observation of this effect, referred to electroluminescence, with the research on the semiconductor *pn*-junction by William Shockley [3] and Heinrich Welker [4] the development towards the modern LED increasingly accelerated with new improved processing technologies. Subsequently, the first optical active, binary GaP semiconductor crystal with an orange to red light emission pattern was synthesized during the 1950s [2, 5–7]. Dating the early 1960s Nick Holonyak reported the first application of GaAs and GaAsP based Light Amplification by Stimulated Emission of Radiation (LASER) devices [2]. Later in 1968 the first commercial red GaAsP LED devices were produced [2, 8]. Over the following decades binary and ternary semiconductor compounds steadily advances regarding their efficiency as well as their spectral properties resulting in a variety of green to (infra)red LED devices. Even though the existence of blue emitting GaN based semiconductors was verified in the late 1960s, reliably processing of such on a large scale proved to be a major challenge with existing manufacturing technology due to significant lattice mismatches during the growth process [2, 9]. As a result most research was ceased up until in the 1980s structural improvements, such as stabilizing AlN buffer layers on sapphire substrate, and finally Nakamuras optimization of the GaN on sapphire growth process with distinct thermal curing set the foundation for the modern LED [2, 10–13]. With further structural and processing advances, these blue light emitters efficiency and reliability largely increased over the following years [14]. The final step towards todays widely spread application of GaN based LED devices was the addition of a wavelength-converting phosphor material, such as a yellow-emitting YAG, onto the emitter in order to generate white light [2, 15–18]. Further, the flexibility of obtaining distinct spectral emission patterns by adjusting the ratio of the GaN to InN concentration ratio in ternary InGaN compounds allows highly diverse and use case specific emitter-phosphor combinations encompassing applications ranging from architectural over healthcare to horticulture [2, 16, 19–31].

On the emitter side the primary development focus over the past two decades was on ceramic substrate package based InGaN emitters in the High-Power (HP) regime ($P_{\mathrm{el,typ}} \geq 1\,\mathrm{W}$) in order to obtain maximum power densities. Even though this technology has matured in terms of a consolidation in utilized materials and manufacturing processes an optimization towards maximum efficiency at such high power densities is challenging due to self heating of the device. Therefore, lately the focus shifted towards devices in Mid-Power (MP) PLCC-package regime ($100\,\mathrm{mW} < P_{\mathrm{el,typ}} < 1\,\mathrm{W}$). As these devices are operated at much lower power densities an operation closer to their efficiency maximum can be achieved. It should be noted, that the MP regime's upper limit varies between 0.5 W to 1 W depending on different definitions. Over the course of this work the above stated definition regarding typical power consumption and package technology is used. Due to their low heat dissipation as a result of a high power conversion efficiency these devices allow to simplify the application's thermal design. Thereby,

MP devices are incorporated increasingly in consumer and professional lighting products accompanied by an steadily increased number of MP PLCC LED devices offered on the market. [32]

1.1 Horticulture LED Lighting Applications

Considering the previous elaborated current developments in emerging lighting applications the horticulture market segment stands out in particular. For one, due to the emerging climate change [33] the traditional field based crop cultivation will face drought and extreme weather related challenges letting greenhouse and indoor cultivation become a sustainable alternative. Second, in order to nourish the worlds steadily growing population while considering the limited amount of available farm land, approaches like indoor vertical farming are required for space efficient crop cultivation. Since these proposed greenhouse and indoor farming approaches require artificial light sources for plant illumination, LED based lighting systems are of major interest due to their efficiency and extraordinary control features [29, 31, 34–36]. This becomes particularly evident when analyzing the current market situation and forecast of horticulture related lighting products ranging from LED devices over luminaries towards smart crop yield control systems ranging up to about 19 billion US Dollar by 2027 [37].

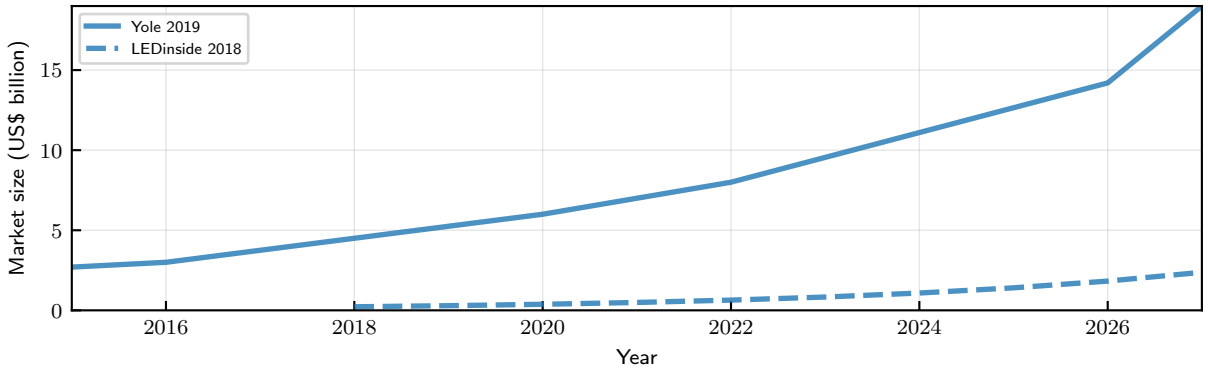

Figure 1.1: Estimated market growth for horticulture LED devices for indoor and greenhouse farming applications according to different sources by the European Union Joint Research Center [37].

1.2 Moisture and LED Reliability

Despite the fact that state-of-the-art LED devices for standard applications, such as white phosphor-converted Light-emitting Diode (pcLED) for indoor lighting, feature an exceptional long lifetime of several 10 000 h while operated within the manufacturers specifications [32, 38–40] devices under harsher conditions like e.g. in greenhouse environments may face lifetime reducing challenges. Comparing horticulture lighting to indoor lighting applications the operational and in specific the environmental conditions highly differ. Climatic conditions indoors can be assumed mostly static around $T \approx 22\,°\mathrm{C}$ and rH $\approx 40\,\%$ to $60\,\%$ [41]. In contrast, LED devices in horticultural applications are subjected to elevated stress conditions due to longer switching cycles and high air moisture. In greenhouses luminaries may additionally be subjected to elevated temperatures during the day due to direct exposure to sunlight. Depending on the application the air moisture can also be supplemented with fertilizer

particles which provide a potential hazard for the LED devices.
In terms of reliability, a decrease in optical power or changes in the spectral composition would decrease crop yield and is therefore not desired [29, 42]. Identifying the impact of environmental stress on the performance of a LED is an ongoing scope in reliability research [32, 38, 39]. However, in the past, the focus of such reliability investigations has been on the temperature and current side while environmental humidity was only sparsely investigated. This is also reflected in typical test standards like IES TM-21 [43]. Especially, when concerning new packaging, phosphor and processing technologies for such applications further studies are mandatory.
The scope of this thesis, therefore, is the identification of moisture-related reliability issues as well as the modeling of the corresponding lifetime. Considering the prolonged lifetime of a LED, an ADT at 24 different (rH_A, T_A, I_F)-conditions on 480 state-of-the-art MP LED devices containing different phosphor materials is carried out. Both, the results and observed degradation effects of the ADT are put into perspective with respect to an extensive literature review on past LED reliability studies. Finally, the degradation behavior and subsequently, the devices lifetime with regard to the applied stress conditions is modeled. Since the most common physics based models do not encompass temperature, current and humidity together as independent stress variables alternative modeling approaches are investigated.

1.3 Outline of This Thesis

For the ease of readability this work is structured in seven chapters. Beginning with this chapter an introduction is provided to the reader followed by an overview on the physical background on LED technology in chapter 2. Next, in the first part of chapter 3, standards and procedures for LED reliability testing are discussed before an in depth literature review on degradation mechanisms of LED devices is given in the second part of chapter 3. Based on the literature research a ADT experiment is designed in chapter 4 whose results are discusses subsequently in chapter 5. With respect to the measured degradation trajectories these very are modeled in chapter 6. Finally, a discussion and outlook for further work is presented in chapter 7.

2 Blue and Phosphor-converted Mid-Power LEDs

Over the course of this chapter the reader is provided with a comprehensive overview on physical and technological properties MP LEDs. The first section will elaborate on the basic principles of III-N semiconductors for LED applications. Next, the basics of phosphors for wavelength-conversion is presented. Subsequently, the structural properties of PLCC packages are discussed before finally giving an overview on LED performance metrics in the last section.

2.1 III-Nitride Semiconductors for Blue Light-Emitting Diodes

This section emphasizes on the physical and electrical properties of binary and ternary III-Nitride semiconductors for Light-emitting Diode (LED) applications. Starting with the structural design of the III-Nitride material system, followed by the generation of blue light emission pattern and the electrical properties of such devices.

2.1.1 The Material System of III-Nitride Semiconductor Compounds

Structural Properties

Due to their high radiative efficiency III-N(itride) compound semiconductors are the prevalent material system for blue LEDs [2]. These compounds combine group III elements, such as Indium (In), Gallium (Ga) or Aluminium (Al), with Nitrogen (N) as a group V element to form a III-V semiconductor. Common III-N compounds are either of a binary type, hosting one group III/V element each, such as GaN, and ternary types incorporating two group III elements and one group V element, such as $In_xGa_{1-x}N$ or $Al_xIn_{1-x}N$ [2, 44–46]. III-N compounds are characterized by their Wurtzite crystal structure (hexagonal) shown in fig. 2.1 in contrast to a Zinc-Blende crystal structure (cubic) present in other III-V semiconductor compounds with higher period group V elements like Phosphorus (P) or Arsenic (As) [47].

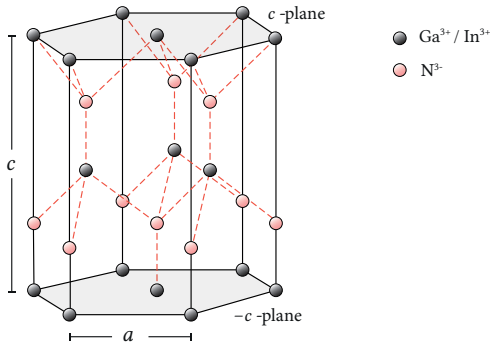

Figure 2.1: Wurtzite crystal structure of a III-N semiconductor lattice unit cell [48], reproduced with the authors permission.

The Wurtzite structure features two interlacing hexagonal close-packed (HCP) lattice structures yielding two parallel c-planes occupied by the group III element(s). Its geometrical properties are described by the Wurtzite crystal cell's lattice constants $a = (2\sqrt{2}/\sqrt{3}) \cdot (r_{\mathrm{III}} + r_{\mathrm{V}})$ (in-plane) and $c = (8/3) \cdot (r_{\mathrm{III}} + r_{\mathrm{V}})$ (out-of-plane) with the tetrahedron covalent radii r_{III} and r_{V}[45] presented in table 2.1. At equilibrium condition in an ideal III-N Wurtzite structure the III/N elements electrical dipoles cancel each other out resulting in a cells net electrical field of $\vec{E} = \vec{0}\,\mathrm{N\,C^{-1}}$ thus no polarization should be present. However, a polarization in the c-plane has been observed due to lattice mismatches [49–51]. The present electric field $\vec{E} \neq \vec{0}\,\mathrm{N\,C^{-1}}$ in the c-plane generates a small directional charge difference $\Delta\vec{Q}_c$ between both c-planes of the Wurtzite crystal. In addition to lattice mismatches, spontaneous polarization effects were observed in the crystal's growth direction [51].

Table 2.1: Lattice constants a, c and the band gap energy E_{g} of different binary III-N Wurtzite semiconductor compounds at room temperature $T = 300\mathrm{K}$ [2, 45].

Compound	a (Å)	c in (Å)	E_{g} (eV)
AlN	3.112	4.982	6.28
GaN	3.191	5.185	3.425
InN	3.545	5.703	0.77

Band Structures of III-N Semiconductors

Covalent bonds between two neighboring atoms in a III-N crystal lattice are formed as a result of their overlapping valence electron orbitals. Those valence electrons can either be tied to their atom or available as free charge carriers within the lattice depending on their electron energy. Since energy is quantized according to the wave function $\Psi(\vec{r}, t)$, electrons can only occupy discrete energy states. The highest energy levels at $T = 0\,\mathrm{K}$ occupied by valence electrons tied to their atom is denoted as the valence band E_{v} and the lowest energy levels of vacancies for free electrons is denoted as the conduction band E_{c} respectively. Occupation of states within the resulting band gap $E_{\mathrm{g}} = E_{\mathrm{c}} - E_{\mathrm{v}}$ is forbidden due to the wave functions properties. Furthermore, the energy level defined by the chemical potential in equilibrium state at $T = 0\,\mathrm{K}$ is denoted as the Fermi-level E_{F}, which for undoped semiconductors located close to the band gap center at $E_{\mathrm{F}} \approx 0.5E_{\mathrm{g}} \approx 0.5(E_{\mathrm{c}} - E_{\mathrm{v}})$ as a result from Fermi-Dirac-statistics [52]. Typical band gaps of semiconductors range up to $E_g(\mathrm{SiO_2}) \approx 11\,\mathrm{eV}$ [53] at low temperatures. Considering III-N semiconductors at room temperature of $T = 300\,\mathrm{K}$ typical band gap energies of binary, wurtzite structured compounds are presented in table 2.1. For ternary III-N compounds the theoretical E_{g} [2] is determined according to eq. (2.1) with the bowing parameter E_{b} set to $-1\,\mathrm{eV}$ for AlGaN [54], $-2.4\,\mathrm{eV}$ for InGaN [55] and $-3\,\mathrm{eV}$ for AlInN [56].

$$E_{\mathrm{g}}^{\mathrm{AB}} = E_{\mathrm{g}}^{\mathrm{A}} + (E_{\mathrm{g}}^{\mathrm{B}} - E_{\mathrm{g}}^{\mathrm{A}})x + x(1-x)E_{\mathrm{b}} \tag{2.1}$$

In blue LED applications ternary InGaN with a low In_x content of $x \approx 15\,\%$ to $20\,\%$ is predominantly used since its processing is well understood and controllable compared to In_x-rich AlInN alloys with $x \approx 45\,\%$ to $50\,\%$ that also provides blue wavelength emission. The processing issues of InN-rich compounds originate for one from the low dissociation temperature of InN hindering the growth uniformity required [57]. In addition, InN lattice constants a, c differ from

most common substrates, thus, promoting lattice mismatches (Si: 7 %, GaN: 11 %, SiC: 14 %, saphhire: 27 %) [45, 58]. Subsequently, these mismatches introduce compressive and tensile forces into the lattice altering its polarization due to the piezoelectric effect [51, 59, 60]. Thereby created electric fields distort the lattice's band structure and causing a separation of free charge carriers lowering the overall radiative efficiency. This effect is denoted as the Quantum-confined Stark Effect (QCSE) [61–63]. The following paragraphs will therefore emphasize only on (In)GaN based semiconductors with low Indium content used for blue LED applications.

Doping

The beforehand discussed pure (intrinsic semiconductor) III-N crystal structure provides fixed electrical and optical properties. The process of intentional introducing defined impurities (dopants) into the (III-N) host lattice to adjust these properties is referred to as doping. Such dopants are of adjacent groups (II, IV, VI) and occupy lattice positions of either group III (Al, Ga, In) or V (N) elements. Doped (extrinsic) semiconductors thus offer additional charge carriers in the form of either excessive electrons for replacements by higher group elements (Donors; group III $\rightarrow$ IV, V $\rightarrow$ VI) or electron vacancies (holes) for replacements by lower group elements (Acceptors; group III $\rightarrow$ II, V $\rightarrow$ IV). The former are denoted as *n*-type and the latter as *p*-type semiconductors. In order to alter the host lattices conductivity these additional charge carriers need to be ionized by an activation energy E_a either elevating the donors free electrons into the conduction or lowering the acceptors free holes into the valence band respectively. Simultaneously, the Fermi level shifts towards the corresponding band. [2, 45, 58]
The *n*-doping of (In)GaN semiconductors is mainly achieved by replacing Ga atoms with Silicon yielding free carrier concentrations of about $10^{17}\,\mathrm{cm}^{-3}$ to $10^{19}\,\mathrm{cm}^{-3}$ [64]. Since the activation energy of these Si_Ga donor charge carriers of $12\,\mathrm{meV} \leq E_\mathrm{a} \leq 17\,\mathrm{meV}$ [65] is lower than the crystals thermal energy at room temperature of $k_B T \approx 25\,\mathrm{meV}$ an ionization automatically takes place. However, unintentional *n*-doping (autodoping) has also been reported as a result of Oxygen contaminants from the growth process substituting Nitrogen atoms as well as Nitrogen vacancies resulting from poor processing acting as donors [58, 65–68].
Implanting acceptors into the (In)GaN lattice by *p*-doping has proven to be far more challenging. For one introducing group IV elements turns out not to be purposeful, since these elements rather substitute group III elements [58]. Secondly, the passivation of Magnesium acceptors by residue Hydrogen bonding with Nitrogen [11, 69, 70]. Thirdly, the rather high activation energy of Mg at room temperature of $E_\mathrm{a} = 200\,\mathrm{meV} \gg k_B T$ [58]. Both previous challenges were solved to a certain extend by a proper processing followed by an additional thermal annealing step reversing the passivation and activating the implanted Mg-donors [13].

2.1.2 The pn-Junction

The fundamental building block of semiconductor devices in electronics is the *pn*-junction consisting of two oppositely doped layers of a single semiconductor. This simple *pn*-junction is referred to as a p-n-homojunction diode as fig. 2.2 shows. In order to achieve an equilibrium state, free charge carriers in the interfaces proximity diffuse towards the opposite doped region to recombine with their counterparts. The average distance of these (minority) carriers diffuse into the opposite doped layer before recombining is specified by the diffusion length $L_\mathrm{n,p}$

in eq. (2.2) with the diffusion constant $D_{n,p}$, the charge carriers lifetimes $\tau_{n,p}$ and the charge carriers mobility $\mu_{n,p}$. This process is illustrated in the right part of fig. 2.2.

$$L_{n,p} = \sqrt{D_{n,p}\tau_{n,p}} \quad \text{with} \quad D_{n,p} = \frac{k_B T}{q}\mu_{n,p} \tag{2.2}$$

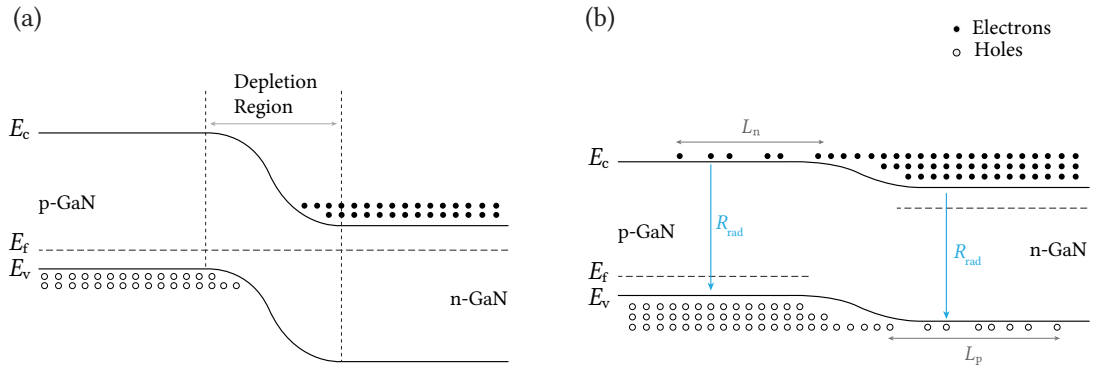

Figure 2.2: The *pn*-junction: (left) Depletion region forming a potential barrier at the junction, (right) length of minority charge carriers with an external forward bias voltage to lower the potential barrier [48], reproduced with the authors permission.

Resulting from these diffusion processes the interface area is depleted of free charge carriers, denoted as the depletion region, leaving ionized donors and acceptors introducing a net charge on the *p*-side and *n*-side respectively. The thus generated electrical potential across the depletion region – the diffusion voltage V_D – displayed in the left part of fig. 2.2 is given by eq. (2.3) with the absolute temperature T, Boltzmann's constant k_B, the elementary charge q, the concentrations of acceptors and donors N_A and N_D as well as the semiconductor materials intrinsic carrier concentration n_i.

$$V_D = \frac{k_B T}{q} \ln\left(\frac{N_A N_D}{n_i^2}\right) \tag{2.3}$$

Further, eq. (2.2) implies a broadening of the minority charge carriers distribution with increasing temperature. As a consequence, the charge carrier density decreases and thus the possibility of radiative recombination is lowered. An detailed explanation on this matter is provided in section 2.1.3. To overcome this issue a sandwich structure of a small band gap semiconductor between two wide band gap materials also known as Quantum Well (QW) or double *pn*-heterojunction is introduced as highlighted in fig. 2.3. Both wide band gap regions act as a barrier to trap charge carriers in between due to their bands abrupt energy gradient. The resulting high charge carrier concentration along the small band gap area – the active region – significantly increases radiative recombination. Current state of the art LED semiconductors use Multi Quantum Well (MQW) structures to further increase and control the charge carriers radiative recombination [2, 45]. It is noteworthy, that (In)GaN alloys display a higher band to band energy difference in the conduction than the valence band [71].

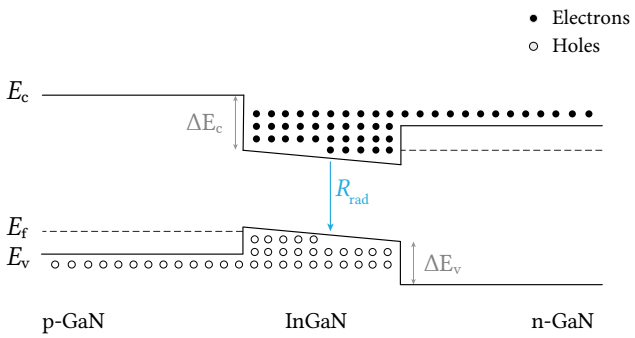

Figure 2.3: Illustration of a *pn*-heterojunction of an InGaN semiconductor device with a QW charge carrier confinement [48], reproduced with the authors permission.

2.1.3 Radiative and non-Radiation Recombination of Free Charge Carriers

While transitioning from a higher energy state to a lower one, an electron releases its excessive energy $\Delta E = qV_D \approx E_g$. This process is called recombination and can either happen by emitting a photon (radiative) or a phonon (non-radiative) [72, 73]. Although both processes occur in LED semiconductors, the former is clearly preferred. The following paragraphs elaborate on both types of recombination as well as the resulting spectral emission properties for radiative recombination.

Direct and Indirect Semiconductors

In general, semiconductors are categorized by their valence bands maximum $E_{v,max}(k_v)$ and conduction bands minimum $E_{c,min}(k_c)$ alignment within the momentum ($\vec{k}$) space diagram. Due to the conservation of momentum $k_c \approxeq k_v$ is required for recombination processes. Direct semiconductors, like (In)GaN, naturally fulfill $k_c \approxeq k_v$ since both bands extreme points are aligned within the $\vec{k}$-space as shown in fig. 2.4. Alongside with momentum conservation also energy must be preserved by releasing a photon $E_{Photon} = hf \approx E_{c,min} - E_{v,max}$. For indirect semiconductors, like Si, the momentum of both bands is not aligned $k_c \neq k_v$. Thus, an additional momentum $\Delta k = k_c - k_v$ has to be introduced to fulfill conservation of momentum. Usually Δk is generated by emitting a phonon (lattice vibration) with the energy $E_{Phonon} = E_{c,min} - E_{v,max} - hf$ lowering the probability of radiative recombination. [2, 45]

Radiative Recombination of Free Charge Carriers

Considering a direct semiconductor at equilibrium condition with a given electron n_0 and hole concentration p_0 the intrinsic charge carrier concentration is given due to the law of mass action by $n_i^2 = n_0 p_0$. Additional charge carriers Δn, Δp, are generated by e.g. applying a current to the semiconductor. The total charge carrier concentration for electrons subsequently is $n = n_0 + \Delta n$ and $p = p_0 + \Delta p$ for holes respectively. As electrons and holes recombine the total carrier concentration decreases over time. This decrease is denoted as the recombination rate R_{rad} defined by the bimolecular rate equation in eq. (2.4) showing a proportionality

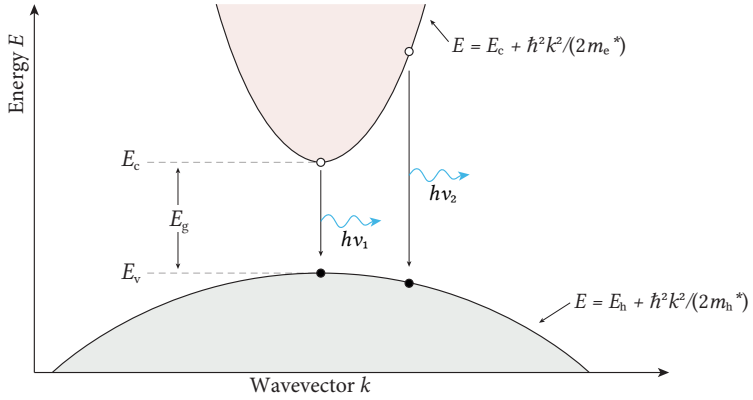

Figure 2.4: Charge carrier distribution of a direct semiconductor represented in E-k-diagram by means of its aligned valence and conduction bands momentum. [48], reproduced with the authors permission.

to n, p with the bimolecular recombination coefficient B. Usually B is in the magnitude of $10^{-12}\,\mathrm{cm^3\,s^{-1}}$ to $10^{-9}\,\mathrm{cm^3\,s^{-1}}$ [2, 46, 74–79].

$$R_{\mathrm{rad}} = -\frac{\mathrm{d}n}{\mathrm{d}t} = Bnp \tag{2.4}$$

Within the relatively small active region an nearly equal electron and hole $n \approx p$ concentration can be assumed. Injecting a current increases the excessive charge carriers concentration substantially to $\Delta n, \Delta p \gg n_0, p_0$ yielding $n = \Delta n \approx \Delta p = p$. Thus, eq. (2.4) can be simplified to $R_{\mathrm{rad}} = Bn^2$ stating the radiative recombination an quadratic dependency on the charge carrier concentration.

Non-Radiative Recombination of Free Charge Carriers

Direct semiconductors can also be prone to non-radiative recombination processes, namely: Shockley-Read-Hall (SRH) and Auger recombination. Promoted by lattice defects, such as impurities or dislocations [80, 81], additional deep level trap energy states E_{T} can arise within the band gap. The process of trap assisted recombination is denoted as SRH recombination R_{SRH} [72] and involves two phonon generating reactions following eq. (2.5) and eq. (2.6).

$$\mathrm{Trap^0} + \mathrm{e^-} \longrightarrow \mathrm{Trap^-} + \mathrm{E_{Phonon,1}} \tag{2.5}$$

$$\mathrm{Trap^-} + \mathrm{h^+} \longrightarrow \mathrm{Trap^0} + \mathrm{E_{Phonon,2}} \tag{2.6}$$

Both phonons energies correspond to the band to trap energy difference $E_{\mathrm{c}} - E_{\mathrm{T}}$ for $E_{\mathrm{Phonon,1}}$ and $E_{\mathrm{T}} - E_{\mathrm{v}}$ for $E_{\mathrm{Phonon,2}}$ respectively. In this two part reaction the slower reaction part of both eq. (2.5) and eq. (2.6) limits the overall recombination rate. Thus the probability of a recombination is proportional to the product of the total trap N_{T} and carrier n concentration. Considering the thermal velocity v_{th} and the trap's capture-cross-section σ_{e} the SRH recombination rate is defined by $R_{\mathrm{SRH}} = \sigma_{\mathrm{e}} v_{\mathrm{th}} N_{\mathrm{T}} n = An$ where A is the SRH coefficient. Typically A decreases with increased fabrication quality of the semiconductor and takes values in the order

of $10^6\,\mathrm{s}^{-1}$ to $10^9\,\mathrm{s}^{-1}$ [2, 74–79].
Auger recombination R_{Auger} on the other hand, occurs if upon recombination with its counterpart a charge carriers energy is passed to a third carrier of that type within the energy band. Subsequently, the excess energy of the third particle is emitted as a phonon. This recombination can occur as an *eeh process* involving two electrons given by the reaction in eq. (2.7) or respectively as an *ehh process* following eq. (2.8). [2]

$$\mathrm{e}^- + \mathrm{e}^- + \mathrm{h}^+ \longrightarrow \mathrm{e}^- + \mathrm{E}_{\mathrm{Phonon}} \tag{2.7}$$
$$\mathrm{e}^- + \mathrm{h}^+ + \mathrm{h}^+ \longrightarrow \mathrm{h}^+ + \mathrm{E}_{\mathrm{Phonon}} \tag{2.8}$$

Subsequently, assuming an equal charge carrier concentration $n \approx p$ the Auger recombination rate can is calculated by $R_{\mathrm{Auger}} = (C_{\mathrm{eeh}} + C_{\mathrm{ehh}})n^3 = Cn^3$. The Auger coefficient C typically ranges from $10^{-31}\,\mathrm{cm}^6\,\mathrm{s}^{-1}$ to $10^{-29}\,\mathrm{cm}^6\,\mathrm{s}^{-1}$ [74–79].

ABC-Model of Recombination

The overall recombination R of the active region is found according to eq. (2.9) by summing the three recombination rates specified above.

$$R = R_{\mathrm{SRH}} + R_{\mathrm{rad}} + R_{\mathrm{Auger}} = An + Bn^2 + Cn^3 \tag{2.9}$$

It should be noted, that no leakage of charge carriers out of the QW is assumed in the following. Thus, the induced charge carrier generation or injection rate G within the active regions volume V_{active} must equal the recombination rate R (eq. (2.10)).

$$\frac{I_{\mathrm{F}}}{qV_{\mathrm{active}}} = G \stackrel{!}{=} R = An + Bn^2 + Cn^3 \tag{2.10}$$

The ratio of emitted photon energy $E_{\mathrm{Photon}} = hf$ to the total injected energy $E_{\mathrm{tot}} = E_{\mathrm{Photon}} + E_{\mathrm{Phonon}}$ is directly proportional to the ratio of radiative recombination processes R_{rad} to all recombination processes R shown in eq. (2.11) which is denoted as the internal quantum efficiency η_{IQE}.

$$\eta_{\mathrm{IQE}} = \frac{R_{\mathrm{rad}}}{R} = \frac{Bn^2}{An + Bn^2 + Cn^3} \propto \frac{E_{\mathrm{Photon}}}{E_{\mathrm{tot}}} \tag{2.11}$$

Further considering solely radiative recombination $A, C = 0$ and $B \neq 0$ in eq. (2.10) the optical power P_{opt} is obtained by eq. (2.12).

$$G = R|_{A,C=0} \quad \xrightarrow{|\cdot E_{\mathrm{Photon}}} \quad P_{\mathrm{opt}} = Bn^2 hf V_{\mathrm{active}} \tag{2.12}$$

Since the charge carrier concentration is proportional to the injection current $n \propto I_{\mathrm{F}}$ three observations can be stated from eq. (2.11): Firstly, SRH recombination dominates within the low injection range due to the linear n-term and increases steadily. Secondly, the efficiency maximum $\eta_{\mathrm{IQE,max}}$ is located at moderate current conditions as $B \gg C$. Thirdly, at very high injection currents the substantially small Auger coefficient C is compensated by the cubic n^3-term resulting in an efficiency droop η_{Droop} described by eq. (2.13). The droop's shape is highly dependent on the device's structure and material parameters. [2, 82–85]

$$\eta_{\mathrm{Droop}} = 1 - \frac{\eta_{\mathrm{IQE,max}}}{\eta_{\mathrm{IQE}}} \tag{2.13}$$

Spectral Emission

Starting from the beforehand discussed radiative recombination and emission of photons of a certain frequency f the following paragraph will derive the quasi monochromatic emission spectrum with its characteristic peak wavelength λ_p and Full Width Half Mid (FWHM) as well as its thermal properties. The photon emission in LED semiconductors origins from spontaneous recombination effects induced by an electric current yielding a quasi monochromatic spectrum. In contrast, LASER semiconductors require the stimulation by additional, external photons that produce a narrow, nearly monochromatic spectrum with $\text{FWHM}_{\text{LASER}} \ll \text{FWHM}_{\text{LED}}$.
In order to determine the emission spectrum, first, the conduction and valence band shapes within the $\vec{k}$-space are analyzed. The electrons and holes, both feature a parabolic dispersion within the conductance and valence band respectively following eq. (2.14) with the reduced Planck constant $\hbar$, the wave number k, the electrons and holes effective masses m_e^*, m_h^* and the band edges E_c, E_v.

$$E_e(k) = E_c + \frac{\hbar^2 k^2}{2m_e^*} \qquad E_h(k) = E_v - \frac{\hbar^2 k^2}{2m_h^*} \tag{2.14}$$

Considering the conservation of energy and momentum the energy of a photon at a certain wave number is obtained according to eq. (2.15) also denoted as the joint dispersion relation.

$$E_{\text{Photon}} = hf \approx E_g \approx E_e(k) - E_h(k) \approx E_g + \frac{\hbar^2 k^2}{2m_r^*} \quad \text{with} \quad m_r^* = \frac{m_e^* m_h^*}{m_e^* + m_h^*} \tag{2.15}$$

From rearranging the joint dispersion relation from eq. (2.15) in terms of $k(E)$ the joint Density of States (DOS) $\rho(E)$ in a given volume can be inferred. The distribution of charge carriers along these states is given by the Boltzmann distribution $f_B(E)$. The spectral emission is therefore directly proportional to the superposition of $\rho(E)$ and $f_B(E)$ shown in eq. (2.16).

$$P_{\text{opt}}(E) \propto \rho(E) \cdot f_B(E) \approx \sqrt{E - E_g} \exp\left(-\frac{E}{k_B T}\right) \tag{2.16}$$

Subsequently, λ_p and the FWHM can be derived according to eq. (2.17) and eq. (2.18) by taking the Planck-Einstein relation $E = hf = \frac{hc}{\lambda}$ into account. Both parameters λ_p and FWHM are illustrated for a real blue InGaN spectrum in the left plot fig. 2.5.

$$E_{\text{max}} = E_g + \frac{1}{2} k_B T \quad \longrightarrow \quad \lambda_p = \frac{hc}{E_{\text{max}}} \tag{2.17}$$

$$\text{FWHM}_E = 1.8kT \quad \longrightarrow \quad \text{FWHM}_\lambda = \frac{1.8kT\lambda_p^2}{hc} \tag{2.18}$$

Accompanied by the spectrums temperature dependency in eq. (2.16) the band gap exhibits an additional temperature dependency that can be modeled according to the Varshni formula in eq. (2.19) with the material dependent fitting parameters α_V, β_V [71, 86, 87].

$$E_g(T) = E_g(T_0) - \frac{\alpha_V T^2}{T + \beta_V} \tag{2.19}$$

As a result the peak wavelength, the FWHM and the amplitude of the emitted spectrum varies with temperature. Latter can be attributed to enhanced carrier leakage as well as non-radiative deep level and surface recombination. This amplitude change can be modeled by eq. (2.20) with

the characteristic temperature T_1. The temperatures effect on the LED spectrum is displayed in the right plot of fig. 2.5.

$$P_{\text{opt}}(T) = P_{\text{opt,300 K}} \cdot \exp\left(\frac{T - 300\,\text{K}}{T_1}\right) \tag{2.20}$$

Consequently in MQW structure semiconductors a discrete superposition of multiple emission spectra depending on the physical design should be expected. Despite that, a broadened spectrum has been observed in several studies whereupon intermediate states occurring within the structure were suggested [88, 89]. Modeling such MQW spectra by means of physical or probabilistic functions is still an ongoing subject [90].

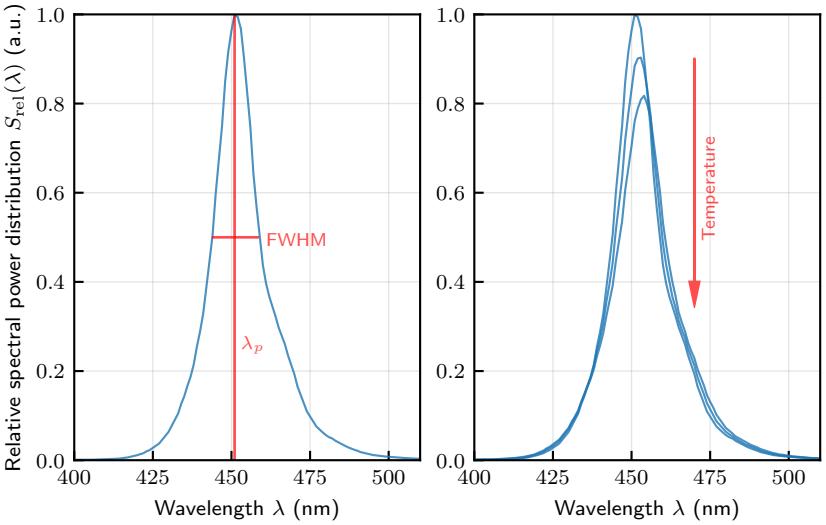

Figure 2.5: Typical spectrum of a blue InGaN emitter: (left) spectrum with its characteristic peak wavelength λ_p as well as FWHM and (right) temperature dependence of the emitted spectrum.

2.1.4 Electrical Characteristics

Operating the LED at forward bias conditions by applying a positive voltage – forward voltage V_F – to the *pn*-junction a positive current I_F flow is initiated due charge carrier injection into the neutral region of the semiconductor promoting radiative recombination. Measuring I_F while varying V_F exhibits two characteristics of the function $I_F(V_F)$: First, a sudden increase of I_F at $V_F \approx V_D$ occurs since more majority charge carriers diffuse through depletion region due to a lowered potential barrier $\Delta E = q(V_D - V_F)$. Second, at voltages far below the thermal voltage $V_F \ll V_T = k_B T q^{-1}$ a small current – the saturation current I_s – with a magnitude of 10^{-6} A to 10^{-12} A is measured as a result of minority carrier drifting into opposite doped region. This IV-characteristic of an ideal diode is described by the general Shockley equation in eq. (2.21) with the diodes cross-sectional are A and the minority carrier lifetimes τ_n, τ_p. It should be noted that the saturation current has a temperature dependency $I_s \propto T^{3/2}$ resulting from the DOS $\rho(E)$ influence on the intrinsic charge carrier density n_i^2.

$$I_F = I_s\left[\exp\left(\frac{qV}{k_B T}\right) - 1\right] \quad \text{with} \quad I_s = qA\left[\sqrt{\frac{D_p}{\tau_p}}\frac{n_i^2}{N_D} + \sqrt{\frac{D_n}{\tau_n}}\frac{n_i^2}{N_A}\right] \tag{2.21}$$

As LED devices usually are operated under forward bias conditions $V_F \gg V_T$ the former eq. (2.21) is simplified to eq. (2.22) where the ideality factor is introduced to consider deviations in experimental measurements from the ideal diode characteristic. For an ideal diode n_{ideal} is set to $n_{ideal} = 1$ while measurements show $n_{ideal} > 1$. [2]

$$I_F = I_s \exp\left(\frac{V_F - V_D}{n_{ideal} V_T}\right) \tag{2.22}$$

In real diodes however, the IV-characteristic diverges from that of an ideal diode given by equations eq. (2.21) and eq. (2.22). Such a real characteristic is shown in part (a) of fig. 2.6. Reasons can be found on the one hand by non-radiative recombination processes and on the other hand by parallel and series parasitic resistances R_p and R_s as fig. 2.6 highlights. The modified Shockley equation eq. (2.23) takes both deviations from the ideal IV-characteristic into account. Due to the transcendental form ($x = f(x)$) of eq. (2.23) a solution can be found by approximation or assistance of the LabertW function [91, 92].

$$I_F - \frac{V_F - I_F R_s}{R_p} = I_s(T) \exp\left(\frac{V_F - I_F R_s}{n_{ideal} V_T}\right) \tag{2.23}$$

The previously introduced ideality factor is used to model non-radiative recombination into eq. (2.23). At the very low injection regime $V_F \leq V_T$ defect induced trap assisted tunneling processes are the predominating cause of deviations from the ideal IV-characteristic that are recognized by an $n_{ideal} \geq 2$. SRH recombination processes, present at $V_F > 2V_T$, can be considered with $n_{ideal} = 2$ [93, 94]. However, in some cases the actual n_{ideal} highly differs from the beforehand describes theoretical values. In such cases, n_{ideal} is obtained by linearizing eq. (2.22) and deriving it towards V_F yielding eq. (2.24) [95–98].

$$n_{ideal}(I_F) = \frac{q}{k_B T}\left[\frac{\mathrm{d}(\ln I_F)}{\mathrm{d}V_F}\right]^{-1} \tag{2.24}$$

Subsequently, by taking the derivative of $n_{ideal}(I_F)$ with respect to I_F the ideality factor is extracted at the functions range of lowest slope as presented in eq. (2.25). Both to the ideality factor adjacent ranges of higher slope are not suitable for a valid expression of n_{ideal} due to the influence of the corresponding parasitic resistances R_p and R_s.

$$\frac{\mathrm{d}n_{ideal}}{\mathrm{d}I_F} = \begin{cases} \ll 0, & \text{for } R_p\text{-limited} \\ \approx 0, & \text{for ideal diode} \\ \gg 0, & \text{for } R_s\text{-limited} \end{cases} \tag{2.25}$$

These limiting parasitic resistances are the second contributor to these deviations from the ideal IV-characteristic and become primarily apparent in low injection region as parallel R_s and in the high injection regime as series resistance R_s. Former provides additional low impedance current paths surpassing the active region, e.g. surface currents. Latter are introducing regions of low conductivity, e.g. poor contacting, into the current path resulting in a voltage drop that lowers the forward voltage across the pn-junction. Both parasitic resistances are determined following eq. (2.26) with regard to their corresponding injection regions.

$$R_p = \left.\frac{\mathrm{d}V_F}{\mathrm{d}I_F}\right|_{V_F \to 0} \quad \text{and} \quad R_s = \left.\frac{\mathrm{d}V_F}{\mathrm{d}I_F}\right|_{V_F \gg V_D} \tag{2.26}$$

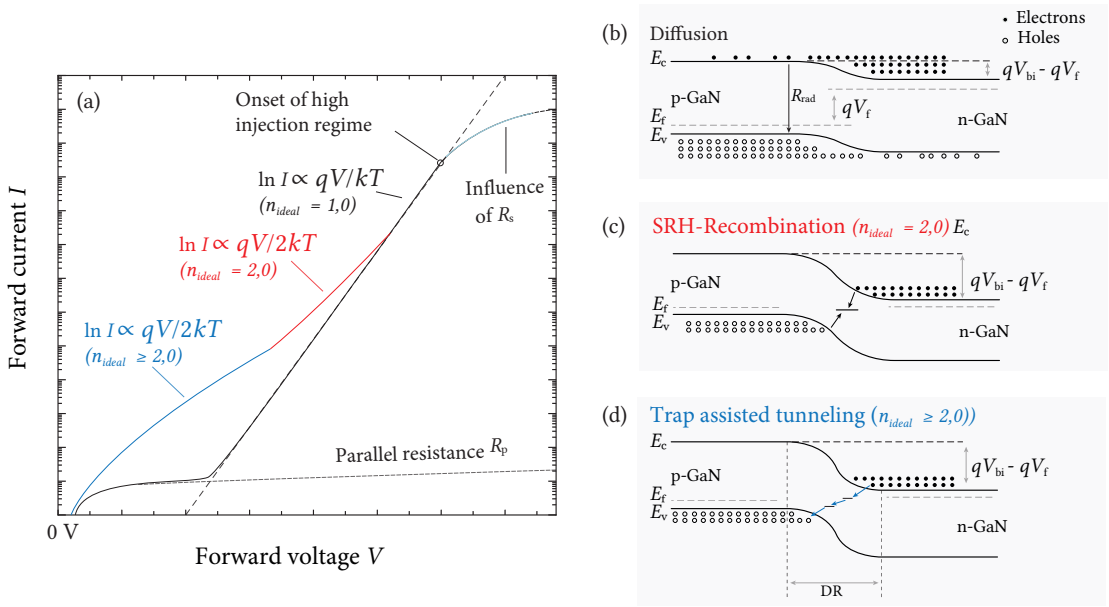

Figure 2.6: (a) Semi-logarithmic *IV*-characteristic of a real LED *pn*-junction with various conduction mechanisms, (b) diffusion current of the ideal diode around $n_{\text{ideal}} = 1$, (c) non-radiative SRH-recombination around $n_{\text{ideal}} = 2$ and (d) trap assisted tunneling processes [48]. Reproduced with the authors permission.

2.2 Phosphors for Wavelength-Conversion of Blue LED Spectra

Most lighting applications require use-case specific, polychromatic spectra across the Visible Spectrum (VIS) range which are only possible to realize up to a limited extend with pure semiconductor based emitters while maintaining reasonable manufacturing effort [99]. Therefore, the most common approach is the application of a photo-luminescent inorganic phosphor layer onto the LED die that converts the emitted (narrow) spectrum located at $\lambda_{p,1}$ into a (broadened) spectrum centered at $\lambda_{p,2}$. A conversion where $\lambda_{p,1} < \lambda_{p,2}$ is denoted as down-conversion and $\lambda_{p,1} > \lambda_{p,2}$ as up-conversion, respectively. Former are the predominating method of wavelength conversion in the context of LED due to their extraordinary high efficiency. This section emphasizes on the principles of wavelength conversion and provides an overview on commonly utilized materials and their properties.

2.2.1 Principle of Spectral Excitation and Emission of Photo-Luminescent Materials

In contrary to the beforehand discussed current-induced electro-luminescence in (In)GaN semiconductors, the excitation in inorganic phosphor materials is induced by optical radiation and thus denoted as Photo-Luminescence (PL). With further regard to the excited electrons lifetime τ_e, PL is categorized into fluorescence with short lifetimes of 10 ns to 100 ns and phosphorescence usually showing lifetimes of $\tau_e > 100\,\mu s$. Since phosphorescent materials are prone to saturation effects that limit their efficiency at high intensities of radiation they are not suited for LED applications.

Similar to semiconductors, phosphors are composed of a host lattice that is further doped with intentional impurities, so called activator and sensitizer atoms. Activator atoms are optically active elements, mainly rare earth lanthanides (Ce, Pr, Eu, Er), that emit a photon

upon relaxation of an excited electron. Often the electron excitation is directly triggered by absorption of an incoming photon (eq. (2.27)) [100, 101]. Alternatively, the incoming photon is absorbed by a sensitizer atom (eq. (2.28)), such as Mn or O, that further transfers its energy the activator atom (eq. (2.29)). The excessive energy of the down-conversion process is released as heat (lattice vibration) and the energy difference $\Delta E = |E_{\text{Photon}}(\lambda_2) - E_{\text{Photon}}(\lambda_1)| > 0$ is referred to as the Stokes shift.

$$E_{\text{Photon}}(\lambda_1) \xrightarrow{Activator} E_{\text{Photon}}(\lambda_2) + E_{\text{Phonon}}(hf_1) \tag{2.27}$$

$$E_{\text{Photon}}(\lambda_1) \xrightarrow{Sensitizer} E_{\text{Phonon}}(hf_1) \tag{2.28}$$

$$E_{\text{Photon}}(\lambda_1) \xrightarrow{Sensitizer} E_{\text{Phonon}}(hf_1) \xrightarrow{Activator} E_{\text{Photon}}(\lambda_2) + E_{\text{Phonon}}(hf_2) \tag{2.29}$$

Both, activator and sensitizer atoms, are implanted into the host lattice by substituting cations like Y or Ca. Since the absorption of photons and phonons is intended to take place in the dopant atoms, the host lattice is required to be optically transparent within the VIS with a stiff and stable crystal structure. Elements of the upper periodic systems columns (N, O, F, S) that provide a comparatively high E_g fulfill these requirements. An overview of typical blue light exited phosphors used in LED applications is given by table 2.2.

Table 2.2: Overview of typical phosphors for LED applications excited by blue (In)GaN emitters [102] with their excitation λ_{ex} and emission λ_{em} peak wavelengths as well as their quenching temperatures T_q.

Type	Compound	λ_{ex} (nm)	λ_{em} (nm)	T_q (K)
Green	$Ca\,Y_2\,Al_4\,Si\,O_{12} : Ce^{3+}$	450	540	420
	$Ca_3\,Sc_2\,Si_3\,O_{12} : Ce^{3+}$	455	505	-
	$Sr\,Ba\,Si\,O_4 : Eu^{2+}$	430	512	440
Yellow	$Y_3\,Al_5\,O_{12} : Ce^{3+}$ (YAG)	450	565	>600
	$Y_3\,Mg_2\,Al\,Si_2\,O_{12} : Ce^{3+}$	480	600	-
	$Li-\alpha\text{-}Si\,Al\,O\,N : Eu^{2+}$	460	573	-
Red	$Lu_2\,Ca\,Mg_2\,Si_3\,O_{12} : Ce^{3+}$	477	605	500
	$Ca\,Zn\,O\,S : Eu^{2+}$	460	650	400
	$\beta\text{-}Si\,Al\,O\,N : Pr^{2+}$	460	624	-

2.2.2 Thermal Quenching

The likelihood whether an exited electron will emit a photon or a phonon depends highly on the phosphor compounds temperature aside from unintended impurities that are avoidable by proper processing. At high temperatures the phosphors luminescence efficiency $\eta_{LE}(T) = \frac{W_r}{W_r + W_{nr}}$ reduces substantially as the probability of radiative relaxation W_r decreases and non-radiative relaxations W_{nr} increase. This process is denoted as thermal quenching [21, 103–106].

As shown in eq. (2.30) the luminescence efficiency has an inverse exponential dependence on the temperature where A_q is a material specific constant and $I(T)$ are the measured intensities.

$$\eta_{\mathrm{LE}}(T) = \frac{W_{\mathrm{r}}}{W_{\mathrm{r}} + W_{\mathrm{nr}}} = \frac{1}{1 + A_q \exp\left(-\frac{E_{\mathrm{q}}}{k_{\mathrm{B}} T}\right)} = \frac{I(T)}{I(0\,\mathrm{K})} \tag{2.30}$$

Further, the quenching temperature T_{q} specifies the temperature at which the likelihood of a non-radiative relaxation is at 50% and thus $\eta_{\mathrm{LE}}(T) = 0.5$. A phosphor compound's temperature robustness therefore scales with T_{q} which is proportional to the Debye temperature given by eq. (2.31) with the compound's volume V_{ph}, the compound's molecular mass M, the unit cell's atom count N, B_{H} as the adiabatic bulk modulus and the mean phonon velocity $\langle v \rangle$.

$$T_{\mathrm{q}} \propto \Theta_{\mathrm{D}} = \frac{\hbar}{k_{\mathrm{B}}} \left(6\pi^2 V_{\mathrm{ph}}^{1/2} N\right)^{\frac{1}{3}} \sqrt{\frac{B_{\mathrm{H}}}{M}} \langle v \rangle \tag{2.31}$$

The origin of thermal quenching in LED phosphors is still subject to current research. Commonly it is assumed that a non-radiative electron relaxation takes place at the cross-over point where the ground states and the excited states parabolas overlap in k-space. The probability to elevate an electron onto this cross-over point increases with temperature. A more recent explanation is the elevation of the excited electron into the host lattices conduction band by thermal ionization that provides a stronger agreement with recent experiments [106].

2.3 Materials and Properties of LED Packages for Mid-Power LEDs

Over the course of this section the package assembly of a semiconductor emitter for the final LED application is discussed. Therefore, first the assembly of typical Surface Mount Device (SMT) Plastic Leaded Chip Carrier (PLCC) packages is examined with an assessment of their thermal properties. Subsequently, common (optical) polymers used in LED packages are presented.

2.3.1 LED Package Types

Regarding their application, LED packages have to provide different beneficial optical, thermal and electrical properties to assure a proper functionality. While due to their exceptional small form factor the maximum light extraction states a challenge especially in Low-Power (LP) packages, managing heat dissipation is a predominant design task in High-Power (HP) packages as a result of their high current densities. Mid-Power (MP) packages, as an intermediate between the both previous mentioned, however, have to handle both challenges up to a certain degree simultaneously. With respect to the scope of this thesis, injection molded SMT PLCC packages will be further focused in the following. Nonetheless, it should be mentioned that aside from PLCC also ceramic substrate based and chip-scale SMT packages are widely used. [2, 107–109] A typical structure of a PLCC package is presented in section 2.3.1. This package is based on a conductive and highly reflective lead frame coated with a composite of Ag, Cu and/or Ni. On this frame an injection molded, reflective, white housing cup is placed to provide stability to the package and reflect lateral emitted light. The actual LED die is attached to the lead frame in the center of the package area with an transparent adhesive epoxy resin. This allows the lead frame to reflect downward emitted light towards the package top surface. It should be noted that a aside from single die configurations also package configurations with multiple dies connected in parallel or series exist as shown in section 2.3.1. An electrical contact between the

die(s) and the lead frame is established by Au bond wires. Finally, to provide a defined optical extraction path and protecting the die against environmental contaminants the housing cup is filled with an encapsulant – typically a siloxane based polymer. For the case of a phosphor deployment, section 2.3.1 displays different variants of phosphor distributions inside the cup. In most mid-power pcLED variants a proximate phosphor distribution is chosen due to the ease of manufacturing since the mixture of encapsulant and phosphor can be applied in a single step. However, the curing time in this process becomes crucial to prevent phosphor sedimentation. [107, 110, 111]

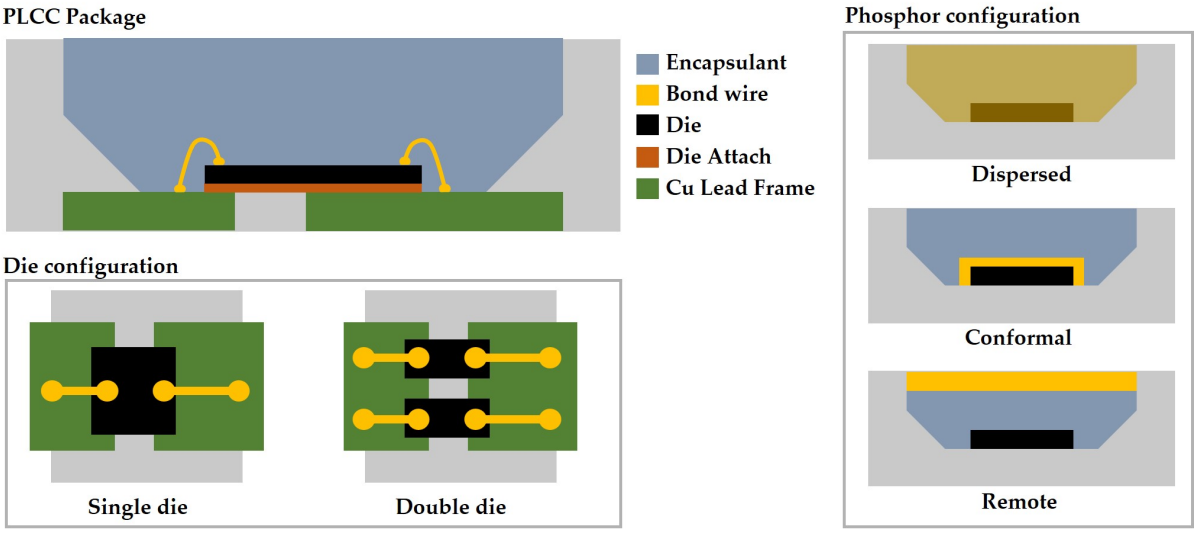

Figure 2.7: Schematic structure of typical Plastic Leaded Chip Carrier packages for mid-power LED applications: (a) key structure of a PLCC package, (b) top view of a single and double die configuration, (c) different phosphor distribution schemes [2].

As elaborated in the previous sections, both the dies and phosphors efficiency is highly temperature dependent. Therefore, a proper thermal package design in terms of heat dissipation is essential. In fig. 2.8 the equivalent thermal circuit of a phosphor-converted Light-emitting Diode (pcLED) package is shown.

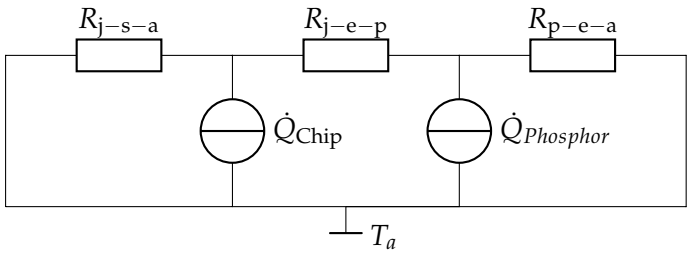

Figure 2.8: Schematic of heat flow inside a PLCC package [111].

Two heat sources $\dot{Q}$ can be identified: First, the LED die produces an undesired thermal power loss $P_{\text{th,Chip}} = P_{\text{el}} - P_{\text{opt}}$ during the conversion from electrical to optical power. This power loss is attributed to Ohmic losses in parasitic series resistances ($P_{\text{th,Chip}} = I^2 R_{\text{s}}$) and non-radiative recombination processes as Auger- or SRH-recombination. As a result a heat flux $\dot{Q}_{\text{Chip}} = \frac{\mathrm{d}P_{\text{th,Chip}}}{\mathrm{d}t}$ is induced into the package. Second, due to the phosphors thermal quenching a fraction of the dies emitted optical power is converted to heat $P_{\text{th,Phosphor}} = P_{\text{opt}}(1 - \eta_{\text{le}}(T))$ that subsequently induces a heat flux $\dot{Q}_{\text{Phosphor}}$. In order to achieve thermal equilibrium with the ambient surrounding, both heat fluxes are dissipated towards the packages surface. Along this path package material-specific thermal resistances $R_{\text{th}} = d(\kappa_{\text{c}} A)^{-1}$ introduce a temperature difference $\Delta T = \dot{Q} R_{\text{th}}$ where d is the materials thickness, A the cross-sectional area and κ_{c} the thermal conductivity. With respect to fig. 2.8 two main heat dissipation paths are observed. The first path $R_{\text{th,j-s-a}}$ mainly dissipates heat generated by $\dot{Q}_{\text{Chip}}$ from the dies junction (j) via the die attach and solder pads (s) towards the ambient (a). However, a small fraction of $\dot{Q}_{\text{Chip}}$ is also dissipated into the encapsulant (e) and phosphor (p) through $R_{\text{th,j-e-p}} \ll R_{\text{th,j-s-a}}$ combining with second heat flux induced by $\dot{Q}_{Phosphor}$ that is dissipated towards the packages upper surface via $R_{\text{p-e-a}}$. If no phosphor is applied to the package $\dot{Q}_{Phosphor}$ is shorted and the dissipation path towards the upper surface becomes $R_{\text{th,j-e-a}}$. It should further be noticed, that a very small fraction of heat is dissipated parallel via convection ($\propto \Delta T$) and as radiation ($\propto \Delta T^4$).

2.3.2 Optical Polymers in LED Packaging

Within the final package assembly, polymeric materials serve various functions such ranging from providing mechanical stability to defining and enhancing the overall light extraction of the package. The four most commonly used polymers – Bisphenol-A Polycarbonate (BPA-PC), Poly(methyl methacrylate) (PMMA), Epoxy Polymers as well as siloxanes like Polydimethylsiloxane (PDMS) and Polymethylphenylsiloxane (PMPS) – are presented below. A brief summary of these optical polymers key features is given in table 2.3.

Table 2.3: [39, 112].

Polymer	PMMA	BPA-PC	Epoxy	PDMS	PMPS
T_{g} (°C)	105	145	>110	−127	−23
CTE ($10^{-5}\,\text{K}^{-1}$)	7	6.5	2.3	93	-
γ_{T} ($10^{-3}\,\text{N m}^{-1}$)	41.1	-	-	21.5	25.5
P_{CO_2} (Barrer)	0.34	8	-	3250	-
$P_{\text{H}_2\text{O}}$ (10^3 Barrer)	3.2	-	-	36	-
RI (-)	1.5	1.6	1.53	1.42	1.55

T_{g}: glass temperature, CTE: Coefficient of Thermal Expansion, γ_{T}: Surface Tension, P_x: gas permeability, RI: refractive index
(-): no (valid) information available

Epoxy (Molding) Compounds

In electronic packaging Epoxy Molding Compounds (EMC) are used widely for housing since they offer various advantages as table 2.4 highlights. Especially in LED packages EMC have two main applications as die attachment adhesive and as housing cup in PLCC packages. Since both applications demand different properties, such as high adhesive strength or high stiffness, its good and variable processability stands out. Often the epoxy group shown in eq. (2.32) is utilized as a linker molecule between other application specific molecules. [2, 39, 108, 113]

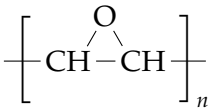

(2.32)

Table 2.4: Advantages and disadvantages of Epoxy Molding Compounds used in LED applications [2, 39, 108, 113].

Advantages	Disadvantages
Low cost	High photo-thermal degradation
Wide availability	High brittleness
Good processability	
High thermal stability	
High moisture resistance	
High adhesive strength	

Polycarbonate

Bisphenol-A Polycarbonate in LED applications is most commonly used polycarbonate for lenses, in housing cups linked by EMC and in early LED generation encapsulants. Its molecule structure presented in eq. (2.33) provides a high stiffness but is very sensitive to photo-thermal stress due to the weak carbonate group as shown in table 2.5. [2, 39, 108]

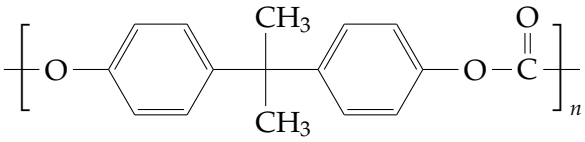

(2.33)

Polymethyl methacrylate

As of its excellent transmittance in the Ultraviolet Spetrum (UV)-VIS range Poly(methyl methacrylate) (eq. (2.34)) is very well suited for lenses in LED packages. On the downside, the acid part of its ester group (R−C(=O)−OH) is very prone to (hygro-)thermal degradation. table 2.6 gives an overview on the advantages and disadvantages of PMMA. [2, 39, 108]

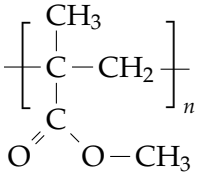

(2.34)

Table 2.5: Advantages and disadvantages of Bisphenol-A Polycarbonate used in LED applications [2, 39, 108].

Advantages	Disadvantages
Wide availability	High photo-thermal degradation
High thermal stability	
High moisture resistance	
High elastic module	
High fracture resistance	

Table 2.6: Advantages and disadvantages of Poly(methyl methacrylate) used in LED applications [2, 39, 108].

Advantages	Disadvantages
Wide availability	Low moisture stability
Very low cost	Low thermal stability
High stiffness	Low abrasion resistance
High transmittance	

Silicone

Currently silicone polymers (eq. (2.35)), in particular PDMS and PMPS, are widely utilized in LED package encapsulants and lenses. A key feature of silicone based encapsulants is their modifiability as Si atom of the Si−O backbone offers place for two organic group attachments like methyl (CH_3) or phenyl (C_6H_5). These organic attachments offer two benefits by first shielding the siloxane backbone and on secondly tuning the polymers optical and thermal properties by adjusting the attachments ratio. However, these benefits are accompanied by higher costs and a high gas and moisture permeability that may trigger additional degradation effects. table 2.7 gives a summary of the advantages and disadvantages of silicones. [2, 39, 108]

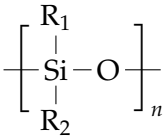

(2.35)

2.4 Efficiency Metrics

Derived from the previous discussed efficiencies of the separate LED parts this section will define an overall efficiency [2, 114]. This definition follows the path from the electrical input power P_{el} applied to the LED contact pads to the optical output power P_{opt} extracted from the packages surface. The power conversion efficiency η_{PCE} shown in eq. (2.36) specifies this ratio of extracted P_{opt} to injected P_{el} with the efficiency metrics for the following parameters: forward-voltage η_{VfE}, injection η_{IE}, radiation η_{RE}, light extraction η_{LEE} as well as the internal

Table 2.7: Advantages and disadvantages of siloxane polymers used in LED applications [2, 39, 108].

Advantages	Disadvantages
Good processability	Low stiffness
High transmittance	High Coefficient of Thermal Expansion (CTE)
High mechanical stress absorbance	Low adhesive strength
High biocompatibility	High moisture and gas permeability
High electrical stability	High cost

η_{IQE} and external quantum efficiency η_{EQE}. The respective metrics are defined in the subsequent paragraphs.

$$\eta_{PCE} = \eta_{VfE} \cdot \eta_{IE} \cdot \eta_{RE} \cdot \eta_{LEE} = \eta_{VfE} \cdot \eta_{IQE} \cdot \eta_{LEE} = \eta_{VfE} \cdot \eta_{EQE} \tag{2.36}$$

Forward-voltage efficiency

The total forward-voltage V_F of a LED is results from the addition of the semiconductors band gap energy hf/q and the additional voltage drop induced by parasitic series resistances along the current injection path $\Delta V_F = R_s I_F$ presented in section 2.1.4. Following the produced heat loss in R_s is calculated by $P_{th} = I_F(V_F - hfq^{-1})$. Subsequently, the forward-voltage efficiency η_{VfE} can be expressed following eq. (2.37).

$$\eta_{VfE} = \frac{P_{el} - P_{th}}{P_{el}} = \frac{hf}{qV_F} \tag{2.37}$$

Injection Efficiency

In section 2.1.3 the absence of charge carrier leakage was assumed for simplification and thus an injection efficiency of $\eta_{IE} = 1$ implied. However, in real LED a fraction charge carriers leaks out of the active region $\eta_{IE} < 1$ as a result of low hetero structure barriers or large polarization fields and thereupon recombine non-radiatively at the contacts or confinement regions. Since the number of injected electrons equal those of injected holes, the injection efficiency η_{IE} is described accordingly to eq. (2.38).

$$\eta_{IE} = \frac{I_{F,active}/q}{I_F/q} \tag{2.38}$$

Radiative Efficiency

As discussed in section 2.1.3 and section 2.1.3 charge carriers in the active region recombine by emission of an photon or phonon. The ratio between radiative and non-radiative recombination is described by radiative efficiency η_{RE} in eq. (2.39). The radiative efficiency highly corresponds to the quality of the semiconductor material.

$$\eta_{RE} = \frac{P_{opt,active}/hf}{I_{F,active}/q} = \frac{\tau_{radiative}^{-1}}{\tau_{non-radiative}^{-1} + \tau_{radiative}^{-1}} \tag{2.39}$$

Internal Quantum Efficiency

Combining η_{IE} and η_{RE} yields the full definition of the internal quantum efficiency η_{IQE} describing the in eq. (2.40) presented ratio of emitted photons from the active region to injected electrons.

$$\eta_{\mathrm{IQE}} = \eta_{\mathrm{IE}} \cdot \eta_{\mathrm{RE}} = \frac{P_{\mathrm{opt,active}}/hf}{I_{\mathrm{F}}/q} \tag{2.40}$$

Light Extraction Efficiency

Real LED devices show a discrepancy between the theoretical released photons from the active region and the actual measured photon yield. This difference is defined by the light extraction efficiency η_{LEE} given in eq. (2.41)). The reasons for a decreased η_{LEE} are manifold and range from absorption of photon within the semiconductor or metallic contacts to backscattering at interface region to total internal reflection trapping photons inside the semiconductor. In addition, the phosphors luminous efficiency $\eta_{\mathrm{LE}} \leq 1$ presented in section 2.2.2 has to be taken into account for pcLEDs otherwise η_{LE} may be neglected or set to 1.

$$\eta_{\mathrm{LEE}} = \eta_{\mathrm{LE}} \cdot \frac{P_{\mathrm{opt}}/hf}{P_{\mathrm{opt,active}}/hf} \tag{2.41}$$

External Quantum Efficiency

The relation between overall light extraction into free space to injected charge carriers is denoted by the external quantum efficiency η_{EQE} given in eq. (2.42) as a product of η_{IQE} and η_{LEE}.

$$\eta_{\mathrm{EQE}} = \eta_{\mathrm{LEE}} \cdot \eta_{\mathrm{IQE}} = \frac{P_{\mathrm{opt}}/hf}{I_{\mathrm{F}}/q} \tag{2.42}$$

3 Degradation Effects in Harsh Environments

This chapter provides an in-depth exploration of Light-emitting Diode (LED) degradation effects induced by harsh environmental conditions with a focus on package related failures. The first section presents common Accelerated Stress Test (AST) standards and methodologies in LED degradation experiments. Subsequently, the second section provides an all-encompassing literature review on degradation effects, their causes and the underlying processes.

3.1 Accelerated Stress Tests for LED Degradation Studies

During the design process of (opto)electronic components, like LEDs [115], it is aspired to reveal potential design flaws that may result in a gradual or complete failure over the course of the operational life of a Device Unter Test (DUT). Considering the LEDs potential prolonged lifetime of several 10^4 h at recommended operating conditions ASTs are carried to obtain an estimate on the devices expected lifetime and the influence of different stress factors on this very. In general, ASTs are grouped by their type, acceleration method, stress loading, stress source, stress type and the DUTs operational state as shown below within the Design of Experiment (DoE) procedure [116–118]:

1. **Test Type:** Accelerated Life Test (ALT) and Accelerated Degradation Test (ADT) are the two prevalent types. An ALT is carried out until a defined percentage of a population has exhibited a predefined failure criterion. This can either be complete loss of operation (catastrophic failure) or the gradual passing of a threshold parameter (parametric failure). Such tests are suitable for pass/fail setups and quantitative lifetime estimation. In scenarios that require an insight into the underlying degradation processes and their velocity ADT are applied by monitoring the population's performance during the whole test period. The additional information gain suits ADT for qualitative studies.

2. **Acceleration Method:** Typically AST are carried out at stress levels within DUTs specified operating conditions. Tests with stress levels exceeding those conditions are denoted as Highly Acclerated Stress Test (HAST) such as HALT and HADT.

3. **Stress:** The lifetime or performance limiting stress variable(s) S_i. In the context of LED degradation studies, primarily electrical (current, voltage) or environmental variables (ambient temperature, relative humidity) are evaluated.

4. **Stress Source:** It is distinguished between intrinsic and extrinsic stress sources. An intrinsic stress is provoked solely by the DUTs operational condition, like the LEDs forward current. Environmental conditions as ambient temperature or relative humidity represent extrinsic stress sources. However, an interaction of both source types is possible depending on the selected DUT and DoE.

5. **Stress Loading Profile:** By varying the stress level different operating and environmental conditions, like DUT switching or weather changes, are simulated to provoke specific

failures mechanisms. The majority of LED AST is exercised under a constant bias c_0 in the form of a function $S_i(t) = c_0$. Alternative loading profiles can be ramp functions $S_i(t) = c_0 + mt$ where m is the ramps slope, step up or step down profiles $S_i(t) = c_0 \pm \sum_i c_i H(t - t_i)$ with the time shifted Heaviside Step Function $H(t)$ or cyclic profiles $S_i(t) = f(t + t_P)$ with a periodic behavior.

3.1.1 Industry Standards for LED Reliability Tests

The vast majority of semiconductor related standardization aspects, including reliability tests, are defined by the Joint Electron Device Engineering Council Solid State Technology Assiciation (JEDEC). Based on JEDEC JESD22 standards [119–124] use case specific derivatives have been implemented, such as for automotive lighting qualification (AEC-Q102 [125]) by the Automotive Electronics Council (AEC) or for general lighting purposes (LM-80 [43]) by the Illuminating Engineering Society (IES). The AEC-Q102 standard focuses on a quantitative qualification by applying pass/fail criterions over time periods of 1000 h. Whereas, LM-80 considers the LEDs performance by means of luminous/radiant/photon flux, forward voltage and chromaticity coordinates at time periods of at least 6000 h with measurement intervals of $\Delta t = 1000$ h. Table 3.1 gives an overview on prevailing test methods.

Table 3.1: Commonly used JEDEC standards in reliability testing and their use case specific derivations for LED reliability AST

Test	Loading	Duration	JESD22	Derived Standard
WHTOL	bias	1000 h	A101[119]	AEC-Q102-A2a[125]
WHTOL	bias	1000 h	A101[119]	AEC-Q102-A2b[125]
PTC	cyclic	$N = 1000$	A104[121]	AEC-Q102-A3a [125]
TC	cyclic	$N = 1000$	A105[122]	AEC-Q102-A4[125]
HTOL	bias	1000 h	A108[123]	AEC-Q102-B1a[125]
HTOL	bias	1000 h	A108[123]	AEC-Q102-B1b[125]
HTOL	bias	1000 h	A108[123]	LM-80[43]
PC	-	-	A113[124]	AEC-Q102 A1[125]

PC: Pre Conditioning, HTOL: High Temperature Operating Life, WHTOL: Wet High Temperature Operating Life, TC: Temperature Cycling, PTC: Power Temperature Cycling

3.2 Causes, Effects and Mechanisms of LED Degradation

This section presents a comprehensive literature review on the causes and effects of LED degradation. First, relevant physical processes and chemical reactions are explained for the reader's further understanding. Following, possible occurring failure mechanisms in the die itself, the interconnects and the LED package, along with their failure causes and effects, are examined. Each section first provides a detailed explanation of the mechanisms that occur and finally gives a tabular summary with relevant sources.

3.2.1 Basic Physical Effects and Chemical Reactions

Diffusion [113] describes the process of particle transport, e.g. moisture or dopants, between two regions of different concentrations. The spatial difference in concentration $C(\vec{r},t) = \mathbf{C}$ with $\vec{r} = \{x,y,z\}$ provokes a concentration flux $\vec{J}(\vec{r},t) = \mathbf{J}$ along the concentration fields gradient. The particles quantity and direction of movement from regions with higher concentration towards those with a lower concentration can be modeled by Fick's first law in eq. (3.1) [126] with the temperature dependent diffusion coefficient $D(T)$. Subsequently, the change in concentration at a given spatial coordinate $\vec{r}_i$ is derived from eq. (3.2) according to Fick's second law [126].

$$\mathbf{J} = -D(T)\vec{\nabla}\mathbf{C} \tag{3.1}$$

$$\frac{\partial \mathbf{C}}{\partial t} = \vec{\nabla}\mathbf{J} = \vec{\nabla}\left(D(T)\vec{\nabla}\mathbf{C}\right) \tag{3.2}$$

Further, the diffusion coefficient $D(T)$ has an Arrhenius-like exponential dependency of the temperature T as shown for the isotropic (non-directionally) case in eq. (3.3) with a pre-factor D_0, Boltzmann's constant k_B and the activation energy E_a. In anisotropic (directionally) cases, as e.g. in cristal lattices, the diffusion coefficient becomes a tensor $\mathbf{D}(T) = \vec{D}_{xyz}(T) \in \mathbb{R}^{3\times3}$. It should be noted that polymers however, exhibit different diffusion coefficients for temperatures above and below the their glass transition temperature $D_1(T < T_\mathrm{g}) \neq D_2(T \geq T_\mathrm{g})$ [127].

$$D(T) = D_0 \exp\left(-\frac{E_\mathrm{a}}{k_\mathrm{B}T}\right) \tag{3.3}$$

Considering the scenario of *moisture absorption* into a polymeric medium a direct moisture concentration measurement inside a given volume V is not possible, thus the relation between the mass uptake at a given time M_t with respect to the equilibrium state M_∞ at complete saturation level shown eq. (3.4) is utilized.

$$\frac{C_t}{C_\mathrm{sat}} \propto \frac{M_t}{M_\mathrm{sat}} \tag{3.4}$$

To give a simplified example [128, 129] of the above scenario a one-dimensional ($\vec{r} = \{x\}$), infinite plate with the thickness h is considered. Separating the temporal and spatial part of eq. (3.2) yields an Partial Differential Equation (PDE) of the type $\partial_t f(t,x) = k\partial_x^2 f(t,x)$. Applying a Taylor series expansion on the PDEs analytical solution results in the approximation eq. (3.5). Subsequently, the diffusion coefficient $D(T)$ can be derived from the initial linear slope at $M_t/M_\mathrm{sat} < 0.5$ of the first order expansion with a reasonable low error further simplifying eq. (3.5) to eq. (3.6) additionally pointing out the $\sqrt{t}$-dependence of the diffusion process.

$$\frac{M_t}{M_\mathrm{sat}} = 1 - \frac{8}{\pi}\sum_{n=0}^{\infty}\frac{1}{(2n+1)^2}\exp\left[-\frac{(2n+1)^2\pi^2 D(T)}{h^2}t\right] \tag{3.5}$$

$$0.5 \overset{!}{>} \frac{M_t}{M_\mathrm{sat}} \approx \sqrt{cD(T)t} \quad \text{with} \quad c = \frac{16}{\pi l^2} \tag{3.6}$$

Especially in polymers, multiple experiments [128–131] reported a non-Fickian moisture uptake. These observations can attributed structural changes introduced by former moisture absorption in the polymer [128]. For this reason additive Dual-Stage [128] or Multi-Stage [130] diffusion

models were proposed that superimpose multiple Fickian or Fickian with non-Fickian diffusion trajectories like $C(\vec{r},t) = \sum_i C_i(\vec{r},t)$.

Subjected to excessive heat, (UV-VIS) radiation or the presence of catalyst residuals (e.g. Pt from siloxane processing) polymers can undergo an *Autoxidation Cycle* [132, 133] enforcing chain scission (depolymerization) and cross-linking reactions (linkage between polymer chains). This chain reaction cycle includes three phases: Initiation by free polymer radical ($R^\bullet$) formation (1), propagation through Oxygen intake and peroxy radical ($ROO^\bullet$) creation (2) and finally termination of available radicals (3).

1. The cycle is initiated by the generation of free radicals due to thermal or radiative bond cleavage by either Hydrogen abstraction following the reaction in eq. (3.7) or scissioning of C−C bonds as eq. (3.8) shows.

$$R{-}H \xrightarrow{hf,T} R^\bullet + H^\bullet \tag{3.7}$$

$$R{-}R \xrightarrow{hf,T} R^\bullet + R^\bullet \tag{3.8}$$

2. After initiation, the chain reaction propagates further under increasing Oxygen intake following eq. (3.9) and peroxy radical generation. The newly formed highly reactive peroxy radicals subsequently cleave additional polymer bonds resulting in additionally chain scission according eq. (3.10). Highly thermally- and radiation-unstable Hydroperoxide (ROOH) side products are then decomposed into free oxy ($O^\bullet$) and hydroxy ($^\bullet OH$) radicals (eq. (3.11)) that further accelerate chain scission (eq. (3.12) and eq. (3.13)). Additional, excessive water resulting as a byproduct of eq. (3.13) can further initiate hydrolysis reactions.

$$R^\bullet \xrightarrow{O_2} R{-}OO^\bullet \tag{3.9}$$

$$R{-}OO^\bullet \xrightarrow{R-H} R^\bullet + R{-}OOH \tag{3.10}$$

$$R{-}OOH \xrightarrow{hf,T} R{-}O^\bullet + {}^\bullet OH \tag{3.11}$$

$$R{-}O^\bullet \xrightarrow{R-H} R^\bullet + R{-}OH \tag{3.12}$$

$${}^\bullet OH \xrightarrow{R-H} R^\bullet + H_2O \tag{3.13}$$

3. Lastly the chain reaction gets terminated by cross-linking of free radicals to non-radical products. Various termination reactions are possible like bonding of two backbone structures (eq. (3.14)) as a reverse reaction of eq. (3.10) likewise the termination of oxy or peroxy radicals eventually forming chromophore impurities (eqs. (3.15) to (3.18)). Moreover, Oxygen released as a byproduct in eq. (3.10) and eq. (3.18) propagates the chain reaction cycle.

$$R^\bullet + R^\bullet \longrightarrow R{-}R \tag{3.14}$$

$$2\,R{-}OO^\bullet \longrightarrow ROOR + O_2 \tag{3.15}$$

$$R^\bullet + R{-}OO^\bullet \longrightarrow ROOR \tag{3.16}$$

$$R^\bullet + R{-}O^\bullet \longrightarrow ROR \tag{3.17}$$

$${}^\bullet OH + R{-}OO^\bullet \longrightarrow R{-}OH + O_2 \tag{3.18}$$

As formerly indicated the presence of water, due to external moisture ingress or as a reaction side product of preceded Autoxidation reactions, can initiate *Hydrolysis* [134] reactions scissioning the polymeric backbones Si−O or C−O bonds in solixanes and carbon-based polymers respectively. The reverse reaction, e.g. if one product is an alcohol and the other is acidic, establishing cross-linkage between polymer chains is denoted as *Condensation*. The formation of chromophore impurities by the latter is equally possible.

$$\mathrm{R-O-R + H_2O \underset{\text{Condensation}}{\overset{\text{Hydrolysis}}{\rightleftharpoons}} R{-}OH + HO{-}R} \tag{3.19}$$

3.2.2 Die Level

The semiconductor chip itself is prone to multiple degradation mechanisms limiting and reducing the optical output power emitted into the package [32, 38, 135]. As summarized in table 3.2 the four most prominent effects are *Lattice Defects*, *Die Cracking*, *Dopant Diffusion* and *Electromigration*.

Lattice Defects as shown in fig. 3.1 support the creation of energy levels within the band gap and thus enhancing non-radiative Shockley-Read-Hall (SRH) recombination resulting in a reduction of optical power [136]. These defects firstly occur native through misplacements within the semiconductor lattice by (In)Ga or N atoms missing at their expected lattice location, presence of such at unexpected locations (interstitials) or occupation of their counterparts position (substutionals). Secondly, impurities introduced by the production process provide an extrinsic cause of such defects. The p- and n-type conductivity is controlled by adding Mg and Si to the doping process both lead to impurities. Hydrogen ions, as a residual from the processes precursors enhances the passivation of p-type dopants like Mg [11, 137, 138]. Carbon and Oxygen promote undesired parasitic yellow luminescence at Ga vacancies [139–144]. Besides increased SRH recombination, an increase in shunt current bypassing the radiative center via tunneling through mid-gap defects in the Quantum Well (QW), spacer layer and Electron Blocking Layer (EBL) can lower the overall optical power [145, 146].

Originating from previously discussed native and extrinsic defects *Dopant Diffusion* processes towards the active region are triggered [126, 147]. Due to their Fickian behavior, Joule heating and high temperature in general accelerates the diffusion of residual H^+ resulting in the previously described Mg acceptor passivation and a decreased electrical field within the depletion region. This however, increases the forward current and therefore lowers the charge carrier lifetimes as a result of faster deep level recombination [138, 147].

Electromigration represents another diffusion path from the Ohmic contacts towards the die initiated due to elevated electrical stress. Here metallic ions diffuse in the direction of the active region forming conductive paths along preexisting lattice defects [148–151]. In extreme cases, the conductive path shunts the active region and thus enables a high current flow thermally destroying the device.

Resulting from misaligned process parameters during the manufacturing, such as material concentrations or temperature slopes, alongside with high Joule heating during operation *Die Cracking* is promoted as illustrated in fig. 3.1. The consequences range from a decrease in optical power up to total breakdown depending on the cracks location. These cracks occur in the form of open groves or facets along the LED's die as a result to thermomechanical stress of wrongly adjusted heating or cooling slopes. This stresses is induced by the large difference in Coefficient of Thermal Expansion (CTE) between the substrate layer (Sapphire, Silicon) and the

(In)GaN [152–154]. To reduce emerging thermomechanical stress a buffer layer with a moderate CTE (e.g. AlAs, AlN, AlGaN, SiN or superlattices) is introduced in between both [10, 155–163].

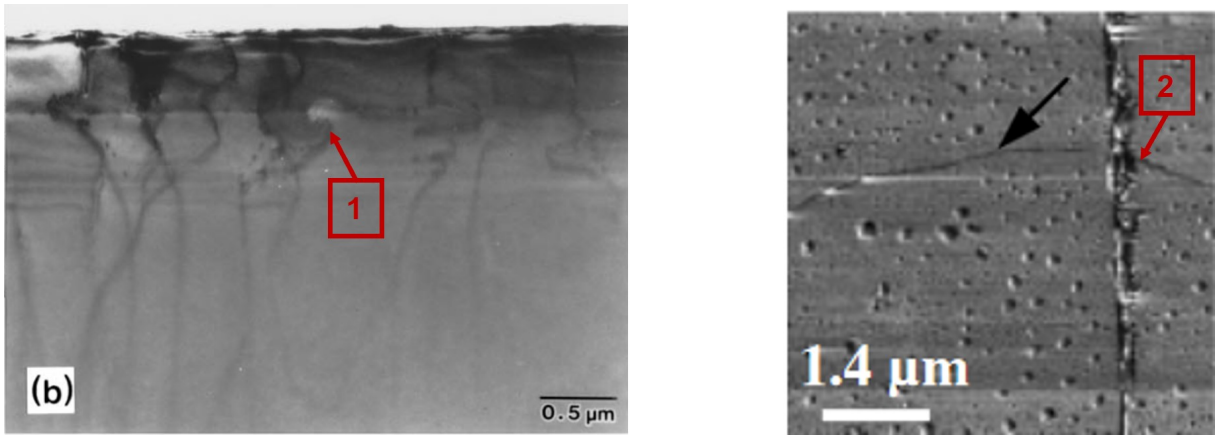

Figure 3.1: Examples of typical die level failures: (1) TEM image of lattice defects [164], (2) die cracking [153].

Table 3.2: Summary of die level degradation mechanisms, their stress cause and effect, the resulting failure mode and type based on [32, 38, 135] extended by additional primary sources.

Mechanism	Effect	Cause	Mode	Type	Source
Lattice Defect	Thermo-mechanical Stress	High Joule Heating Poor Processing	$\Phi \downarrow$ $I_{r,leak} \uparrow$ $R_s \uparrow$ $R_p \downarrow$	P	[11, 136, 137, 139–146, 154, 164–180]
Die Cracking	Thermo-mechanical Stress	High Joule Heating High Temperature Poor Processing	$\Phi \downarrow$	P/C	[152–154, 165, 181]
Dopant Diffusion	Thermal Stress	Poor Processing High Joule Heating High Temperature	$\Phi \downarrow$ $R_s \uparrow$ $I_F \uparrow$	P	[174, 182–194]
Electromigration	Electrical Overstress	High Temperature	OC	P/C	[148–151, 195]

Failure Mode: (OC) Open Circuit
Failure Type: (P)arametric, (C)atastrophic

3.2.3 Interconnect Level

To connect the die to the packages electrical contact pads in Plastic Leaded Chip Carrier (PLCC) packages wire bonding is the prevailing method. *Bond Wire Fatigue and Fracture, Metallic Contact*

Diffusion and *Electrostatic Discharge (ESD)* are the main acting failures at the interconnect level [32, 38, 135, 196] shown in table 3.3 and following explained in detail. Examples of the subsequent discussed failures are presented in fig. 3.2.
Thermomechanical stress introduced by high current to the interconnects promotes *Bond Wire Fatigue and Fracture*. Due to a difference in CTE of the bond wire ball and the contact surface the contact wears out over time detaching it from its contact surface [197–200]. At currents above the maximum specified operating point bond wire evaporation has been reported. Additionally, as a result of moisture ingress hygrothermal stress fosters shear forces on the bond wires due to the packages and encapsulants hygroscopic swelling [113].
Thermal and hygrothermal stress can further cause *Metallic Contact Diffusion*. In addition to the beforehand described diffusion on the metal-semiconductor interface, a metal-metal type diffusion was observed at the packages contact pads due to the Kirkendall Effect altering the contacts conductivity and subsequently increasing the parasitic series resistance R_s [201–204]. Moreover, if both metals have a sufficiently large difference in electronegativity moisture ingress can promote electrolysis effects [205–207].
ESD as the third failure mechanism on the interconnect level is mainly caused by an electrical overstress due to transient high voltage pulses. Even though pulses in both forward and reverse polarity may cause damage, the LED is rather sensitive to the latter due to avalanche breakdown effects [208, 209]. Studies revealed that in particular the contact layers and bonding pads edges as well as V-pits with prominent threading dislocations are prone to ESD [208–213]. A reduction ESD sensitivity can either be achieved by optimizing the manufacturing process by growing the (In)GaN onto the substrate at high temperatures of above 1000 °C [209, 214] or increasing the internal capacitance C_i to lower the overall dissipated energy $E_d = Q_c^2 C_i^{-1}$ where Q_c is the stored charge in C_i [215–217].

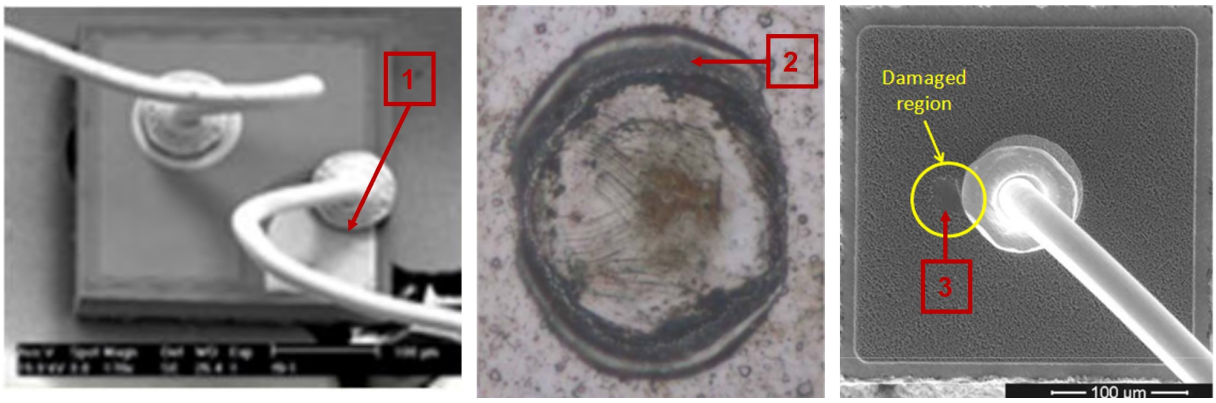

Figure 3.2: Examples of typical interconnect level failures: (1) bond pad/wire fatigue resulting in the detachmend of the bond pad from the die [165], (2) electromigration of Cu atoms into the bond attach area resulting in oxidation of the interconnect [207] and (3) damage of the bond pad areas surrounding due to electrical overstress [210].

3.2.4 Package Level

The package site, housing the die and enhancing the LEDs optical performance, is prone to various thermal and moisture related failures namely *Encapsulant Carbonization*, *Delamination*, *Reflective Layer Tarnishing*, *Encapsulant Yellowing*, *Bubble Generation*, *Lens Cracking* and *Phosphor*

Table 3.3: Summary of interconnect level degradation mechanisms, their stress cause and effect, the resulting failure mode and type based on [32, 38, 135, 196] extended by additional primary sources.

Mechanism	Effect	Cause	Mode	Type	Source
Bond Wire Fatigue and Fracture	Electrical Overstress	High Current	OC	C	[165, 197–200, 218]
	Thermo-mechanical Stress	Thermal Cycling Material Mismatch			
	Hygrothermal Stress	High Moisture			
Metallic contact diffusion	Thermal Stress	High Current High Temperature	$\Phi \downarrow$ $R_s \uparrow$ SC	P P C	[154, 170, 174, 201–207, 219–221]
	Hygrothermal Stress	High Moisture			
ESD	Thermal Stress	Poor Material Properties	OC	C	[165, 209–217, 222–225]
	Electrical Overstress	High Voltage			

Failure Mode: (SC) Short Circuit, (OC) Open Circuit
Failure Type: (P)arametric, (C)atastrophic

Degradation [32, 38, 39, 108, 135, 196] as summarized in table 3.4 and discussed below. In addition, examples of these effects are demonstrated in fig. 3.3.
Several studies observed dark spots on the dies and wire bonds surface reducing the devices overall light output [181, 219, 226–232]. Energy dispersive X-ray spectroscopy (EDX) analysis revealed an accumulation of Carbon and Oxygen at these dark spots originating from a *Carbonization of the Encapsulant* in proximity to the die induced by high temperature. A conductive path is initiated at these spots enabling parasitic current paths that substantially increase the encapsulants temperature and thereby starting a positive feedback loop.
The proper interfacing between different package materials, such as die to encapsulant or encapsulant to plastic mold, plays a key role in achieving a maximum light extraction efficiency from the package. Defects at these interface regions are referred to as *Delamination*. Experiments and simulations revealed a separation of the interface creating an air gap between both materials [151, 165, 200, 218, 223, 226–228, 233, 234]. This gap however, alters the interfaces reflectance from $\rho_{tot} = \rho(n_1, n_2)$ to $\rho_{tot} = \tau(n_1, n_{air})\rho(n_{air}, n_2)$ with the transmission τ and the materials refractive indices n_i. These air gaps are formed as a result of difference in material expansion leading to an adhesive force reduction between both materials at the interface. Experiments identified two sources for material expansion provoking shear forces at the interface layer: thermally induced stress due to the materials different CTE and hygromechanical stress caused by hydroscopic swelling due to moisture ingress. Both effects are correlated to a proper selection of interfacing materials. Furthermore, delamination at the dies interface lowers the packages thermal performance since these gaps add a large thermal impedance into heat conduction

path. Due to increased heating of the package thermally induced degradation effects can be accelerated.
Depending on the LED packages configuration *Tarnishing of the Reflective Layer* may decrease the light output substantially. The tarnishing is visible a gray or black deposit on the reflective layers surface caused by an oxidation reaction with air pollutants like Hydrogen Sulfide (H_2S) [40, 230, 235–239]. Especially highly reflective coatings of Ag or Ag-Cu alloys show an elevated vulnerability to sulfur-rich contaminants [240–244]. The underlying reaction can be split in multiple concurrent reactions triggered by Oxygen as well as Silver Oxide producing Silver Oxide (eq. (3.20)) or Silver Sulfide (eq. (3.21)) respectively. An acceleration of both reactions with temperature was observed as well as a maximum in reactivity at moderate humidity of around 54%rH [243]. It is notable that in eq. (3.21) water is produced as a side product that can provoke further hygrothermal and hygromechanical driven failure mechanisms.

$$O_2 + 4\,Ag \longrightarrow 2\,Ag_2O \tag{3.20}$$

$$Ag_2O + H_2S \longrightarrow Ag_2S + H_2O \tag{3.21}$$

Encapsulant Yellowing represents yet another important source of decrease in optical power and chromaticity shift of the LED [108, 245]. This term includes changes in the encapsulants structure and appearance ranging from slight discoloration, noticeable yellowing while maintaining parts of its transparency up to strong enbrittlement. The yellowing degree is determined by the applied stress, predominantly photodegradation and (hygro-)thermal stress, as well as the material in use, such as Bisphenol-A Polycarbonate (BPA-PC) and Epoxy Molding Compounds (EMC) [226, 230, 246–270] or Siloxanes like Polydimethylsiloxane (PDMS) and Polymethylphenylsiloxane (PMPS) [232, 248, 271–276]. Irradiation induced photodegradation is mainly attributed to UV radiation. At the Ultraviolet Spetrum (UV) range photon energy $E_{ph} \leq 300\,nm$ is absorbed by the Methyl ($-CH_3$) and Phenyl groups (cyclic $-C_6H_5$) aggregated around the polymeric backbone. By cleaving either aromatic groups or abstracting H^+ from such, an UV-enables Autoxidation cycle is initiated altering the polymers backbone structure (BPA-PC [39, 269, 277, 278], PDMS and PMPS [39, 276, 279]). Alongside with macroradical Autoxidation products presented in eqs. (3.9) and (3.11) also impurities (e.g. Pt residuals from the siloxane curing process) are suspected to majorly contribute to the yellow appearance since their absorption range into the blue to green Visible Spectrum (VIS) range [39, 260, 280, 281]. (Hygro-)thermal stress on the other hand provokes the breaking of bonds with low electronegativity like C–C and C=(O)–O from the BPA-PC backbone subsequently triggering auto-oxidation or hydrolysis reactions respectively [282–284]. Further Siloxane encapsulants feature a higher temperature resistance than BPA-PC based encapsulants. Studies revealed predominantly cross-linking due to condensed Silanol (SiOH) below $T < 300\,°C$. At temperatures above $T > 340\,°C$ the silicone backbone is prone to oxidation resulting in chain scission [39, 279, 285–288].
A visual noticeable *Bubble Generation* inside the encapsulant has been reported after exposing the LED to high temperature and high moisture conditions [196, 230, 250, 289–296]. Those bubbles may be attributed to either out-gassing of byproducts, like H_2O, CO_2, CO, H_2 or O_2, from the encapsulants degradation or air trapped during the encapsulants curing process due to poor processing. Similar to air gaps caused by delamination these bubbles alter the encapsulants transmission resulting in an overall decrease of light extraction efficiency.
Likewise to the latter, *Lens Cracking* is easily detectable through visual inspection. Induced by

thermomechanical or hygromechanical stress, cracks are inflicted by shear forces that change the lenses emission pattern. As a consequence the optical power is substantially reduced [108, 297–300].

In the case of a phosphor-converted Light-emitting Diode (pcLED) the *Phosphor* is also prone to *Degradation* under harsh environmental conditions causing a shift in chromaticity and a decrease in optical power. Subjected to elevated thermal conditions, either by the dies internal Joule heating or due to thermal quenching [301–310] of the phosphor itself, activator oxidation was reported [104, 311, 312]. A recent literature study on the thermal stability Eu^{2+} doped (oxy)nitride phosphors by Tian et al. [104] concluded that aside from excessive heat also a higher phosphor concentration as well as host lattices with high atomic bond covalence largely benefit the overall thermal degradation. The presence of elevated moisture is a second major degradation cause [237, 273, 276, 291, 294, 313–318]. As a result of moisture ingress hydrolysis effects damage the host lattice [276]. Further, within the prevailing extended water concentration, dissolving of the phosphor has been reported [294, 318].

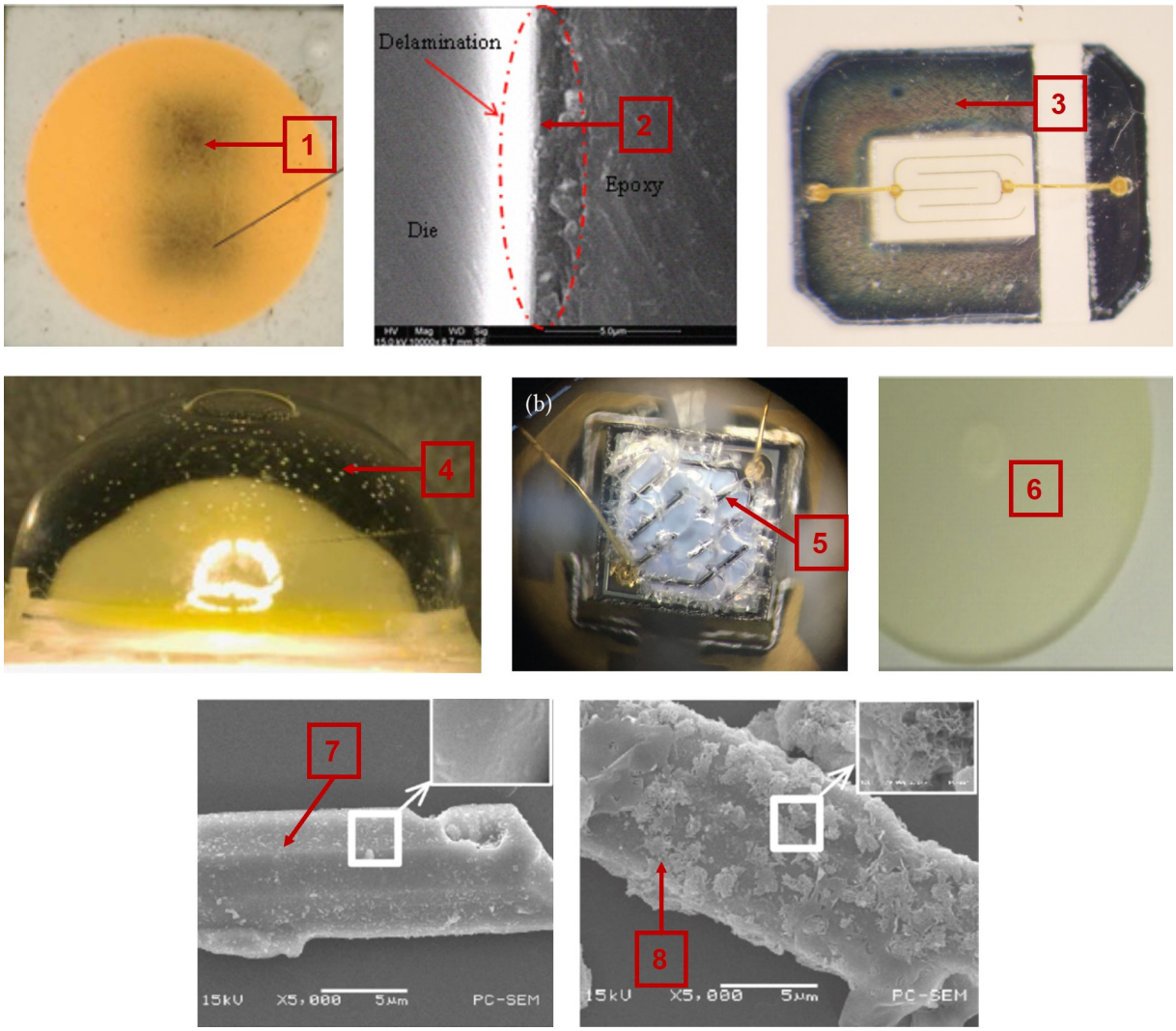

Figure 3.3: Examples of typical package level failures: (1) carbonization of the encapsulant along the dies / interconnects surface [273], (2) delamination of die from the encapsulant [228], (3) tarnishing / oxidation of the reflective lead-frame coating, (4) bubble generation within the encapsulant [295], (5) cracking of the encapsulant [298], (6) discoloration / yellowing of the polymer encapsulant [270] and (7,8) moisture induced phosphor degradation [319].

Table 3.4: Summary of package level degradation mechanisms, their stress cause and effect, the resulting failure mode and type based on [32, 38, 39, 108, 135, 196] extended by additional primary sources.

Mechanism	Effect	Cause	Mode	Type	Source
Encapsulant Carbonization	Electrical Overstress	High Joule Heating High Temperature	$\Phi \downarrow$	P	[219, 226–228, 233, 234, 320]
Delamination	Thermo-mechanical Stress Hygromechanical Stress	Material Mismatch Thermal Stress High Moisture	$\Phi \downarrow$ $R_{\text{th}} \uparrow$	P	[151, 165, 200, 218, 223, 226–228, 233, 234]
Reflective Layer Tarnishing	Oxidation	High Temperature Contamination	$\Phi \downarrow$ $\Delta u'v'$	P	[40, 230, 235–244]
Encapsulant Yellowing	Photodegradation Thermal Stress Hygrothermal Stress	High (UV) Radiation High Joule Heating High Temperature Phosphor Presence High Moisture	$\Phi \downarrow$ $\Delta u'v'$	P	[226, 230, 232, 246–276, 281]
Bubble Generation	Hygromechanical Stress	High Moisture Poor Processing	$\Phi \downarrow$	P	[196, 230, 289–295]
Lens Cracking	Thermo-mechanical Stress Hygromechanical Stress	High Temperature Poor Thermal Design High Moisture	$\Phi \downarrow$	P	[108, 297–300]
Phosphor Degradation	Thermal Stress Hygrothermal Stress	High Temperature High Joule Heating High Moisture	$\Phi \downarrow$ $\Delta u'v'$	P	[104, 237, 273, 276, 291, 294, 301–319]

Failure Type: (P)arametric, (C)atastrophic

4 Experiment - Accelerated Degradation Test

Based on the insights regarding LED devices and their degradation mechanism gathered in chapter 2 and chapter 3, this section, first, derives two research questions. Thereupon, an ADT experiment is designed. The last section, finally, presents performance metrics for degradation analysis derived from the previous measured parameters.

4.1 Research questions

The literature study on degradation effects of LED devices presented in section 3.2 revealed that especially moisture combined with high temperature can severely impact the LEDs optical performance. Considering ADT related studies [131, 196, 204, 226, 229–231, 273, 274, 289, 293–295, 318, 321–337], however, the following observations became apparent: First, in the early stages of LED reliability research (until 2005) fundamental electro-thermal mechanisms were investigated. In the following years a broad assessment of reliability studies was conducted to reveal electro-thermal degradation effects on research as well as commercial devices. Lately, since about 2015 an increased number of studies on the impact of environmental stress conditions on the device, such as moisture ingress, emerged. Secondly, while early studies focused mainly on high-power devices, a recently mid-power devices are gaining more attention due to an increased commercial interest. Third, only a few environmental stress related studies on mid-power devices have been conducted so far – mostly on white pcLEDs. The formerly commercial interest in LED devices for human-centered applications lately has expanded towards other fields of application such as horticultural lighting applications.
These new application fields have different spectral requirements demanding for phosphors aside from common YAG:Ce phosphors for white LED devices. As a result of the previous stated observations three research questions with respect to the devices reliability were derived:

Q1: How is moisture from the environmental surrounding impacting the optical performance of a LED device (for horticulture applications) with respect to different phosphor types?

Q2: If and how are devices under storage conditions ($I_F = 0$) affected by moisture ingress?

Q3: Which of the three common stress factors – electrical current, temperature or humidity – is the main contributor to the devices degradation?

4.2 Experimental Design

This section describes the DoE conducted with respect to the research questions presented in section 4.1 by first discussing a proper DUT selection and further elaborating on the test and measurement methods and procedure.

4.2.1 Device under Test

A market research of currently (January, 2021) commercial available LEDs for horticultural use cases has been conducted to select a proper DUT. The following list of criteria was used as a selection basis:

1. *Availability*: Widely commercially available devices for horticultural applications provided by common distributor.
2. *Power rating*: Mid-power rated ($P_{el} \leq 1\,W$) at typical operating conditions.
3. *Packaging*: Plastic Leaded Chip Carrier package design.
4. *Comparability*: Devices from one product line with a common LED emitter and package type.
5. *Spectral diversity*: Typical horticulture use case specific spectra like magenta, lime, photosynthetic active white or blue provided by different phosphor configurations (none, single and multiple phosphors).

Since LEDs for horticultural applications were fairly recently introduced to the market only the Lumileds LUXEON SunPlus 2835 product line [338] met the above listed requirements. Despite an extensive market research, other product lines exhibited either a high-power rating at typical operating currents or a lack of spectral diversity. An overview of the selected DUT types and their key parameters is given in table 4.1. Regarding their spectra, a blue LED was selected as a baseline to compare the pcLED devices to. To incorporate multiple different phosphor composites pcLEDs with a single phosphor lime and magenta spectrum as well as a multi-phosphor white spectrum were selected as shown in fig. 4.1.

Table 4.1: Overview of DUTs from the Lumileds LUXEON SunPlus 2835 product line used for this experiment [338].

Color	$I_{F,max}^{(a)}$ (mA)	$I_{F,typ}^{(a,b)}$ (mA)	$V_{F,typ}^{(b)}$ (V)	$R_{th,j-s}$ ($K\,W^{-1}$)	α_V ($mV\,K^{-1}$)	Part Number
Hort. White	480	120	2.85	13	-2.0	L1SP-PNK1002800000
Purple	480	120	2.85	13	-2.0	L1SP-PRP0002800000
Royal Blue	240	120	3.00	25	-2.5	L1SP-RYL0002800000
Lime	240	120	3.00	25	-1.7	L1SP-LME0002800000

[(a)] Horticulture White and Purple facilitate two parallel emitters thus $I_{F,max}$ is doubled, [(b)] measured at a junction temperature $T_j = 25\,°C$

4.2.2 Test Conditions

In accordance with the majority of conducted studies and common test standards an Accelerated Degradation Test design with a constant bias Wet High Temperature Operating Life stress level is selected for this experiment. This results in four independent variables to be recorded: time t and three acceleration variables $\mathbf{S} : \{S_i \in [rH_A, T_A, I_F]\}$ with the relative humidity rH_A,

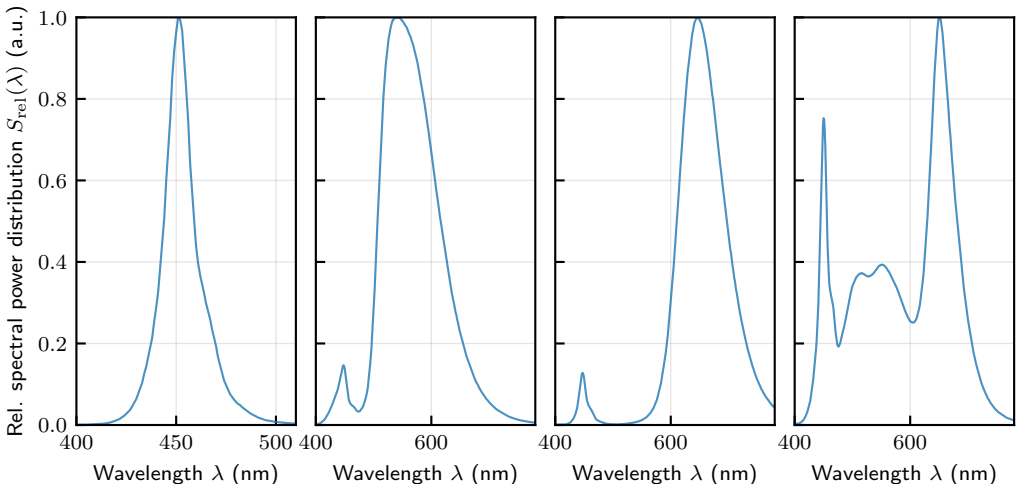

Figure 4.1: Relative spectral power distributions of the selected test subjects. From left to right: Royal Blue, Lime, Purple and Horticulture White.

ambient temperature T_A and the drive current I_F. Each variables stress bias levels are specified to represent real use cases – like dry shelf storage to greenhouse operational scenarios [339] or (im)proper thermal design of a luminaire as well as different drive current levels – while maintaining a broad stress level distribution as presented in table 4.2. Permutation of these stress levels from table 4.2 yields a total of 24 test conditions for each DUT type.

Table 4.2: Constant bias stress levels used for the experiments Accelerated Degradation Test.

Stress variable S_i	Stress level
Relative humidity rH_A	25 %, 55 % and 85 % [a]
Ambient temperature T_A	65 °C and 85 °C[b]
Drive current I_F	0 mA, 75 mA, 150 mA and 300 mA [c]
	0 mA, 150 mA, 300 mA and 600 mA [d]

[a] lower/upper recommended moisture range for greenhouses [339], [b] proper and inporper thermal luminaire design, [c] Blue and Lime DUT, [d] Horticulture White and Purple DUT.

4.2.3 Test Setup

Due to the large number of test conditions in total $N = 5$ DUT are tested per condition and LED type. Therefore, each DUT is placed on a separate 30 mm × 33 mm aluminum metal-core Printed Ciruit Board (PCB) alongside with a PT100 Resistance Temperature Detector (RTD) to measure the solder point temperature T_s in close proximity to the LED. Following, each conditions five DUT are screw-mounted on a separate 300 mm × 55 mm × 8 mm die cast aluminum heat sink plate and electrical connected in series. All plates sharing identical S_{rH} and S_T conditions are subsequently placed in one of three climate chamber of the type Memmert HCP105 that is set to the corresponding environmental conditions. Each LED string is powered by an individual

DC power supply of either the type Keithley 2200-72-1 or Rohde & Schwarz NGE103. During the whole test all environmental and electrical parameters were continuously monitored to ensure a steady operation. The test setup is schematically illustrated in fig. 4.2.

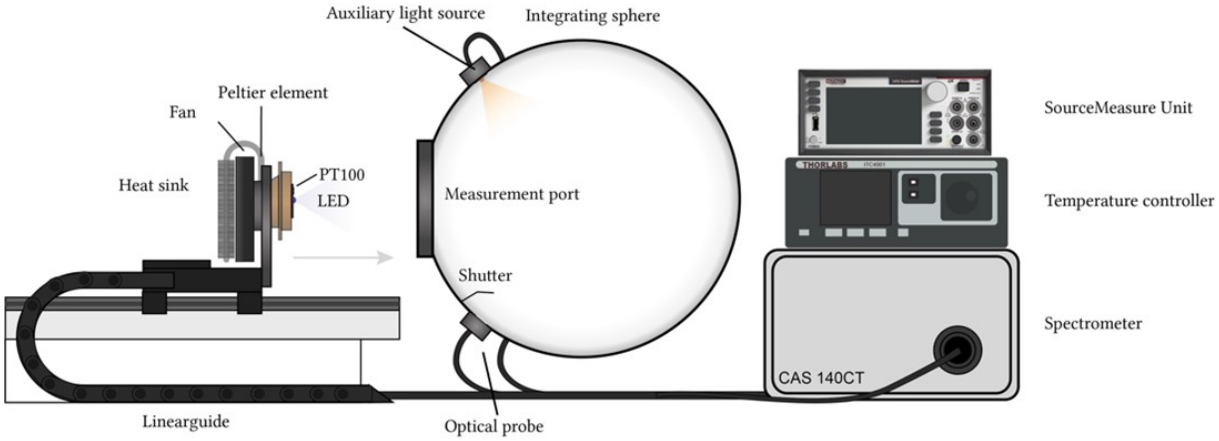

Figure 4.2: Test setup with three climate chambers and a computer controlled power supply and temperature measurement rack.

4.2.4 Measurement Setup

The identification of certain degradation effects, as previously discussed in section 3.2, often requires multiple measurement parameter. Therefore, a comprehensive set of spectral, electrical and thermal measurements as well as visual inspection are performed over the course of the experiment with the electro-optical measurement setup shown in fig. 4.3 and an Mentor Graphics T3ster® thermal impedance measurement system. The following paragraphs highlight the domain specific measurement setups. All measurements are conducted at laboratory conditions of $T_A = 25\,°C$ and $rH_A \approx 30\,\%$.

Temperature Stabilization

Considering the thermal sensitivity of a LED device, a proper thermal management during the measurement is crucial in order to prevent inaccurate results due to internal self heating or ambient induced temperature changes. For this purpose, the PCB is mounted on a thermoelectric tempered massive copper block ($m_{CU} \gg m_{DUT}$) with an electrical socket providing connections for LED driving and RTD temperature feedback reading as the left side of fig. 4.3 highlights. The temperature control for stabilizing the DUT to $T_s = T_{set} \pm 0.1\,K$ as well as RTD reading and driving the thermoelectric Peltier device is managed by a Thorlabs ITC4020 TEC Controller.

Electrical Measurement

The DUT is simultaneously electrically driven and measured by a Keithley 2450 type Source Measure Unit (SMU) in 4-wire Kelvin measurement configuration. During measurements the SMU provides two modes of operation: In order to measure IV-characteristics the SMU enters a *Voltage sweeping mode* and sweeps through a given voltage range $V_{sweep} = [V_{min}, V_{max}]$ with a resolution of n_{IV} steps. This mode provides an accuracy for voltage sourcing of $\leq 150\,ppm$ and

Figure 4.3: Electro-optical measurement setup for spectral and electrical LED characterization.

$\leq 300\,\text{ppm}$ for a current measurement, respectively. Alternatively, for driving the DUT the SMU is put into *constant current source mode* acting as a current source with a sourcing accuracy of $\leq 670\,\text{ppm}$ and $\leq 150\,\text{ppm}$ of voltage reading accuracy.

Spectral Measurement

The spectrally resolved measurement of the optical power is carried out by a setup consisting of a PTFE coated integrating (Ulbricht) sphere with a diameter of $d = 30\,\text{cm}$ connected via a fiber to an UV-VIS array-spectrometer model CAS140CT-152 by Instrument Systems. The spectrometer features a spectral measurement range of 200 nm to 800 nm with a resolution of $\Delta\lambda = 2.7\,\text{nm} \pm 0.3\,\text{nm}$. A spectral measurement is performed by the following protocol:

1. The DUT is placed at the integrating sphere's port by assistance of a linear guidance.
2. While DUT the temperature stabilizes the spectrometer performs a dark current measurement.
3. The SMU is set to the specified forward current.
4. The SMUs output is enabled and instantly a spectral measurement is triggered to prevent undesired self heating of the DUT.
5. Upon completion of the spectral measurement the SMUs output is disabled and both the spectral and electrical measurement values are read from the instruments.

Thermal Impedance Measurement

Often degradation effects in the electrical or optical domain can be traced back to structural changes within the package. With respect to the ongoing test of the DUT a non-destructive measurement method is mandatory which omits destructive measurement methods such as

micrographs. Therefore, a thermal impedance Z_{th} measurement method is selected that reveals structural changes by means of changes in thermal resistance R_{th} and thermal capacitance C_{th}. Computer tomography scanning was also considered but discarded due its comparatively long measurement time that would result in a reduction of the overall measurement throughput. A Z_{th} measurement [340] consists of two consecutive steps – a calibration measurement and the actual Z_{th} impedance measurement:

1. *Calibration measurement*: First, the forward voltage coefficient α_V is determined. Therefore, the DUT is stabilized to a given temperature before conducting a V_F measurement with the before mentioned SMU. To prevent self heating, the DUT is driven a short pulsed ($\approx 200\,\mu s$) current. This process is repeated at three different temperatures $T_j \approx T_s = [25\,°C, 50\,°C, 75\,°C]$. Due to the forward voltage's linear temperature dependence α_V at a fixed $I_{F,meas}$ is determined by a linear regression of the form $V_F(T_j|I_{F,meas}) = \alpha_V T_j + V_{F,0}$. For blue (In)GaN LED devices the α_V ranges from $-4.5\,mV\,K^{-1}$ to $-1\,mV\,K^{-1}$ [341]. This procedure is referred to as the *forward voltage method* [342]. Alternatively, a calibration measurement is also possible by the less accurate *peak-wavelength method* [2].

2. Z_{th} *measurement*: The DUT is first thermally stabilized at $T_s = [25\,°C$. Next, a thermal step function is introduced into the DUT by applying a heating current of $I_{F,heat} = 200\,mA$ over a duration of $t_{heat} = 60\,s$. Subsequently, the forward voltage change is continuously monitored at a measurement current of $I_{F,meas} = 1\,mA$ for $t_{meas} = 60\,s$. By taking the previous determined forward voltage coefficient α_V into account a thermal step response $\Delta T_j(t)$ is derived from $V_F(t)$. As shown in eq. (4.1) this step response correlates to the specific materials along the heat dissipation paths of the DUT expressed by R_{th} and C_{th}.

$$\Delta T_j(t) = P_{th} \sum_i R_{th,i} \left[1 - \exp\left(\frac{t}{\tau_{th,i}}\right)\right] \quad \text{with} \quad \tau_{th,i} = R_{th,i} C_{th,i} \tag{4.1}$$

   With the time constant spectrum $R^*(\tau)$ the time dependent thermal impedance is subsequently determined by eq. (4.2). By translating the continuous $Z_{th}(t)$ function into a discrete one $Z_{th}(n\Delta t)$ both $R'_{th,i}$ and $C'_{th,i}$ for each structural part are derived for a Foster network equivalent thermal circuit. A further transformation into a Cauer network equivalent thermal circuit yields the physically accurate $R_{th,i}$ and $C_{th,i}$ presented in fig. 4.4.

$$Z_{th}(t) = \int_0^\infty R^*(\tau) \left[1 - \exp\left(\frac{t}{\tau}\right)\right] d\tau \tag{4.2}$$

Lastly, the thermal properties of the LEDs package structure is visualized by plotting an differential structure function of the cumulative thermal resistance $R_{th}^{\Sigma} = \sum_i R_{th,i}$ versus $k_{th} = dC_{th}/dR_{th}$ as shown in fig. 4.4. Following, the actual junction temperature calculates to $T_j = P_{th} R_{th}^{\Sigma} + T_A$.

Visual Inspection

A visual inspection is carried out by a Bresser Advance ICD 10-160x optical microscope with a MikroCamII digital camera extension. The DUT is therefore illuminated by a cool white correlated color temperature ring light source. Subsequently, a digital photo of the image is saved.

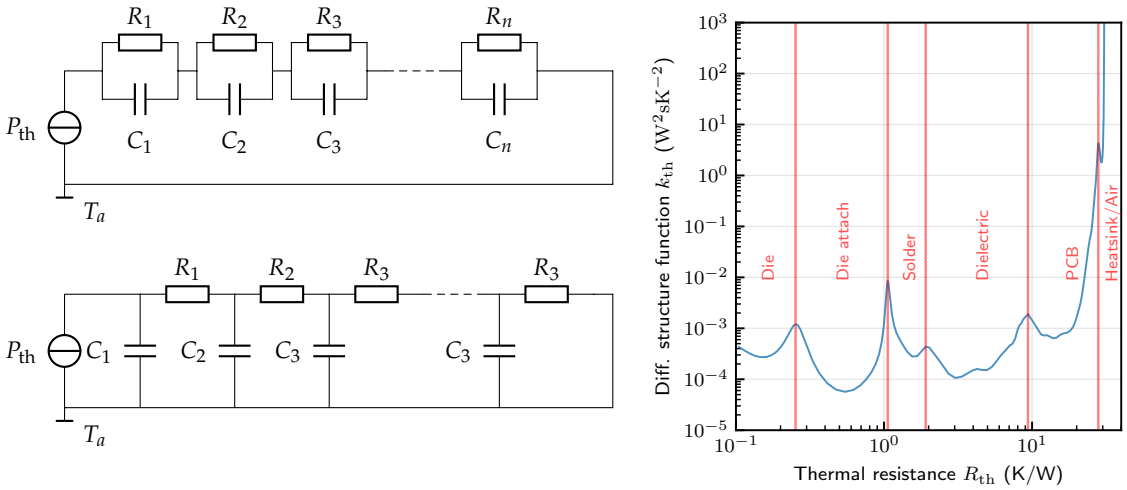

Figure 4.4: Thermal representation of a LED packages internal structure: (top left) Foster and (bottom left) Cauer thermal equivalent circuit as well as (right) differential structure function.

4.2.5 Test and Measurement Procedure

During the course of the experimental period, a long-term stable white pcLED reference is measured before each measurement cycle to allow compensation of any measurement setup related drift errors afterwards. The references Spectral Power Distribution (SPD) $S(\lambda|t, I_{\text{F}})$ is measured at five forward currents $I_{\text{F}} \leq I_{\text{F,max}}$ to track drive-point specific changes up into its high injection region while assuring not to trigger unintended current related degradation effects. Afterwards, an averaged correction factor $\bar{\gamma}(t;\lambda)$ for each measurement cycle is determined according to eq. (4.3).

$$\bar{\gamma}(t;\lambda) = \frac{1}{5}\sum_{I\in I_{\text{F}}} \frac{S_{\text{ref}}(\lambda|0,I)}{S_{\text{ref}}(\lambda|t,I)} \tag{4.3}$$

As a results of conducting a reference measurement at the beginning of every measuring date a sum of $N = 688$ reference measurements were obtained at 140 measurement dates with five measurement currents each. A total of 12 measurements were discarded due to errors during the spectral measurement. The correction factors of these 12 measurements were later linearly interpolated between the previous and subsequent date. As fig. 4.5 shows the V_{F} uncertainty is normally distributed with $\sigma = 90.7\,\text{ppm}$. Even if the extended 2σ uncertainty is assumed the values are well within the specifications provided by the manufacturer. Also the $\bar{\gamma}(t;\lambda)$ corrected optical power shown in fig. 4.5 presents a similar normally distributed behavior with $\sigma = 116.9\,\text{ppm}$. Due to the normal distribution of both uncertainties a setup drift is ruled out as also indicated by fig. 4.5.

The experimental procedure is split into measurement and test section. During the test each DUT is operated inside a climate chamber at the predefined stress conditions. In total this results in 80 devices under test – 4 DUT types $\times$ 4 I_{F} conditions $\times$ 5 DUT – simultaneously operated in each climate chamber at a given environmental condition (rH_{A}, T_{A}). The test period Δt_{Test} between two consecutive measurements is adaptability adjusted, ranging from daily measurement periods up to several weeks depending on the past degradation history. Since especially in the early test stage of $t \lessapprox 300\,\text{h}$ drastic performance changes may occur, measurements are performed on a daily basis. Depending on the past degradation history

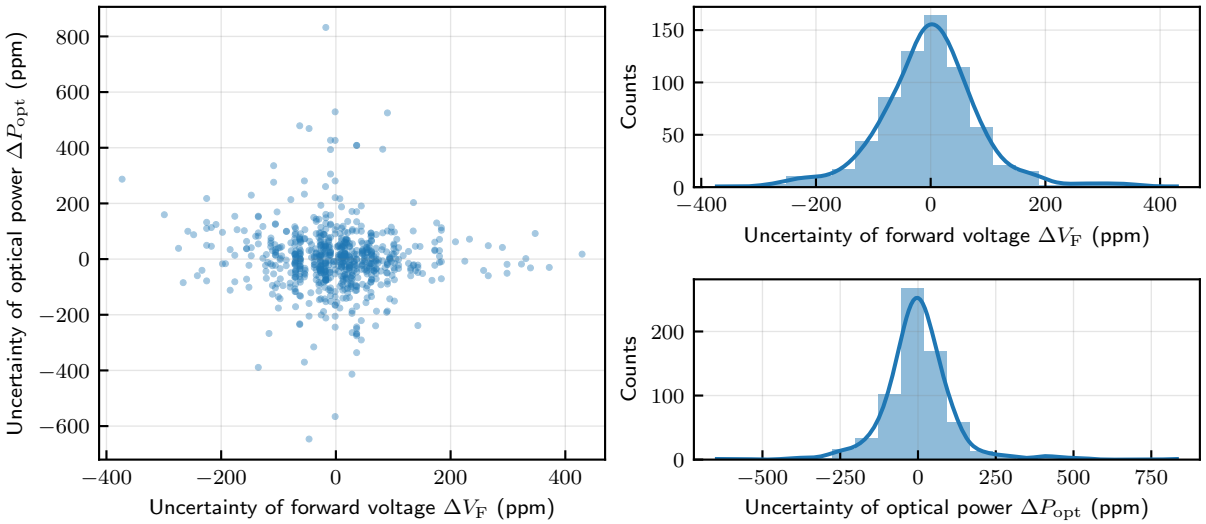

Figure 4.5: Stability of $N = 688$ reference LED measurements taken over the whole course of the experiment at different measurement currents: (left) correlation between normalized forward voltage and normalized optical power uncertainty, (b) normalized optical power uncertainty after spectral correction and (c) normalized forward voltage uncertainty.

either a regular or extended measurement is performed. A regular measurement includes a spectral measurement at nine different drive currents in the range of 1 mA to 10^2 mA and a forward biased IV characterization. For the extended measurement an additionally visual inspection is performed of every DUT as well as a thermal characterization of two predefined DUT per ($\mathrm{rH_A}$, T_{A}, I_{F})-condition. In total a normal measurement of 80 DUT takes about 4 h for the extended one this time doubles to 8 h. The whole test and measurement cycle is listed below:

1. Perform a spectral measurement of the reference LED.
2. Perform either a regular or extended measurement according to the experimental time schedule for all available devices.
3. Stop experiment if $P_{\mathrm{opt}}(t)$ has dropped below 70 % of its initial value L_{70} for the majority of devices under test else progress.
4. Place DUT in climate chamber and ramp up ($\approx$ 1 h) $\mathrm{rH_A}$ and T_{A} to test conditions.
5. Expose DUT for Δt_{Test} to specified stress conditions ($\mathrm{rH_A}$, T_{A}, I_{F}).
6. Let the DUT acclimatize for $t = 1$ h during ramp down of $\mathrm{rH_A}$ and T_{A} to lab environmental conditions to prevent unintentional damage to the DUT resulting from thermal-mechanical shock.
7. Remove the DUT from the climate chamber.

4.3 Derived Parameters

On the basis of the optical, electrical and thermal parameters previously obtained, further metrics relevant for a comprehensive analysis are computed. This section presents in particular derived optical and physics related metrics or calculations that were not covered in chapter 2.

Normalized Output Power

Often a qualitative comparison of degradation trajectories of different stress levels **S** challenging due to a high variability in magnitude resulting e.g. from different drive currents. Therefore, all optical power measurement values of a DUT at a certain stress condition **S** are referenced to their initial value $t = 0\,\mathrm{h}$. The normalized output power $\mathrm{NOP}(t;\mathbf{S})$, also denoted as the lumen maintenance $\mathrm{LM}(t;\mathbf{S})$ is presented in eq. (4.4) according to [43].

$$\mathrm{NOP}(t;\mathbf{S}) = \mathrm{LM}(t;\mathbf{S}) = \frac{P_{\mathrm{opt}}(t;\mathbf{S})}{P_{\mathrm{opt}}(0;\mathbf{S})} \tag{4.4}$$

Chromaticity Coordinates

Aside from the change in optical power the change in emitted chromaticity holds additional information about underlying degradation effects. Commonly, the CIE 1976 UCS chromaticity coordinates u', v' (eq. (4.5)) drift $\Delta u'v'$ [343] is taken into account for degradation analysis [32, 39, 344].

$$u' = \frac{6Y}{X + 15Y + 3Z}, \qquad v' = \frac{9Y}{X + 15Y + 3Z} \tag{4.5}$$

$$\Delta u'v'(t) = \sqrt{[u'(t) - u'(0)]^2 + [v'(t) - v'(0)]^2} \tag{4.6}$$

The Tristimulus X, Y and Z are derived from the SPD $S(\lambda) = P_{\mathrm{opt}}/(hf)$ with the standard observer color matching functions $\bar{x}(\lambda)$, $\bar{y}(\lambda)$ and $\bar{z}(\lambda)$ [343].

$$\begin{aligned} X &= K_{\mathrm{m}} \int \bar{x}(\lambda) S(\lambda) \mathrm{d}\lambda \\ Y &= K_{\mathrm{m}} \int \bar{y}(\lambda) S(\lambda) \mathrm{d}\lambda \\ Z &= K_{\mathrm{m}} \int \bar{z}(\lambda) S(\lambda) \mathrm{d}\lambda \end{aligned} \tag{4.7}$$

Phosphor to Blue Ratio

In order to get a first idea of the degradation site in a pcLED evaluating both the dies and phosphors peak wavelength ratio (phosphor to blue ratio, PBR) ξ has proven to be a suitable metric.

$$\xi = \frac{P_{\mathrm{opt,ph}}(\lambda_{\mathrm{p,ph}})}{P_{\mathrm{opt,die}}(\lambda_{\mathrm{p,die}})} = \begin{cases} < 1, & \text{phosphor degradation} \\ \approx 1, & \text{die degradation} \\ > 1, & \text{encapsulant degradation} \end{cases} \tag{4.8}$$

Yellowing Index

Especially when analyzing the discoloration or yellowing of polymers the yellowing index YI is considered as a metric for comparison. Despite its official discontinuation the YI standard ASTM D1925 [345] presented in eq. (4.9) is usually applied in LED degradation studies [108].

$$\mathrm{YI} = 100\,\% \cdot \left(\frac{1.28X - 1.06Z}{Y} \right) \tag{4.9}$$

(Maximum) Internal Quantum Efficiency and ABC-Model Parameters

The direct measurement of η_{IQE} is not possible within a LED package. However, under consideration of eq. (2.42) as assuming η_{LEE} a constant parameter and no leakage current ($\eta_{\mathrm{IE}} = 1$), η_{IQE} can be approximated by eq. (4.10) with the the maximum internal quantum efficiency $\eta_{\mathrm{IQE,max}}$ and its corresponding forward current $I_{\mathrm{IQE,max}} = I_{\mathrm{EQE,max}}$ [84, 114].

$$\eta_{\mathrm{EQE}}(I) = \frac{1}{\eta_{\mathrm{IQE,max}}} - \frac{1 - \eta_{\mathrm{IQE,max}}}{2\eta_{\mathrm{IQE,max}}} \left(1 + \frac{I}{I_{\mathrm{IQE,max}}} \eta_{\mathrm{EQE}}(I) \right) \sqrt{\frac{I_{\mathrm{IQE,max}}}{I} \eta_{\mathrm{EQE}}(I)} \tag{4.10}$$

The unknown parameter $\eta_{\mathrm{IQE,max}}$ is subsequently derived from the linear expression given by eq. (4.11) where $P_{\mathrm{norm}}(I) = P_{\mathrm{opt}}(I)/P_{\mathrm{opt,max}}$ is the optical power normalized with respect to the forward current and the slope $\tilde{m}$ [84].

$$\frac{\eta_{\mathrm{EQE,max}}}{\eta_{\mathrm{EQE}}(I)} = \tilde{m} \left[P_{\mathrm{norm}}^{0.5}(I) - P_{\mathrm{norm}}^{-0.5}(I) \right] + \eta_{\mathrm{IQE,max}} \tag{4.11}$$

Following, the ABC-models recombination coefficients and charge carrier concentration is determined. Therefore, according to [2], the bimolecular recombination coefficient B is set to an arbitrarily reasonable value of $B = 1 \times 10^{-12}\,\mathrm{cm^3\,s^{-1}}$. Since the actual structural parameters of the LED chip are also unknown the chip area A_{Chip}, the number of QW n_{QW} and the thickness of each QW d_{QW} are assumed to $A_{\mathrm{Chip}} = 1\,\mathrm{mm^2}$, $n_{\mathrm{QW}} = 5$ and $d_{\mathrm{QW}} = 3.5\,\mathrm{nm}$. Subsequently, by taking $\eta_{\mathrm{IQE,max}}$ into account, both recombination coefficients, A and C, are obtained from eq. (4.12) and eq. (4.13) with $r = qV_{\mathrm{active}}/\eta_{\mathrm{IE}}$ as well as from eq. (4.14) the charge carrier concentration n, respectively.

$$A = \sqrt{\frac{\eta_{\mathrm{EQE,max}} \left(1 - \eta_{\mathrm{IQE,max}}\right)^2 B}{4r\eta_{\mathrm{IQE,max}}}} \tag{4.12}$$

$$C = A^3 \frac{4r^2}{\eta_{\mathrm{EQE,max}}^2 \left(1 - \eta_{\mathrm{IQE,max}}\right)^2} \tag{4.13}$$

$$n = \sqrt{\frac{P_{\mathrm{opt}}/(hf)}{\eta_{\mathrm{IE}}\eta_{\mathrm{LEE}}V_{\mathrm{active}}B}} \tag{4.14}$$

5 Results and Degradation Analysis

Based on the experimental procedure highlighted in chapter 4 this chapter presents the obtained results followed by a subsequent analysis and discussion of the observed degradation effects with respect to the current state of literature elaborated in chapter 2 and chapter 3. In order to identify production outliers or binning variation in the DUT types population, first, a comprehensive initial characterization is conducted by means of the devices electrical, optical and thermal characteristics. Afterwards, the ADT results are presented and analyzed. Since all four DUT mainly differ by their die (single or two in parallel) and phosphor configuration while having the same package structure and a similar (In)GaN emission pattern of around 450 nm the Royal Blue device is firstly analyzed to provide a baseline for comparison. Subsequently, the Lime, Purple and Horticulture White devices are examined. Concluding, an overview on the overall identified degradation mechanisms is given in section 5.5.
It is noteworthy, that the following initial and degradation analysis is performed at fixed operating point with a nominal forward current of $I_{\mathrm{nom}} = I_{\mathrm{m}} = 100\,\mathrm{mA}$ if not specified otherwise. Further, due to a SMU configuration issue for the IV-measurement no representative IV-characteristics were recorded for the (55 % and 85 %, 85 °C)-conditions, reducing the total amount of IV-characteristics to $N = 80$ per DUT type. Since each group of DUT reaches the stop criteria defined in section 4.2.5 after different aging periods the total aging time varies from several 100 h to 6000 h.

5.1 Royal Blue LED Samples

The following section discusses the observed degradation effects of the Royal Blue DUT [338] during the experiment presented in chapter 4.

5.1.1 Initial Characterization

For the Royal Blue DUT a total of $N = 120$ devices have been characterized that subsequently were aged at the 24 previously specified ($\mathrm{rH_A}$, T_{A}, I_{F})-conditions. However, one device of the (25 %, 65 °C, 0 mA)-condition was removed from the further evaluation due to an error in the spectral measurement data at its initial 0 h characterization leaving a total of $N = 119$ analyzed devices.
The distribution and dependence of P_{opt} with respect to V_{F} is shown in fig. 5.1. On the left side of fig. 5.1 the mean optical power and its corresponding forward voltage is presented which ranges from $1.62 \pm 0.05\,\mathrm{mW}$ and $2.51 \pm 0.004\,\mathrm{V}$ at 1 mA to $312.62 \pm 3.15\,\mathrm{mW}$ and $3.14 \pm 0.017\,\mathrm{V}$ at 200 mA. At each of the nine measured forward currents I_{m} both the optical power and forward voltage are normally distributed as exemplary highlighted in the center plot of fig. 5.1 at I_{nom}, therefore it is assumed that all Royal Blue DUT originate from one production bin. This assumption is further confirmed by the SPD in the right plot of fig. 5.1 with a narrow main emission peak distribution of $\lambda_{\mathrm{p}}(I_{\mathrm{nom}}) = 452.7 \pm 1.5\,\mathrm{nm}$. The SPD additionally reveals a secondary peak at $\approx 467\,\mathrm{nm}$ which is attributed to phonon-replica transitions occurring

due to lattice defects resulting from GaN/InN lattice mismatches [346]. Varying the junction temperature T_j from 25 °C to 75 °C decreases the band gap causing a shift towards longer wavelengths of $\Delta\lambda_p = +2.24\,\text{nm}$. Simultaneously, a decrease in optical peak power of about $\Delta P_{opt}(\lambda_p) = -18.8\,\%$ originating from thermally enhanced SRH recombination is observed. In contrast, at room temperature a variation of $I_m = 1\,\text{mA}$ to 200 mA yields a shift towards smaller wavelengths of $\Delta\lambda_p = -3.84\,\text{nm}$ since band distortions QCSE within the QW structure are compensated by the increasing external electrical field applied.

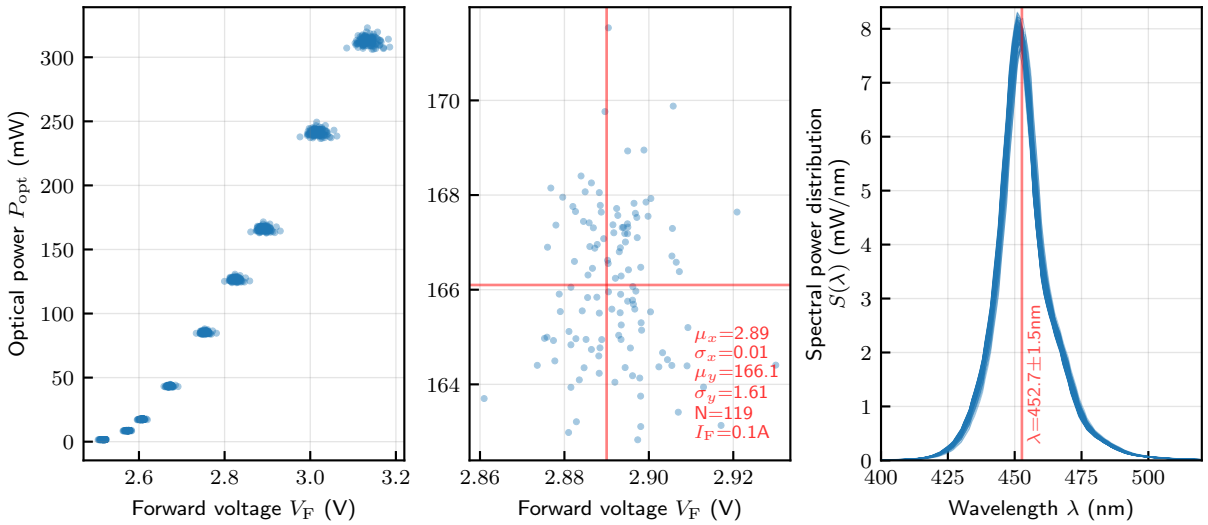

Figure 5.1: Initial optical measurements of the Royal Blue DUT: (left) optical power P_{opt} vs. forward voltage V_F at nine distinct measurement currents I_m, (middle) distribution of V_F and P_{opt} at $I_m = 100\,\text{mA}$ and (right) all measured SPDs at $I_m = 100\,\text{mA}$ with the die's mean emission peak wavelength $\lambda_p = \lambda_b$. All measurements respective sample count, mean, standard deviation and measurement condition are highlighted in red.

Addressing the external quantum efficiency η_{EQE}, fig. 5.2 presents the operating point dependent η_{EQE} and its distribution. Within the range of the given I_m shown in the left plot of fig. 5.2 the maximum EQE is determined to $\eta_{EQE,max} = 59.1 \pm 0.72\,\%$ at $I_m = 10\,\text{mA}$ which is in agreement with the value range of measurements in the literature [18, 114, 347, 348]. The average droop thus is specified to $\eta_{Droop} = -6.15\,\%$.
Regarding the electrical parameters a total of $N = 79$ IV-characteristics have been recorded as depicted by fig. 5.3. The left plot of fig. 5.3 displays the IV-characteristic of the remaining Royal Blue devices. Within the low injection area $V_F < 1.75\,\text{V}$ a strong deviation from the ideal diode characteristic is noticeable that can be attributed to parasitic shunt current paths with a high variance in parallel resistance of $R_p = 18.6 \pm 4.84\,\text{G}\Omega$. Only three devices exhibit distinct mid-gap tunneling [145, 146] in the low injection regime at $0.75\,\text{V} < V_F < 2.3\,\text{V}$. Along the diode region of $V_F = 2.3\,\text{V}$ to $2.7\,\text{V}$ a near ideal diode behavior is present with an ideality factor of $n_{ideal} = 1.18 \pm 0.03$. Increasing the forward voltage to $V_F > 2.7\,\text{V}$ reveals the expected dominance of parasitic series resistances in the high injection regime with $R_s = 2.13 \pm 0.06\,\Omega$. Derived from the above analyzed SPD additional colorimetric parameters such as the CIE UCS 1976 chromaticity coordinates u', v' [343] and the yellowing index YI [345] are of interest, as changes in such are linked to specific failure modes [344]. Since this DUT is a

monochromatic LED both chromaticity coordinates are distributed along the spectral locus at $(u', v')^T = (0.2 \pm 0.0015, 0.082 \pm 0.002)^T$ presented in the left plot of fig. 5.4. On the right side of fig. 5.4 the distribution of the initial yellowing index is displayed with a YI $\approx -2715 \pm 75$. Furthermore, the initial junction to solder pad thermal resistance of $R_{\mathrm{th,j-s}} = 22.19 \pm 3.38\,\mathrm{K\,W^{-1}}$ is in agreement with the manufacturer's specifications [338].

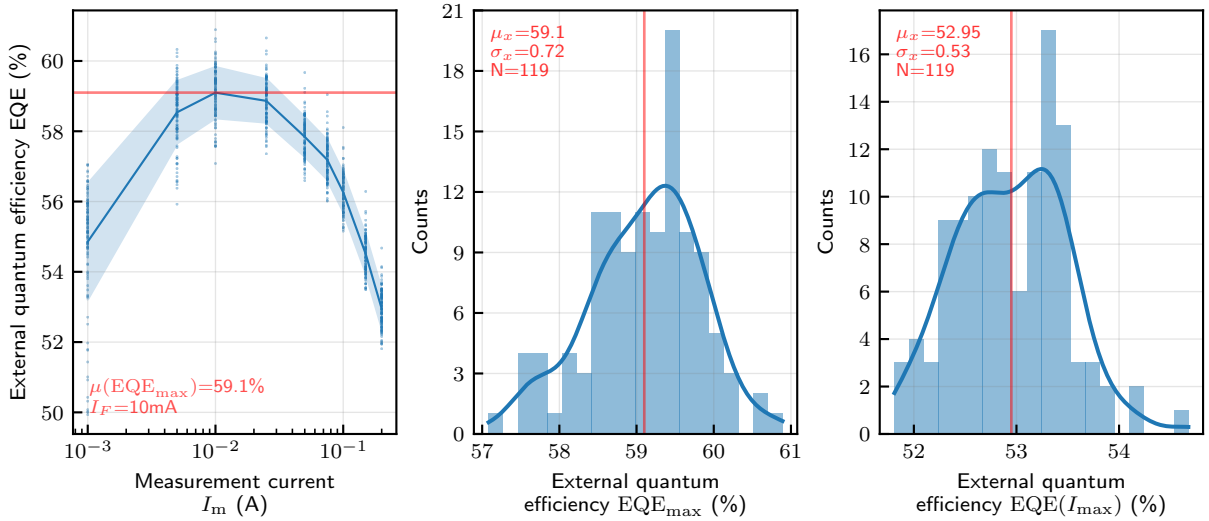

Figure 5.2: Initial EQE measurements of blue DUT: (left) external quantum efficiency EQE at nine distinct measurement currents I_m, (middle) distribution of maximum external quantum efficiency $\mathrm{EQE_{max}}$ at $I_\mathrm{EQE,max}$ and (right) distribution of EQE at maximum measurement current $I_\mathrm{m,max}$. All measurements respective sample count, mean, standard deviation and measurement condition are highlighted in red.

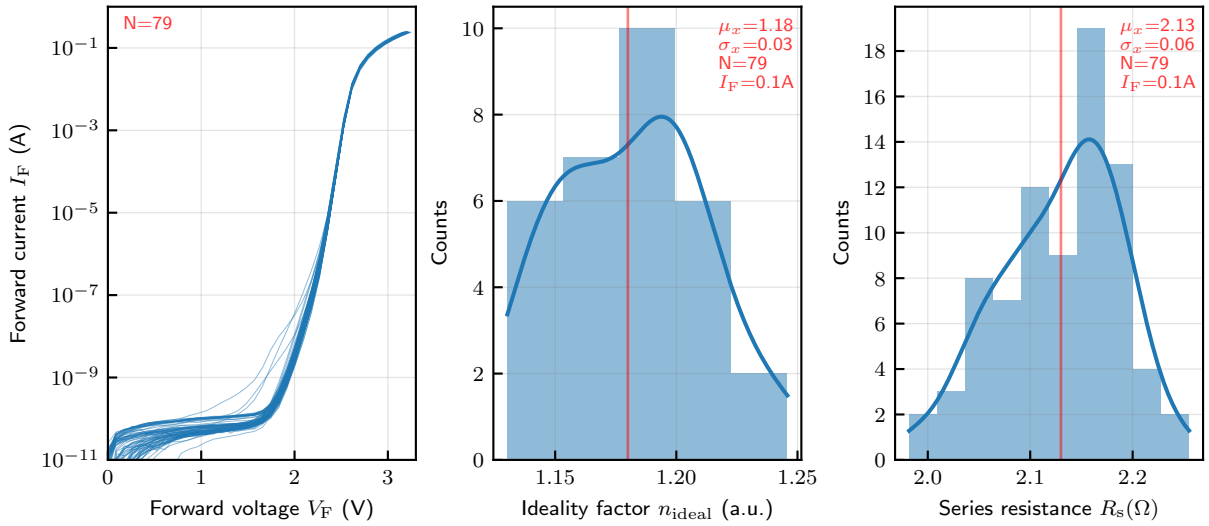

Figure 5.3: Initial electrical measurements of blue DUT: (left) IV-characteristic, (middle) distribution of the ideality factor n_ideal and (right) distribution of the parasitic series resistance R_s. All measurements respective sample count, mean, standard deviation and measurement condition are highlighted in red.

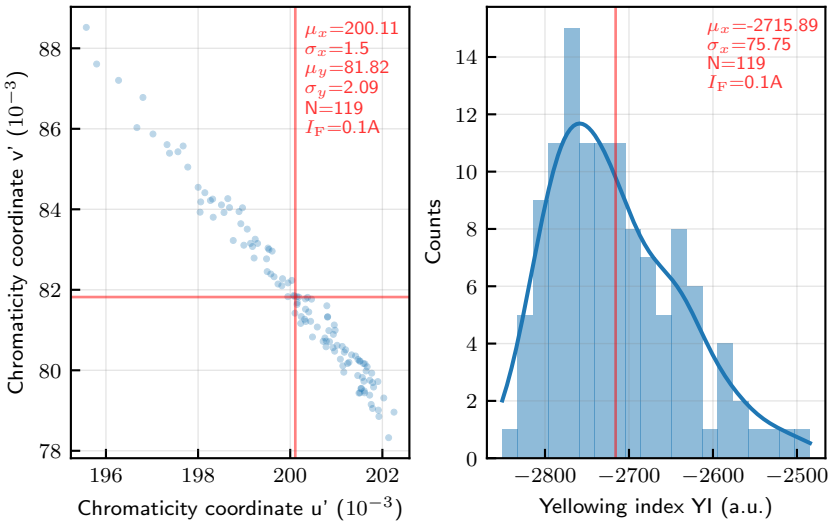

Figure 5.4: Initial colorimetric measurements of blue DUT: (left) distribution of the CIE 1976 UCS chromaticity coordinates u', v' and (right) distribution of the ASTM D1925 yellowing index YI. All measurements respective sample count, mean, standard deviation and measurement condition are highlighted in red.

5.1.2 Results and Degradation Analysis

The following degradation analysis provides an all-encompassing discussion of the different failure site discussed in section 3.2. Since each stress parameter impacts different structural parts of the LED device, in a first step, the electrical and efficiency parameters are analyzed in order to determine the degradation of the die itself and its interconnects. Subsequently, a link to the package degradation will be established by investigating the stress conditions impact on the overall optical power decrease shown in fig. 5.5.

Electrical and Efficiency Parameters

Considering the change in forward voltage over time as shown in fig. 5.6 an initial decrease of $\Delta V_F(t) \approx -5\,\text{mV}$ to $0\,\text{mV}$ within the first hours of operation was measured. This decrease strongly correlates to the observed initial optical power increase in fig. 5.5.
According to former studies [349] the observed initial change in both parameters, optical power and forward voltage, is attributed to the activation of Mg acceptors on the p-side. As a result the hole injection efficiency on the p-side is enhanced due to an increased p-conductivity. A decrease of the parasitic series resistance as an alternative explanation can further be ruled out, since only a $\Delta R_s \approx 10^{-3}\,\Omega$ was observed for all DUT which can be traced back to minor fitting inaccuracies from the extraction of R_s from the IV-characteristic. However, at $t \gg t_0$ a gradual increase $V_F(t)$ for all devices aged under operating conditions ($I_{Test} > 0\,\text{mA}$) is noticeable, whereas no substantial change occurs at storage condition ($I_{Test} = 0\,\text{mA}$). This leads to the assumption that predominantly forward current induced diffusion processes contribute to the increase in $\Delta V_F(t)$. During the diffusion processes H atoms diffuse towards the n-side resulting in negatively charged point defects on the p-side. These H atoms originate from formerly passivated Mg–H complexes on the p-side that were broken by the interaction with hot carriers [349]. The subsequent acceptor decompensation of these point defects result in a steady increase

in R_s [298]. From fig. 5.6 also thermal effects as a second, subsidiary contributor to the increase of $\Delta V_F(t)$ can be suspected, since the diffusion constant (eq. (3.3)) and subsequent both the diffusion length and rate are temperature dependent. This assumption is backed up by a comparatively slow increase in R_s that correlates to the overall increase of each DUT forward voltage. However, the (55 %, 85 °C, 300 mA)-condition presents a drastic $\Delta V_F(t)$ increase at around 50 h when compared to the other conditions. While no explicit correlation regarding the optical power was observed, it is suspected that the formation of Kirkendall voids and electrolysis at the Au – Ag lead-frame to bond-wire interface triggered this behavior [204]. In fig. 5.7 a micrograph Scanning Electron Microscope (SEM) recording of the cathode sides bond wire ball of both an unaged and an aged DUT is shown. Compared to the unaged DUT the aged DUT exhibits an accumulation of residues in the lower left of the bond ball. An EDX revealed that these dark colored residues are Cu deposits. As the electronegativity of both Cu ($\chi = 1.9$) and Ag ($\chi = 1.93$) is about the same, the accumulation of Cu possibly results from moisture enabled Cu – Ag electrolysis effects.

In order to gain further insight regarding the main contributor to the reduction in optical power of the DUT the degradation trajectory of the external quantum efficiency $\eta_{EQE}(t, I_m)$ with respect to measurement current is analyzed. Stating from eq. (2.42) it can be assumed that in case of a noticeable LED die degradation the internal quantum efficiency would exhibit distinguishable trajectories η_{IQE} for different measurement currents I_m attributed to an increase of either non-radiative SRH-recombination in the low injection regime or Auger processes in the high injection region. In case of a uniform, measurement current independent degradation trajectory the root cause of the decrease in P_{opt} can be linked to a change of the package's light extraction efficiency η_{LEE}. As exemplary demonstrated in the left and center of fig. 5.8, a uniform decrease in η_{EQE} is observed. However, at low measurement currents of $I_m = 1$ mA a

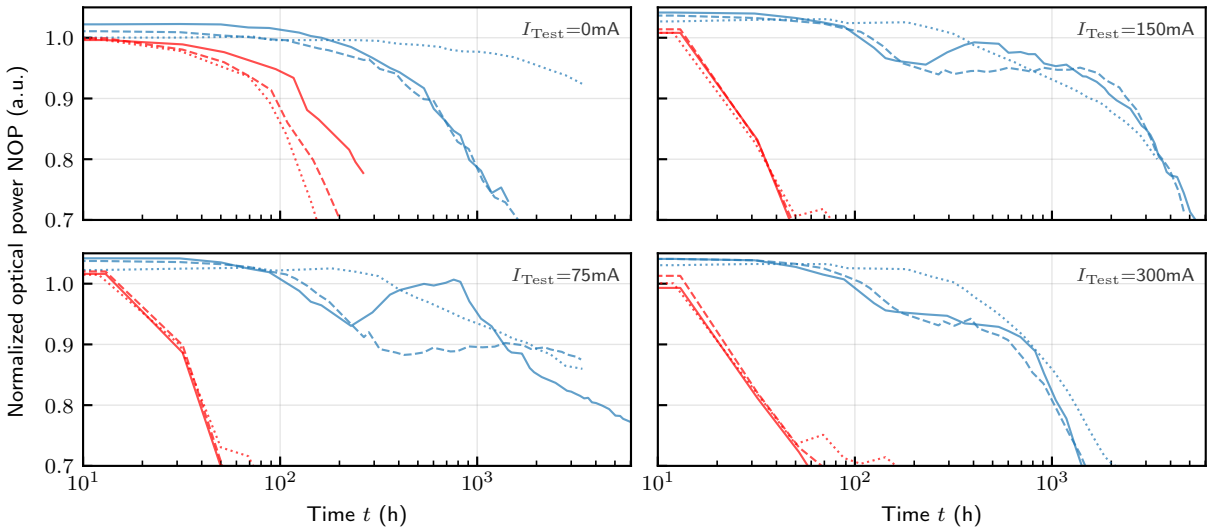

Figure 5.5: Normalized optical power NOP degradation trajectories of the Royal Blue DUT for each of the 24 investigated stress conditions separated by the stress current I_{Test}: (top left) 0 mA, (top right) 150 mA, (bottom left) 75 mA and (bottom right) 300 mA. Each plot displays the stress temperatures T_{Test} in (blue) 65 °C and (red) 85 °C as well as the stress humidity rH_{Test} as (dotted line) 25 %, (dashed line) 55 % and (solid line) 85 %.

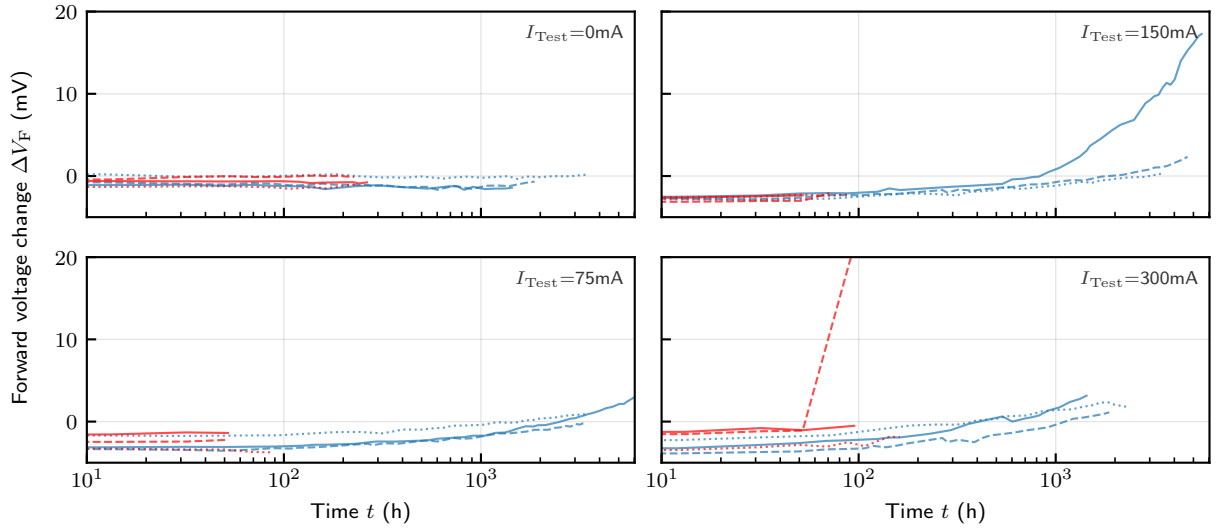

Figure 5.6: Change in forward voltage ΔV_{F} of the Royal Blue DUT for each of the 24 investigated stress conditions separated by the stress current I_{Test}: (top left) 0 mA, (top right) 150 mA, (bottom left) 75 mA and (bottom right) 300 mA. Each plot displays the stress temperatures T_{Test} in (blue) 65 °C and (red) 85 °C as well as the stress humidity $\mathrm{rH}_{\mathrm{Test}}$ as (dotted line) 25 %, (dashed line) 55 % and (solid line) 85 %.

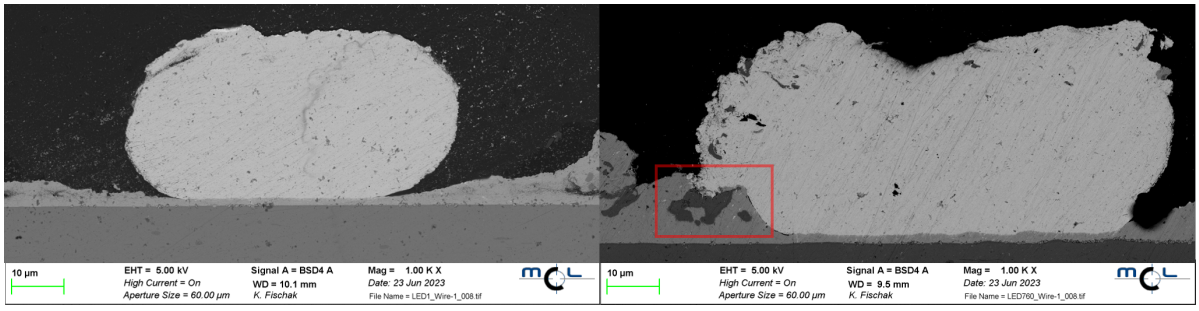

Figure 5.7: SEM micrograph of cathode side the wire bond ball attach to the lead-frame: (left) unaged and (right) aged blue DUT with a sudden rise in forward voltage.

minimal deviation in $\Delta\eta_{\mathrm{EQE}}$ occurs due to a slight increase of non-radiative SRH-recombination as shown in the right plot of fig. 5.8. The increase of non-radiative SRH-recombination is assumed to result from the emergence of point defects which introduce parasitic current paths for injected charge carriers. A strong decrease of the parasitic shunt resistance in the order of several magnitudes from $10^{10}\,\Omega$ to $10^{6}\,\Omega$ confirms this assumption. With respect to typical operating conditions of $I_{\mathrm{F}} \gg 1\,\mathrm{mA}$ the external quantum efficiency, however, can be simplified to $\eta_{\mathrm{EQE}}(t) \propto \eta_{\mathrm{LEE}}(t)$ since no significant changes within the measured current regimes where observed as the center plot of fig. 5.8 shows. Concluding the main decrease in optical power can be attributed to package related degradation mechanisms by means of reflectivity and transmittance changes of the used optical materials.
Analyzing the efficiency decrease $\Delta\eta_{\mathrm{EQE}}$ for all test conditions as presented in fig. 5.9 allows to formulate three further observations: firstly, temperature induced stress has a significant higher impact on $\Delta\eta_{\mathrm{EQE}}$ and thus on η_{LEE} compared to humidity stress. This results from the fact that diffusion processes, regardless if carrier related within the die or moisture related at

the package level, scale according to eq. (3.3) with the temperature [32]. Secondly, as previously discussed at elevated stress currents an inverse proportionality $P_{\mathrm{opt}} \propto \Delta\eta_{\mathrm{EQE}} \propto I_{\mathrm{Test}}^{-1}$ should be expected as the probability of defects introduced to the die increases [154, 331]. At conditions of $T_{\mathrm{Test}} = 65\,°\mathrm{C}$ and $I_{\mathrm{Test}} > 0\,\mathrm{mA}$ this assumption withstands. However, at $T_{\mathrm{Test}} = 85\,°\mathrm{C}$ and $I_{\mathrm{Test}} > 0\,\mathrm{mA}$ conditions as well as for all $I_{\mathrm{Test}} = 0\,\mathrm{mA}$ conditions this assumption breaks which further indicate degradation effects that are rather related to the package's optical materials than the semiconductor. Finally, the third observation shows at the $T_{\mathrm{Test}} = 65\,°\mathrm{C}$ condition an intermediate increase of $\Delta\eta_{\mathrm{EQE}}$ at elevated humidity conditions $\mathrm{rH}_{\mathrm{Test}}$ that also seems to be attributed to a package related degradation mechanism, since no correlations in the electrical and thermal parameters were found.

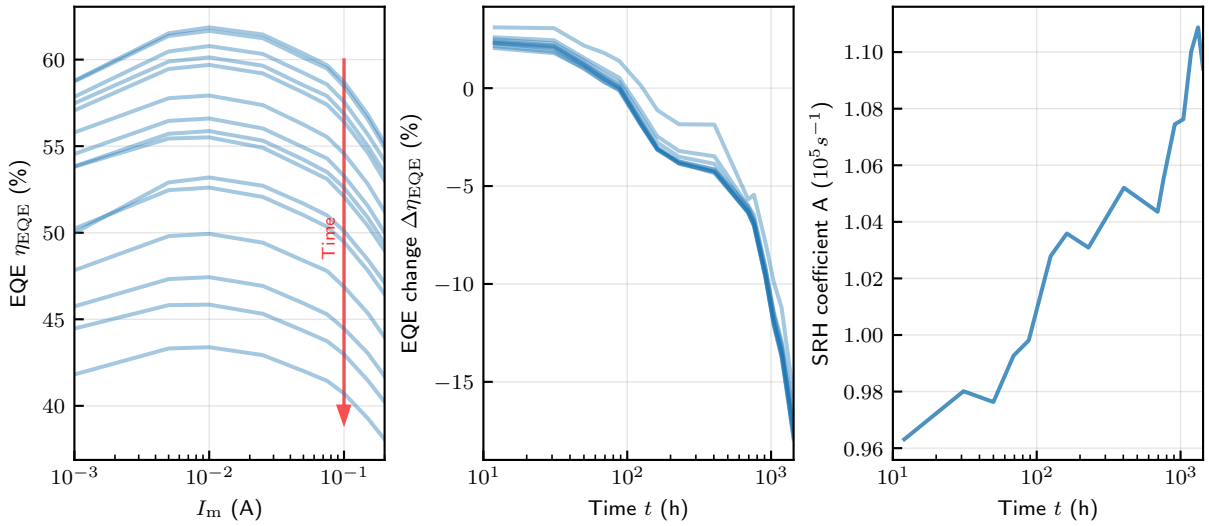

Figure 5.8: External quantum efficiency η_{EQE} with respect to aging time t and measurement current I_{m} exemplary for one blue DUT of the (85 %, 65 °C, 300 mA)-condition: (left) calculated η_{EQE} for different I_{m} at various aging times, (center) absolute change in EQE over time for different I_{m} and (right) the ABC-model's SRH coefficient A with respect to aging time.

Optical Degradation

Since previous analysis identified the package as the predominating degradation site subsequently a detailed investigation is carried out on the two main optical structures of the package with respect to their optical properties – the lead-frame coating's reflectance and the encapsulant's transmittance. Therefore, first the absolute shift in CIE 1976 UCS chromaticity coordinates $\Delta u'(t) = u'(t) - u'(t_0)$ and $\Delta v'(t) = v'(t) - v'(t_0)$ according to [344] presented in fig. 5.10 is investigated. Comparing storage ($I_{\mathrm{Test}} = 0\,\mathrm{mA}$) to operating $I_{\mathrm{Test}} > 0\,\mathrm{mA}$ conditions reveals a single trajectory under storage conditions while at operating conditions a second effect takes places that becomes apparent as a „bump" especially at the lower temperature conditions $T_{\mathrm{Test}} = 65\,°\mathrm{C}$. At this temperature also a faster degradation trajectory is observed under storage conditions which leads to the assumption of two concurring degradation effects. The dominating degradation effect which is present under storage and operating condition exhibits a strong shift towards the yellow region of the CIE 1976 UCS as both left plots of fig. 5.10 show. Considering fig. 5.11 reveals the emergence of encapsulant yellowing as well

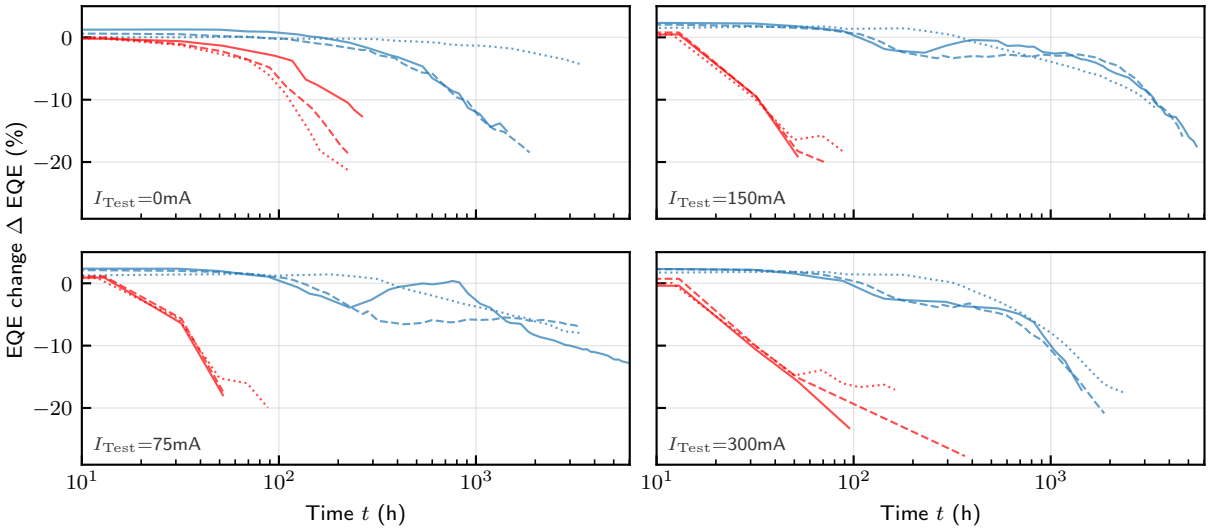

Figure 5.9: Change in external quantum efficiency η_{EQE} of the Royal Blue DUT for each of the 24 investigated stress conditions separated by the stress current I_{Test}: (top left) 0 mA, (top right) 150 mA, (bottom left) 75 mA and (bottom right) 300 mA. Each plot displays the stress temperatures T_{Test} in (blue) 65 °C and (red) 85 °C as well as the stress humidity $\mathrm{rH}_{\mathrm{Test}}$ as (dotted line) 25 %, (dashed line) 55 % and (solid line) 85 %.

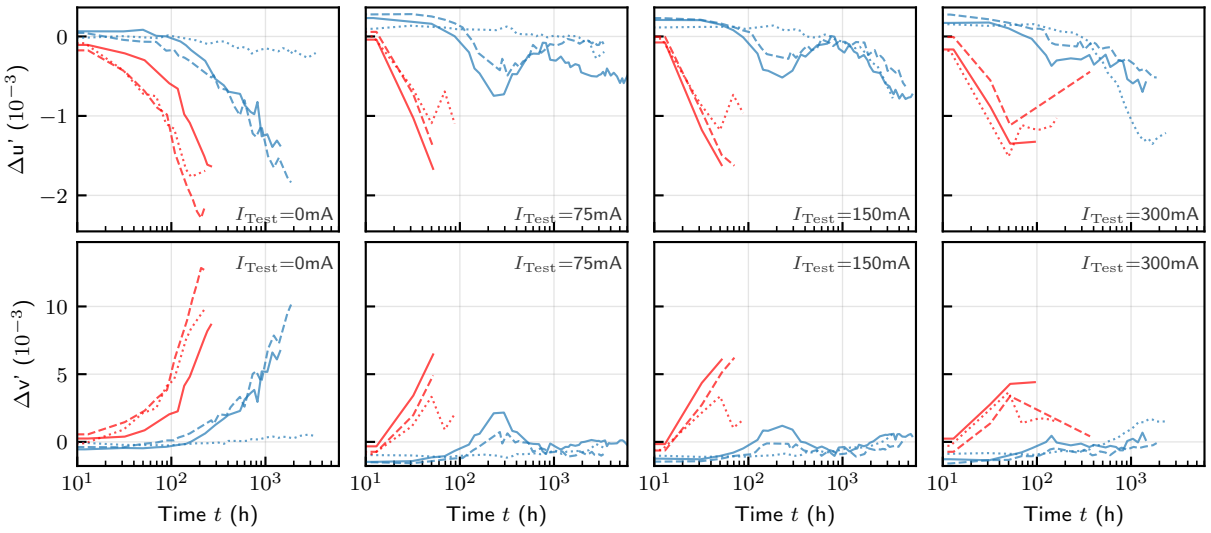

Figure 5.10: Change in CIE 1976 UCS chromaticity coordinates (top) $\Delta u'$ and (bottom) $\Delta v'$ of the Royal Blue DUT for each of the 24 investigated stress conditions separated by the stress current I_{Test}: (left to right) 0 mA, 75 mA, 150 mA and 300 mA. Each plot displays the stress temperatures T_{Test} in (blue) 65 °C and (red) 85 °C as well as the stress humidity $\mathrm{rH}_{\mathrm{Test}}$ as (dotted line) 25 %, (dashed line) 55 % and (solid line) 85 %.

as bubble generation within the encapsulant. Both effects are known for a reduction of the encapsulants transmittance especially within the blue wavelength region [39, 108] which in turn gives an explanation for the strong yellow shift which is also apparent in the YI.
When aging the DUT under operating conditions a slower yellowing rate can be reported accompanied by discoloration of the lead-frame reflector and the formation of micro fractures

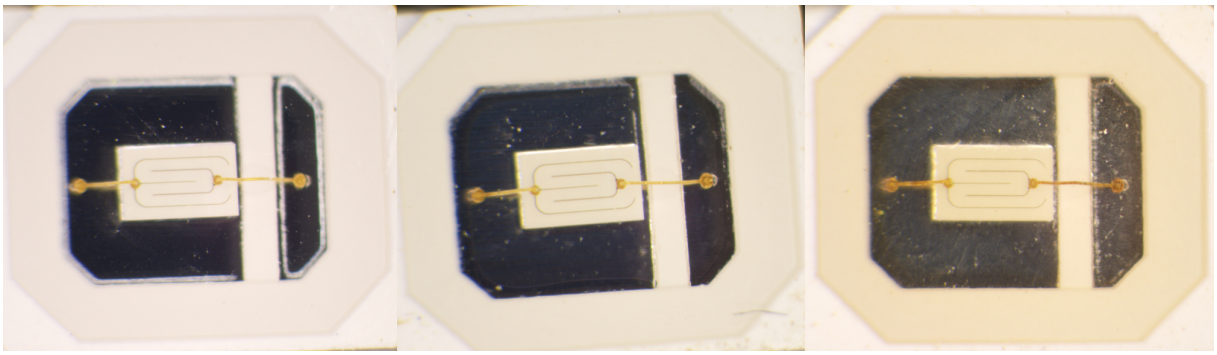

Figure 5.11: Encapsulant yellowing of the royal blue DUT aged at (85 %, 65 °C, 0 mA)-condition at different aging times: (left) 0 h, (center) 537 h and (right) 1434 h.

as exemplary presented in fig. 5.12. Since the DUT is operated, the die introduces an internal heat source into the package that elevates the junction's temperature within the package to $T_j > T_{Test}$. As a result moisture ingress into the package is impeded which results in a decreased yellowing rate. Similarly, less bubbles are generated as less moisture can condensate at micro-cavities. The lead-frame reflector's discoloring, however, occurs due to progressing oxidation reactions of the Ag containing reflective coating with sulfur from the environment following eq. (3.20) and eq. (3.21) [240]. Subsequently, the reflectance significantly decreases especially towards blue wavelengths [241, 350]. Further, a closer inspection shows an area right around the die which is spared from the oxidation at this point of time. This area can be assigned to the die adhesive. Since the die adhesive has a comparably higher adhesive force than the silicone at the dead-frame interface, (sulfur-containing) moisture preferably creeps along the silicone-reflector interface area. In addition, micro fractures start to form that first benefit the direct escape of emitted blue light from the die out of the package. Thus, the on-set of the „bump " can be linked to the start of these fracture's formation. However, at prolonged aging times reflector oxidation and encapsulant yellowing are further promoted due to elevated moisture ingress along previously formed fractures. Additional moisture creepage paths are promoted along the interface between reflector the cup and the encapsulant as both layers are detached from each other. This detachment results from hygroscopic swelling of the silicone

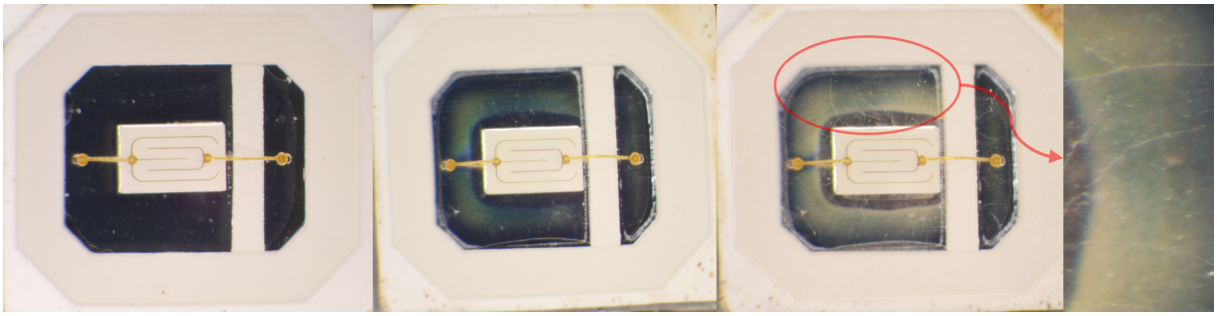

Figure 5.12: Lead-frame tarnishing of the royal blue DUT aged at (85 %, 65 °C, 150 mA)-condition at different aging times: (left) 0 h, (center) 537 h and (right) 1434 h with magnified micro fractures of the encapsulant.

encapsulant. With increased swelling the induced shear forces at the interface surpass the silicones adhesive forces to the cup and thus large cavities are generated as shown in fig. 5.13.

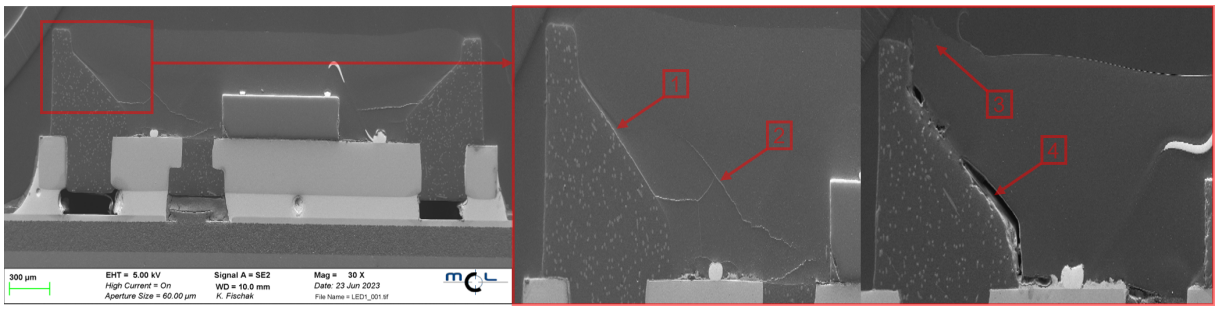

Figure 5.13: SEM micrograph of the moulding cup to encapsulant interface: (left) whole micrograph of an unaged blue DUT, (center) magnification of an unaged interface and (right) close-up of an aged device. Following characteristics are highlighted by numbers: (1) unaged interface, (2) cracks of unaged devices that result from the slicing of the micrograph, (3) swollen silicone of an aged device and (4) detachment and cavities at the interface of an aged device.

5.2 Lime LED Samples

Over the course of this section the experimental data of the $N = 120$ lime DUT [338] aged at a total 24 ($\mathrm{rH_A}$, T_A, I_F)-conditions are presented and their underlying degradation causes are discussed with respect to section 3.2.

5.2.1 Initial Characterization

The initial variation of the operating point specific optical power at nine different measurement currents $I_\mathrm{m} = 1\,\mathrm{mA}$ to $200\,\mathrm{mA}$ is presented in the left plot of fig. 5.14. These range from $1.32 \pm 0.04\,\mathrm{mW}$ and $2.53 \pm 0.005\,\mathrm{V}$ at $1\,\mathrm{mA}$ to $250.71 \pm 2.55\,\mathrm{mW}$ and $3.13 \pm 0.026\,\mathrm{V}$ at $200\,\mathrm{mA}$. Due to the broad cluster-free distribution of the corresponding P_opt and V_F data which are exemplary shown for I_nom in the center plot of fig. 5.14, a single production bin is assumed. This is also confirmed by the narrow distributed SPD presented in fig. 5.14 (right) with a blue direct emitter peak at $\lambda_\mathrm{p,die} = 448.59 \pm 1.19\,\mathrm{nm}$ and a phosphor emission peak at $\lambda_\mathrm{p,ph} = 541.63 \pm 0.92\,\mathrm{nm}$. Similar to the royal blue DUT also a blue side peak at $\approx 467\,\mathrm{nm}$ is present which confirms the assumption of the same semiconductor structure for the royal blue and the lime DUT. Comparing both peaks average optical power $P_\mathrm{opt}(\lambda_\mathrm{p,die}) = 0.16\,\mathrm{mW\,nm^{-1}}$ and $P_\mathrm{opt}(\lambda_\mathrm{p,ph}) = 1.11\,\mathrm{mW\,nm^{-1}}$ reveals that a significant amount of emitted blue light is down-converted due to either a very high phosphor concentration, a very high luminescence efficiency at room temperature $\eta_\mathrm{LE}(25\,°\mathrm{C})$ or both. These observation in combination with the emission pattern suggests the use of a Ce-doped oxyflouride $(\mathrm{Sr,Ca})_3\,(\mathrm{Al,Si})\,\mathrm{O_4}\,(\mathrm{F,O}){:}\mathrm{Ce^{3+}}$ with an excitation peak wavelength of $\lambda_\mathrm{p,ex} = 450\,\mathrm{nm}$ and emission peak at $\lambda_\mathrm{p,em} = 540\,\mathrm{nm} - 550\,\mathrm{nm}$ [102].

Regarding the varying T_j from $25\,°\mathrm{C}$ to $75\,°\mathrm{C}$ at I_nom a red shift of the die emission peak of $\Delta\lambda_\mathrm{p,die} = +2.65\,\mathrm{nm}$ and $\Delta\lambda_\mathrm{p,ph} = +4.30\,\mathrm{nm}$ for the phosphor emission peak, respectively, was observed due to a temperature induced band gap shrinkage. Analogous the peak optical power dropped by $\Delta P_\mathrm{opt}(\lambda_\mathrm{p,die}) = -17.8\,\%$ due to thermally promoted SRH recombination in the die emitter and $\Delta P_\mathrm{opt}(\lambda_\mathrm{p,ph}) = -6.0\,\%$ resulting from thermal quenching. Varying the operating

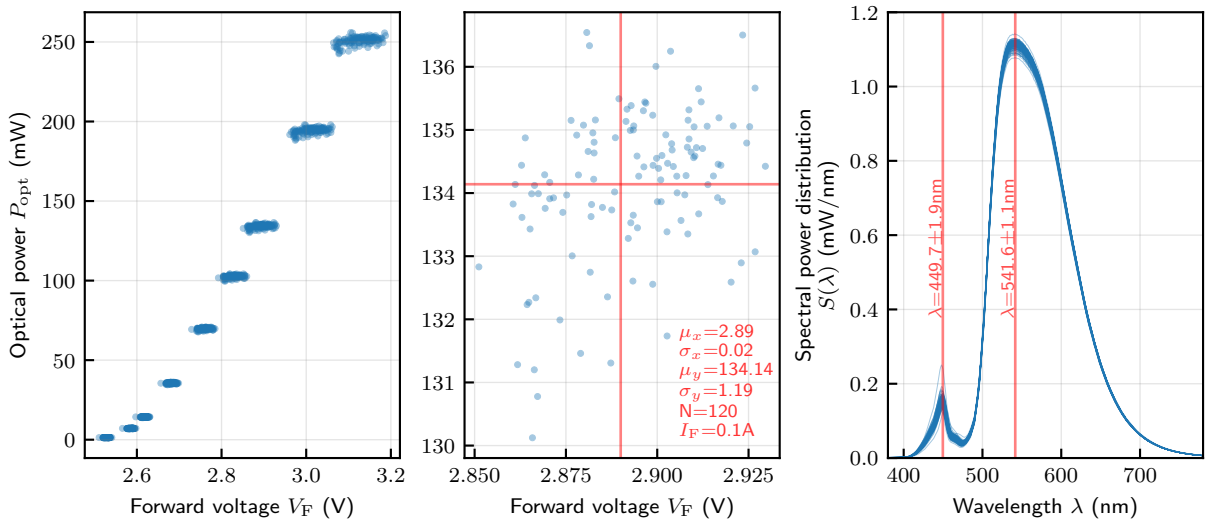

Figure 5.14: Initial optical measurements of the Lime DUT: (left) optical power P_{opt} vs. forward voltage V_F at nine distinct measurement currents I_m, (middle) distribution of V_F and P_{opt} at $I_m = 100\,mA$ and (right) all measured SPDs at $I_m = 100\,mA$ with the die's mean emission peak wavelength $\lambda_p = \lambda_b$. All measurements respective sample count, mean, standard deviation and measurement condition are highlighted in red.

current at room temperature returns a blue shift for the die $\Delta\lambda_{p,die} = -4.68\,nm$ since the Quantum-confined Stark Effect (QCSE) is reduced at elevated charge carrier injection levels. However, the phosphor peak exhibits a small red shift $\Delta\lambda_{p,ph} = -0.28\,nm$ that is attributed to a band gap decrease as a result from phosphor self heating due to thermal quenching.
In fig. 5.15 the average injection current dependent external quantum efficiency η_{EQE} of the lime DUT is presented. At $I_{m,max} = 10\,mA$ the maximum EQE is determined to $\eta_{EQE,max} = 48.45 \pm 0.56\,\%$. Compared to the royal blue DUT the lime DUT only yields about 82 % of the royal blues maximum EQE. Considering the reported phosphor's luminescence efficiency $\eta_{LE} \approx 85\,\%$ [102] the observed decrease in maximum EQE ranges within the phosphor's η_{LE}. Further, the mean efficiency droop of $\eta_{Droop} = -5.99\,\%$ is similar to that of the royal blue DUT.
The IV-characteristics of $N = 80$ initial measured DUT are drawn in fig. 5.16. Apart from one single DUT, all IV-characteristics follow a similar pattern with a noticeable parasitic parallel resistance of $R_p = 18.5 \pm 4.89\,G\Omega$ derived from the low injection regime at $V_F < 1.75\,V$. For the one deviating case trap assisted tunneling processes are responsible for the distortion of the IV-characteristic in the low injection regime that may originate from impurities introduced during the manufacturing process. This outlier characteristic is also present in the center plot of fig. 5.16 as $n_{ideal} = 1.38$ that is larger than the average ideality factor that was determined to $n_{ideal} = 1.19 \pm 0.05$. At the high injection regime of $V_F > 2.7\,V$ a parasitic series resistance of $R_s = 2.01 \pm 0.08\,\Omega$ can be reported. Again, these parameters align with the previously reported parameters of the royal blue DUT further manifesting the assumption that the same die structure is present in both devices.
Considering the measured SPD the CIE UCS 1976 chromaticity coordinates u', v' presented in fig. 5.17 are calculated to [343] $(u', v')^T = (0.187 \pm 0.0001, 0.558 \pm 0.0007)^T$. A proper color binning can be assumed due to both coordinates distribution very low variation. However, a few devices deviate from this narrow distribution which may be attributed to inconsistent

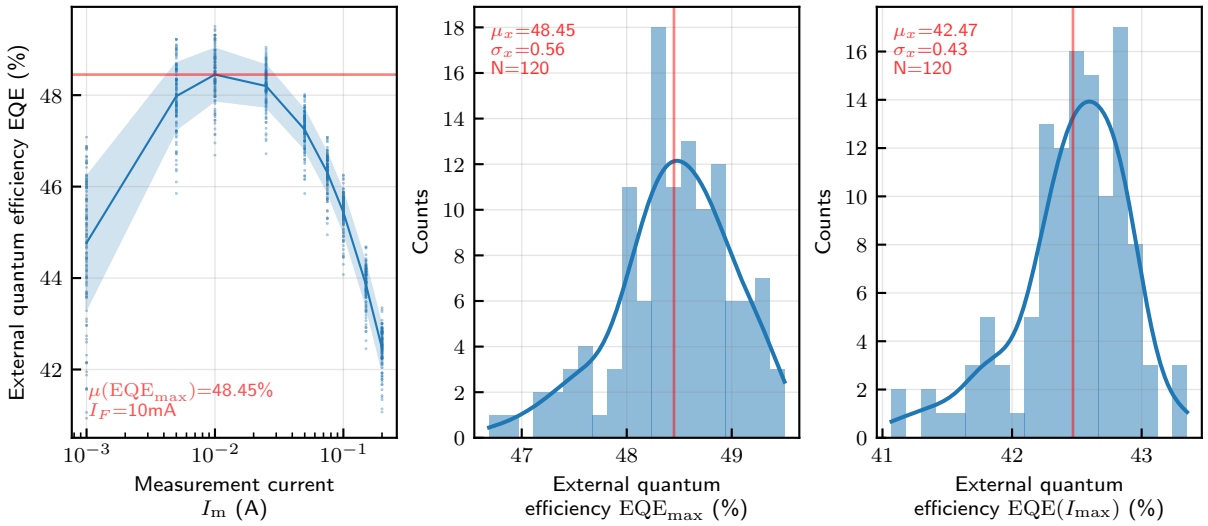

Figure 5.15: Initial EQE measurements of lime DUT: (left) external quantum efficiency EQE at nine distinct measurement currents I_m, (middle) distribution of maximum external quantum efficiency $\mathrm{EQE}_{\mathrm{max}}$ at $I_{\mathrm{EQE,max}}$ and (right) distribution of EQE at maximum measurement current $I_{\mathrm{m,max}}$. All measurements respective sample count, mean, standard deviation and measurement condition are highlighted in red.

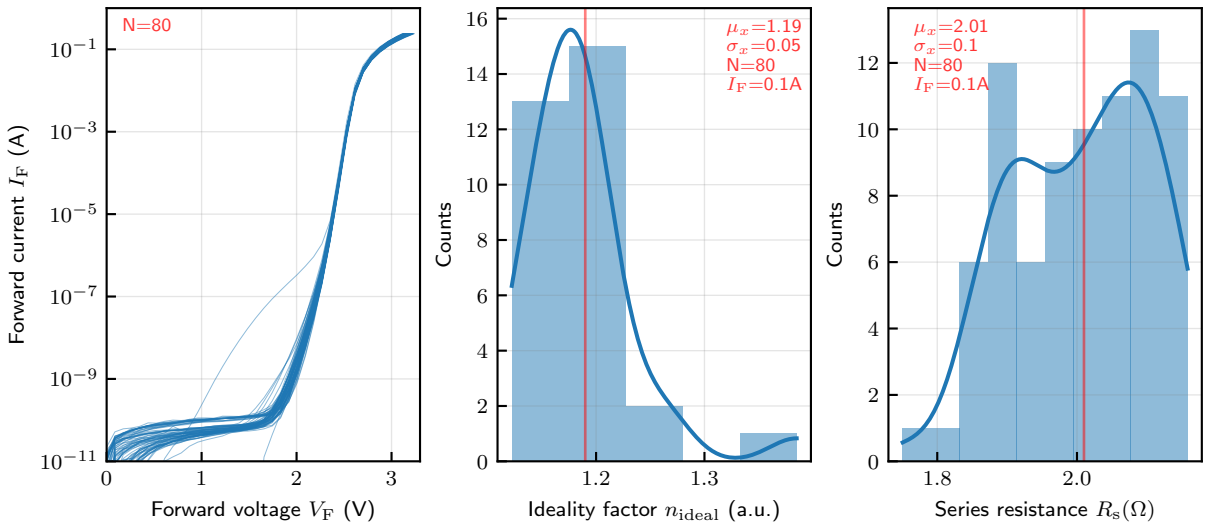

Figure 5.16: Initial electrical measurements of lime DUT: (left) *IV*-characteristic, (middle) distribution of the ideality factor n_{ideal} and (right) distribution of the parasitic series resistance R_s. All measurements respective sample count, mean, standard deviation and measurement condition are highlighted in red.

phosphor contents admixing resulting in a more blueish appearance $(0.186, 0.553)^T$ for too low phosphor content and $(> 0.187, > 0.559)^T$ for too high admixing, respectively. Especially, a single DUT with too low admixing is represented as an outlier in the right plot of fig. 5.17 with a yellowing index of YI = 79.11 compared to the average of YI $\approx 83.54 \pm 0.72$. In addition, with respect to the datasheet [338], an initial junction to solder pad thermal resistance of $R_{\mathrm{th,j-s}} = 22.38 \pm 2.38\,\mathrm{K\,W^{-1}}$ was measured.

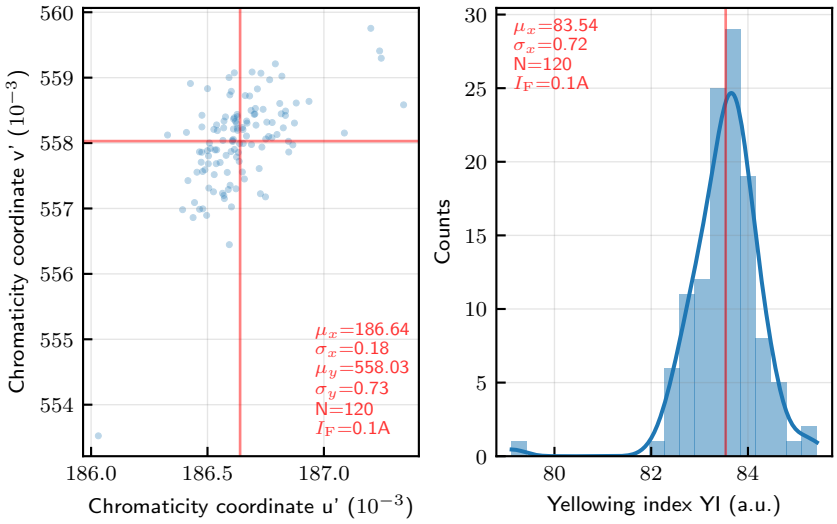

Figure 5.17: Initial colorimetric measurements of lime DUT: (left) distribution of the CIE 1976 UCS chromaticity coordinates u', v' and (right) distribution of the ASTM D1925 yellowing index YI. All measurements respective sample count, mean, standard deviation and measurement condition are highlighted in red.

5.2.2 Results and Degradation Analysis

Hereafter, the results obtained from the aging experiment beforehand characterized lime devices aged at 24 stress conditions defined in chapter 4 are presented and discussed regarding their origin. An overview on the devices' relative decrease in optical power is highlighted in fig. 5.18. In order to investigate the root cause of the presented degradation trajectories the different structural parts of the LED package are analyzed starting from the die's electrical and efficiency parameters up to the optical parameters of the package.

Electrical and Efficiency Parameters

Degradation effects related to the LED die usually are noticeable in the form of changing electrical parameters. Therefore, first the time-dependent change in forward voltage $\Delta V_F(t)$ displayed in fig. 5.19 is investigated. Within the first hours of operation an initial decrease of $V_F(t) \approx -4\,\mathrm{mV}$ to $0\,\mathrm{mV}$ is observed for all devices that correlates with an increase in optical power presented in fig. 5.18. Since the parasitic series resistances extracted from the IV-characteristic only vary in the range of $\Delta R_s \approx 10^{-3}\,\Omega$ no substantial decrease in series resistance is concluded. This hints, similar to the case of the blue DUT, towards an activation Mg acceptors on the semiconductors p-side [349] that promoted p-side acceptor decompensation [298]. Subsequently, $V_F(t)$ steadily increases while aged under operating conditions ($I_{Test} > 0\,\mathrm{mA}$). Analogous to the in depth discussed observations for the royal blue DUT, diffusion processes triggered by injected charge carriers and elevated temperature are suspected for the $V_F(t)$ increase [349]. Further, a similar sudden increase in $V_F(t)$ was observed at around 50 h for the (55 %, 85 °C, 300 mA)-condition. Since no current or voltage anomalies were found in the test protocol a bond-wire attach related defect promoted by electrolysis similar to the blue DUT is assumed [204].

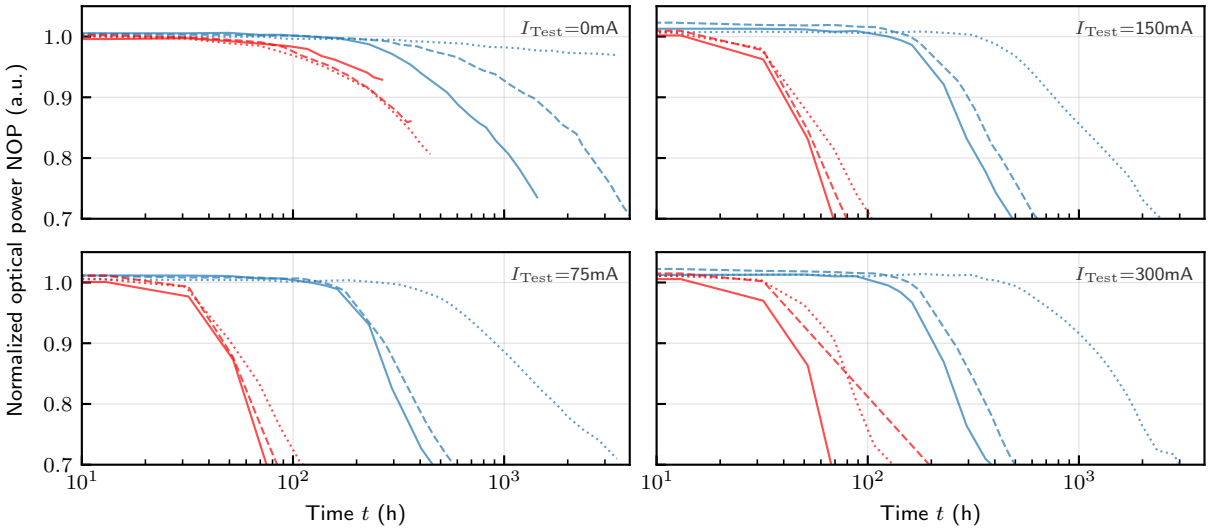

Figure 5.18: Normalized optical power NOP degradation trajectories of the lime DUT for each of the 24 investigated stress conditions separated by the stress current I_{Test}: (top left) 0 mA, (top right) 150 mA, (bottom left) 75 mA and (bottom right) 300 mA. Each plot displays the stress temperatures T_{Test} in (blue) 65 °C and (red) 85 °C as well as the stress humidity $\mathrm{rH}_{\mathrm{Test}}$ as (dotted line) 25 %, (dashed line) 55 % and (solid line) 85 %.

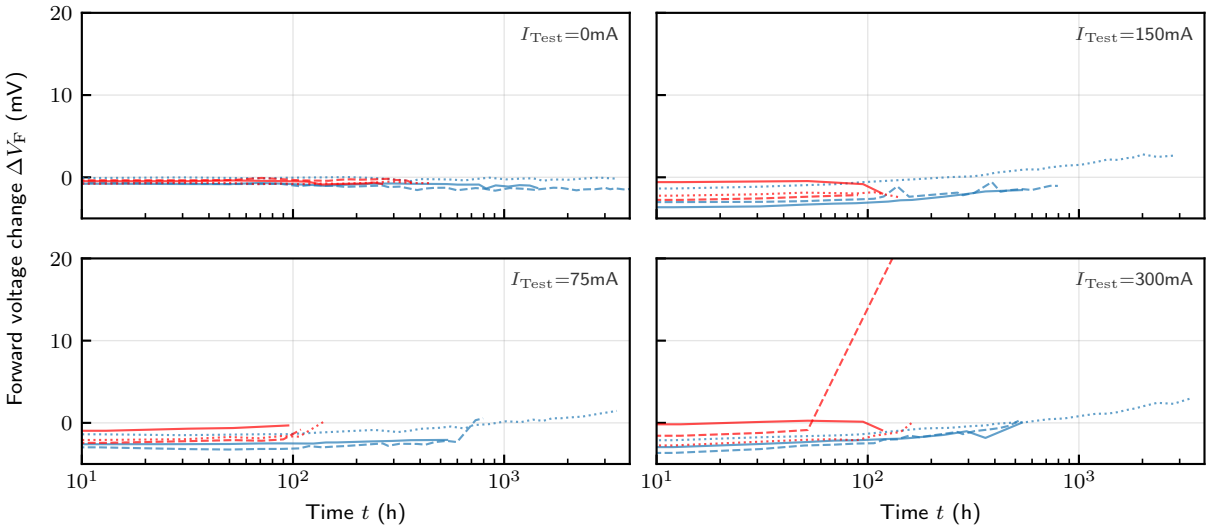

Figure 5.19: Change in forward voltage ΔV_{F} of the lime DUT for each of the 24 investigated stress conditions separated by the stress current I_{Test}: (top left) 0 mA, (top right) 150 mA, (bottom left) 75 mA and (bottom right) 300 mA. Each plot displays the stress temperatures T_{Test} in (blue) 65 °C and (red) 85 °C as well as the stress humidity $\mathrm{rH}_{\mathrm{Stress}}$ as (dotted line) 25 %, (dashed line) 55 % and (solid line) 85 %.

In a next step the time and current dependence of the external quantum efficiency $\eta_{\mathrm{EQE}}(t, I_{\mathrm{m}})$ is analyzed. Trend-wise all DUT exhibit a comparable degradation trajectory with varying magnitude as exemplary shown in fig. 5.21. Therefore, an exemplary discussion based on one DUT of the (85 %, 65 °C, 300 mA)-condition presented in fig. 5.8 is performed. After the initial performance decrease discussed above the EQE does not change significantly within the first

150 h as both the left and center plot of fig. 5.8 indicate. Following a rapid decrease in EQE over the whole measured current regime is observed. As the center plot shows no significant measurement current dependency of the EQE, die related degradation effects are dismissed as the main degradation contributors. This assumption is confirmed by the rather small changes of the SRH coefficient A (right plot of fig. 5.8) and Auger-coefficient C which would be expected at least one magnitude higher than observed for an significant degradation effect. The main contributor must be therefore located within the package along the optical path of the light emitted from the die onto the package's surface. Thus, according to eq. (2.42) the internal quantum efficiency presents no relevant time-dependency during the test period. As a result, the light extraction efficiency exhibits a strong time-dependency and thus majorly contributes to the change in EQE by $\eta_{\mathrm{EQE}}(t) \propto \eta_{\mathrm{LEE}}(t)$.

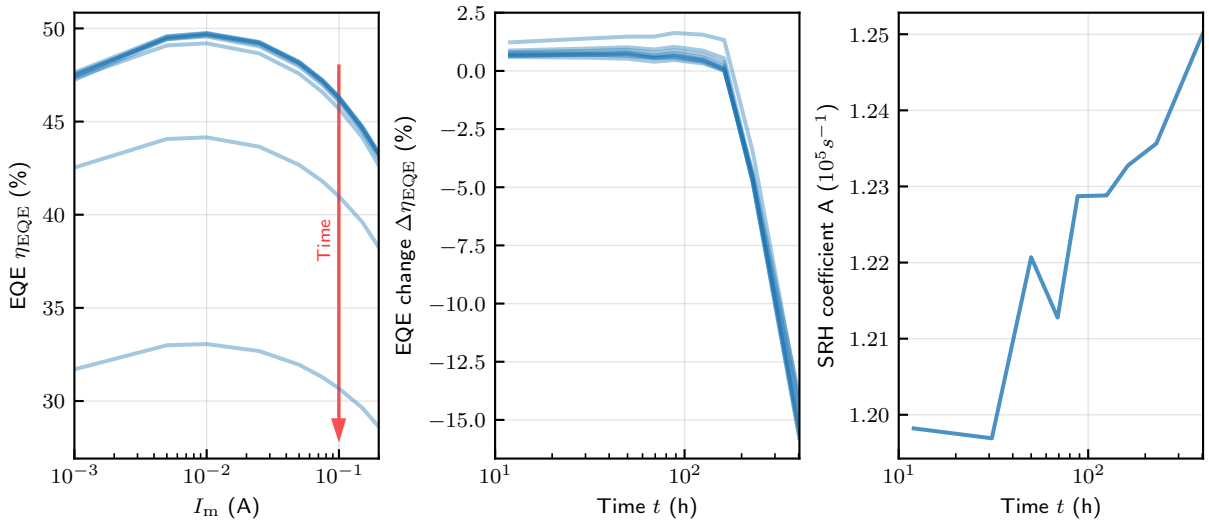

Figure 5.20: External quantum efficiency η_{EQE} with respect to aging time t and measurement current I_{m} exemplary for one lime DUT of the (85 %, 65 °C, 300 mA)-condition: (left) calculated η_{EQE} for different I_{m} at various aging times, (center) absolute change in EQE over time for different I_{m} and (right) the ABC-model's SRH coefficient A with respect to aging time.

Optical Degradation

Considering the before evaluated results regarding the die and interconnect failure sites, following the packages encapsulant, lead-frame reflector and phosphor degradation will be examined in order to describe the observed optical power and EQE decrease. First the calculated absolute shift in CIE 1976 UCS chromaticity coordinates $\Delta u'(t)$ and $\Delta v'(t)$ shown in fig. 5.22 are analyzed.

At elevated temperature conditions $T_{\mathrm{Test}} = 85\,°\mathrm{C}$ a common shift trajectory towards yellow/red coordinates ($\Delta u'(t) > 0$, $\Delta v'(t) < 0$) becomes evident. While the moisture level seems to have a subordinate impact, the shift trajectories acceleration scales well with I_{Test}. In contrast for the lower $T_{\mathrm{Test}} = 65\,°\mathrm{C}$ condition an intermediate „bump" on the $\Delta u'(t)$ axis indicates a second mechanism becoming present that yields a blue shift ($\Delta u'(t) < 0$, $\Delta v'(t) < 0$). This behavior becomes also evident noticeable the Yellowing Index. In addition to the current level, also the moisture level impacts both the general shifts trajectory as well as the on-set of this secondary

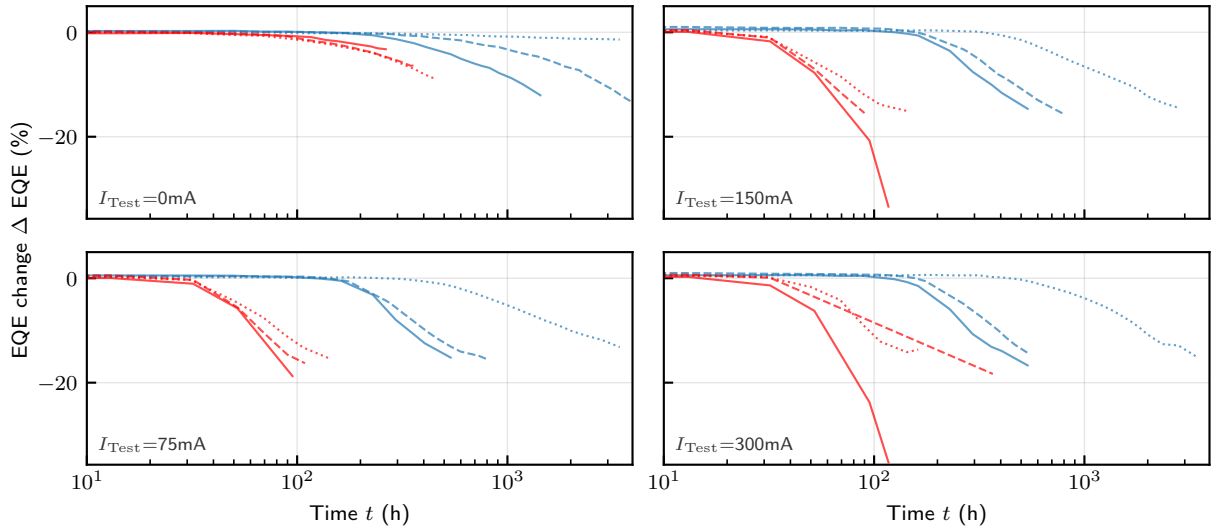

Figure 5.21: Change in external quantum efficiency η_{EQE} of the lime DUT for each of the 24 investigated stress conditions separated by the stress current I_{Test}: (top left) 0 mA, (top right) 150 mA, (bottom left) 75 mA and (bottom right) 300 mA. Each plot displays the stress temperatures T_{Test} in (blue) 65 °C and (red) 85 °C as well as the stress humidity $\mathrm{rH}_{\mathrm{Test}}$ as (dotted line) 25 %, (dashed line) 55 % and (solid line) 85 %.

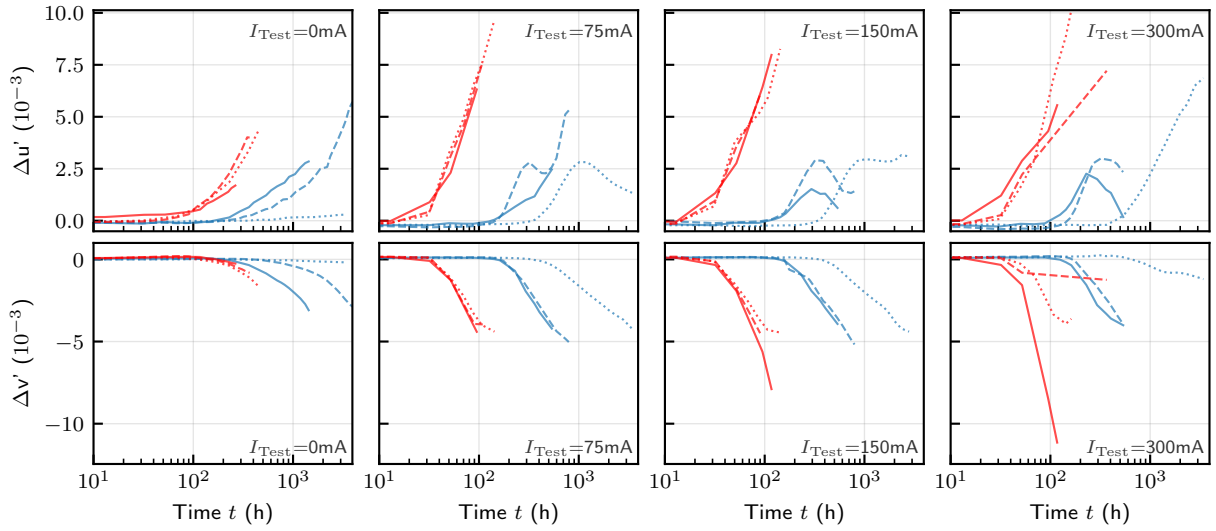

Figure 5.22: Change in CIE 1976 UCS chromaticity coordinates (top) $\Delta u'$ and (bottom) $\Delta v'$ of the lime DUT for each of the 24 investigated stress conditions separated by the stress current I_{Test}: (left to right) 0 mA, 150 mA, 75 mA and 300 mA. Each plot displays the stress temperatures T_{Test} in (blue) 65 °C and (red) 85 °C as well as the stress humidity $\mathrm{rH}_{\mathrm{Test}}$ as (dotted line) 25 %, (dashed line) 55 % and (solid line) 85 %.

degradation effect. Considering the peak wavelength's position the measurement data reveal a stable blue peak of around $\Delta\lambda_{\mathrm{p,die}}(t \gg t_0) \approx \Delta\lambda_{\mathrm{p,die}}(0)$ while the green phosphors peak wavelength change is $\Delta\lambda_{\mathrm{p,ph}}(t) \propto \Delta u'(t) < 0$.
Similar to the royal blue DUT lead-frame mirror tarnishing and encapsulant yellowing are expected. Due to the encapsulant's phosphor content a direct visual inspection via light

microscopy of both former mentioned degradation effects proves difficult. However, adjusting the RGB settings of the taken image can highlight the underlying degradation effects up to a certain level as shown in fig. 5.23.

The left images in fig. 5.23 show a lime DUT at its initial state before aging. At this initial stage

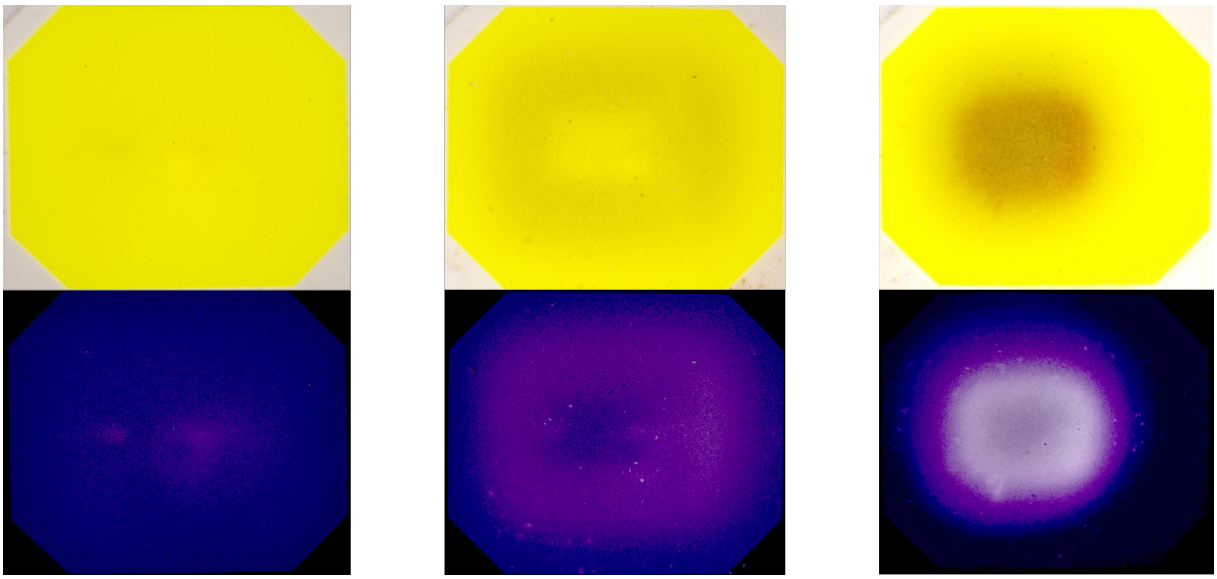

Figure 5.23: Visible degradation effects of the lime DUT with (top) the original image and (bottom) color modified image exemplary highlighting the distinct degradation effects: DUT (left) before aging, (center) phosphor dissolving and lead-frame reflector tarnishing and (right) encapsulant carbonization.

only the tips of the bond-wires are visible by RGB adjustment. After aging slight darkening is visible. Adjusting the RGB settings reveals the underlying lead-frame reflector and the centered LED die as the center image of fig. 5.23 presents. In addition, the area along the molded cup appears brighter. Therefore, two conclusions can be drawn: firstly the darkened area represents the tarnished lead-frame mirror which itself drastically reduces the reflected light from the packages bottom layer to its surface. Secondly, the phosphor content becomes more transparent as a result of phosphor dissolution [204].

By comparing the phosphor's and die's spectrums peak optical power ratio as shown in fig. 5.24 reveals a significantly decrease of the phosphor's spectral emission. Since the dissolution process requires a solvent, the dissolution progresses faster with increasing moisture content diffused into the package. The diffusion rate itself has a positive temperature dependence which explains the observed higher degradation rate at elevated temperatures. Simultaneously, the encapsulant's yellowing advances as hinted by the observed yellow chromaticity shift. The emerging „bump" on the $\Delta u'(t)$ axis may be attributed to concurring directions of moisture diffusion due to temperature differences between the inner package and the ambient. At this aging stage previously entered moisture could be driven out of the package. Since those beforehand trapped water molecules were scattering especially blue light due to Rayleigh scattering ($\propto \lambda^{-4}$) an increase in emitted blue light can be found after evaporating these moisture contents from the encapsulant. From the right columns pictures of fig. 5.23 a third degradation mechanism can be derived. In particular at very elevated stress conditions a brown to black residue begins to form on top of the die. Similar effects were observed in former

studies that linked the encapsulant's carbonization due to high temperatures [273]. These temperatures of several 100 °C result from high injection currents for one causing excessive Joule heating at the die area which reduces the phosphor's efficiency causing additional heat to be generated by the phosphor during the down-conversion.

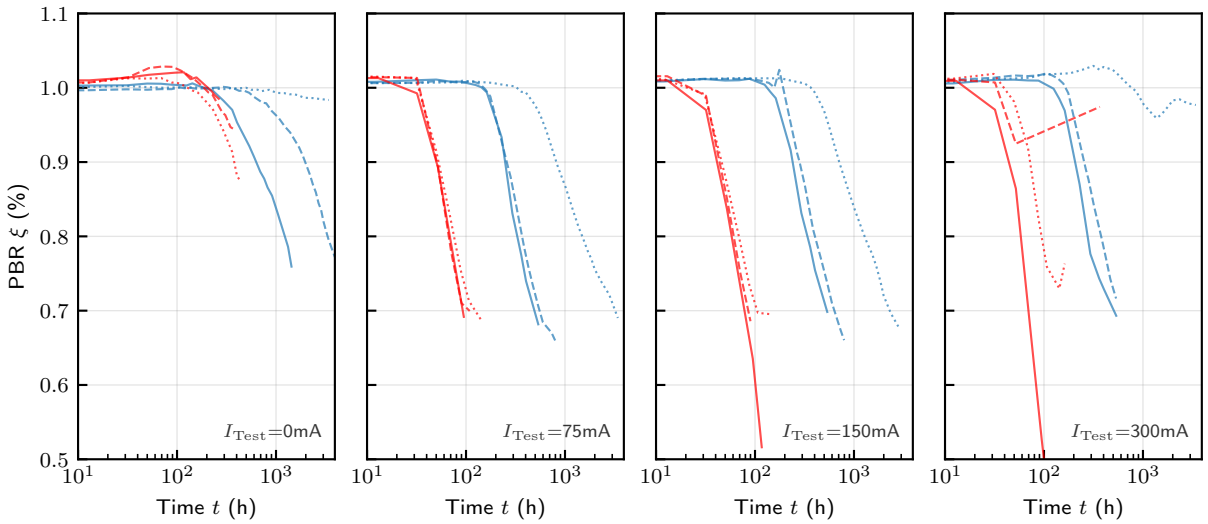

Figure 5.24: Relative phosphor to chip peak power ratio ξ of the lime DUT for each of the 24 investigated stress conditions separated by the stress current I_{Test}: (left to right) 0 mA, 150 mA, 75 mA and 300 mA. Each plot displays the stress temperatures T_{Test} in (blue) 65 °C and (red) 85 °C as well as the stress humidity rH_{Test} as (dotted line) 25 %, (dashed line) 55 % and (solid line) 85 %.

5.3 Purple LED Samples

This section presents the measurement results of the purple DUT [338] and provides subsequent a discussion of the origins of the observed aging experiment from chapter 4. Therefore, an initial characterization of the $N = 118$ devices aged under 24 different (rH_A, T_A, I_F)-conditions. Prior it should be noted, that two devices aged at elevated temperature conditions of $T_{Test} = 85$ °C exhibited an early catastrophic failure (open circuit) during the first aging period and thus were removed from the following discussion.

5.3.1 Initial Characterization

Analogous to the previous sections an initial characterization of the purple device will be performed as a baseline for the following degradation analysis starting with drive point dependent optical power output. Measuring the DUT at varying forward currents $I_m = 1$ mA to 400 mA yields the left plot of fig. 5.25 presenting an average measured optical power and forward voltage ranging from 0.97 ± 0.03 mW and 2.52 ± 0.004 V at 1 mA to 362.49 ± 3.74 mW and 3.16 ± 0.021 V at 400 mA. Compared to the royal blue and lime device the maximum forward current is doubled due to the parallel chip configuration while maintaining a the optical power at a comparable level. The presented data exhibits no obvious voltage or power clusters as the center plot of fig. 5.25 highlights for I_{nom}. Thus no electrical voltage or power binning is assumed. The SPD also presents a narrow wavelength and power distribution as the right plot of fig. 5.25 displays. The emission peaks of the die and the red phosphor are determined to

$\lambda_{p,die} = 448.21 \pm 0.69\,\text{nm}$ with a side peak at about 467 nm and $\lambda_{p,ph} = 646.11 \pm 1.15\,\text{nm}$, respectively. This further confirms the assumption that the same principal semiconductor structure was used for all devices, whereby only the chip area and thus the volume of the active region mainly was adjusted for the two chip configuration. The average peak optical power yields a ratio of 1 : 7.7 with $P_{opt}(\lambda_{p,die}) = 0.14\,\text{mW nm}^{-1}$ and $P_{opt}(\lambda_{p,ph}) = 1.08\,\text{mW nm}^{-1}$. Commonly, red Eu-doped nitride phosphors, such as $(Sr, Ba)_2\,Si_5\,N_8 : Eu^{2+}$ or $(Sr, Ca)\,Al\,Si\,N_3 : Eu^{2+}$, are widely used in LED applications [102]. However, a clear determination of the phosphor type is difficult, since these phosphors are specifically tuned regarding their Sr and Eu content to meet the desired emission pattern in combination with a specific LED emitter. Measuring the

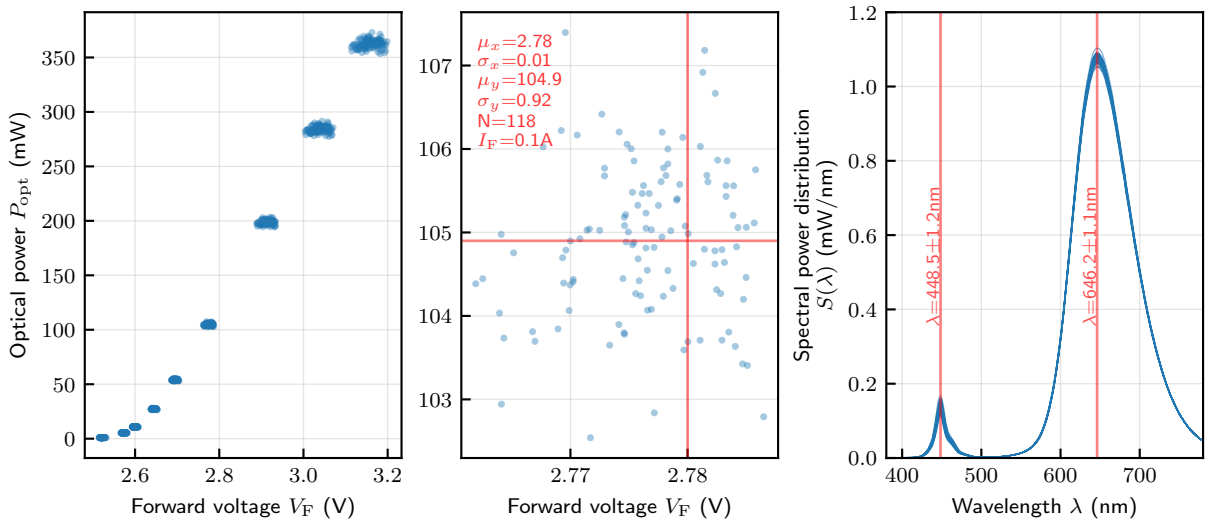

Figure 5.25: Initial optical measurements of the Purple DUT: (left) optical power P_{opt} vs. forward voltage V_F at nine distinct measurement currents I_m, (middle) distribution of V_F and P_{opt} at $I_m = 100\,\text{mA}$ and (right) all measured SPDs at $I_m = 100\,\text{mA}$ with the die's mean emission peak wavelength $\lambda_p = \lambda_b$. All measurements respective sample count, mean, standard deviation and measurement condition are highlighted in red.

temperature dependence over a range of $T_j = 25\,°\text{C}$ to 75 °C at a drive current of I_{nom} a red shift of the LED emitters peak wavelength of $\Delta\lambda_{p,die} = +2.43\,\text{nm}$ and a minor blue shift of $\Delta\lambda_{p,ph} = -0.44\,\text{nm}$ of the phosphor's peak wavelength is observed. Former can be attributed to a temperature induced lowering of the band gap energy, the latter however, could be attributed to quenching processes. Simultaniously, a drop in optical power at the corresponding peak wavelengths was observed of $\Delta P_{opt}(\lambda_{p,die}) = -20.4\,\%$ and $\Delta P_{opt}(\lambda_{p,ph}) = -7.4\,\%$, respecively, where the first is attributed to to thermally enhanced SRH recombination of the LED chip and the second results from thermal quenching in combination with a reduced blue light emission of the die. The dependence of the forward current over the defined current range is determined to $\Delta\lambda_{p,die} = -2.55\,\text{nm}$ and $\Delta\lambda_{p,ph} = -0.72\,\text{nm}$ and results from a decrease of the QCSE and self heating due to thermal quenching, respectively. Further, varying the injection current yields the external quantum efficiency η_{EQE} characteristic presented in the left plot of fig. 5.26. The maximum EQE of $\eta_{EQE,max} = 37.01 \pm 0.38\,\%$ at a forward current of $I_{m,max} = 25\,\text{mA}$ with a resulting average efficiency droop of $\eta_{Droop} = -6.33\,\%$ similar to the blue and lime DUT.
In fig. 5.27 the initial IV-characteristics of $N = 80$ purple devices are presented. The vast majority of devices follow a similar IV-characteristics apart from three devices that exhibit trap

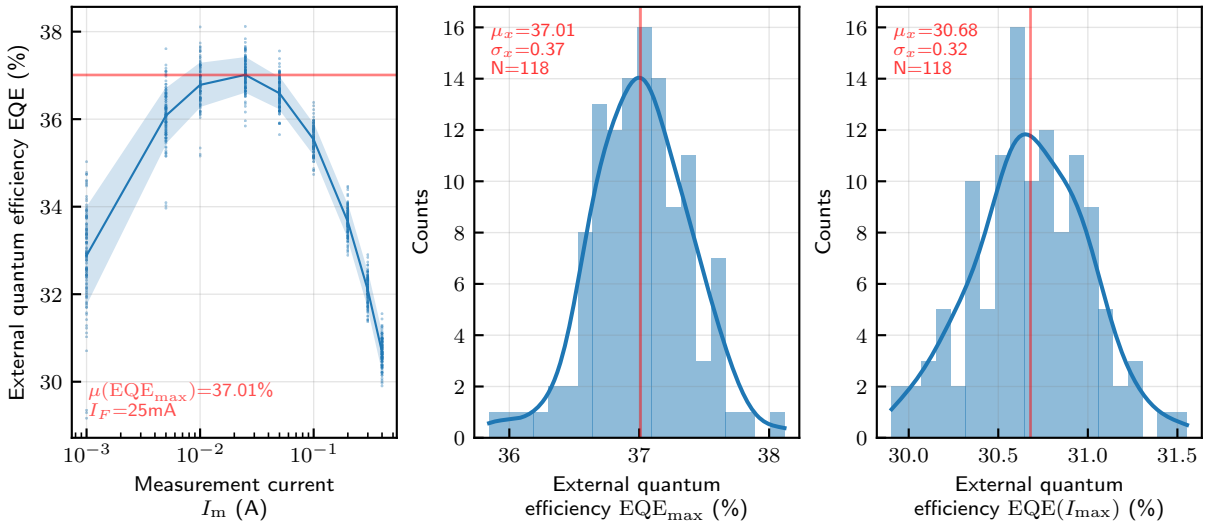

Figure 5.26: Initial EQE measurements of purple DUT: (left) external quantum efficiency EQE at nine distinct measurement currents I_{m}, (middle) distribution of maximum external quantum efficiency $\mathrm{EQE}_{\mathrm{max}}$ at $I_{\mathrm{EQE,max}}$ and (right) distribution of EQE at maximum measurement current $I_{\mathrm{m,max}}$. All measurements respective sample count, mean, standard deviation and measurement condition are highlighted in red.

assisted tunneling processes in the low injection regime at $V_{\mathrm{F}} < 1.75\,\mathrm{V}$. Both, the parallel and series parasitic resistances are derived from the *IV*-characteristics and are narrowly distributed at $R_{\mathrm{p}} = 16.1 \pm 4.49\,\mathrm{G\Omega}$ and $R_{\mathrm{s}} = 0.98 \pm 0.03\,\Omega$. The of value R_{s} was expected to be approximately half of the blue or lime devices R_{s} since two chips are operated in parallel. Further, the ideality factor is close to an ideal diode characteristic with $n_{\mathrm{ideal}} = 1.15 \pm 0.07$ with one outlier of $n_{\mathrm{ideal}} = 0.86$ which traced back to a fitting error during the calculation since it ranges for all further measurements within the shown distribution.
The CIE UCS 1976 chromaticity coordinates u', v' are determined to $(u', v')^T = (0.465 \pm 0.002, 0.503 \pm 0.002)^T$. For all devices the chromaticity coordinates are broad, but normally distributed along the spectral locus' purple boundary as shown in fig. 5.28. Based on the chromaticity coordinates underlying tristimulus values X, Y and Z the yellowing index results to $\mathrm{YI} \approx 239.65 \pm 2.28$. A small set of outliers observable within the CIE 1976 UCS ($(u', v')^T = (< 0.462, < 0.500)^T$) as well as regarding their Yellowing Index $\mathrm{YI} < 235$ is probably attributed to a lower phosphor content admixing and thus a small manufacturing process uncertainty. Similar to both before measured devices' thermal resistance also the purple DUT is well within the manufacturer's specification [338] with $R_{\mathrm{th,j-s}} = 12.70 \pm 0.99\,\mathrm{K\,W^{-1}}$.

5.3.2 Results and Degradation Analysis

The results obtained from the aging experiment described in chapter 4 are presented in fig. 5.29. Based on fig. 5.29 a significant decrease in optical power scaling well with temperature and drive current is observable. In addition, a correlation between the decline in optical power and humidity is present for all devices aged under operating conditions $I_{\mathrm{Test}} > 0\,\mathrm{mA}$. The root causes for the observed trajectories in fig. 5.29 are discussed below.

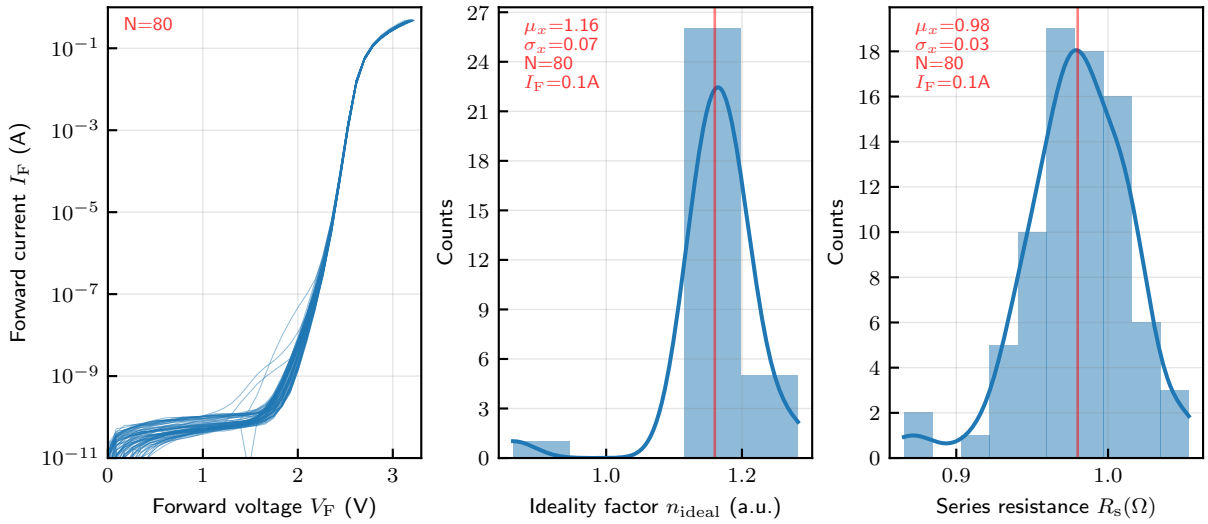

Figure 5.27: Initial electrical measurements of purple DUT: (left) IV-characteristic, (middle) distribution of the ideality factor n_{ideal} and (right) distribution of the parasitic series resistance R_s. All measurements respective sample count, mean, standard deviation and measurement condition are highlighted in red.

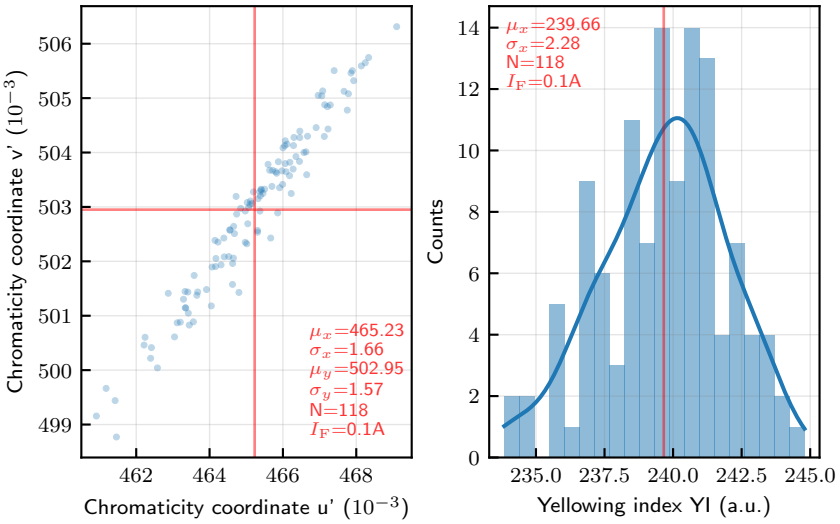

Figure 5.28: Initial colorimetric measurements of purple DUT: (left) distribution of the CIE 1976 UCS chromaticity coordinates u', v' and (right) distribution of the ASTM D1925 yellowing index YI. All measurements respective sample count, mean, standard deviation and measurement condition are highlighted in red.

Electrical and Efficiency Parameters

First, the device's electrical parameters are examined in order to identify any die related degradation effects. In fig. 5.30 the devices change in forward voltage $\Delta V_F(t)$ over the course of the experiment is displayed. After an initial decrease of $V_F(t \leq 50\,\text{h}) \approx -4\,\text{mV}$ to $0\,\text{mV}$ the forward voltage $\Delta V_F(t > 50\,\text{h})$ continuously increases. In accordance to the royal blue and lime DUT (section 5.1.2 and section 5.2.2) an abrupt increase in $\Delta V_F(t)$ is observed for the (55 %, 85 °C, 600 mA)-condition, that, in contrast, is followed by an subsequent decrease. This

diverging behavior from both before discussed devices might result from the fact, that the L_{70} threshold has not been exceeded at this point of the experiment in comparison to the blue and lime DUT.

In agreement with the other device's results no substantial change in parasitic series resistances ($\Delta R_s \approx 10^{-3}\,\Omega$) was found thus pointing towards to an activation Mg acceptors on the semiconductors p-side [349] promoting p-side acceptor decompensation [298]. However, the following $V_F(t)$ increase at operating conditions of $I_{Test} > 0\,mA$ exhibits an exponential behavior that is relatively high compared to both single die devices. This behavior becomes especially present in the high operating current regime. As a underlying degradation process electrolysis triggered Cu migration towards the bond wire attach [204] as elaborated in section 5.1.2 can be assumed alongside with charge carrier induced diffusion processes causing lattice defect. The reason for this comparably higher increase of $\Delta V_F(t)$ is suspected in an unbalanced current loading. Due to the higher diffusion rate one die will exhebit an higher degradation rate that the second die exposed to a lower forward current [349].
In order to further confirm the die's contribution to the overall decrease in optical power of the device its external quantum efficiency $\eta_{EQE}(t, I_m)$ with regard to forward current and operation time is investigated based on the results presented in fig. 5.8 and fig. 5.21. First, the left plot of fig. 5.21 indicates that a roughly uniform external quantum efficiency decrease of present over the whole measurement current range leaves the assumption of a predominantly light extraction efficiency related degradation contributed by the package. However, by inspecting the center plot of fig. 5.21 a growing deviation in degradation rate between measurement current at $t \geq 400\,h$ becomes apparent hinting toward an growing die related contribution in the low injection current regime. Analyzing the SRH-coefficient confirms a rapid increasing

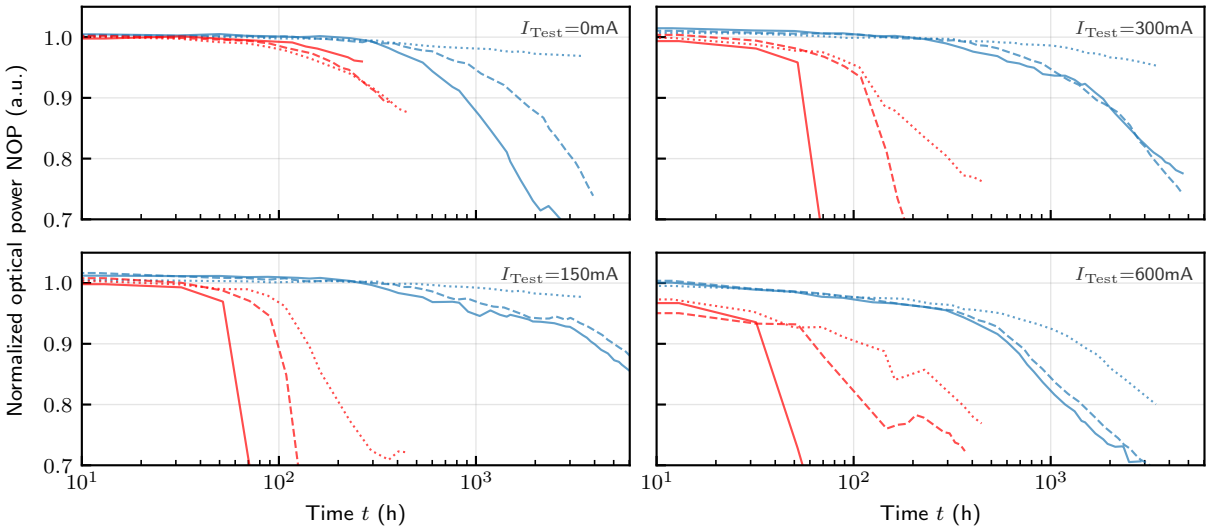

Figure 5.29: Normalized optical power NOP degradation trajectories of the purple DUT for each of the 24 investigated stress conditions separated by the stress current I_{Test}: (top left) 0 mA, (top right) 150 mA, (bottom left) 75 mA and (bottom right) 300 mA. Each plot displays the stress temperatures T_{Test} in (blue) 65 °C and (red) 85 °C as well as the stress humidity rH_{Test} as (dotted line) 25 %, (dashed line) 55 % and (solid line) 85 %.

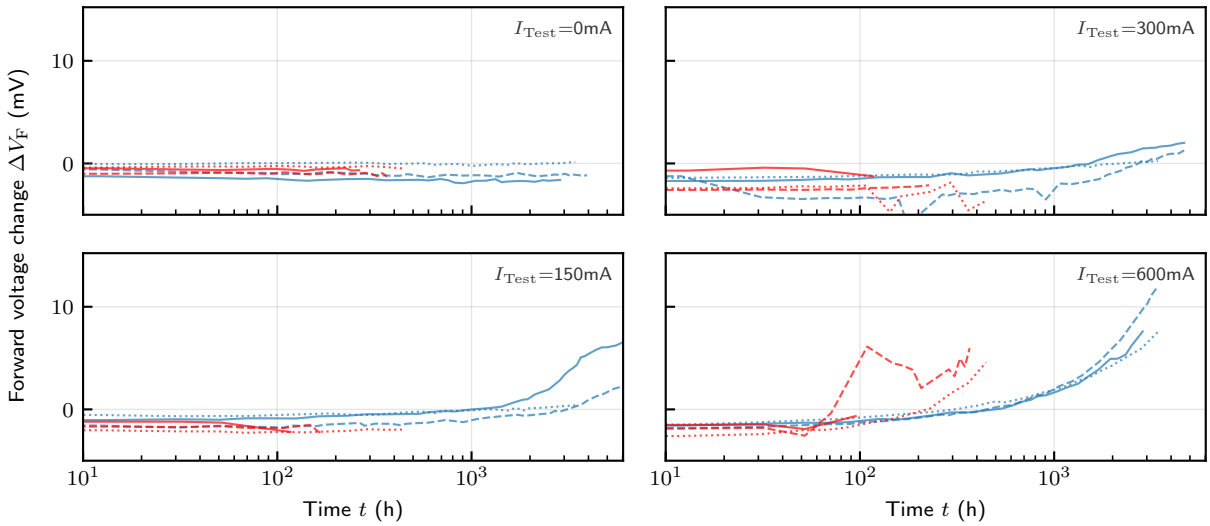

Figure 5.30: Change in forward voltage ΔV_{F} of the purple DUT for each of the 24 investigated stress conditions separated by the stress current I_{Test}: (top left) 0 mA, (top right) 150 mA, (bottom left) 75 mA and (bottom right) 300 mA. Each plot displays the stress temperatures T_{Test} in (blue) 65 °C and (red) 85 °C as well as the stress humidity rH_{Test} as (dotted line) 25 %, (dashed line) 55 % and (solid line) 85 %.

die related contribution starting at around $t \geq 400\,\text{h}$ which agrees with the previous $\Delta V_{\text{F}}(t)$ observations. Therefore it can be concluded, the external quantum efficiency is dependent on both time and current resulting in the following expression $\eta_{\text{EQE}}(t, I_{\text{m}}) = \eta_{\text{LEE}}(t) \cdot \eta_{\text{IQE}}(I_{\text{m}})$. Yet it should be noted, that for $t < 400\,\text{h}$ the light extraction efficiency $\eta_{\text{LEE}}(t)$ predominates while at $t \gg 400\,\text{h}$ the current dependent internal quantum efficiency $\eta_{\text{IQE}}(I_{\text{m}})$ will mainly influence the degradation. The overall change in external quantum efficiency $\Delta\eta_{\text{EQE}}$ is shown in fig. 5.21. Due to the fact, that even under storage conditions ($I_{\text{Test}} = 0\,\text{mA}$) a decrease in external quantum efficiency exists non-current induced and thus rather package related contributions within the optical path to η_{LEE} are concluded.

Optical Degradation

Following the degradation of the optical path will be examined by means of the CIE 1976 UCS chromaticity coordinates shift $\Delta u'(t)$ and $\Delta v'(t)$ and the phosphor-to-chip ration shown in fig. 5.33 and fig. 5.35, respectively. At storage conditions ($I_{\text{Test}} = 0\,\text{mA}$) a distinct blue shift ($\Delta u'(t) < 0$, $\Delta v'(t) < 0$) which scales well with temperature and humidity can be observed within the CIE 1976 UCS as well as it becomes apparent in the PBR. Latter suggests a decrease in phosphor emission which can be attributed to a moisture and temperature promoted dissolution of phosphor particles resulting in a higher blue light transmittance of the encapsulant [204]. Under operating conditions at lower temperature $T_{\text{Test}} = 65\,°\text{C}$ a combination of different shift directions can be observed which first approaches yellow ($\Delta u'(t) > 0$, $\Delta v'(t) > 0$) then heads towards blue ($\Delta u'(t) < 0$, $\Delta v'(t) < 0$) and finally towards yellow again. This combination hints towards a yellowing of the encapsulant followed by phosphor dissolution which becomes overwhelmed by a final encapsulant yellowing process. Alongside small fractures arise that promote further moisture ingress. The phosphor dissolution is shown in the middle picture of fig. 5.34. In contrast within the high temperature regime at $T_{\text{Test}} = 85\,°\text{C}$ a more chaotic

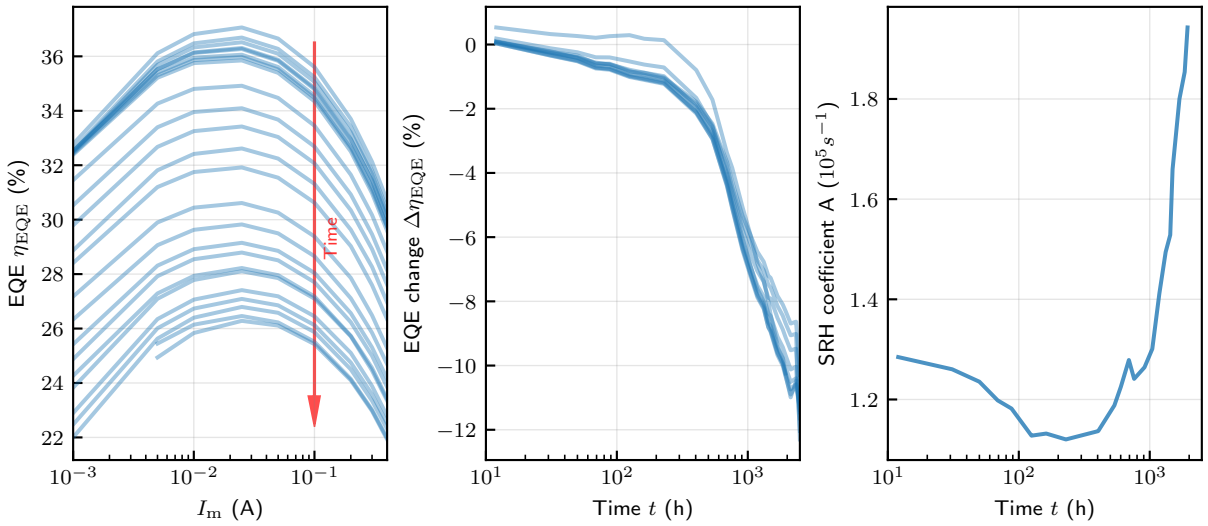

Figure 5.31: External quantum efficiency η_{EQE} with respect to aging time t and measurement current I_m exemplary for one purple DUT of the (85 %, 65 °C, 600 mA)-condition: (left) calculated η_{EQE} for different I_m at various aging times, (center) absolute change in EQE over time for different I_m and (right) the ABC-model's SRH coefficient A with respect to aging time.

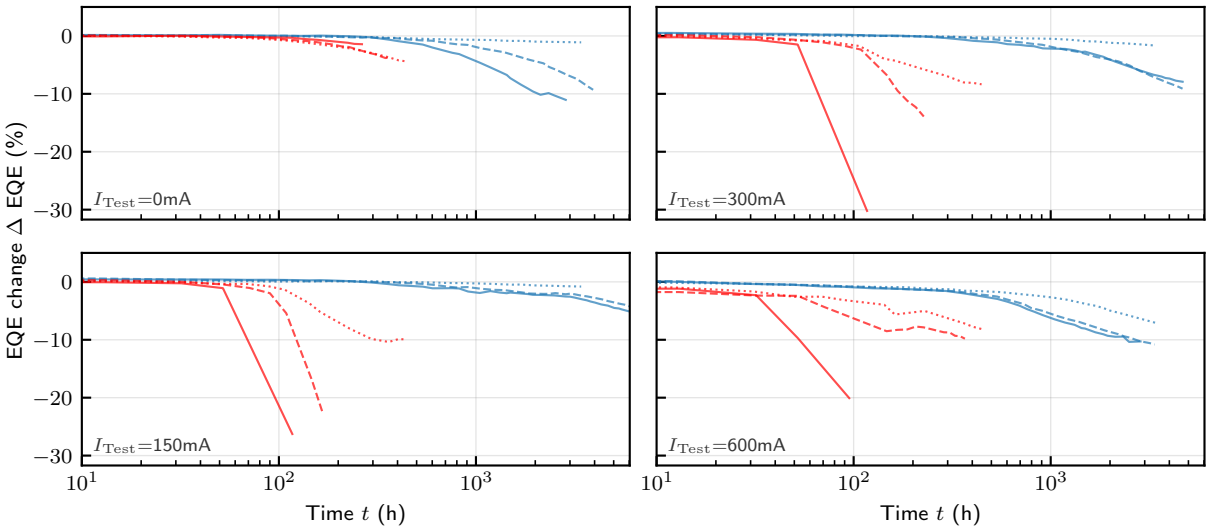

Figure 5.32: Change in external quantum efficiency η_{EQE} of the purple DUT for each of the 24 investigated stress conditions separated by the stress current I_{Test}: (top left) 0 mA, (top right) 150 mA, (bottom left) 75 mA and (bottom right) 300 mA. Each plot displays the stress temperatures $T_{Testress}$ in (blue) 65 °C and (red) 85 °C as well as the stress humidity rH_{Test} as (dotted line) 25 %, (dashed line) 55 % and (solid line) 85 %.

behavior emerges. While at lower humidity and high current $I_{Test} = 600$ mA conditions the trajectories follow those of at lower temperatures, a sudden and rather drastic blue shift is exhibited by the moderate current conditions. The first case be attributed to a yellowing of the encapsulant as also the increasing Yellowing Index suggests. The latter observations can be drawn to a combination of severe encapsulant cracking and phosphor dissolution. Under high temperature hygrothermal stress moisture ingress causes the encapsulant to swell

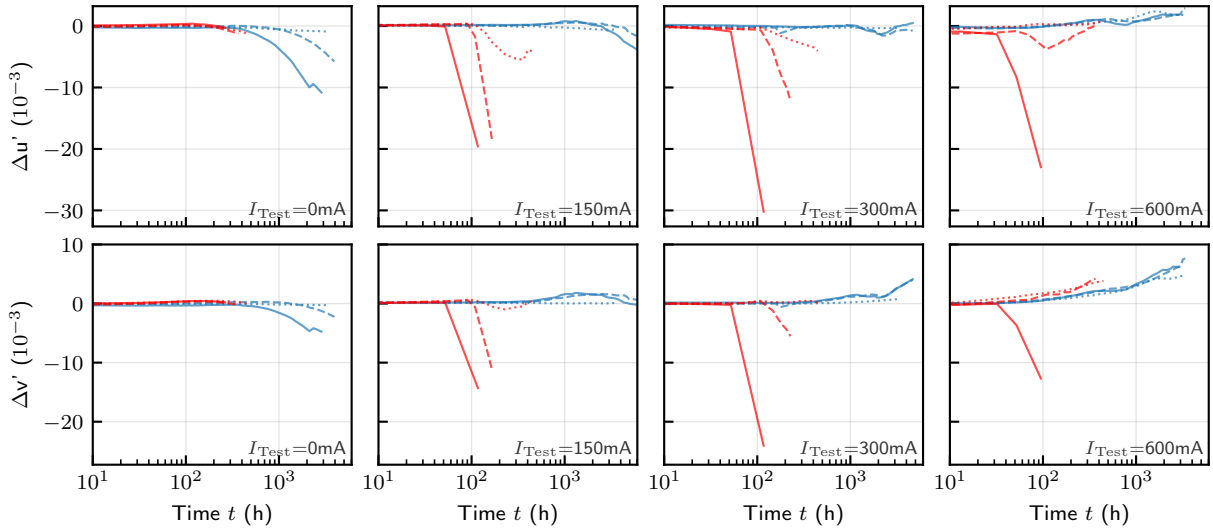

Figure 5.33: Change in CIE 1976 UCS chromaticity coordinates (top) $\Delta u'$ and (bottom) $\Delta v'$ of the purple DUT for each of the 24 investigated stress conditions separated by the stress current I_{Test}: (left to right) 0 mA, 150 mA, 75 mA and 300 mA. Each plot displays the stress temperatures T_{Test} in (blue) 65 °C and (red) 85 °C as well as the stress humidity rH_{Test} as (dotted line) 25 %, (dashed line) 55 % and (solid line) 85 %.

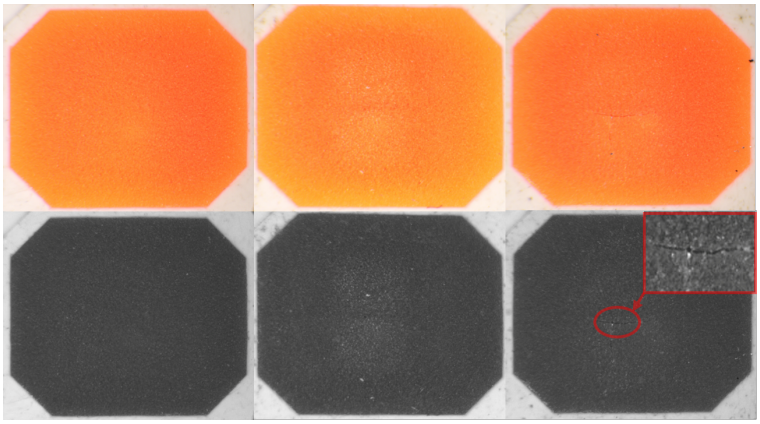

Figure 5.34: Visible degradation effects of the purple DUT with (top) the original image and (bottom) gray scaled image highlighting the distinct degradation effect. The following effects are shown exemplary from left to right: DUT before aging, phosphor dissolving and lead-frame reflector tarnishing and encapsulant cracking.

and become enbrittle especially in the region of highest temperature right above the die. Small fractures formed this way promote further moisture ingress resulting in large cracks as displayed in the right plot of fig. 5.34 alongside with elevating the dissolution rate in this region. Subsequently, more blue light escapes the package either direct along the cracks or through the more transparent encapsulant.

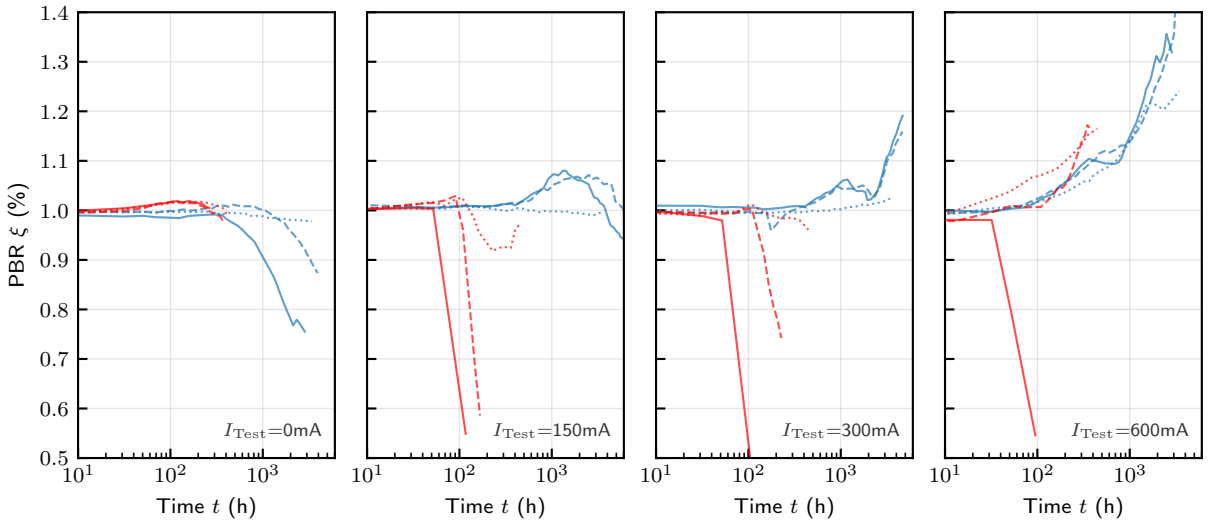

Figure 5.35: Relative phosphor to chip peak power ratio ξ of the purple DUT for each of the 24 investigated stress conditions separated by the stress current I_{Test}: (left to right) 0 mA, 150 mA, 75 mA and 300 mA. Each plot displays the stress temperatures T_{Test} in (blue) 65 °C and (red) 85 °C as well as the stress humidity rH_{Test} as (dotted line) 25 %, (dashed line) 55 % and (solid line) 85 %.

5.4 White LED Samples

Following the measurement results of the horticulture white DUT [338] obtained from the experiment presented in chapter 4 are highlighted alongside with an investigation of the observed degradation effects root causes. This section, therefore, first provides an initial characterization of $N = 117$ devices subjected to 24 different (rH_A, T_A, I_F) stress conditions. Similar to the purple DUT again a total of three test subjects exhibited an early stage open circuit catastrophic failure during the first 12 h test period and thus were dismissed from the subsequent analysis.

5.4.1 Initial Characterization

In order to obtain an insight on the initial uncertainties of the devices originating from e.g. the manufacturing process all $N = 117$ devices are characterized. At first the device point dependent characteristics are investigated along with the overall spectral emission pattern. By sweeping the forward current from $I_m = 1$ mA to 400 mA $I_m = 1$ mA to 400 mA the typical exponential diode IVL-characteristic is obtained since $P_{opt} \propto I_F(V_F)$. The observed optical power and voltage ranges from 1.23 ± 0.05 mW and 2.51 ± 0.004 V at 1 mA to 473.51 ± 3.49 mW and 3.20 ± 0.014 V at 400 mA as shown in the left plot of fig. 5.36. Further, a uniform distribution of P_{opt} and V_F displayed in the center plot suggests no manufacturer side optical power or voltage binning of the devices. On the spectral side a blue emitter placed at $\lambda_{p,die} = 450.52 \pm 0.83$ nm accompanied by a 467 nm side peak is combined with two or three phosphor wavelength-converters of $\lambda_{p,ph1} = 515.75 \pm 0.69$ nm, $\lambda_{p,ph2} = 550.59 \pm 0.75$ nm and $\lambda_{p,ph1} = 651.0 \pm 0.1$ nm respectively. Due to the similar blue emission pattern the same die structure as used for the purple DUT can be assumed for the horticulture device. The presence of three phosphor peaks firstly suggests that also three phosphors might have been used, however, as elaborated in a publication by Zhou et al. [351] a similar peak emission pattern can be achieved by a

cyan-green $Lu_2\,Ba\,Al_4\,Si\,O_{12}:Ce^{3+}$ and a standard red $(Ca,Sr)\,Al\,Si\,N_3:Eu^{2+}$ phosphor. Further, despite the comparatively high peak power variations with respect to the other devices the overall variation in optical power of the SPD aligns with the previous analyzed test subjects. These variations influence on the CIE 1976 UCS chromaticity coordinates distribution will be discussed at a later point in this section. The overall peak powers and their ratios are as follows: $P_{\mathrm{opt}}(\lambda_{\mathrm{p,die}}) = 0.83\,\mathrm{mW\,nm^{-1}}$, $P_{\mathrm{opt}}(\lambda_{\mathrm{p,ph1}}) = 0.42\,\mathrm{mW\,nm^{-1}}$, $P_{\mathrm{opt}}(\lambda_{\mathrm{p,ph2}}) = 0.44\,\mathrm{mW\,nm^{-1}}$ and $P_{\mathrm{opt}}(\lambda_{\mathrm{p,ph3}}) = 1.11\,\mathrm{mW\,nm^{-1}}$ with corresponding ratios of 1 : 0.50, 1 : 0.53 and 1 : 1.34.

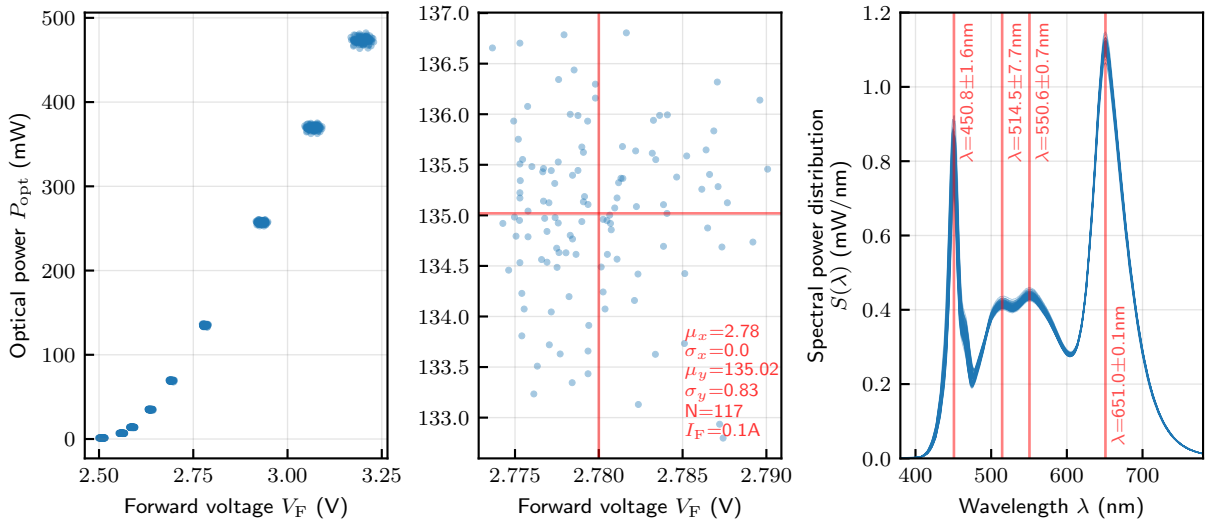

Figure 5.36: Initial optical measurements of the White DUT: (left) optical power P_{opt} vs. forward voltage V_{F} at nine distinct measurement currents I_{m}, (middle) distribution of V_{F} and P_{opt} at $I_{\mathrm{m}} = 100\,\mathrm{mA}$ and (right) all measured SPDs at $I_{\mathrm{m}} = 100\,\mathrm{mA}$ with the die's mean emission peak wavelength $\lambda_{\mathrm{p}} = \lambda_{\mathrm{b}}$. All measurements respective sample count, mean, standard deviation and measurement condition are highlighted in red.

Similar to the lime and purple DUT temperature induced wavelength shift of the die emitter towards the red spectrum $\Delta\lambda_{\mathrm{p,die}} = +2.54\,\mathrm{nm}$ when increasing the junction temperature from $T_{\mathrm{j}} = 25\,^{\circ}\mathrm{C}$ to $75\,^{\circ}\mathrm{C}$ is observed due to temperature dependent decrease of the band gap energy. Alongside the optical power decreases by $\Delta P_{\mathrm{opt}}(\lambda_{\mathrm{p,die}}) = -11.4\,\%$ as a result of thermally enhanced SRH-recombination. In contrast, a blue shift of $\Delta\lambda_{\mathrm{p,die}} = -3.77\,\mathrm{nm}$ is observed with increasing forward current induced charge carriers which lower opposed electrical within the die and thus reduce the QCSE. Contrarily, a red temperature induced red shift of all three phosphor peaks of $\Delta\lambda_{\mathrm{p,die}} = +2.54\,\mathrm{nm}$ and a blue shift of $\Delta\lambda_{\mathrm{p,ph1}} = -16.87\,\mathrm{nm}$, $\Delta\lambda_{\mathrm{p,ph2}} = -1.28\,\mathrm{nm}$ and $\Delta\lambda_{\mathrm{p,ph3}} = -1.83\,\mathrm{nm}$ can be determined due to thermal quenching behavior of the phosphor. Resulting from thermal quenching as well as reduced emissions from the die itself the peak's overall power is reduced by $\Delta P_{\mathrm{opt}}(\lambda_{\mathrm{p,ph1}}) = -6.1\,\%$, $\Delta P_{\mathrm{opt}}(\lambda_{\mathrm{p,ph2}}) = -7.9\,\%$ and $\Delta P_{\mathrm{opt}}(\lambda_{\mathrm{p,ph3}}) = -10.4\,\%$.
By further considering fig. 5.37 the average, maximum external quantum efficiency EQE can be determined to $\eta_{\mathrm{EQE,max}} = 47.42 \pm 0.42\,\%$ at a forward current of maximum efficiency of $I_{\mathrm{m,max}} = 25\,\mathrm{mA}$. Compared to the maximum measured forward current of $I_{\mathrm{m}} = 400\,\mathrm{mA}$ the horticulture white DUT exhibits a significant higher efficiency droop of $\eta_{\mathrm{Droop}} = -18\,\%$ with respect to the previous discussed test subjects. This most likely reasons from the multi-phosphor

composition exhibiting a distinct thermal quenching at higher excitation power levels and thus decreasing the light extraction efficiency η_{LEE} of the device.

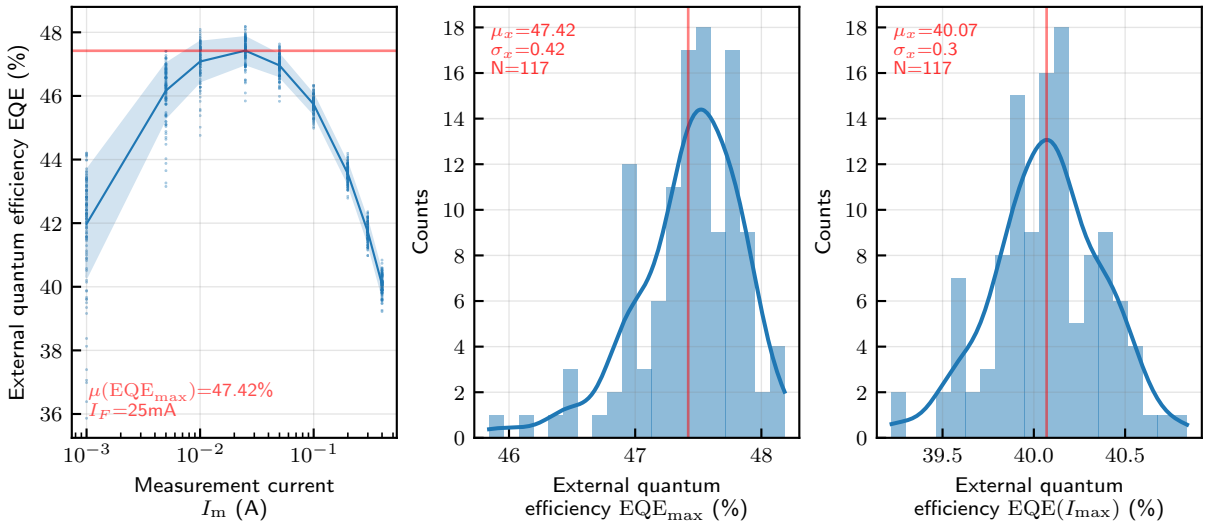

Figure 5.37: Initial EQE measurements of white DUT: (left) external quantum efficiency EQE at nine distinct measurement currents I_{m}, (middle) distribution of maximum external quantum efficiency $\mathrm{EQE}_{\mathrm{max}}$ at $I_{\mathrm{EQE,max}}$ and (right) distribution of EQE at maximum measurement current $I_{\mathrm{m,max}}$. All measurements respective sample count, mean, standard deviation and measurement condition are highlighted in red.

With regard to the electrical parameters initially $N = 80$ IV-characteristics were analyzed as presented in fig. 5.38. Apart from nine outliers exhibiting trap assisted tunneling processes in the low injection regime at $V_{\mathrm{F}} < 1.75\,\mathrm{V}$, all devices follow a common IV-characteristics as the left plot of fig. 5.38 presents. Along the ideal diode characteristic in the forward voltage region of $2.0\,\mathrm{V} \leq V_{\mathrm{F}} \leq 2.7\,\mathrm{V}$ a narrow distributed ideality factor of $n_{\mathrm{ideal}} = 1.20 \pm 0.05$ is obtained as displayed in the center plot. Deviations from the ideal diode characteristic in the low injection regime $V_{\mathrm{F}} < 1.75\,\mathrm{V}$ are attributed to a parasitic parallel resistance of $R_{\mathrm{p}} = 14.3 \pm 6.05\,\mathrm{G\Omega}$ originating from parallel, non-radiating current path around the active region [145, 146]. Whereas in the high injection region a parasitic series resistance of $R_{\mathrm{s}} = 0.1.1 \pm 0.03\,\Omega$ is obtained from the IV-characteristic at $V_{\mathrm{F}} \geq 2.7\,\mathrm{V}$. Again, the obtained values agree with measurements presented in the previous section drawing the conclusion that the same parallel semiconductor configuration as also for the purple DUT is used.
In the following the previously identified peak power variations shown in the SPD of fig. 5.36 are investigated in terms of color binning with regard to the CIE 1976 UCS chromaticity coordinates u', v' and the yellowing index highlighted in fig. 5.39. The chromaticity coordinates obtained from the SPD are calculated to $(u', v')^T = (0.2222 \pm 0.001, 0.4847 \pm 0.002)^T$ with a corresponding yellowing index of $\mathrm{YI} = 37.03 \pm 3.03$. Both metrics show no clustering, thus no distinct color binning is assumed in the device's population.
Also the measured thermal junction to solder resistances fo $R_{\mathrm{th,j-s}} = 9.99 \pm 1.18\,\mathrm{K\,W^{-1}}$ are as those of the previously discussed devices also within and even below the manufacturer's specifications [338].

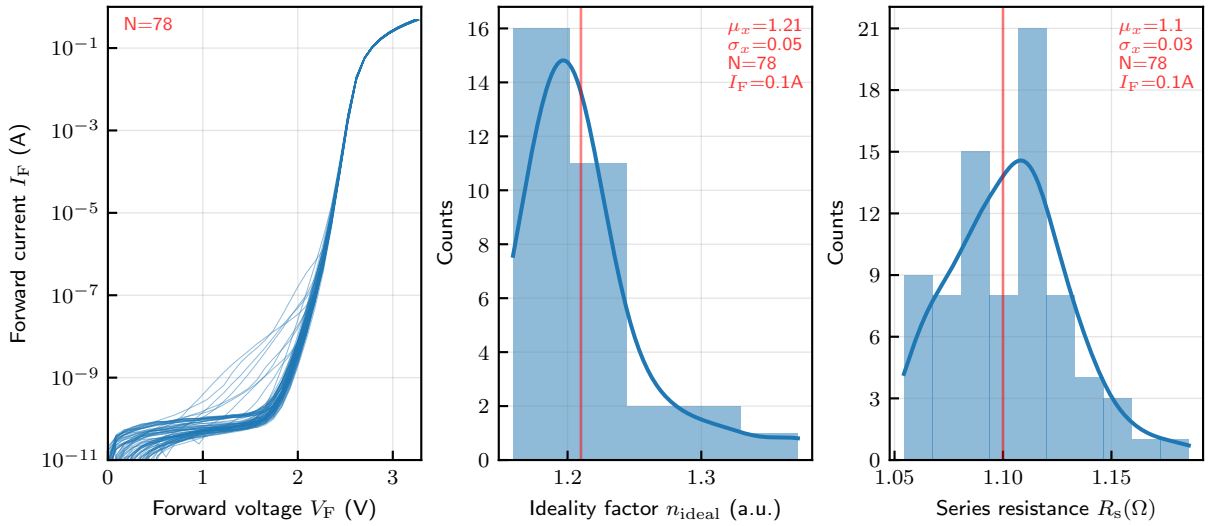

Figure 5.38: Initial electrical measurements of white DUT: (left) IV-characteristic, (middle) distribution of the ideality factor n_{ideal} and (right) distribution of the parasitic series resistance R_s. All measurements respective sample count, mean, standard deviation and measurement condition are highlighted in red.

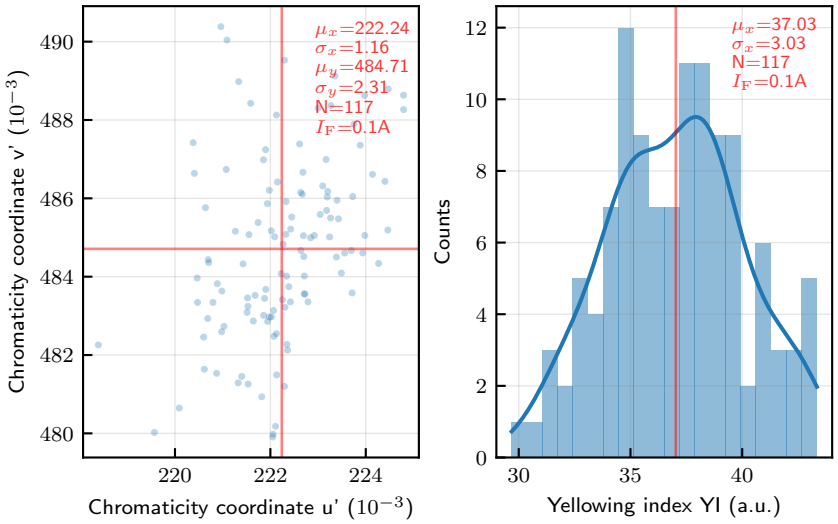

Figure 5.39: Initial colorimetric measurements of white DUT: (left) distribution of the CIE 1976 UCS chromaticity coordinates u', v' and (right) distribution of the ASTM D1925 yellowing index YI. All measurements respective sample count, mean, standard deviation and measurement condition are highlighted in red.

5.4.2 Results and Degradation Analysis

The subsequent part of this section elaborates on the experimental results of the horticulture white DUT that was aged according to the 24 stress conditions proposed in chapter 4. Therefore, the obtained degradation trajectories shown in fig. 5.40 are analyzed regarding their root cause and failure site within the LED package by following the light extraction path from the die up to the packages surface.

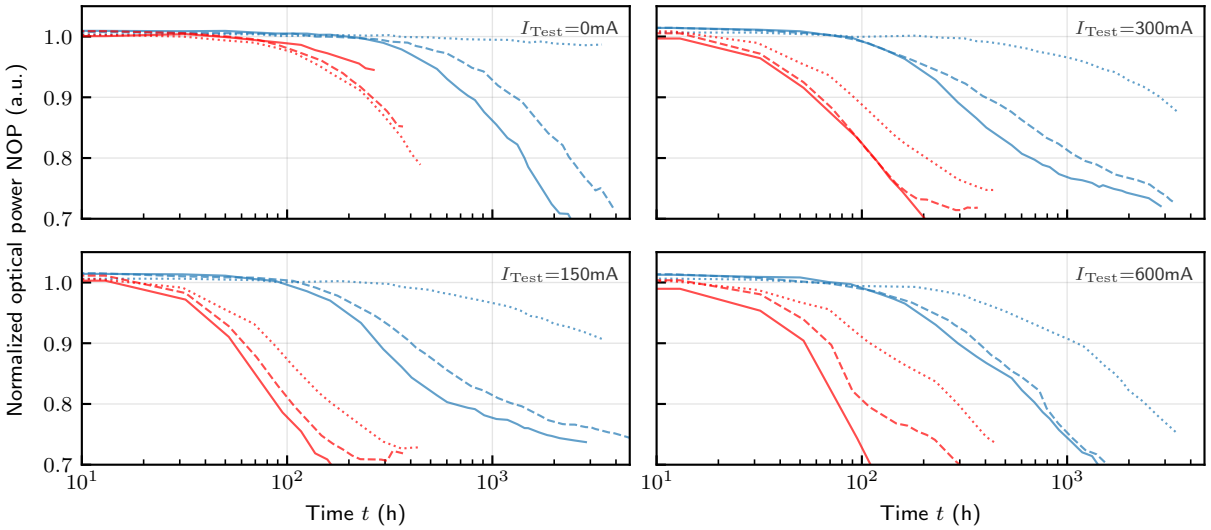

Figure 5.40: Normalized optical power NOP degradation trajectories of the Royal white DUT for each of the 24 investigated stress conditions separated by the stress current I_{Stress}: (top left) 0 mA, (top right) 150 mA, (bottom left) 75 mA and (bottom right) 300 mA. Each plot displays the stress temperatures T_{Stress} in (blue) 65 °C and (red) 85 °C as well as the stress humidity $\mathrm{rH}_{\mathrm{Stress}}$ as (dotted line) 25 %, (dashed line) 55 % and (solid line) 85 %.

Electrical and Efficiency Parameters

First, the forward voltages change over time $\Delta V_{\mathrm{F}}(t)$ presented in fig. 5.41 is investigated to determine whether any die related degradation is apparent. After an initial voltage drop $V_{\mathrm{F}}(t < 20\,\mathrm{h}) \approx -6\,\mathrm{mV}$ to 0 mV an exponential-like increase is observed for the devices under operating conditions at $I_{\mathrm{Test}} > 0\,\mathrm{mA}$ whilst no significant change occurs under storage conditions at $I_{\mathrm{Test}} = 0\,\mathrm{mA}$. The drop apparently scales marginally with temperature and forward current. It further correlates to the initial increase in optical power. Similar to the previous analyzed devices the change parasitic series resistance of $\Delta R_{\mathrm{s}} \approx 10^{-3}\,\Omega$ is not sufficiently pronounced in order to affect the forward voltage significantly. Subsequently, a decompensation of p-side acceptors can be suspected [298]. Since the successive $V_{\mathrm{F}}(t)$ increase is only present under operating conditions, current induced diffusion processes of hot charge carriers across the active region are suspected to promote point defects [349]. Similar to the purple DUT the relative strong voltage increase rate compared to the both devices using a single die configuration can be attributed to a drive current imbalance between both dies enhancing one die's degradation speed significantly. In contrast to the other test subjects no sudden rise of $V_{\mathrm{F}}(t)$ was present for the (55 %, 85 °C, 600 mA)-condition around 50 h which concludes that no drastic electrolysis effects [204] are present for the horticulture white devices.

By further taking the influence of the aging time as well as the measurement current on the external quantum efficiency $\eta_{\mathrm{EQE}}(t, I_{\mathrm{m}}) = \eta_{\mathrm{LEE}}(t) \cdot \eta_{\mathrm{IQE}}(I_{\mathrm{m}})$ into account the contribution of the die's degradation due to the internal quantum efficiency η_{IQE} and the encapsulant's and package's contribution by the light extraction efficiency η_{LEE} is evaluated. As the left plot of fig. 5.42 shows exemplary for one test subject, a approximate uniform decrease in η_{EQE} over the whole measurement current range is present. This suggests that the main degradation contributor is rather be found alongside package than the die. However, towards

the experiments end $t > 1000\,\mathrm{h}$ a noticeable spreading between the measurement currents appears as shown by the center plot. Yet, the no significant change of the SRH-coefficient — which would be expected in the order of at least one magnitude — was observed in the data as highlighted in the right plot. Therefore, an onset of a die related contribution in the late stage of testing can be assumed. In summary, for $t < 1000\,\mathrm{h}$ a package related degradation mechanism along the optical path is present yielding $\eta_{\mathrm{EQE}}(t < 1000\,\mathrm{h}) \propto \eta_{\mathrm{LEE}}(t)$ whereas with prolonged operating time the external quantum efficiency results in $\eta_{\mathrm{EQE}}(t > 1000\,\mathrm{h}, I_{\mathrm{m}}) = \eta_{\mathrm{LEE}}(t) \cdot \eta_{\mathrm{IQE}}(I_{\mathrm{m}})$.
The overall change in external quantum efficiency $\Delta\eta_{\mathrm{EQE}}$ for all test conditions is subsequent presented in fig. 5.43 exhibiting a similar s-shape trajectory over time as the optical power shown in fig. 5.40.

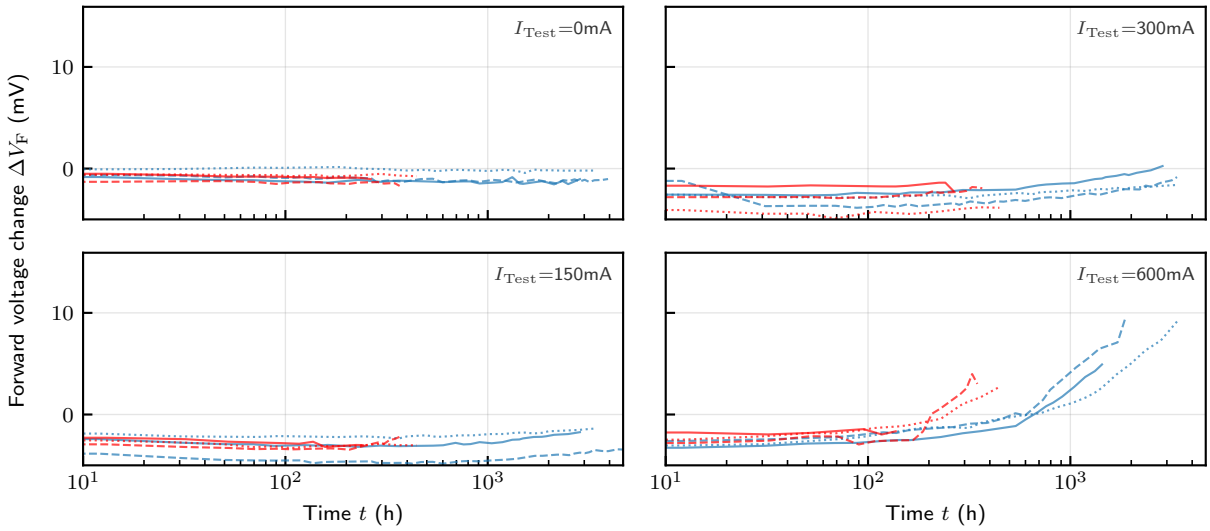

Figure 5.41: Change in forward voltage ΔV_{F} of the white DUT for each of the 24 investigated stress conditions separated by the stress current I_{Stress}: (top left) 0 mA, (top right) 150 mA, (bottom left) 75 mA and (bottom right) 300 mA. Each plot displays the stress temperatures T_{Stress} in (blue) 65 °C and (red) 85 °C as well as the stress humidity $\mathrm{rH}_{\mathrm{Stress}}$ as (dotted line) 25 %, (dashed line) 55 % and (solid line) 85 %.

Optical Degradation

This paragraph examines the degradation effects appearing along the optical path at different parts of the LED package with regard to the devices CIE 1976 UCS chromaticity coordinates shift $\Delta u'(t)$ and $\Delta v'(t)$ and the phosphor to blue ratios change over time. Under storage conditions at $I_{\mathrm{Test}} = 0\,\mathrm{mA}$ first a small green shift ($\Delta u'(t) < 0$, $\Delta v'(t) > 0$) until $t \approx 300\,\mathrm{h}$ followed by a significant blue shift ($\Delta u'(t) < 0$, $\Delta v'(t) < 0$) can be observed in fig. 5.44 for all climate conditions. By taking additional the PBR presented in fig. 5.45 into consideration the degradation of the encapsulant becomes obvious for the first two peaks of the green-yellow phosphor. However, the red phosphor exhibits a drastic emission decrease. Therefore, it can be assumed that during the first 300 h a yellowing of the encapsulant takes place as also observed for the other devices with a simultaneous dissolution of the red phosphor followed

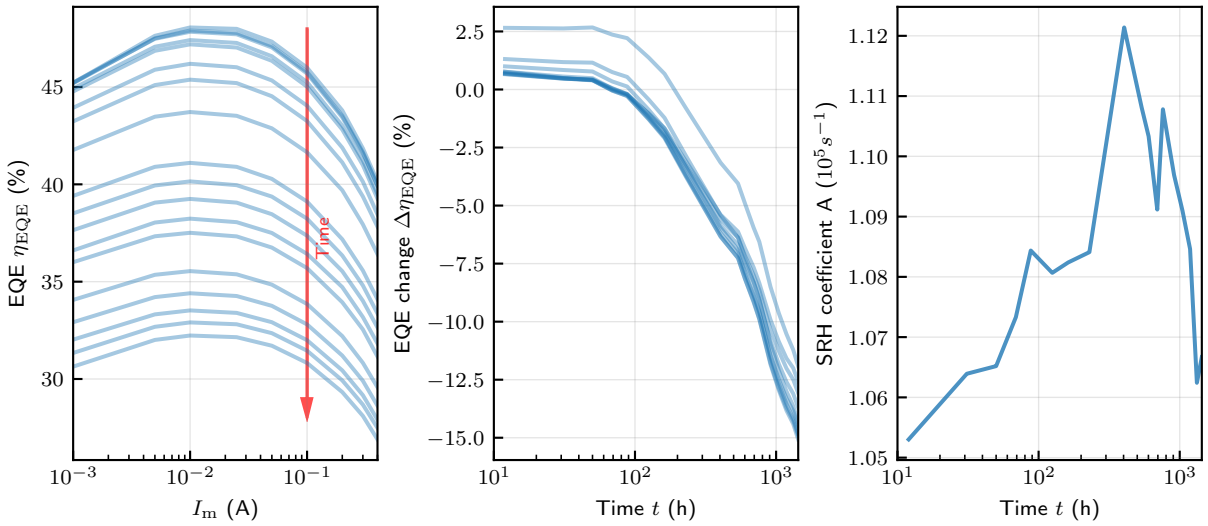

Figure 5.42: External quantum efficiency η_{EQE} with respect to aging time t and measurement current I_m exemplary for one white DUT of the (85 %, 65 °C, 300 mA)-condition: (left) calculated η_{EQE} for different I_m at various aging times, (center) absolute change in EQE over time for different I_m and (right) the ABC-model's SRH coefficient A with respect to aging time.

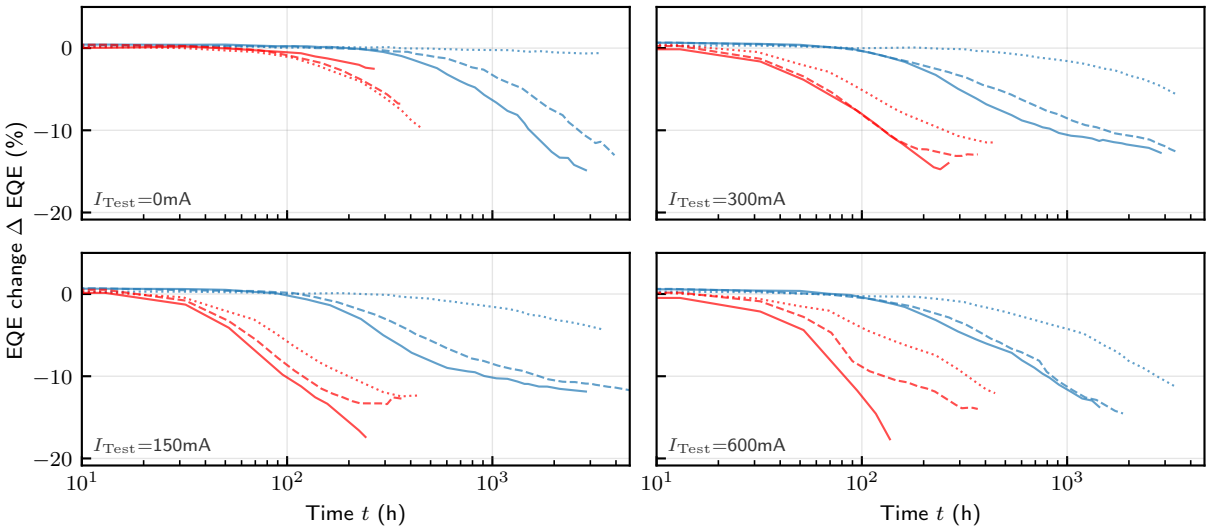

Figure 5.43: Change in external quantum efficiency η_{EQE} of the white DUT for each of the 24 investigated stress conditions separated by the stress current I_{Stress}: (top left) 0 mA, (top right) 150 mA, (bottom left) 75 mA and (bottom right) 300 mA. Each plot displays the stress temperatures T_{Stress} in (blue) 65 °C and (red) 85 °C as well as the stress humidity rH_{Stress} as (dotted line) 25 %, (dashed line) 55 % and (solid line) 85 %.

by a subsequent dissolution of the yellow-green phosphor with an onset at about 300 h [204]. Inspecting the chromaticity coordinates reveals a rather uniform blue shifting trajectory that saturates at a certain point in time and scales with temperature and humidity but not with current. Especially at high current conditions an intermediate green-shift becomes visible for all but the highest climate condition. A possible origin for this behavior might be the higher dissolution rate of the red phosphor compared to the green-yellow phosphor thus

enhancing the green to yellow spectral content of the SPD. This behavior agrees with overall faster dissolution rate of the red phosphor observed at the other current conditions.
Further a continuous decrease in optical power during the first few hundred hours without

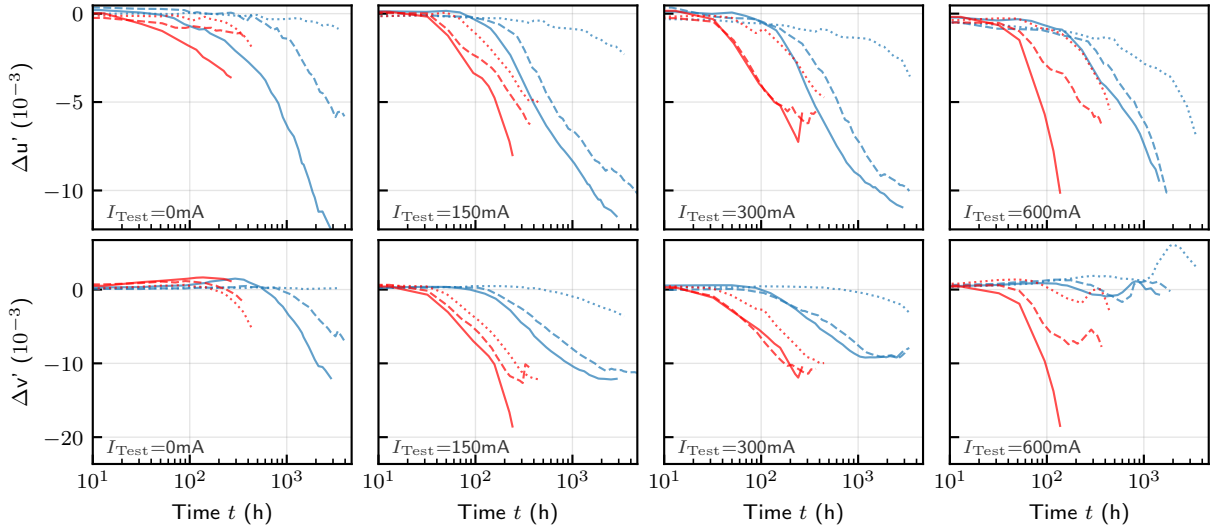

Figure 5.44: Change in CIE 1976 UCS chromaticity coordinates (top) $\Delta u'$ and (bottom) $\Delta v'$ of the white DUT for each of the 24 investigated stress conditions separated by the stress current I_{Stress}: (left to right) 0 mA, 150 mA, 75 mA and 300 mA. Each plot displays the stress temperatures T_{Stress} in (blue) 65 °C and (red) 85 °C as well as the stress humidity $\text{rH}_{\text{Stress}}$ as (dotted line) 25 %, (dashed line) 55 % and (solid line) 85 %.

a significant change in the CIE 1976 UCS is present. As the RGB-adjusted picture of an aged device in the center of fig. 5.46 shows, a noticeable tarnishing of the lead-frames reflective coating becomes apparent. Therefore, less blue light is reflected and subsequently down-converted as also indicated by the PBR. Also the formation of encapsulant cracks above the die at very high elevated stress conditions as shown in the right part of fig. 5.46 was registered which agrees with an observed strong blue shift in fig. 5.45 since more direct blue light escapes the package without being either absorbed by a yellowed encapsulant nor down-converted by one of the phosphors.

5.5 Conclusion and Findings

This section provides an overview over the observed degradation effects and their impact on the test subjects optical performance. Therefore, the stress types impact on the various failure sites similar to section 3.2.4 will be highlighted subsequently.

Die Level

An *initial increase in optical power* accompanied by a *forward voltage drop* was exhibited by all devices. This effect is definitely not a failure by definition, yet it should be taken into account for further application designs, e.g. in luminaires, by scheduling a defined burn in or at least tempering phase of about 100 h before operation. Since this procedure is not economically feasible a short period high temperature tempering of 400 °C to 800 °C might address these

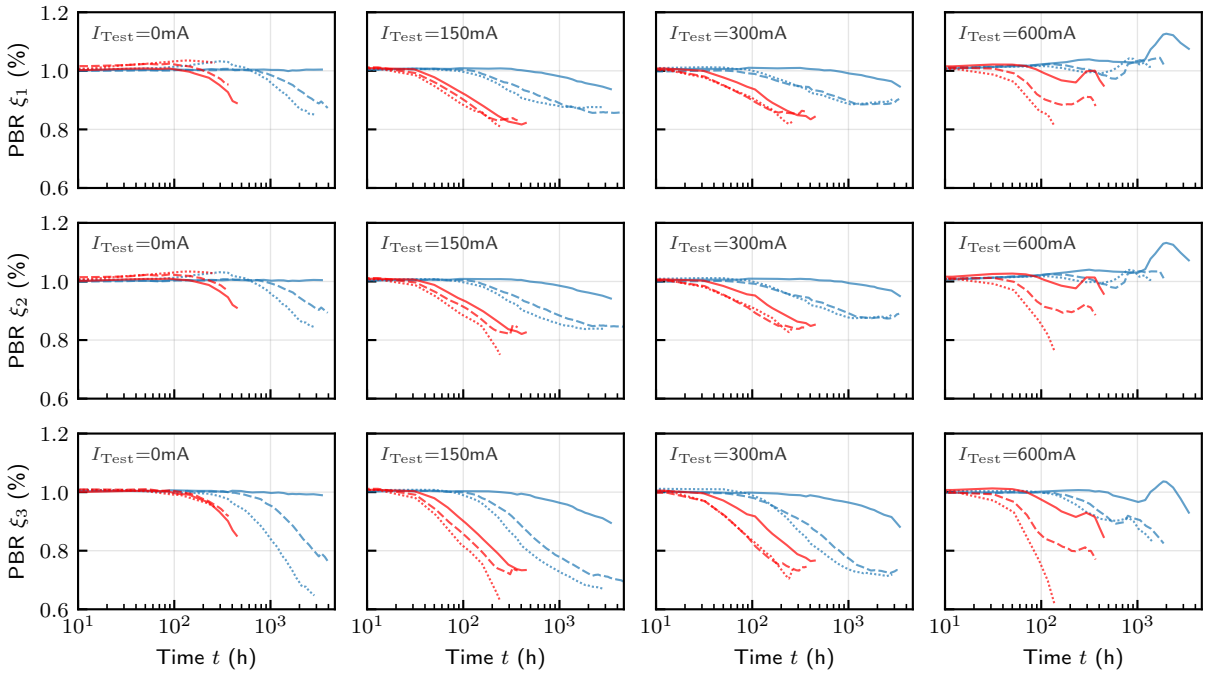

Figure 5.45: Relative phopshor to chip peak power ratios (first row) ξ_1, (second row) ξ_2 and (third row) ξ_3 of the white DUT for each of the 24 investigated stress conditions separated by the stress current I_{Stress}: (left to right) 0 mA, 150 mA, 75 mA and 300 mA. Each plot displays the stress temperatures T_{Stress} in (blue) 65 °C and (red) 85 °C as well as the stress humidity $\mathrm{rH}_{\mathrm{Stress}}$ as (dotted line) 25 %, (dashed line) 55 % and (solid line) 85 %.

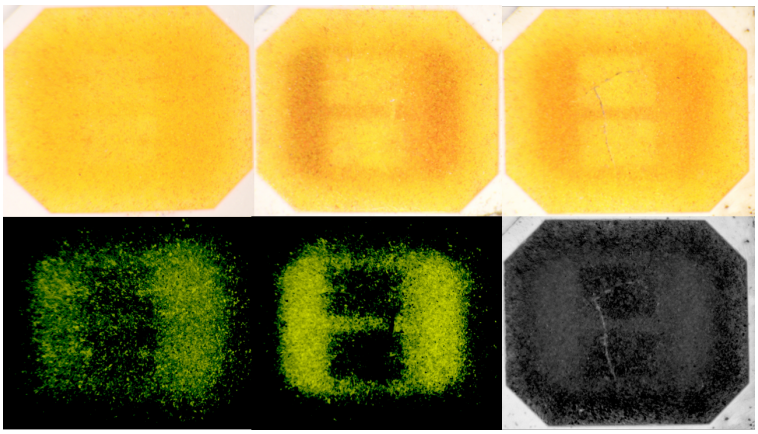

Figure 5.46: Visible degradation effects of the white DUT with (top) the original image and (bottom) gray scaled image highlighting the distinct degradation effect. The following effects are shown exemplary from left to right: DUT before aging, phosphor dissolving and lead-frame reflector tarnishing and encapsulant cracking.

problems.

The subsequent *increase in forward voltage* due to *diffusion related point defects* was observed for all devices. However, both the purple and horticulture white test subjects which used a parallel die configuration experienced a larger increase due to imbalanced current flow between both

dies resulting in a higher defect generation rate in one dies.

Interconnect Level

The *ingress of moisture* promoted the accumulation of copper at the bond wire attachment on the lead-frame due to *electrolysis at Cu – Au interface*. As a result the *forward voltage drastically increased*. Due to the increased series resistance enhanced Joule heating can further damage the device at all levels. An additional separation layer between the copper heat slug and the lead-frame could be a possible solution to prevent the observed copper accumulation.

Package Level

Sulfur particles containing moisture ingress enables the *oxidation of the lead-frames reflective layer*. As a result less light is reflected from the bottom of the package towards the packages surface resulting in an decrease in optical power. A decreased oxidation rate around the die attach suggests that the application of highly adhesive and water repellent coating layer between lead-frame and encapsulant might slow down the oxidation process.
Persistent exposure to *high moisture and elevated temperatures* promote to *moisture absorbance by silicone encapsulant*. Due to the moisture intake the silicone swells and shear forces are introduced into the package enabling follow-up effects:

- Detachment of the silicone from the reflective moulding cup as the induced shear forces cancel out the silicones adhesive forces at the cups interface. This issue might be addressed by an mechanical design adjustment in order to dissipate uprising shear forces.
- Moisture ingress triggered an Autoxidation cycle promoting in cross-linking and chain cleavage of the silicone polymer encapsulant. A yellow discoloration of the encapsulant was the result which lowered the overall optical power of the device.
- Both, shear forces and Autoxidation enhance the enbrittlement as well as the formation of cracks of the silicone encapsulant. As a result a direct blue light escape path is formed altering the overall spectral emission pattern of the device. Simultaneously, a higher level moisture directly penetrates the packages deeper layers triggering further degradation effects.

Moisture ingress opposes an additional threat to phosphor-converted devices since water molecules promote phosphor dissolution by destroying the host lattices structure yielding lower wavelength-conversion rates. This effect was especially present in the nitride based red phosphor of the horticulture white test subject.
In general a highly transparent and water repellent coating applied to the encapsulants surface on the packages top side should decrease the moisture ingress an thus prolong the devices lifetime.

6 Lifetime Modeling for LED Devices

Degradation data recorded in ALT or ADT presented in section 3.1 reveal a general estimate of the devices total lifetime or, respectively, a deeper understanding of its degradation trajectory and the underlying physical effect of such at a certain stress level. Latter is of special interest on the manufacturers side in terms of design improvement while on the application side often a more generalized model for lifetime estimation based on the operation profile is desired for e.g. predictive maintenance. Therefore, this chapter will first provide a literature overview of common physical and stochastic lifetime modeling approaches before applying a set of suitable models on the data collected in chapter 4 and chapter 5. Afterwards, the different modeling results are discussed and compared to each other in order to find a "fitting" model for the given data set.

6.1 Current State of Model- and Data-Driven Modeling Approaches

According to previous conducted literature studies on lifetime and degradation modeling [39, 352–357] three different approaches were identified: Model-Driven (MD), Data-driven (DD) and hybrid approaches as a combination of both previous types. In scenarios with an extensive prior knowledge about the specific DUT and its underlying degradation process a Model-Driven approach is able to provide a physically accurate model with limited available data [352]. An outline of the most relevant empirical, physics-based models is presented in section 6.1.1. If, in contrast, only sparse domain knowledge is available or the underlying model is of high complexity, statistical- and Machine Learning (ML)-based DD approaches offer an useful alternative to MD ones. Depending on the quantity and quality of available data different DD approaches are suitable. Especially, for large data sets of high complexity Neural Network (NN) related models state an accurate approach. Yet, often a major disadvantage of a NN is the limited interpretability of the underlying model itself. On the other hand, stochastic processes and regression models as subgroups of statistical-based DD approaches offer better interpretable modeling approaches for data sets low to moderate complexity and size. A suitable selection of statistical DD approaches is highlighted in section 6.1.2.

6.1.1 Model-based approaches: Decay and Linkage Function

In the domain of physics-based MD approaches it is distinguished between the degradation trajectories model $y(t) = f_{\mathrm{D}}(t|\boldsymbol{\theta}_{\boldsymbol{\alpha}}(\mathbf{S}))$ (decay function) at a given set of stress levels $\mathbf{S} = S_{i,j}$ with j stress levels of i types of stress and the coupling model between different stress levels $\boldsymbol{\theta}_{\boldsymbol{\alpha}}(\mathbf{S}) = f_{\mathrm{L}}(\mathbf{S}|\boldsymbol{\theta}_S)$ (linkage function). Since the values for $\boldsymbol{\theta}_{\boldsymbol{\alpha}}(\mathbf{S})$ are determined as free fitting parameters for each decay function separately the selection of a proper and highly accurate decay function model is essential.

Decay Functions for Modeling Degradation Trajectories

In the context of flux decay modeling methods as provided by e.g. IES TM-21 [358] an exponential decay model is typically chosen. However, several cases of such exponential models leading to inaccuracies have been reported [359–361]. In table 6.1 a collection of common decay functions and their free parameters are shown with a subsequent illustration in fig. 6.1. Regarding the free fitting parameters it should be noted that B usually denotes the initial decay starting point, the acceleration factor $\alpha = \alpha(\mathbf{S})$ defines the stress dependent degradation velocity and n scales the dependent variable t. In most cases this factor is set to $n = 1$. Nonetheless,

Table 6.1: Continuous decay functions for modeling lumen maintenance.

Function name	Decay function $f_{\mathrm{D}}(t\|\boldsymbol{\theta}_{\boldsymbol{\alpha}})$	Free parameters $\boldsymbol{\theta}_{\boldsymbol{\alpha}}$ [(a)]
Linear	$B - \alpha t^n$	B, α, n
Exponential	$B \exp\left[-\alpha t^n\right]$	B, α, n
Square Root	$B - \alpha\sqrt{t^n}$	B, α, n
Logarithmic	$B - \alpha \ln\left[t^n\right]$	B, α, n
Inverse Sigmoid	$\mathrm{B}\ \frac{1}{1+\beta \exp[-\alpha t^n]}$	B, α, n, β
Bobashevs' Model [359]	$\exp\left[-\alpha t^n\right] \cdot \left[B + \lambda\left(1 - \exp\left[-\beta t^n\right]\right)\right]$	B, α, β, λ, n
Baes' Model [360]	$B_1 \exp\left[-\alpha_1 t^n\right] + B_2 \exp\left[-\alpha_2 t^n\right]$	B_1, B_2, α_1, α_2, n

[(a)] The scaling factor n is typically assumed to $n = 1$.

the first five models in table 6.1 assume a single underlying degradation mechanism while both Bobashevs' [359] and Bae's [360] models are a multiplicative and respectively additive superposition of two exponential-like models. An alternative to such model superposition approaches is a segmented decay model also known as segmented regression introduced by Muggeo [362] presented in fig. 6.2. This approach proposes a non-linear model following eq. (6.1) where c is the y-axis intercept, α, β are the respective acceleration factors for each segment, ψ is the corresponding breakpoint, $H(\cdot)$ is the Heaviside step function and ζ is a noise term.

$$y(t) = c + \alpha t + \beta(t - \psi)H(t - \psi) + \zeta \tag{6.1}$$

Pilgrim [363] proposes an iterative computing approach of a Taylor expansion approximating eq. (6.1) starting from an initially guessed breakpoint $\psi^{(0)}$ as shown in eq. (6.2) allowing to find a new breakpoint $\psi^{(1)}$. This approximation is then solvable by ordinary linear regression algorithms. In order to cover trajectories between breakpoints which deviate from a strict linear decay model both the independent variable t as well as the dependent variable $y(t)$ can be linearized by an appropriate function $x' = f_{\mathrm{lin}}(x)$ such as logarithmic transformations for exponential decay sections.

$$y(x) \approx c + \alpha x + \beta(x - \psi^{(0)})H(x - \psi^{(0)}) - \beta(\psi - \psi^{(0)})H(\psi - \psi^{(0)}) + \zeta \tag{6.2}$$

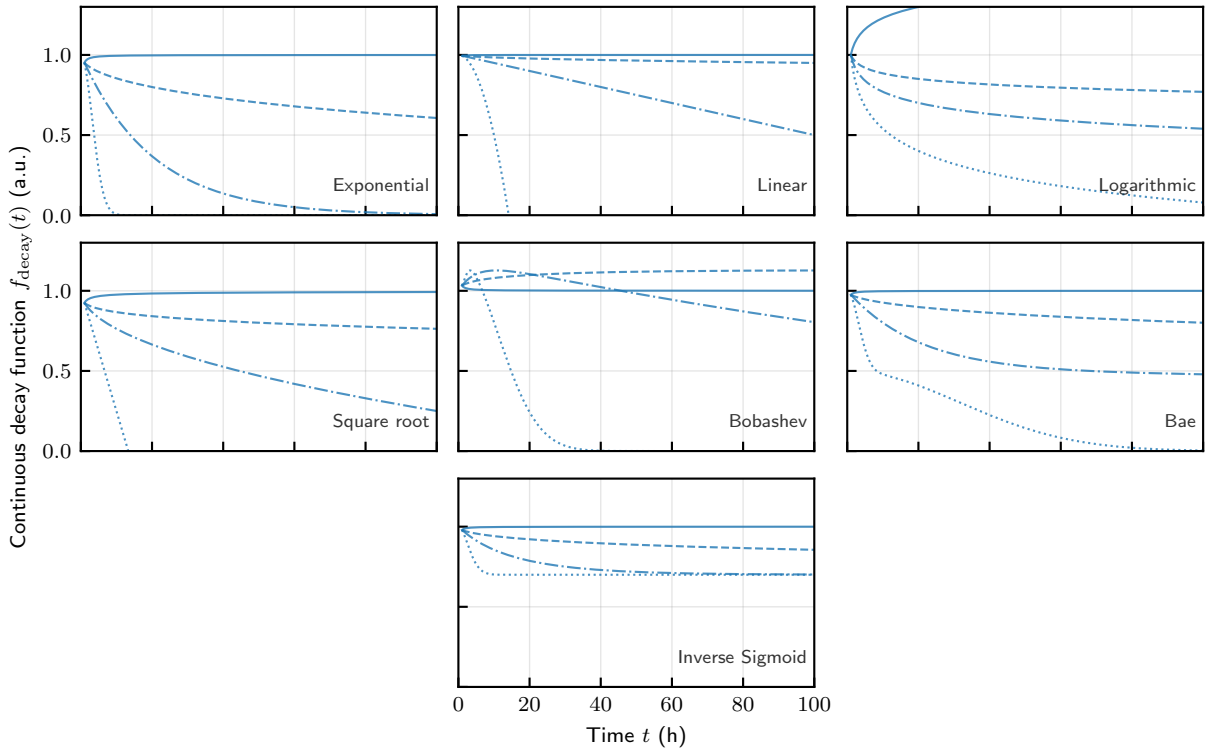

Figure 6.1: Examples of common continuous decay functions for modeling degradation trajectories with different exponential scaling factors n: (solid line) $n = -1$, (dashed line) $n = 0.5$, (dash dotted line) $n = 1$ and (dotted line) $n = 2$.

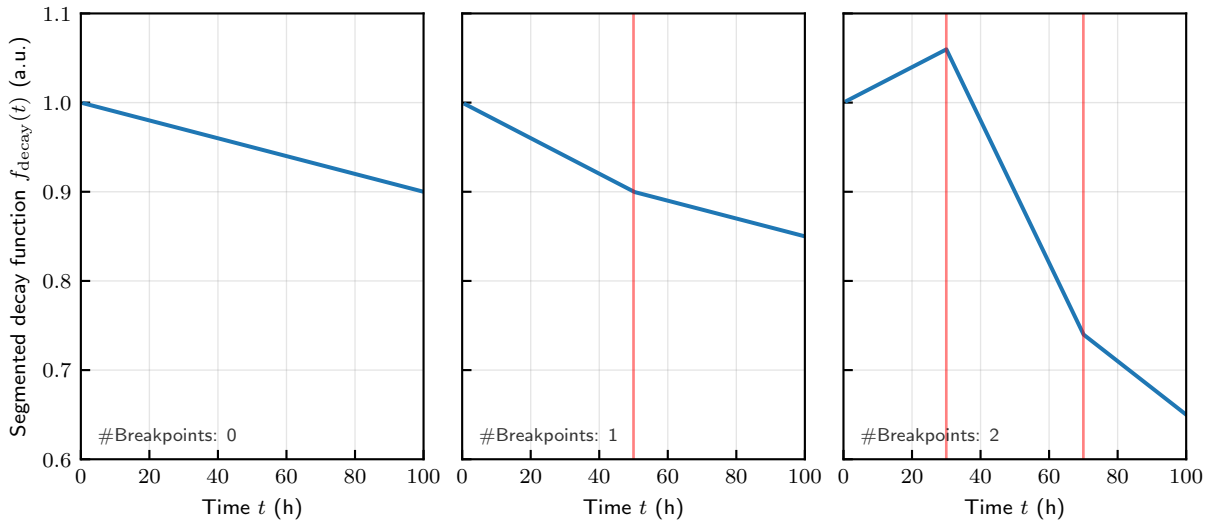

Figure 6.2: Segmented decay functions for modeling degradation trajectories with different number of breakpoints N_ψ: (left) $N_\psi = 0$, (center) $N_\psi = 1$ and (right) $N_\psi = 2$.

Linkage Functions for (Multi-)Stress Interpolation

Yet, the above discussed decay functions often rather present a mathematical approach to describe the observations than imply any physical meaning themselves due to their static

stress level. By modeling the stress type- and stress level-dependent acceleration factors a more insightful empirical, physical relationship between observations at different stress conditions can be obtained.

So far the most common and popular model shown in eq. (6.3) was proposed by Svante Arrhenius in 1898 [364] in order to model the rate of chemical reactions with respect to temperature. The determining factor in the model is the activation energy E_a that is found alongside a pre-exponential factor A as free parameters and Boltzmanns' constant k_B by e.g. curve fitting the model onto the data. In applications with a clear describable reaction of two chemicals E_a describes the lowest energy necessary to start the reaction at a given temperature T. Despite multiple different temperature-dependent reactions might be occurring during a LED ADT, the Arrhenius model still provides a suitable description of the overall acceleration factor behavior if only temperature stress is applied to the DUT. It should be noted, that different application-specific modifications of the original Arrhenius model exist. One of the most common is a single temperature stress form of the later discussed General Eyring model [356] presented in eq. (6.4).

$$\alpha(T|E_a, A) = A \exp\left[-\frac{E_a}{k_B T}\right] \tag{6.3}$$

$$\alpha(T|E_a, A, n) = AT^n \exp\left[-\frac{E_a}{k_B T}\right] \tag{6.4}$$

With respect to semiconductor reliability testing in 1969 James R. Black expanded the Arrhenius model following eq. (6.5) [365] in order to cover the effect of current-induced electromigration processes within the semiconductor device. Therefore, the current is modeled as with an inverse power law relation into eq. (6.3).

$$\alpha(T, I|E_a, A, n) = AI^{-n} \exp\left[-\frac{E_a}{k_B T}\right] \tag{6.5}$$

With the rise of new packaging technologies for integrated circuits such as epoxy mould packages Peck and Hallberg proposed a moisture-temperature reliability model eq. (6.6) for AST of such devices [366]. Similar to Blacks' model the humidity stress factor is introduced by an inverse power law term with an exponential factor n.

$$\alpha(T, \mathrm{rH}|E_a, A, n) = A(\mathrm{rH})^{-n} \exp\left[-\frac{E_a}{k_B T}\right] \tag{6.6}$$

Another more general acceleration model originated from Eyring's transition state model for chemical reactions from 1935 [367] as the General Eyring model in eq. (6.7) [356]. A useful property of this model is the weighting of individual stress types (a_i) and temperature coupling term b_i taking the possible interdependence of different stress types into account. The model in eq. (6.7) can further be transferred into an Arrhenius(-like) model by setting the free parameters $a_i, b_{i\geq 1} = 0$, $b_0 = -\frac{E_a}{k_B}$. The original Arrhenius model is obtained by additionally setting $n = 0$. In the context of temperature, current and humidity related AST the General Eyring model in eq. (6.8) has been proven suitable [356].

$$\alpha(T, S_i|\mathbf{a}, \mathbf{b}) = AT^{-n} \exp\left[\left(a_0 + \frac{b_0}{T}\right) + \sum_{i=1}\left(a_i + \frac{b_i}{T}\right) S_i\right] \tag{6.7}$$

$$\alpha(T, I, \mathrm{rH}|\mathbf{a}, \mathbf{b}) = AT^{-n} \exp\left[-\frac{E_a}{k_B T} + \left(a_1 + \frac{b_1}{T}\right) I + \left(a_2 + \frac{b_2}{T}\right) \mathrm{rH}\right] \tag{6.8}$$

6.1.2 Data-driven Approaches: Statistical Methods

Depending on the DUT and stress loading applied over the course of an AST rather complex degradation trajectories may become apparent exceeding the limits of above discussed MD approaches. Therefore, a Gaussian Process Regression (GPR) based approach that combines stochastic properties from Gaussian Processes with a non-stochastic regression in order to model arbitrary functions based on small sets of observations under various auxiliary conditions. Scenarios, which are not demand the trajectory itself but rather the probability of a device surpassing a certain threshold level at a given time, e.g. in order to plan maintenance intervals, time-to-failure or Remaining Useful Life (RUL) based approaches are more feasible such as Survival Analysis that even cover missing (censored) events.

Gaussian Process Regression

Originating from a background in geostatistics for interpolating the spacial distribution of ground metal deposits for mining applications the GPR [368] — also known as Kriging [369] — is utilized in a variety of disciplines from geosciences [370–372] or social science [373, 374] to the context of reliability testing, modeling and RUL prediction [375–387]. An example of such a GPR is shown in fig. 6.3.

For correlated observations, such as spacial and/or temporal measurements, a GPR $\mathcal{GP}$ presents an useful approach to model the underlying second-order stochastic process $y(\mathbf{x}) = f(\mathbf{x}) + \epsilon$ with the regression model $f(\mathbf{x}) \sim \mathcal{GP}(m(\mathbf{x}), k(\mathbf{x}, \mathbf{x}')) : \mathbb{R}^n \rightarrow \mathbb{R}, (\mathbf{x}, \mathbf{x}') \in \mathbb{R}^n$ and an additive, normally distributed noise component $\epsilon \sim \mathcal{N}(0, \sigma)$. Here $m(\mathbf{x})$ is the models mean function and $k(\mathbf{x}, \mathbf{x}')$ its covariance (also denoted as kernel) function with the independent variables $\mathbf{x} = [t, T, I, \mathrm{rH}]$ in the context of this work. Since the covariance function explains the relationship of the observations features $\mathbf{x}$ and $\mathbf{x}'$ selecting the proper mathematical description of this very is essential for the interpolation and prediction accuracy of the GPR. Commonly a Radial Basis Function (RBF) kernel defined in eq. (6.9) is used for modeling degradation trajectories with a scaling factor η and the length scale ℓ as hyperparameters $\boldsymbol{\theta}$.

$$k(\mathbf{x}, \mathbf{x}'|\boldsymbol{\theta}) = \eta \exp\left[-\frac{\|\mathbf{x} - \mathbf{x}'\|^2}{2\ell^2}\right] \tag{6.9}$$

For training the GPR is assumed as a Bayesian inference problem. Thus, before training the covariance function is placed as a prior over all possible functions meeting the observations. Subsequently, the inferred posterior of this Gaussian process is again a Gaussian Process allowing to analytical compute an estimate for $\boldsymbol{\theta} = \hat{\boldsymbol{\theta}}$ with standard gradient based optimization algorithms. As the GPR not only estimates the underlying function to interpolate between observations but also models this very variance the GPR provides an alternative to conventional (non-)linear regression methods for applications prone to elevated noise levels as well as functions with highly non-linear and non-monotonous properties. Yet, it should be considered that at high dimensional $\mathbf{x}$ and/or large dimensions of each independent variable the computational complexity of $k(\mathbf{x}, \mathbf{x}')$ increases exponentially.

Survival Analysis

From an application point of view rather an estimate on the RUL with regard to stress $\mathbf{S}$ induced by the operating conditions than an actual degradation trajectory is of interest. For such RUL-based prognostics estimating the time of failure (e.g. L_{70}) is crucial. But there are

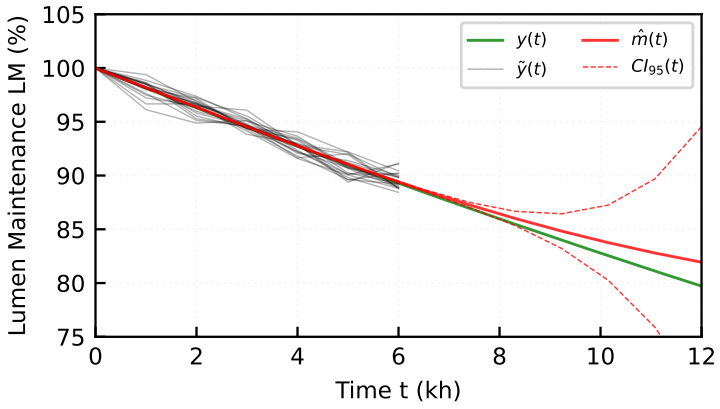

Figure 6.3: Example of a Gaussian Process Regression: (gray line) true observations, (green line) true decay mean function, (solid red line) mean function estimated by GPR and (dashed red lines) 95 % confidence interval of the GPR estimate.

two major challenges with regard to standard AST: covering all possible operating conditions and extending the testing period until a failure event occurs. Both are unfeasible from an economical and practical point of view. Originating from an statistical analysis approach in medical research the non-parametric, statistical approach of Survival Analysis has found application in various disciplines like engineering (Reliability Analysis) or Social Sciences (Event History Analysis) [388–390]. A key feature of Survival Analysis is the computationally lightweight approximation of a failure time distribution for new stress conditions and missing (censored) event occurrences.
Within the context of Survival Analysis the probability of a subjects survival after the time T is given by the survival function $S(t) = P(T > t)$. Concurrently, the hazard function $h(t)$ denotes the chance of the event occurring during the time interval $[t; \Delta t]$ following eq. (6.10). Integrating the hazard $h(t)$ subsequently results the total amount of event occurrences at a time t given by the cumulative hazard function $H(t) = \int_0^t h(t)\mathrm{d}t$. An example of these probability functions is shown in fig. 6.4.

$$h(t) = \lim_{\Delta t \to \infty} \frac{P(t \leq T < \Delta t | T \geq t)}{\Delta t} \geq 0 \tag{6.10}$$

Given a set data points and no external factors both Kaplan-Meier [391] and Nelson-Aalen [392, 393] estimators provide a good approximation on the survival function $\hat{S}(t) \approx S(t)$ and the cumulative hazard function $\hat{H}(t) \approx H(t)$ shown below in equations eq. (6.11) and eq. (6.12) respectively. The number DUT subjected to an event at a specific time T_i denoted by d_i whilst the number subjects surviving past T_i are given by n_i.

$$\hat{S}_{\mathrm{KM}}(t) = \prod_{T_i \leq t} \left(1 - \frac{d_i}{n_i}\right) \tag{6.11}$$

$$\hat{H}_{\mathrm{NA}}(t) = \sum_{T_i \leq t} \left(\frac{d_i}{n_i}\right) \tag{6.12}$$

As previous hinted, often exogenous factors influence affect the probability of survival in a specific manner. Covering such rater complex scenarios David R. Cox introduced the Cox

Proportional Hazard (CPH) model [394] as a regression method for estimating the $h(t)$ presented in eq. (6.13) with the baseline hazard $h_0(t)$ and a free parameter vector $\boldsymbol{\beta} = \{\beta_0, .., \beta_i\}$ where i is e.g. the number of stress types $i = \dim(S_i)$.

$$h(t|\mathbf{S}) = h_0(t) \exp\left[\boldsymbol{\beta} \cdot \mathbf{S}\right] \tag{6.13}$$

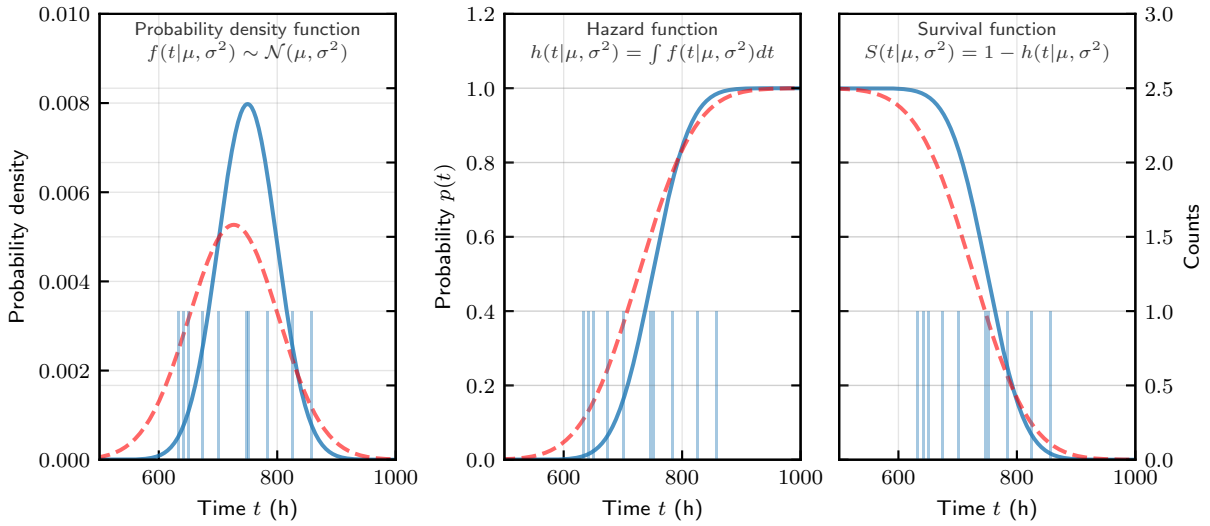

Figure 6.4: Examples of time-to-event observations and their underlying distributions: (blue) true distribution, (red) estimated distribution. Each idstribution is presented as (left) prbability density function, (center) hazard function and (right) survival funtion with the corresponding observations denoted as vertical lines.

6.2 Experiment - Lifetime Modeling

Based on the discussed MD and DD approaches in section 6.1 this section derives two research questions on which subsequently a lifetime modeling experiment is presented.

6.2.1 Research questions

As stated before, the common lifetime modeling approach following the IES TM-21 [358] methodology is prone to inaccuracies in L_x-prediction due to incorrectly specified decay functions as well as neglecting potentially important stress parameters while simply applying an Arrhenius model linkage function. Even though the stochastic L_xB_y provided by EN 62717 [395] provides a better insight on the failure probability B_y at a certain failure threshold level L_x this approach still requires a proper decay function for stochastic modeling. Therefore the above listed research question are derived:

Q4: Which combination of decay and linkage functions are suitable for modeling the obtained ADT data?

Q5: Are Gaussian Process Regression and Survival Analysis potential alternative Data-driven approaches to common methodologies for modeling the life- and failure-time of a LED?

6.2.2 Experimental Design

Following the experimental design for the different presented modeling approaches are highlighted. Starting from MD to DD approaches to presenting suitable model evaluation metrics as well as the models implementation. As a preliminary step to the degradation trajectory process the measurement data are averaged for all DUT of a certain stress condition at each measurement time similar to the procedure recommended in IES TM-21. Further, it is suggested by IES TM-21 to dismiss the initial lumen increase data in order to start from the actual maximum lumen maintenance value. This suggestion was incorporated by fitting two data sets: one starting at $t = 0\,\mathrm{h}$ and one at $t(\max\{y(t)\})$.
All models are implemented and computed on a desktop computer (Intel i5-8600K, 32GB RAM) in the Python programming language (v3.11.4) with the following key packages numpy v1.24.3 [396], pymc v5.6.1 [397], scikit-learn v1.2.2 [398], piecewise-regression v1.3.0 [363] and scikit-survival v0.21.0 [399]. The key parameters of different models are described in the following subsections.

Performance Metric

In the realm of curve fitting the coefficient of determination R^2 is typically considered as a proper goodness of fit metric. However, when comparing different curve fitting models with a varying number of free parameters $\boldsymbol{\theta}$ the R^2 metric does not take these very into account thus R^2 should not be used for model selection tasks. A more suitable metric for model selection is the Bayesian Information Criterion (BIC) which takes the amount of samples as well the number of free parameters into account as shown in eq. (6.14). Here k denotes the number of free parameters, n the number of samples and $\hat{L} = P(y(t)|\hat{\boldsymbol{\theta}})$ is the likelihood of value for the given model. Comparing two models, the model yielding a lower BIC is assumed to be the more suitable model.

$$\mathrm{BIC} = k \cdot \ln(n) - 2\ln(\hat{L}) \tag{6.14}$$

Decay and Linkage Function

The first part of this experiment covers the MD approach by curve fitting a decay and linkage model onto the degradation data collected in chapter 4 by following the steps listed below. It should be noted that the curve fit for the continuous decay and linkage functions is not performed by a common least-squares method as recommended by IES TM-21 instead the Differential Evolution algorithm [400] is used as a global optimizer since it produces results of higher accuracy for the given objective.

1. *Continuous Decay Function*: The decay functions displayed in table 6.1 or curve fitted on the data. Since, the exponential scaling factor n is often neglected, each model is fitted once with a fixed $n = 1$ and once with a varying n. Similarly, two distinct curve fits are performed with and without the initial lumen increase start at $t = 0\,\mathrm{h}$ and at $t(\max\{y(t)\})$ respectively. In total, a set of 20736 curve fits were performed at four LED types, nine measurement currents, 24 stress conditions, six decay functions and four scaling / starting combinations.

2. *Segmented Decay Function*: As the first section of this chapter elaborates a preliminary linearization of either t, $y(t)$ or even both can be feasible to enhance the accuracy of this approach. Therefore, the following seven linearization functions were applied

$x' = f(x) : f(x) = \{x, \ln(x), \log_2(x), \log_{10}(x), x^2, x^3, \sqrt{x}, \sqrt[3]{x}\}$. These functions were permuted among t and $y(t)$. Further, functions with up to three breakpoints $\psi_i : i \in [0,3]$ were evaluated as well as data with and without the initial lumen increase. In total, a number 338688 regressions were performed for four LED types, nine measurement currents, 24 stress conditions, up to three breakpoints, seven t-linearizations, seven $y(t)$-linearizations and two starting points.

3. *Linkage Function*: Finally, the acceleration factors of a selection of the ten most accurate continuous and segmented decay models each are modeled onto the linkage functions shown in eq. (6.3) - eq. (6.8). Apart from the General Eyring model in eq. (6.8) the data are split according to the models required stress level in order to assume steady stress levels for each stress type not covered by the respective linkage model. For this experimental part in sum 11520 models are evaluated for four LED, (5+5) decay models, nine measurement currents and 32 data splits for five linkage models.

Gaussian Process Regression Model

The applied GPR follows a zero knowledge approach with no prior insight on the underlying mean function thus setting $m(\mathbf{x}) = 0$ and utilizing a RBF covariance function resulting in the GPR model described by eq. (6.15) with the multi-feature covariance function in eq. (6.16). Subsequently, five hyperparameters $\boldsymbol{\theta} = [\ell_1, \ell_2, \ell_3, \ell_4, \eta]$ result from large set of different input parameters $\mathbf{x} = [t, T, I, \mathrm{rH}]$.

$$f(\mathbf{x}) = \mathcal{GP}\left(0, k(\mathbf{x}, \mathbf{x}', \boldsymbol{\theta})\right) + \epsilon \tag{6.15}$$

$$k(\mathbf{x}, \mathbf{x}', \boldsymbol{\theta}) = \eta^2 \cdot k_t(\mathbf{t}, \mathbf{t}', \ell_1) \cdot k_T(\mathbf{T}, \mathbf{T}', \ell_2) \cdot k_I(\mathbf{I}, \mathbf{I}', \ell_3) \cdot k_{\mathrm{rH}}(\mathbf{rH}, \mathbf{rH}', \ell_4) \tag{6.16}$$

By further following the zero knowledge approach uniform priors $\mathcal{U}(a,b)$ are selected for the length scales ℓ_i and η as well as a broad positive half-normal distribution $\mathcal{N}^+(\mu,\sigma)$ to address the process noise ϵ as shown below. The final hyperparameter tuning is performed by the L-BFGS-B algorithm [401] in order to find the maximum a posteriori point.

$$\ell_1 \sim \mathcal{U}(0, 20000), \quad \ell_2 \sim \mathcal{U}(0, 1000), \quad \ell_3 \sim \mathcal{U}(0, 10000),$$

$$\ell_4 \sim \mathcal{U}(0, 1000), \quad \eta \sim \mathcal{U}(0, 500), \quad \sigma \sim \mathcal{N}^+(0, 10)$$

As a result this experiment generates 36 models for 4 LED types at 9 measurement currents.

Survival Analysis

As a first step for this experimental part the correct event times $T_i(y = L_x)$ have to be evaluated if an event occurred. Therefore, if a DUT surpassed the L_x threshold the T_i is evaluated by linear interpolation between the two nearest measurement points around the threshold $y(t^-) : t^- = \mathrm{argmax}_t \{y(t) < L_x\}$ and $y(t^+) : t^+ = \mathrm{argmin}_t \{y(t) > L_x\}$ otherwise the event is right-censored and the last measurement time $T_i = \max\{t\}$ is noted. Next, the hazard function alongside with its coefficients $\boldsymbol{\beta}$ is determined by the CPH model. By then increasing the failure threshold towards a maximum threshold value $L_x \to \max\{L_x\}$ an inside regarding the influence of each stress type a given degradation stage can be obtained alongside with the failure time distribution.

6.3 Results and Model Comparison

The results obtained from the lifetime modeling according to the above elaborated experimental steps are presented and discussed over the course of this section. Concluding a comparison of the different modeling approaches is given.

6.3.1 Continuous Decay Functions

The first experimental part investigated the suitability of different continuous decay functions presented in table 6.1. The results of the best three models for each device type as well as the common exponential approach for comparison are highlighted in table 6.2. Each model has been curve fitted on every measurement belonging to a device type. The BIC has then been averaged to provide an overview on the average model performance. Aside from the mean also the median, standard deviation as well as observed minimum and maximum BIC are presented to get further inside into the variance of each models results.

Table 6.2: Model fitting results of the three best continuous decay functions of each DUT by means of their BIC and the results of standard exponential curve fit approach as a baseline.

DUT	$f_D(t)$	t_{Start}	n	BIC (a.u.)				
				Mean	Median	Std	Min	Max
Blue	Bae	y_{max}	Vary	-177.5	-170.2	86.3	-351.7	-35.0
	Bae	t_0	Vary	-176.1	-163.8	88.8	-345.2	-37.4
	IS	t_0	Vary	-175.5	-150.8	102.3	-360.6	-31.4
	Exp	t_0	Fix	-38.7	-42.2	24.0	-84.3	-3.9
Lime	IS	t_0	Vary	-173.3	-182.9	106.3	-409.9	-17.6
	IS	y_{max}	Vary	-163.7	-157.6	104.4	-399.0	-17.6
	Bae	t_0	Vary	-148.0	-122.9	82.8	-416.7	-38.2
	Exp	t_0	Fix	-34.6	-37.8	15.8	-70.7	-6.0
Purple	IS	t_0	Vary	-226.9	-224.9	142.5	-441.5	-12.8
	Bae	t_0	Vary	-225.5	-245.8	129.4	-441.6	-48.5
	IS	y_{max}	Vary	-220.1	-215.9	138.4	-435.7	-20.4
	Exp	t_0	Fix	-43.5	-41.8	22.9	-82.7	-3.5
Horticulture White	IS	y_{max}	Vary	-222.5	-210.6	102.6	-421.7	-67.2
	IS	t_0	Vary	-222.0	-202.2	102.7	-427.0	-67.2
	Bae	y_{max}	Fix	-199.0	-157.9	103.2	-374.8	-57.8
	Exp	t_0	Fix	-39.7	-40.3	15.9	-71.4	-18.2

IS: Inverse Sigmoid model, Exp: Exponential model.

Analyzing the results two conclusions can be drawn: Firstly, for all devices the decay model presented by Bae et al. [360] and the Inverse Sigmoidal model yielded consistently the highest results. Especially varying the exponential time scaling parameter n improves the overall results as also demonstrated by van Driel et al. [361]. Secondly, compared to the typical exponential approach both models yield a substantial higher model performance. This behavior was consistent also for the Logarithmic, Square-root and Linear models. Considering both sets of models, it becomes apparent that the former set provides a non-monotonous decay rate while the latter exhibits a monotonous one. However, the measured data exhibit a certain change in degradation rate due to multiple underlying degradation effects as discussed in the in chapter 5. This distinct behavior can be modeled by a superposition of multiple decay functions, such as provided in the model by Bae et al. [360]. The Inverse Sigmoid model on the other hand shows good results since it sufficiently models the slow onset of the decay in combination with a steep decay transitioning into a steady state as the measurements of the Horticulture White device suggests. Generally, also the model presented by Bobashev et al. [359] was expected to yield promising results, however, the majority of curve fits yielded a fitting error due to a maximum of 100.000 fit iterations reached or at least very poor BIC values. The reason for this behavior is assumed to be found in the models intention of primarily modeling the initial flux increase rather than a subsequent change in degradation trajectory after the onset of the main decay.
Further, all top ranging models exhibit a rather large standard deviation. This behavior results from a huge variation in the number of provided data points for each measurement conditions since especially at highly elevated stress levels a rapid degradation was observed such that only a limited number of data points were generated.

6.3.2 Segmented Decay Functions

The results for the second experimental part regarding the segmented decay function approach are presented in table 6.3 and table 6.4. Similar to the previous analysis the BIC results are averaged and a statistic of each models performance on a respective device is given. Since the number of breakpoints is crucial for the models performance on the given data, both tables provide an overview on the top three models for 0, 1 and 2 breakpoints ψ for each device.
It first stands out, that the majority of the presented results yield higher BIC values than the before discussed continuous models. This behavior was well expected, since the segmented approach aims on modeling distinct curve sections rather than the whole function. In addition, the data were beforehand linearized in order to further improve the curve fitting results. Subsequently, an expected increase in performance with with increasing number of breakpoints N_ψ has been observed over the range of all devices.
Next, the linearization terms are inspected, since these may provide a link to underlying degradation effects. As for the time scale, $t' = t^2$ and $t' = \sqrt{t}$ are well represented in a majority of cases while the normalized optical power is mainly scaled by $y' = \sqrt[3]{y}$. Due to moisture as the main contributor to the degradation of the LED package, two relations can be found: The mass exchange during the diffusion process given by eq. (3.6) has a $\sqrt{t}$-dependency hinting towards the observed moisture diffusion into the encapsulant. The moisture ingress again promoted hydroscopic swelling of the encapsulant and therefore shear forces along the reflector cup to encapsulant interface. Assuming the detachment rate and thus the normalized optical power proportional to the moisture ingress induced shear forces along the encapsulants interface a similar shear force behavior was observed by Shiue et al. [402] at a glass fiber to polymer

coating interface. However, the quadratic and logarithmic time dependency could not be linked to a specific physical effect.

Table 6.3: Model fitting results of the three best segmented decay functions of the blue and lime DUT by means of their BIC with respect to the number of breakpoints N_ψ.

DUT	N_ψ	t'	y'	t_{Start}	BIC (a.u.)				
					Mean	Median	Std	Min	Max
Blue	0	t^2	$\sqrt[3]{y}$	t_0	-229.4	-233.6	114.6	-414.0	-97.0
		$\log_2(t)$	$\sqrt[3]{y}$	t_0	-228.3	-223.0	112.7	-406.5	-76.3
		$\ln(t)$	$\sqrt[3]{y}$	t_0	-228.3	-223.0	112.7	-406.5	-76.3
	1	t^2	$\sqrt[3]{y}$	t_0	-246.6	-238.3	118.8	-447.1	-108.7
		$\sqrt[3]{t}$	$\sqrt[3]{y}$	t_0	-238.9	-228.1	121.7	-415.1	-70.1
		$\log_2(t)$	$\sqrt[3]{y}$	t_0	-238.4	-233.6	123.5	-421.5	-71.8
	2	$\sqrt[3]{t}$	$\log_{10}(y)$	t_0	-260.6	-255.5	112.9	-413.1	-88.0
		$\sqrt{t}$	$\log_{10}(y)$	t_0	-259.8	-253.7	115.4	-416.8	-84.3
		$\sqrt{t}$	$\sqrt[3]{y}$	t_0	-259.2	-257.2	124.3	-442.5	-92.7
Lime	0	t^2	$\sqrt[3]{y}$	t_0	-213.1	-216.0	97.6	-428.0	-85.2
		t^2	$\log_{10}(y)$	t_0	-198.5	-201.1	95.9	-408.7	-64.7
		t^2	$\sqrt{y}$	t_0	-198.0	-200.6	90.7	-398.0	-80.5
	1	t^2	$\sqrt[3]{y}$	t_0	-234.2	-227.0	108.8	-473.4	-86.8
		$\log_{10}(t)$	$\sqrt[3]{y}$	t_0	-233.4	-230.4	114.9	-441.8	-73.6
		$\log_2(t)$	$\sqrt[3]{y}$	t_0	-233.2	-230.4	114.8	-441.8	-73.6
	2	$\sqrt{t}$	$\sqrt[3]{y}$	t_0	-251.6	-246.0	121.4	-512.7	-80.4
		$\log_2(t)$	$\sqrt[3]{y}$	t_0	-250.8	-243.2	120.1	-478.6	-71.6
		t^3	$\sqrt[3]{y}$	t_0	-244.9	-250.2	104.3	-465.3	-83.0

6.3.3 Linkage Functions

In the next step of the experiment various linkage functions were analyzed with respect to both the continuous and segmented decay functions. In the following the focus will be set on the Eyring linkage model, since it incorporates all three available stress variables and should thus be most suitable as a comprehensive model for each decay functions free parameters. In contrast, a further linkage model between each specific one- or two-parameter linkage model would need to be set up which is from a computational and usability point of view not feasible. The Eyring linkage models results are presented in table 6.5, table 6.6 and table 6.7.
Taking the continuous model's linkage function given in table 6.5 into account, a relatively

Table 6.4: Model fitting results of the three best segmented decay functions of the purple and horticulture white DUT by means of their BIC with respect to the number of breakpoints N_ψ.

DUT	N_ψ	t'	y'	t_{Start}	BIC (a.u.)				
					Mean	Median	Std	Min	Max
Purple	0	t^2	$\sqrt[3]{y}$	t_0	-272.4	-259.3	144.8	-552.8	-66.3
		$\sqrt{t}$	$\sqrt[3]{y}$	t_0	-265.0	-271.8	157.9	-530.4	-39.4
		$\sqrt[3]{t}$	$\sqrt[3]{y}$	t_0	-260.6	-261.8	153.8	-517.6	-35.7
	1	$\sqrt{t}$	$\sqrt[3]{y}$	t_0	-296.2	-339.4	155.0	-545.5	-83.7
		$\log_2(t)$	$\sqrt[3]{y}$	t_0	-293.0	-308.0	163.8	-576.0	-75.4
		$\log_{10}(t)$	$\sqrt[3]{y}$	t_0	-292.6	-308.0	164.2	-576.0	-75.4
	2	$\log_2(t)$	$\sqrt[3]{y}$	t_0	-306.7	-333.5	169.8	-597.1	-71.2
		$\sqrt{t}$	$\sqrt[3]{y}$	t_0	-304.4	-339.3	165.1	-578.3	-79.3
		t^3	$\sqrt[3]{y}$	t_0	-300.4	-316.8	151.0	-566.4	-81.3
Horticulture White	0	$\sqrt{t}$	$\sqrt[3]{y}$	t_0	-239.2	-237.2	113.3	-459.5	-77.5
		t^2	$\sqrt[3]{y}$	t_0	-238.0	-223.8	101.2	-433.3	-104.7
		$\sqrt[3]{t}$	$\sqrt[3]{y}$	t_0	-232.4	-226.1	108.1	-431.7	-70.3
	1	$\sqrt{t}$	$\sqrt[3]{y}$	t_0	-271.6	-248.6	121.7	-487.3	-104.2
		$\sqrt[3]{t}$	$\sqrt[3]{y}$	t_0	-269.1	-249.0	122.0	-479.0	-103.1
		t^2	$\sqrt[3]{y}$	t_0	-265.5	-245.8	113.6	-474.2	-106.2
	2	$\sqrt{t}$	$\sqrt[3]{y}$	t_0	-279.5	-253.6	126.9	-519.4	-101.1
		t^2	$\sqrt[3]{y}$	t_0	-278.1	-252.4	121.6	-499.3	-102.6
		$\sqrt[3]{t}$	$\sqrt[3]{y}$	t_0	-276.4	-250.9	126.4	-508.4	-101.1

poor performance in terms of BIC is noticeable. Especially for Baes' model a huge variation for $\hat{\alpha}_1$ and $\hat{\alpha}_2$ was determined. This behavior resulted from the fitting process since either the each part of the models equation was used to model a specific part of the data like e.g. the initial flux increase. Subsequently, an approach with restricted ranges of the free parameters was tested but with a similar result. As for the Exponential base line model a comparative good performance was yielded since here no concurring parameters were present and $\hat{\alpha}$ is expected to have monotonous behavior that fits the Eyring model in contrast to Baes' model and the Inverse Sigmoid model. Yet, as shown in fig. 6.5, while performing reasonable good on the given training data the proposed Eyring linkage model performs very poorly on the provided test data on the top three decay functions as shown in the right plot of fig. 6.5. In this case it was possible only to calculate the Exponential and one of Baes' models due to floating point number overflows generated by the other two models.
Considering the results of the segmented decay function in table 6.6 and table 6.7 it is noticeable, that the majority of results are suitable for a linkage fit. This behavior was well expected as

Table 6.5: Results of the Eyring linkage model curve fit for each free parameter of the continuous decay functions for all DUT by means of their BIC.

DUT	$f_L(t)$	t_{Start}	n	BIC (a.u.)				
				$\hat{\alpha}$	$\hat{\alpha}_1$	$\hat{\alpha}_2$	$\hat{\beta}$	$\hat{n}$
Blue	Bae	t_0	Vary	-	30.3	380.8	-	7.9
	Bae	y_{max}	Vary	-	-27.4	329.3	-	-1.7
	IS	t_0	Vary	135.4	-	-	-45.1	-2.0
	Exp	t_0	Fix	-19.9	-	-	-	-
Lime	Bae	t_0	Vary	-	85.6	378.8	-	-16.2
	IS	t_0	Vary	138.4	-	-	-58.5	6.1
	IS	y_{max}	Vary	138.3	-	-	-45.0	-22.6
	Exp	t_0	Fix	29.1	-	-	-	-
Purple	Bae	t_0	Vary	-	100.7	372.2	-	-10.9
	IS	t_0	Vary	131.8	-	-	-62.4	-16.8
	IS	y_{max}	Vary	159.2	-	-	-43.5	-1.0
	Exp	t_0	Fix	39.6	-	-	-	-
Horticulture White	Bae	y_{max}	Fix	-	51.5	342.3	-	-
	IS	t_0	Vary	123.5	-	-	-96.5	-23.2
	IS	y_{max}	Vary	118.0	-	-	-58.3	-41.1
	Exp	t_0	Fix	-11.2	-	-	-	-

each function segments free parameters represent a separate monotonous function. In this regard the effect of the previous linearization benefits the models performance especially at $N_\psi = 0$ for the blue, purple and white DUT. Here, additional segments can be waived while still resulting in a good BIC score thus making the segmented decay model especially suitable in combination with an Eyring linkage model. However, in cases with multiple changes in degradation slope the computational effort for the segmented model increases rapidly, since each free parameter requires a separate linkage model.

6.3.4 Gaussian Process Regression

Next, a DD-approach is considered by applying a GPR to the measured data yielding a combined decay and linkage model. The results are shown in table 6.8. In terms of BIC, the yielded scores improved by about two magnitudes compared to those of the before evaluated decay and linkage models. Since a GPR is able to approximate arbitrarily non-monotonous and non-steady functions this result was expected. However, in this regard it is important to consider the models variance in order to get an estimate on the model's confidence as exemplary shown in

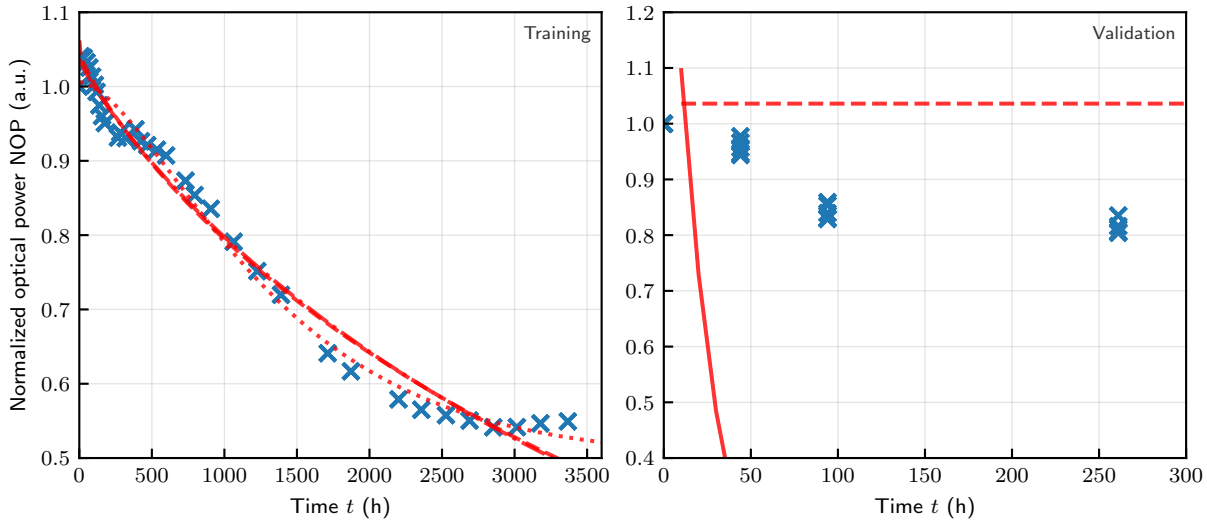

Figure 6.5: Top three continuous decay functions as well as the exponential decay function fitted with the Eyring linkage model: (Left) fitting result for the blue DUT trained at $T = 65\,°C$, $I = 300\,mA$ and $rH = 55\,\%$, (right) the result of the interpolated stress values $T = 75\,°C$, $I = 300\,mA$ and $rH = 55\,\%$ of the blue DUT. The model's estimate is denoted as a red lines for the following decay functions: (solid) BAE's model starting at maximum, (short dashed) BAE's model starting at 0, (long dashed) exponential and (dotted) Inverse Sigmoid.

fig. 6.6. It can be seen that the variance increases exponentially towards the training intervals end due to the RBF kernel exponential properties. In comparison to the previous discussed models, the GPR performs reasonable well on the stress level interpolation presented in a set of test data in the right plot of fig. 6.6. Despite the models mean functions accuracy, the confidence is rather poorly since even the 1σ confidence intervals are way outside of the plots boundaries. Two things might improve this behavior: due to the devices highly accelerated degradation at elevated temperatures, only few data were available at these conditions. Since, the time resolution at high stress levels is difficult to achieve in order to avoid stress cycling due to too short test and measurement periods, it is more appropriate to test at more temperature levels. This, however, comes at the cost increased total experimental time. Secondly, adjusting the kernel function might improve the models confidence and accuracy.

6.3.5 Survival Analysis

As the last model the CPH survival model is evaluated. This model, however, does not approximate the degradation function, but rather estimates the time until a certain degradation level is reached. Here, one distinct CPH model was evaluated for every NOP step from $L_x = NOP \in [0.7, 1]$. The resulting mean survival time for each step is presented in fig. 6.7 exemplary for the blue DUT at for a training an test condition. The training condition shows a reasonable estimation of the underlying mean function that somehow deviates in the early and late degradation phase. Since only five devices were measured at this condition the inter-sample degradation variance affects the accuracy of the estimate. This behavior is specifically present during the initial flux increase, while it consolidates with progressing aging time before becoming vastly present towards the measurement series end as a result of increasing variation in the tested devices trajectories. Regarding the CPH models stress level interpolation capabilities this

Table 6.6: Results of the Eyring linkage model curve fit for each free parameter of the to segmented decay functions of the blue, lime and purple DUT by means of their BIC and with respect to the number of breakpoints N_ψ.

DUT	N_ψ	t'	y'	t_{Start}	BIC (a.u.) $\hat{\alpha}$	$\hat{\beta}_1$	$\hat{\beta}_2$	$\hat{\psi}_1$	$\hat{\psi}_1$	$\hat{c}$
Blue	0	$\ln(t)$	$\sqrt[3]{y}$	t_0	-132.6	-	-	-	-	-76.6
		$\log_2(t)$	$\sqrt[3]{y}$	t_0	-165.4	-	-	-	-	-76.9
		t^2	$\sqrt[3]{y}$	t_0	94.1	-	-	-	-	-29.5
	1	$\log_2(t)$	$\sqrt[3]{y}$	t_0	-174.3	-105.4	-	20.5	-	-80.9
		$\sqrt[3]{t}$	$\sqrt[3]{y}$	t_0	-70.9	-19.8	-	-27.0	-	-17.6
		t^2	$\sqrt[3]{y}$	t_0	89.2	79.1	-	-46.9	-	-212.5
	2	$\sqrt[3]{t}$	$\log_{10}(y)$	t_0	-98.8	-35.9	-17.3	-44.0	-22.9	-185.0
		$\sqrt{t}$	$\log_{10}(y)$	t_0	-38.2	-16.6	-31.3	-41.5	-25.7	-122.7
		$\sqrt{t}$	$\sqrt[3]{y}$	t_0	-56.6	-28.5	-23.7	-32.2	-25.8	-154.7
Lime	0	t^2	$\log_{10}(y)$	t_0	72.7	-	-	-	-	-136.5
		t^2	$\sqrt[3]{y}$	t_0	41.0	-	-	-	-	-29.5
		t^2	$\sqrt{y}$	t_0	43.8	-	-	-	-	-29.5
	1	$\log_{10}(t)$	$\sqrt[3]{y}$	t_0	-141.2	-35.4	-	-56.3	-	-32.7
		$\log_2(t)$	$\sqrt[3]{y}$	t_0	-184.4	-78.6	-	-13.7	-	-119.4
		t^2	$\sqrt[3]{y}$	t_0	26.3	72.2	-	-15.7	-	-24.9
	2	$\log_2(t)$	$\sqrt[3]{y}$	t_0	-191.0	-111.9	-70.9	-37.9	-4.4	-18.8
		$\sqrt{t}$	$\sqrt[3]{y}$	t_0	-87.0	-6.6	21.1	-63.1	-47.4	-28.9
		t^3	$\sqrt[3]{y}$	t_0	152.1	143.4	124.7	-41.6	-5.9	-182.4
Purple	0	$\sqrt[3]{t}$	$\sqrt[3]{y}$	t_0	-69.7	-	-	-	-	-141.8
		$\sqrt{t}$	$\sqrt[3]{y}$	t_0	-31.4	-	-	-	-	-114.8
		t^2	$\sqrt[3]{y}$	t_0	79.0	-	-	-	-	-180.6
	1	$\log_{10}(t)$	$\sqrt[3]{y}$	t_0	-168.0	-54.7	-	-53.5	-	-161.0
		$\log_2(t)$	$\sqrt[3]{y}$	t_0	-208.7	-94.8	-	-12.4	-	-162.8
		$\sqrt{t}$	$\sqrt[3]{y}$	t_0	-91.7	-20.1	-	-42.2	-	-17.7
	2	$\log_2(t)$	$\sqrt[3]{y}$	t_0	-190.7	-73.4	-61.2	-11.2	-1.6	-138.1
		$\sqrt{t}$	$\sqrt[3]{y}$	t_0	-85.0	-1.1	8.9	-43.5	-38.4	-178.3
		t^3	$\sqrt[3]{y}$	t_0	177.6	177.1	92.6	-67.8	40.8	-201.0

Table 6.7: Model fitting results of the three best segmented decay functions of the horticulture white DUT by means of their BIC with respect to the number of breakpoints N_ψ.

DUT	N_ψ	t'	y'	t_{Start}	BIC (a.u.) $\hat{\alpha}$	$\hat{\beta}_1$	$\hat{\beta}_2$	$\hat{\psi}_1$	$\hat{\psi}_1$	$\hat{c}$
Horticulture White	0	$\sqrt[3]{t}$	$\sqrt[3]{y}$	t_0	-69.2	-	-	-	-	-133.8
		$\sqrt{t}$	$\sqrt[3]{y}$	t_0	-58.5	-	-	-	-	-32.8
		t^2	$\sqrt[3]{y}$	t_0	10.5	-	-	-	-	-207.9
	1	$\sqrt[3]{t}$	$\sqrt[3]{y}$	t_0	-147.9	-62.2	-	-73.4	-	-227.6
		$\sqrt{t}$	$\sqrt[3]{y}$	t_0	-127.0	-68.4	-	-60.7	-	-240.6
		t^2	$\sqrt[3]{y}$	t_0	-11.7	13.8	-	-47.3	-	-33.0
	2	$\sqrt[3]{t}$	$\sqrt[3]{y}$	t_0	-158.7	-67.7	-39.8	-89.2	-60.0	-258.1
		$\sqrt{t}$	$\sqrt[3]{y}$	t_0	-123.2	-82.5	-57.5	-51.3	-37.9	-244.0
		t^2	$\sqrt[3]{y}$	t_0	41.0	-0.7	26.7	-70.1	0.6	-32.9

Table 6.8: Results of the GPR model for different devices under test by means of their BIC and the models mean standard deviation $\bar{\sigma}$.

DUT	BIC	$\bar{\sigma}$
Blue	-18680.3	0.027
Lime	-17852.2	0.025
Purple	-15332.3	0.053
Horticulture White	-20501.8	0.018

model shows reasonable good results on the test data for higher aging times. This behavior was well expected, since the model relies on a sufficient number of event occurrences in order to provide an accurate estimate.

6.3.6 Model Comparison

By comparing the above presented and discussed results of the different models the following conclusions can be drawn:

- Continuous decay functions with a monotonous decay rate provide a rough estimate of the degradation trajectory but lack in scenarios with varying decay rates.
- Continuous decay functions with a non-monotonous decay rate offer a higher flexibility at the cost of higher computational complexity. An additional disadvantage of these functions is a rather difficult linkage between different stress levels since these physics-based linkage models assume a monotonous decay rate.

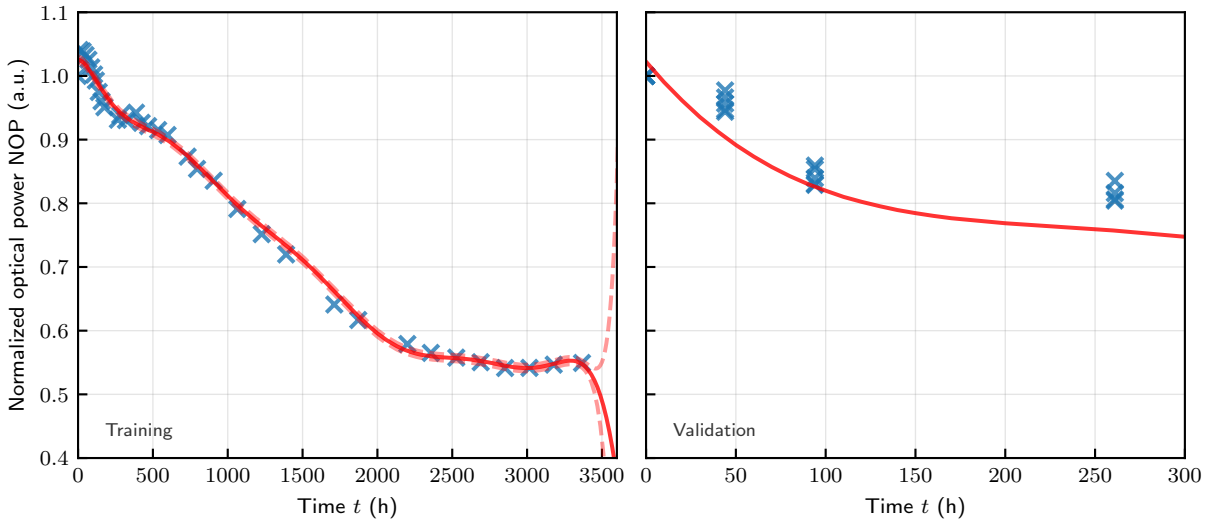

Figure 6.6: (Left) The GPR fitting result for the blue DUT trained at $T = 65\,°C$, $I = 300\,mA$ and $rH = 55\,\%$, (right) the GPR result of the interpolated stress values $T = 75\,°C$, $I = 300\,mA$ and $rH = 55\,\%$ of the blue DUT. The models estimate is denoted as a red line.

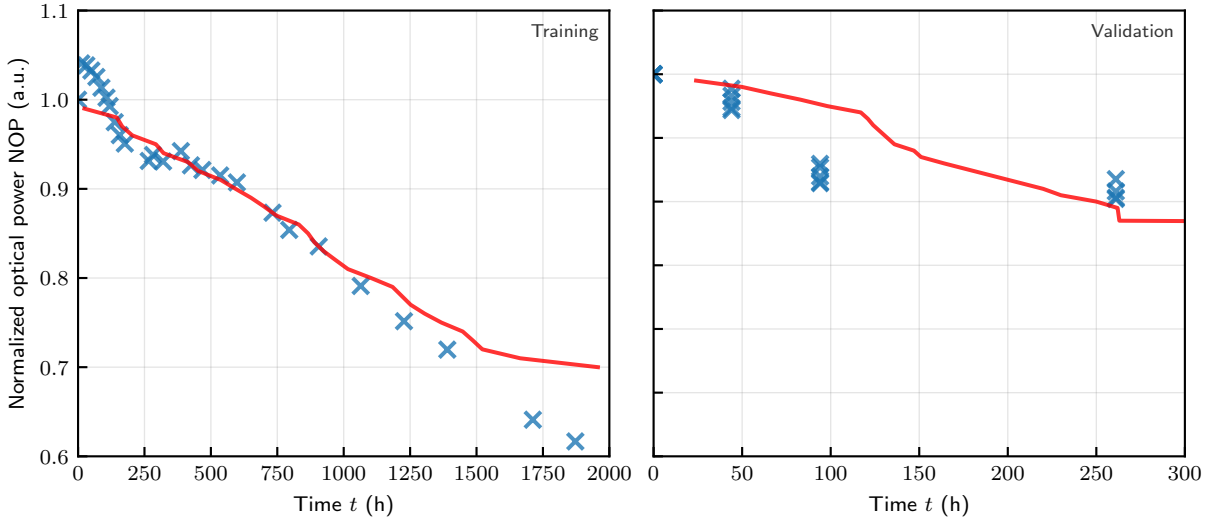

Figure 6.7: Estimation of the degradation trajectory by a CPH survival model evaluated at each $L_x \leq 0.7$: (Left) result for the blue DUT trained at $T = 65\,°C$, $I = 300\,mA$ and $rH = 55\,\%$, (right) the result of the interpolated stress values $T = 75\,°C$, $I = 300\,mA$ and $rH = 55\,\%$ of the blue DUT. The models estimate is denoted as a red line.

- A segmented decay function addresses the disadvantages of both before mentioned models at a cost of higher computational complexity since every free parameter has to be modeled individually.
- All previously discussed linkage models assume a monotonous acceleration regardless of the accepted stress parameters and their levels. The models, however, tend to produce inaccurate results in scenarios with a non-monotonic relationship between a stress level

and the resulting acceleration as present in the humidity influence on the investigated devices of this work.

- A Properly trained GPR model provides a comparatively high accuracy for moderate extrapolation rates even for small sample populations. However, this type of models exhibit a large computational complexity at increasing data set size accompanied by its lack of physical meaning.
- A CPH survival model provides an lightweight computable approach in scenarios with missing or censored data points. However, this modeling approach is subjected to accuracy drawbacks for small sample populations.

7 Conclusion and Future Work

Over the course of this thesis the impact of operational and environmental stress at 24 different (rH_A, T_A, I_F)-conditions on 480 commercial available LED devices of four different types was investigated. Therefore, the devices were subjected to an Accelerated Degradation Test and measured periodically with respect to their optical, electrical and thermal characteristics. Subsequently, an in-depth analysis was carried out in order to identify and differentiate between various degradation effects and failure sites starting from the LED die over its interconnect to the package's optical material along the light extraction path. Then, as a final step the previous obtained degradation trajectories of the devices optical power were modeled according with different approaches to obtain an total lifetime estimate of the devices at certain stress levels. The overall findings will be highlighted in the following with respect to the proposed research questions section 4.1 and section 6.2.

Q1: *How is moisture from the environmental surrounding impacting the optical performance of a LED device (for horticulture applications) with respect to different phosphor types?*
Given the investigated LED devices, multiple moisture ingress related impairments on the devices optical performance were identified. All devices exhibited distinct swelling due to moisture uptake of the silicone encapsulant varying with humidity and temperature level. Especially highly elevated environmental conditions promoted this behavior. As a result from this swelling, shear forces were introduced into the silicone interfacing layers causing the encapsulant to detach from the packages reflector cup enabling moisture creepage along these generated cavities into the packages inner parts. At this stage, the lead-frames reflective layer was exposed to sulfur-containing moisture triggering a tarnishing of this very thus reducing the overall reflected light from the packages bottom. Simultaneously, the encapsulant underwent an autoxidation cycle causing the silicone polymer chains to link and cleave which lead to enbrittlement of the encapsulant. This effect appeared as a yellow discoloration in the early stages and resulted in distinct cracking with prolonged exposure. In addition, the three phosphor-converted device types presented an increasing dissolution of the phosphor particles with progressing aging causing the spectral properties of the device to change significantly. In particular, the green phosphor compound used in the lime device and the white devices red phosphor compound were prone to an increased dissolution rate.
On the interconnects site, moisture ingress induced electrolysis effects at the Cu – Au lead-frame to bond-wire attachment decreasing the conductivity and thus yielding a substantial higher forward voltage of the device. This effect however, has only been observed under moderate humidity and high temperature conditions. However, the origin of this observed effect requires further investigation surpassing the scope of this work.

Q2: *If and how are devices under storage conditions ($I_F = 0$) affected by moisture ingress?*
Since the above autoxidation cycle depends on temperature and moisture content a significant degradation was also observed under storage conditions. In some scenarios the degradation was even higher that at operating conditions. A reason for this behavior might be due to the die acting as an additional heat source under operating conditions decreasing the rate of moisture diffusion into the silicone as long as the encapsulant has not been substantially damaged. Thus, the investigated LED devices should be stored in a dry and moderately tempered environment.

Q3: *Which of the three common stress factors – electrical current, temperature or humidity – is the main contributor to the devices degradation?*
As the theoretical background presented section 3.2, the interaction between a given stress parameter and temperature determines the effects severance. In this context, the temperature often acts as an accelerator on a given effect or reaction like diffusion for example. Results obtained from the conducted ADT verify this theoretical background. For the investigated devices, especially the combination of elevated temperature and moisture levels presented an significant effect on the devices performance. As a root cause the selection of package materials in combination with the PLCC package structure is suspected.

Q4: *Which combination of decay and linkage functions are suitable for modeling the obtained ADT data?*
With respect to the observed degradation trajectories exhibiting at least two distinct underlying time-dependent effects, decay functions with varying decay rate were expected to outperform their static decay rate counterparts. Among the investigated continuous decay functions especially the Inverse Sigmoid and the model proposed by Bae et al. presented significantly more accurate results compared to e.g. the standard Exponential model proposed by IES TM-21. Both models, however, have the downside of no control over the exact transition point between the underlying degradation effects acceleration rates. In this regard, the segmented decay model following the partial regression approach by Muggeo proved to be substantially more accurate than the continuous models since it provides sufficient control over the acceleration rate's transition points.
Among the different investigated linkage functions the Eyring model has proven to be the most suitable on the given multi-stress data. Given the fact, that none of the other proposed models takes all three stress variables into account this result was somewhat expected. Further, the proposed physics-based models assume a monotonic behavior of the acceleration factor since they assume a higher reaction or degradation rate with increasing stress levels. However, due to currents observed non-monotonic impact at moderate current levels, static decay rate-based models will be subjected to significant accuracy drawbacks. The segmented decay models on the other hand showed an acceptable to good accuracy at a disadvantage of requiring one linkage model for each acceleration factor and thus increasing the computational complexity.

Q5: *Are Gaussian Process Regression and Survival Analysis potential alternative Data-driven approaches to common methodologies for modeling the degradation and failure-time of a LED?*
Given the relative small number of evaluated samples for each condition alongside the large number of test conditions especially a GPR yields extraordinary results in terms of

interpolating between stress conditions compared to MD-based approaches. However, at large time extrapolation distances its accuracy decreases exponentially. In addition, its computational complexity increases drastically with the number of dependent variables and observations. In cases were only the time-to-failure is required, especially under the presence of right censored data, the application of a CPH model based Survival Analysis offers a computational lightweight alternative with a reasonable accuracy and should therefore be further investigated in the context of LED lifetime estimation.

Even though the promising results of this work, it reveals the need for future work encompassing several aspects with respect to the observed degradation effects: Firstly, the drive current's non-monotonic influence on the degradation rate needs to be further investigated. Therefore, a single device type ADT with a more granular stress level resolution is proposed in order to identify an empirically accurate degradation model. Secondly, different packages types, such as hermetically sealed packages, and various materials of the packages structural parts should be tested to obtain a better understanding on the critical design elements of an LED device with respect to environmental humidity. Finally, on the modeling side new emerging DD approaches such as physics based neural networks may pose suitable candidates for physically interpretable alternatives to common partly inaccurate or non-physics related MD approaches.

Bibliography

[1] Nikolay Zheludev. "The Life and Times of the LED — a 100-Year History." In: *Nature Photonics* 1.4 (Apr. 2007), pp. 189–192. ISSN: 1749-4893. DOI: 10.1038/nphoton.2007.34.

[2] E. Fred Schubert. *Light-Emitting Diodes*. 2nd ed. Cambridge: Cambridge University Press, 2006. ISBN: 978-0-521-86538-8. DOI: 10.1017/CBO9780511790546.

[3] W. Shockley. "The Theory of P-n Junctions in Semiconductors and p-n Junction Transistors." In: *The Bell System Technical Journal* 28.3 (July 1949), pp. 435–489. ISSN: 0005-8580. DOI: 10.1002/j.1538-7305.1949.tb03645.x.

[4] H. Welker. "Über Neue Halbleitende Verbindungen." In: *Zeitschrift für Naturforschung A* 7.11 (Nov. 1952), pp. 744–749. ISSN: 1865-7109. DOI: 10.1515/zna-1952-1110.

[5] G. A. Wolff, R. A. Hebert, and J. D. Broder. "Electroluminescence of GaP." In: *Physical Review* 100.4 (Nov. 1955), pp. 1144–1145. DOI: 10.1103/PhysRev.100.1144.

[6] R. Braunstein. "Radiative Transitions in Semiconductors." In: *Physical Review* 99.6 (Sept. 1955), pp. 1892–1893. DOI: 10.1103/PhysRev.99.1892.

[7] M. Gershenzon and R. M. Mikulyak. "Light Emission from Forward Biased P-n Junctions in Gallium Phosphide." In: *Solid-State Electronics* 5.5 (Sept. 1962), pp. 313–329. ISSN: 0038-1101. DOI: 10.1016/0038-1101(62)90113-2.

[8] Susan Walsh Sanderson and Kenneth L. Simons. "Light Emitting Diodes and the Lighting Revolution: The Emergence of a Solid-State Lighting Industry." In: *Research Policy* 43.10 (Dec. 2014), pp. 1730–1746. ISSN: 0048-7333. DOI: 10.1016/j.respol.2014.07.011.

[9] H. P. Maruska and J. J. Tietjen. "THE PREPARATION AND PROPERTIES OF VAPOR-DEPOSITED SINGLE-CRYSTAL-LINE GaN." In: *Applied Physics Letters* 15.10 (Oct. 2003), pp. 327–329. ISSN: 0003-6951. DOI: 10.1063/1.1652845.

[10] H. Amano, N. Sawaki, I. Akasaki, and Y. Toyoda. "Metalorganic Vapor Phase Epitaxial Growth of a High Quality GaN Film Using an AlN Buffer Layer." In: *Applied Physics Letters* 48.5 (Feb. 1986), pp. 353–355. ISSN: 0003-6951. DOI: 10.1063/1.96549.

[11] Hiroshi Amano, Masahiro Kito, Kazumasa Hiramatsu, and Isamu Akasaki. "P-Type Conduction in Mg-Doped GaN Treated with Low-Energy Electron Beam Irradiation (LEEBI)." In: *Japanese Journal of Applied Physics* 28.12A (Dec. 1989), p. L2112. ISSN: 1347-4065. DOI: 10.1143/JJAP.28.L2112.

[12] Shuji Nakamura Shuji Nakamura. "GaN Growth Using GaN Buffer Layer." In: *Japanese Journal of Applied Physics* 30.10A (Oct. 1991), p. L1705. ISSN: 1347-4065. DOI: 10.1143/JJAP.30.L1705.

[13] Shuji Nakamura, Naruhito Iwasa, and Masayuki Senoh. "Method of Manufacturing P-type Compound Semiconductor." Pat. US5306662A. 1994.

[14] Leah Y. Kuritzky, Claude Weisbuch, and James S. Speck. "Prospects for 100% Wall-Plug Efficient III-nitride LEDs." In: *Optics Express* 26.13 (June 2018), pp. 16600–16608. ISSN: 1094-4087. DOI: 10.1364/OE.26.016600.

[15] Yoshinori Shimizu, Kensho Sakano, Yasunobu Noguchi, and Toshio Moriguchi. "Light Emitting Device Having a Nitride Compound Semiconductor and a Phosphor Containing a Garnet Fluorescent Material." Pat. US5998925A. Dec. 1999.

[16] Jaehee Cho, Jun Hyuk Park, Jong Kyu Kim, and E. Fred Schubert. "White Light-Emitting Diodes: History, Progress, and Future." In: *Laser & Photonics Reviews* 11.2 (2017), p. 1600147. ISSN: 1863-8899. DOI: 10.1002/lpor.201600147.

[17] Yukio Narukawa, Junya Narita, Takahiko Sakamoto, Kouichiro Deguchi, Takao Yamada, and Takashi Mukai. "Ultra-High Efficiency White Light Emitting Diodes." In: *Japanese Journal of Applied Physics* 45.10L (Oct. 2006), p. L1084. ISSN: 1347-4065. DOI: 10.1143/JJAP.45.L1084.

[18] Yukio Narukawa, Masatsugu Ichikawa, Daisuke Sanga, Masahiko Sano, and Takashi Mukai. "White Light Emitting Diodes with Super-High Luminous Efficacy." In: *Journal of Physics D: Applied Physics* 43.35 (Aug. 2010), p. 354002. ISSN: 0022-3727. DOI: 10.1088/0022-3727/43/35/354002.

[19] M. Khalid Hossain, Shahadat Hossain, Mohammad Hafez Ahmed, Md Ishak Khan, Nazmul Haque, and Gazi A. Raihan. "A Review on Optical Applications, Prospects, and Challenges of Rare-Earth Oxides." In: *ACS Applied Electronic Materials* 3.9 (Sept. 2021), pp. 3715–3746. DOI: 10.1021/acsaelm.1c00682.

[20] Karamjyoti Panigrahi and Angshuman Nag. "Challenges and Strategies to Design Phosphors for Future White Light Emitting Diodes." In: *The Journal of Physical Chemistry C* 126.20 (May 2022), pp. 8553–8564. ISSN: 1932-7447. DOI: 10.1021/acs.jpcc.2c01679.

[21] Jianwei Qiao, Jing Zhao, Quanlin Liu, and Zhiguo Xia. "Recent Advances in Solid-State LED Phosphors with Thermally Stable Luminescence." In: *Journal of Rare Earths* 37.6 (June 2019), pp. 565–572. ISSN: 10020721. DOI: 10.1016/j.jre.2018.11.001.

[22] Mu-Huai Fang, Zhen Bao, Wen-Tse Huang, and Ru-Shi Liu. "Evolutionary Generation of Phosphor Materials and Their Progress in Future Applications for Light-Emitting Diodes." In: *Chemical Reviews* 122.13 (July 2022), pp. 11474–11513. ISSN: 0009-2665. DOI: 10.1021/acs.chemrev.1c00952.

[23] Akvilė Viršilė, Margit Olle, and Pavelas Duchovskis. "LED Lighting in Horticulture." In: *Light Emitting Diodes for Agriculture: Smart Lighting*. Ed. by S. Dutta Gupta. Singapore: Springer, 2017, pp. 113–147. ISBN: 978-981-10-5807-3. DOI: 10.1007/978-981-10-5807-3_7.

[24] Andreas Bielawny, Thorsten Schupp, and Cornelius Neumann. "Automotive Lighting Continues to Evolve." In: *Optics and Photonics News* 27.11 (Nov. 2016), pp. 36–43. ISSN: 1541-3721. DOI: 10.1364/OPN.27.11.000036.

[25] Bruno Gayral. "LEDs for Lighting: Basic Physics and Prospects for Energy Savings." In: *Comptes Rendus Physique*. Demain l'énergie 18.7 (Sept. 2017), pp. 453–461. ISSN: 1631-0705. DOI: 10.1016/j.crhy.2017.09.001.

[26] Wachta Henryk and Paulina Bojda. "Usability of Luminaries with LED Sources to Illuminate the Window Areas of Architectural Objects." In: *2016 13th Selected Issues of Electrical Engineering and Electronics (WZEE)*. May 2016, pp. 1–6. DOI: 10.1109/WZEE.2016.7800250.

[27] Jinmin Li and G. Q. Zhang, eds. *Light-Emitting Diodes: Materials, Processes, Devices and Applications*. Vol. 4. Solid State Lighting Technology and Application Series. Cham: Springer International Publishing, 2019. ISBN: 978-3-319-99210-5 978-3-319-99211-2. DOI: 10.1007/978-3-319-99211-2.

[28] Jessika Luth Richter, Leena Tähkämö, and Carl Dalhammar. "Trade-Offs with Longer Lifetimes? The Case of LED Lamps Considering Product Development and Energy Contexts." In: *Journal of Cleaner Production* 226 (July 2019), pp. 195–209. ISSN: 0959-6526. DOI: 10.1016/j.jclepro.2019.03.331.

[29] László Sipos, Ildikó Fruzsina Boros, László Csambalik, Géza Székely, András Jung, and László Balázs. "Horticultural Lighting System Optimalization: A Review." In: *Scientia Horticulturae* 273 (Nov. 2020), p. 109631. ISSN: 0304-4238. DOI: 10.1016/j.scienta.2020.109631.

[30] Ching-Cherng Sun, Xuan-Hao Lee, Ivan Moreno, Chen-Hao Lee, Yeh-Wei Yu, Tsung-Hsun Yang, and Te-Yuan Chung. "Design of LED Street Lighting Adapted for Free-Form Roads." In: *IEEE Photonics Journal* 9.1 (Feb. 2017), pp. 1–13. ISSN: 1943-0655. DOI: 10.1109/JPHOT.2017.2657742.

[31] Jens Balasus, Janis Blank, Sebastian Babilon, Tim Hegemann, and Tran Quoc Khanh. "Energy Efficient Lighting in Plant Factories: Addressing Utilance." In: *Agronomy* 11.12 (Dec. 2021), p. 2570. ISSN: 2073-4395. DOI: 10.3390/agronomy11122570.

[32] Willem Dirk van Driel, Xuejun Fan, and Guo Qi Zhang, eds. *Solid State Lighting Reliability Part 2*. Vol. 3. Solid State Lighting Technology and Application Series. Cham: Springer International Publishing, 2018. ISBN: 978-3-319-58174-3 978-3-319-58175-0. DOI: 10.1007/978-3-319-58175-0.

[33] Katherine Calvin et al. *IPCC, 2023: Climate Change 2023: Synthesis Report. Contribution of Working Groups I, II and III to the Sixth Assessment Report of the Intergovernmental Panel on Climate Change [Core Writing Team, H. Lee and J. Romero (Eds.)]. IPCC, Geneva, Switzerland.* Tech. rep. Intergovernmental Panel on Climate Change (IPCC), July 2023. DOI: 10.59327/IPCC/AR6-9789291691647.

[34] Martina Loi, Alessandra Villani, Francesco Paciolla, Giuseppina Mulè, and Costantino Paciolla. "Challenges and Opportunities of Light-Emitting Diode (LED) as Key to Modulate Antioxidant Compounds in Plants. A Review." In: *Antioxidants* 10.1 (Jan. 2021), p. 42. ISSN: 2076-3921. DOI: 10.3390/antiox10010042.

[35] Sanusi Shamsudeen Nassarawa, Asem Mahmoud Abdelshafy, Yanqun Xu, Li Li, and Zisheng Luo. "Effect of Light-Emitting Diodes (LEDs) on the Quality of Fruits and Vegetables During Postharvest Period: A Review." In: *Food and Bioprocess Technology* 14.3 (Mar. 2021), pp. 388–414. ISSN: 1935-5149. DOI: 10.1007/s11947-020-02534-6.

[36] Liang Zheng, Huaming He, and Weitang Song. "Application of Light-emitting Diodes and the Effect of Light Quality on Horticultural Crops: A Review." In: *HortScience* 54.10 (Oct. 2019), pp. 1656–1661. ISSN: 0018-5345, 2327-9834. DOI: 10.21273/HORTSCI14109-19.

[37] Georges Zissis, Paolo Bertoldi, and SERRENHO Tiago Ribeiro. *Update on the Status of LED-Lighting World Market since 2018*. Tech. rep. Jan. 2021. DOI: 10.2760/759859.

[38] W.D. van Driel and X.J. Fan, eds. *Solid State Lighting Reliability: Components to Systems*. New York, NY: Springer New York, 2013. ISBN: 978-1-4614-3066-7 978-1-4614-3067-4. DOI: 10.1007/978-1-4614-3067-4.

[39] Willem Dirk van Driel and Maryam Yazdan Mehr, eds. *Reliability of Organic Compounds in Microelectronics and Optoelectronics: From Physics-of-Failure to Physics-of-Degradation*. Cham: Springer International Publishing, 2022. ISBN: 978-3-030-81575-2 978-3-030-81576-9. DOI: 10.1007/978-3-030-81576-9.

[40] Alexander Herzog, Max Wagner, Simon Benkner, Babak Zandi, Willem D. van Driel, and Tran Quoc Khanh. "Long-Term Temperature-Dependent Degradation of 175 W Chip-on-Board LED Modules." In: *IEEE Transactions on Electron Devices* 69.12 (Dec. 2022), pp. 6830–6836. ISSN: 1557-9646. DOI: 10.1109/TED.2022.3214169.

[41] *DIN EN 16798-1:2022-03, Energetische Bewertung von Gebäuden_- Lüftung von Gebäuden_- Teil_1: Eingangsparameter Für Das Innenraumklima Zur Auslegung Und Bewertung Der Energieeffizienz von Gebäuden Bezüglich Raumluftqualität, Temperatur, Licht Und Akustik_- Modul M1-6; Deutsche Fassung EN_16798-1:2019*. Mar. 2022. DOI: 10.31030/3327351.

[42] Miguel Urrestarazu, Cinthia Nájera, and María del Mar Gea. "Effect of the Spectral Quality and Intensity of Light-emitting Diodes on Several Horticultural Crops." In: *HortScience* 51.3 (Mar. 2016), pp. 268–271. ISSN: 0018-5345, 2327-9834. DOI: 10.21273/HORTSCI.51.3.268.

[43] *ANSI/IES LM-80-21: Approved Method: Measuring Maintenance of Light Output Characteristics of Solid-State Light Sources*. Approved Method. New York, USA: Illuminating Engineering Society, 2021, p. 15.

[44] R. R. Pelá, C. Caetano, M. Marques, L. G. Ferreira, J. Furthmüller, and L. K. Teles. "Accurate Band Gaps of AlGaN, InGaN, and AlInN Alloys Calculations Based on LDA-1/2 Approach." In: *Applied Physics Letters* 98.15 (Apr. 2011), p. 151907. ISSN: 0003-6951. DOI: 10.1063/1.3576570.

[45] Keh Yung Cheng. *III–V Compound Semiconductors and Devices: An Introduction to Fundamentals*. Graduate Texts in Physics. Cham: Springer International Publishing, 2020. ISBN: 978-3-030-51901-8 978-3-030-51903-2. DOI: 10.1007/978-3-030-51903-2.

[46] Tae-Yeon Seong, Jung Han, Hiroshi Amano, and Hadis Morkoç, eds. *III-Nitride Based Light Emitting Diodes and Applications*. Vol. 133. Topics in Applied Physics. Singapore: Springer Singapore, 2017. ISBN: 978-981-10-3754-2 978-981-10-3755-9. DOI: 10.1007/978-981-10-3755-9.

[47] S. Strite and H. Morkoç. "GaN, AlN, and InN: A Review." In: *Journal of Vacuum Science & Technology B: Microelectronics and Nanometer Structures Processing, Measurement, and Phenomena* 10.4 (July 1992), pp. 1237–1266. ISSN: 1071-1023. DOI: 10.1116/1.585897.

[48] Alexander Georg Herzog. "Analyse des degradationsverhaltens GaN-basierter LEDs im ultravioletten und grünen spektralbereich." PhD thesis. Darmstadt, Germany: Technische Universität Darmstadt, Dec. 2020.

[49] William A. Melton and Jacques I. Pankove. "GaN Growth on Sapphire." In: *Journal of Crystal Growth* 178.1-2 (June 1997), pp. 168–173. ISSN: 00220248. DOI: 10.1016/S0022-0248(97)00082-1.

[50] S. Yu. Karpov. "Suppression of Phase Separation in InGaN Due to Elastic Strain." In: *MRS Internet Journal of Nitride Semiconductor Research* 3 (1998), e16. ISSN: 1092-5783. DOI: 10.1557/S1092578300000880.

[51] Fabio Bernardini, Vincenzo Fiorentini, and David Vanderbilt. "Spontaneous Polarization and Piezoelectric Constants of III-V Nitrides." In: *Physical Review B* 56.16 (Oct. 1997), R10024–R10027. ISSN: 0163-1829, 1095-3795. DOI: 10.1103/PhysRevB.56.R10024.

[52] Paul Adrien Maurice Dirac and Ralph Howard Fowler. "On the Theory of Quantum Mechanics." In: *Proceedings of the Royal Society of London. Series A, Containing Papers of a Mathematical and Physical Character* 112.762 (Jan. 1926), pp. 661–677. DOI: 10.1098/rspa.1926.0133.

[53] Eleonora Vella, Fabrizio Messina, Marco Cannas, and Roberto Boscaino. "Unraveling Exciton Dynamics in Amorphous Silicon Dioxide: Interpretation of the Optical Features from 8 to 11 eV." In: *Physical Review B* 83.17 (May 2011), p. 174201. DOI: 10.1103/PhysRevB.83.174201.

[54] Feng Yun, Michael A. Reshchikov, Lei He, Thomas King, Hadis Morkoç, Steve W. Novak, and Luncun Wei. "Energy Band Bowing Parameter in AlxGa1-xN Alloys." In: *Journal of Applied Physics* 92.8 (Oct. 2002), pp. 4837–4839. ISSN: 0021-8979. DOI: 10.1063/1.1508420.

[55] L Siozade, J Leymarie, P Disseix, A Vasson, M Mihailovic, N Grandjean, M Leroux, and J Massies. "Modelling of Thermally Detected Optical Absorption and Luminescence of (In,Ga)N/GaN Heterostructures." In: *Solid State Communications* 115.11 (Aug. 2000), pp. 575–579. ISSN: 0038-1098. DOI: 10.1016/S0038-1098(00)00249-0.

[56] J Wu, W Walukiewicz, K. M Yu, J. W Ager, S. X Li, E. E Haller, Hai Lu, and William J Schaff. "Universal Bandgap Bowing in Group-III Nitride Alloys." In: *Solid State Communications* 127.6 (Aug. 2003), pp. 411–414. ISSN: 0038-1098. DOI: 10.1016/S0038-1098(03)00457-5.

[57] S. Krukowski et al. "Thermal Properties of Indium Nitride." In: *Journal of Physics and Chemistry of Solids* 59.3 (Mar. 1998), pp. 289–295. ISSN: 0022-3697. DOI: 10.1016/S0022-3697(97)00222-9.

[58] Pietro Pampili and Peter J. Parbrook. "Doping of III-nitride Materials." In: *Materials Science in Semiconductor Processing*. Advanced Doping Methods in Semiconductor Devices and Nanostructures 62 (May 2017), pp. 180–191. ISSN: 1369-8001. DOI: 10.1016/j.mssp.2016.11.006.

[59] O. Ambacher et al. "Pyroelectric Properties of Al(In)GaN/GaN Hetero- and Quantum Well Structures." In: *Journal of Physics: Condensed Matter* 14.13 (Mar. 2002), p. 3399. ISSN: 0953-8984. DOI: 10.1088/0953-8984/14/13/302.

[60] Fabio Bernardini and Vincenzo Fiorentini. "Macroscopic Polarization and Band Offsets at Nitride Heterojunctions." In: *Physical Review B* 57.16 (Apr. 1998), R9427–R9430. DOI: 10.1103/PhysRevB.57.R9427.

[61] J. Stark. "Observation of the Separation of Spectral Lines by an Electric Field." In: *Nature* 92.2301 (Dec. 1913), pp. 401–401. ISSN: 1476-4687. DOI: 10.1038/092401b0.

[62] D. A. B. Miller, D. S. Chemla, T. C. Damen, A. C. Gossard, W. Wiegmann, T. H. Wood, and C. A. Burrus. "Band-Edge Electroabsorption in Quantum Well Structures: The Quantum-Confined Stark Effect." In: *Physical Review Letters* 53.22 (Nov. 1984), pp. 2173–2176. DOI: 10.1103/PhysRevLett.53.2173.

[63] M. Leroux, N. Grandjean, M. Laügt, J. Massies, B. Gil, P. Lefebvre, and P. Bigenwald. "Quantum Confined Stark Effect Due to Built-in Internal Polarization Fields in (Al,Ga)N/GaN Quantum Wells." In: *Physical Review B* 58.20 (Nov. 1998), R13371–R13374. DOI: 10.1103/PhysRevB.58.R13371.

[64] Shuji Nakamura, Takashi Mukai Takashi Mukai, and Masayuki Senoh Masayuki Senoh. "Si- and Ge-Doped GaN Films Grown with GaN Buffer Layers." In: *Japanese Journal of Applied Physics* 31.9R (Sept. 1992), p. 2883. ISSN: 1347-4065. DOI: 10.1143/JJAP.31.2883.

[65] W. Götz, N. M. Johnson, C. Chen, H. Liu, C. Kuo, and W. Imler. "Activation Energies of Si Donors in GaN." In: *Applied Physics Letters* 68.22 (May 1996), pp. 3144–3146. ISSN: 0003-6951. DOI: 10.1063/1.115805.

[66] H. P. Maruska and J. J. Tietjen. "THE PREPARATION AND PROPERTIES OF VAPOR-DEPOSITED SINGLE-CRYSTAL-LINE GaN." In: *Applied Physics Letters* 15.10 (Nov. 1969), pp. 327–329. ISSN: 0003-6951, 1077-3118. DOI: 10.1063/1.1652845.

[67] M. Ilegems and H. C. Montgomery. "Electrical Properties of N-Type Vapor-Grown Gallium Nitride." In: *Journal of Physics and Chemistry of Solids* 34.5 (May 1973), pp. 885–895. ISSN: 0022-3697. DOI: 10.1016/S0022-3697(73)80090-3.

[68] Chris G. Van de Walle and Jörg Neugebauer. "First-Principles Calculations for Defects and Impurities: Applications to III-nitrides." In: *Journal of Applied Physics* 95.8 (Mar. 2004), pp. 3851–3879. ISSN: 0021-8979. DOI: 10.1063/1.1682673.

[69] Shuji Nakamura, Naruhito Iwasa, Masayuki Senoh Masayuki Senoh, and Takashi Mukai Takashi Mukai. "Hole Compensation Mechanism of P-Type GaN Films." In: *Japanese Journal of Applied Physics* 31.5R (May 1992), p. 1258. ISSN: 1347-4065. DOI: 10.1143/JJAP.31.1258.

[70] Herbert Paul Maruska and Walden Clark Rhines. "A Modern Perspective on the History of Semiconductor Nitride Blue Light Sources." In: *Solid-State Electronics* 111 (Sept. 2015), pp. 32–41. ISSN: 0038-1101. DOI: 10.1016/j.sse.2015.04.010.

[71] I. Vurgaftman and J. R. Meyer. "Band Parameters for Nitrogen-Containing Semiconductors." In: *Journal of Applied Physics* 94.6 (Sept. 2003), pp. 3675–3696. ISSN: 0021-8979. DOI: 10.1063/1.1600519.

[72] W. Shockley and W. T. Read. "Statistics of the Recombinations of Holes and Electrons." In: *Physical Review* 87.5 (Sept. 1952), pp. 835–842. DOI: 10.1103/PhysRev.87.835.

[73] W. van Roosbroeck and W. Shockley. "Photon-Radiative Recombination of Electrons and Holes in Germanium." In: *Physical Review* 94.6 (June 1954), pp. 1558–1560. DOI: 10.1103/PhysRev.94.1558.

[74] J. Hader, J. V. Moloney, B. Pasenow, S. W. Koch, M. Sabathil, N. Linder, and S. Lutgen. "On the Importance of Radiative and Auger Losses in GaN-based Quantum Wells." In: *Applied Physics Letters* 92.26 (July 2008), p. 261103. ISSN: 0003-6951. DOI: 10.1063/1.2953543.

[75] M. Zhang, P. Bhattacharya, J. Singh, and J. Hinckley. "Direct Measurement of Auger Recombination in In0.1Ga0.9N/GaN Quantum Wells and Its Impact on the Efficiency of In0.1Ga0.9N/GaN Multiple Quantum Well Light Emitting Diodes." In: *Applied Physics Letters* 95.20 (Nov. 2009), p. 201108. ISSN: 0003-6951. DOI: 10.1063/1.3266520.

[76] Matteo Meneghini, Nicola Trivellin, Gaudenzio Meneghesso, Enrico Zanoni, Ulrich Zehnder, and Berthold Hahn. "A Combined Electro-Optical Method for the Determination of the Recombination Parameters in InGaN-based Light-Emitting Diodes." In: *Journal of Applied Physics* 106.11 (Dec. 2009), p. 114508. ISSN: 0021-8979. DOI: 10.1063/1.3266014.

[77] Ansgar Laubsch, Matthias Sabathil, Johannes Baur, Matthias Peter, and Berthold Hahn. "High-Power and High-Efficiency InGaN-Based Light Emitters." In: *IEEE Transactions on Electron Devices* 57.1 (Jan. 2010), pp. 79–87. ISSN: 1557-9646. DOI: 10.1109/TED.2009.2035538.

[78] Ümit Ozgur, Huiyong Liu, Xing Li, Xianfeng Ni, and Hadis Morkoç. "GaN-Based Light-Emitting Diodes: Efficiency at High Injection Levels." In: *Proceedings of the IEEE* 98.7 (July 2010), pp. 1180–1196. ISSN: 1558-2256. DOI: 10.1109/JPROC.2010.2043210.

[79] Martin F. Schubert, Sameer Chhajed, Jong Kyu Kim, E. Fred Schubert, Daniel D. Koleske, Mary H. Crawford, Stephen R. Lee, Arthur J. Fischer, Gerald Thaler, and Michael A. Banas. "Effect of Dislocation Density on Efficiency Droop in GaInN/GaN Light-Emitting Diodes." In: *Applied Physics Letters* 91.23 (Dec. 2007), p. 231114. ISSN: 0003-6951. DOI: 10.1063/1.2822442.

[80] G. A. Baraff and M. Schlüter. "Electronic Structure, Total Energies, and Abundances of the Elementary Point Defects in GaAs." In: *Physical Review Letters* 55.12 (Sept. 1985), pp. 1327–1330. DOI: 10.1103/PhysRevLett.55.1327.

[81] R. L. Longini and R. F. Greene. "Ionization Interaction between Impurities in Semiconductors and Insulators." In: *Physical Review* 102.4 (May 1956), pp. 992–999. DOI: 10.1103/PhysRev.102.992.

[82] Giovanni Verzellesi, Davide Saguatti, Matteo Meneghini, Francesco Bertazzi, Michele Goano, Gaudenzio Meneghesso, and Enrico Zanoni. "Efficiency Droop in InGaN/GaN Blue Light-Emitting Diodes: Physical Mechanisms and Remedies." In: *Journal of Applied Physics* 114.7 (Aug. 2013), p. 071101. ISSN: 0021-8979. DOI: 10.1063/1.4816434.

[83] Takashi Mukai, Motokazu Yamada, and Shuji Nakamura. "Characteristics of InGaN-Based UV/Blue/Green/Amber/Red Light-Emitting Diodes." In: *Japanese Journal of Applied Physics* 38.7R (July 1999), p. 3976. ISSN: 1347-4065. DOI: 10.1143/JJAP.38.3976.

[84] Sergey Karpov. "ABC-model for Interpretation of Internal Quantum Efficiency and Its Droop in III-nitride LEDs: A Review." In: *Optical and Quantum Electronics* 47.6 (June 2015), pp. 1293–1303. ISSN: 0306-8919, 1572-817X. DOI: 10.1007/s11082-014-0042-9.

[85] Xiaoyang Li, Yuqing Hu, Enrico Zio, and Rui Kang. "A Bayesian Optimal Design for Accelerated Degradation Testing Based on the Inverse Gaussian Process." In: *IEEE Access* 5 (2017), pp. 5690–5701. ISSN: 2169-3536. DOI: 10.1109/ACCESS.2017.2683533.

[86] Y. P. Varshni. "Temperature Dependence of the Energy Gap in Semiconductors." In: *Physica* 34.1 (Jan. 1967), pp. 149–154. ISSN: 0031-8914. DOI: 10.1016/0031-8914(67)90062-6.

[87] I. Vurgaftman, J. R. Meyer, and L. R. Ram-Mohan. "Band Parameters for III–V Compound Semiconductors and Their Alloys." In: *Journal of Applied Physics* 89.11 (June 2001), pp. 5815–5875. ISSN: 0021-8979, 1089-7550. DOI: 10.1063/1.1368156.

[88] Anna Vaskuri, Hans Baumgartner, Petri Kärhä, György Andor, and Erkki Ikonen. "Modeling the Spectral Shape of InGaAlP-based Red Light-Emitting Diodes." In: *Journal of Applied Physics* 118.20 (Nov. 2015), p. 203103. ISSN: 0021-8979, 1089-7550. DOI: 10.1063/1.4936322.

[89] Anna Vaskuri, Petri Kärhä, Hans Baumgartner, Olli Kantamaa, Tomi Pulli, Tuomas Poikonen, and Erkki Ikonen. "Relationships between Junction Temperature, Electroluminescence Spectrum and Ageing of Light-Emitting Diodes." In: *Metrologia* 55.2 (Mar. 2018), S86–S95. ISSN: 0026-1394. DOI: 10.1088/1681-7575/aaaed2.

[90] Simon Benkner, Alexander Herzog, Stefan Klir, Willem D. Van Driel, and Tran Quoc Khanh. "Advancements in Spectral Power Distribution Modeling of Light-Emitting Diodes." In: *IEEE Access* 10 (2022), pp. 83612–83619. ISSN: 2169-3536. DOI: 10.1109/ACCESS.2022.3197280.

[91] Safae Aazou, Matthew Schuette White, Martin Kaltenbrunner, Zouheir Sekkat, Daniel Ayuk Mbi Egbe, and El Mahdi Assaid. "LambertW Function to Extract Physical Parameters of a Schottky Barrier Diode from Its I–V Characteristics." In: *Energies* 15.5 (Jan. 2022), p. 1667. ISSN: 1996-1073. DOI: 10.3390/en15051667.

[92] Abdelaziz Rabehi, Bachir Nail, Hicham Helal, Abdelmalek Douara, Abderrezzaq Ziane, Mohammed Amrani, Boudali Akkal, and Zineb Benamara. "Optimal Estimation of Schottky Diode Parameters Using a Novel Optimization Algorithm: Equilibrium Optimizer." In: *Superlattices and Microstructures* 146 (Oct. 2020), p. 106665. ISSN: 0749-6036. DOI: 10.1016/j.spmi.2020.106665.

[93] Chul Huh, William J. Schaff, Lester F. Eastman, and Seong-Ju Park. "Temperature Dependence of Light-Output Performance of InGaN/GaN Multiple-Quantum-Well Light-Emitting Diodes with Various In Compositions." In: 5187 (Jan. 2004), pp. 330–335. DOI: 10.1117/12.515648.

[94] Dawei Yan, Hai Lu, Dunjun Chen, Rong Zhang, and Youdou Zheng. "Forward Tunneling Current in GaN-based Blue Light-Emitting Diodes." In: *Applied Physics Letters* 96.8 (Feb. 2010), p. 083504. ISSN: 0003-6951. DOI: 10.1063/1.3327332.

[95] Gyeong Won Lee, Jong-In Shim, and Dong-Soo Shin. "On the Ideality Factor of the Radiative Recombination Current in Semiconductor Light-Emitting Diodes." In: *Applied Physics Letters* 109.3 (July 2016), p. 031104. ISSN: 0003-6951. DOI: 10.1063/1.4959081.

[96] Hisashi Masui. "Diode Ideality Factor in Modern Light-Emitting Diodes." In: *Semiconductor Science and Technology* 26.7 (Apr. 2011), p. 075011. ISSN: 0268-1242. DOI: 10.1088/0268-1242/26/7/075011.

[97] Hisashi Masui, Shuji Nakamura, and Steven P. DenBaars. "Technique to Evaluate the Diode Ideality Factor of Light-Emitting Diodes." In: *Applied Physics Letters* 96.7 (Feb. 2010), p. 073509. ISSN: 0003-6951, 1077-3118. DOI: 10.1063/1.3318285.

[98] J. C. Ranuárez, F. J. García Sánchez, and A. Ortiz-Conde. "Procedure for Determining Diode Parameters at Very Low Forward Voltage." In: *Solid-State Electronics* 43.12 (Dec. 1999), pp. 2129–2133. ISSN: 0038-1101. DOI: 10.1016/S0038-1101(99)00181-1.

[99] G. F. Yang, Q. Zhang, J. Wang, Y. N. Lu, P. Chen, Z. L. Wu, S. M. Gao, and G. Q. Chen. "InGaN/GaN Multiple Quantum Wells on Selectively Grown GaN Microfacets and the Applications for Phosphor-Free White Light-Emitting Diodes." In: *Reviews in Physics* 1 (Nov. 2016), pp. 101–119. ISSN: 2405-4283. DOI: 10.1016/j.revip.2016.06.001.

[100] D. L. Dexter. "A Theory of Sensitized Luminescence in Solids." In: *The Journal of Chemical Physics* 21.5 (1953), pp. 836–850. ISSN: 0021-9606. DOI: 10.1063/1.1699044.

[101] Th. Förster. "Zwischenmolekulare Energiewanderung und Fluoreszenz." In: *Annalen der Physik* 437.1-2 (1948), pp. 55–75. ISSN: 1521-3889. DOI: 10.1002/andp.19484370105.

[102] Nicola Armaroli and Henk J. Bolink, eds. *Photoluminescent Materials and Electroluminescent Devices*. Topics in Current Chemistry Collections. Cham: Springer International Publishing, 2017. ISBN: 978-3-319-59302-9 978-3-319-59304-3. DOI: 10.1007/978-3-319-59304-3.

[103] Sadao Adachi. "Review—Temperature Dependence of Luminescence Intensity and Decay Time in Mn4+-Activated Fluoride and Oxyfluoride Phosphors." In: *ECS Journal of Solid State Science and Technology* 10.2 (Feb. 2021), p. 026002. ISSN: 2162-8777. DOI: 10.1149/2162-8777/abe0af.

[104] Junhang Tian and Weidong Zhuang. "Thermal Stability of Nitride Phosphors for Light-Emitting Diodes." In: *Inorganic Chemistry Frontiers* 8.22 (2021), pp. 4933–4954. DOI: 10.1039/D1QI00993A.

[105] Shruti Hariyani, Anna C. Duke, Thorben Krauskopf, Wolfgang G. Zeier, and Jakoah Brgoch. "The Effect of Rare-Earth Substitution on the Debye Temperature of Inorganic Phosphors." In: *Applied Physics Letters* 116.5 (Feb. 2020), p. 051901. ISSN: 0003-6951. DOI: 10.1063/1.5142167.

[106] Mahdi Amachraa, Zhenbin Wang, Hanmei Tang, Shruti Hariyani, Chi Chen, Jakoah Brgoch, and Shyue Ping Ong. *Unified Theory of Thermal Quenching in Inorganic Phosphors*. https://arxiv.org/abs/1910.12420v2. Oct. 2019.

[107] Muna E. Raypah, Mutharasu Devarajan, Anas A. Ahmed, and Fauziah Sulaiman. "Thermal Characterizations Analysis of High-Power ThinGaN Cool-White Light-Emitting Diodes." In: *Journal of Applied Physics* 123.10 (Mar. 2018), p. 105703. ISSN: 0021-8979. DOI: 10.1063/1.5016359.

[108] M. Yazdan Mehr, A. Bahrami, W. D. van Driel, X. J. Fan, J. L. Davis, and G. Q. Zhang. "Degradation of Optical Materials in Solid-State Lighting Systems." In: *International Materials Reviews* 65.2 (Feb. 2020), pp. 102–128. ISSN: 0950-6608. DOI: 10.1080/09506608.2019.1565716.

[109] Laixia Nian, Xiaoming Pei, Zhili Zhao, and Xinzhong Wang. "Review of Optical Designs for Light-Emitting Diode Packaging." In: *IEEE Transactions on Components, Packaging and Manufacturing Technology* 9.4 (Apr. 2019), pp. 642–648. ISSN: 2156-3985. DOI: 10.1109/TCPMT.2019.2895729.

[110] Anton Alexeev, Grigory Onushkin, Jean-Paul Linnartz, and Genevieve Martin. "Multiple Heat Source Thermal Modeling and Transient Analysis of LEDs." In: *Energies* 12.10 (Jan. 2019), p. 1860. ISSN: 1996-1073. DOI: 10.3390/en12101860.

[111] Yupu Ma, Run Hu, Xingjian Yu, Weicheng Shu, and Xiaobing Luo. "A Modified Bidirectional Thermal Resistance Model for Junction and Phosphor Temperature Estimation in Phosphor-Converted Light-Emitting Diodes." In: *International Journal of Heat and Mass Transfer* 106 (Mar. 2017), pp. 1–6. ISSN: 0017-9310. DOI: 10.1016/j.ijheatmasstransfer.2016.10.058.

[112] T. A. Barbari, W. J. Koros, and D. R. Paul. "Gas Transport in Polymers Based on Bisphenol-A." In: *Journal of Polymer Science Part B: Polymer Physics* 26.4 (1988), pp. 709–727. ISSN: 1099-0488. DOI: 10.1002/polb.1988.090260401.

[113] X.J. Fan and E. Suhir, eds. *Moisture Sensitivity of Plastic Packages of IC Devices*. Boston, MA: Springer US, 2010. ISBN: 978-1-4419-5718-4 978-1-4419-5719-1. DOI: 10.1007/978-1-4419-5719-1.

[114] Jong-In Shim and Dong-Soo Shin. "Measuring the Internal Quantum Efficiency of Light-Emitting Diodes: Towards Accurate and Reliable Room-Temperature Characterization." In: *Nanophotonics* 7.10 (Oct. 2018), pp. 1601–1615. ISSN: 2192-8614. DOI: 10.1515/nanoph-2018-0094.

[115] D.A. Steigerwald, J.C. Bhat, D. Collins, R.M. Fletcher, M.O. Holcomb, M.J. Ludowise, P.S. Martin, and S.L. Rudaz. "Illumination with Solid State Lighting Technology." In: *IEEE Journal of Selected Topics in Quantum Electronics* 8.2 (Mar. 2002), pp. 310–320. ISSN: 1558-4542. DOI: 10.1109/2944.999186.

[116] Shah Limon, Om Prakash Yadav, and Haitao Liao. "A Literature Review on Planning and Analysis of Accelerated Testing for Reliability Assessment." In: *Quality and Reliability Engineering International* 33.8 (2017), pp. 2361–2383. ISSN: 1099-1638. DOI: 10.1002/qre.2195.

[117] Bryan Dodson, Harry Schwab, and Lockheed Martin Corp. *Accelerated Testing: A Practitioner's Guide to Accelerated and Reliability Testing*. 2nd ed. SAE International, Aug. 2021. ISBN: 978-1-4686-0350-7. DOI: 10.4271/9781468603514.

[118] Jeffrey E. Gunn, Sushil K. Malik, and Purabi M. Mazumdar. "Highly Accelerated Temperature and Humidity Stress Test Technique (HAST)." In: *19th International Reliability Physics Symposium*. Apr. 1981, pp. 48–51. DOI: 10.1109/IRPS.1981.362972.

[119] JEDEC Solid State Technology Association. *Steady-State Temperature-Humidity Bias Life Test*. Standard JESD22-A101D.01. Arlington, USA: JEDEC Solid State Technology Association, 2021.

[120] JEDEC Solid State Technology Association. *High Temperature Storage Life*. Standard JESD22-A103E.01. Arlington, USA: JEDEC Solid State Technology Association, 2021.

[121] JEDEC Solid State Technology Association. *Temperature Cycling*. Standard JESD22-A104F. Arlington, USA: JEDEC Solid State Technology Association, 2020.

[122] JEDEC Solid State Technology Association. *Power and Temperature Cycling*. Standard JESD22-A105D. Arlington, USA: JEDEC Solid State Technology Association, 2020.

[123] JEDEC Solid State Technology Association. *Temperature, Bias, and Operating Life*. Standard JESD22-A108G. Arlington, USA: JEDEC Solid State Technology Association, 2022.

[124] JEDEC Solid State Technology Association. *Preconditioning of Nonhermetic Surface Mount Devices Prior to Reliability Testing*. Standard JESD22-A113I. Arlington, USA: JEDEC Solid State Technology Association, 2020.

[125] *AEC-Q102 Rev.A: Failure Mechanism Based Stress Test Qualification for Discrete Optoelectronic Semiconductors in Automotive Applications*. Tech. rep. USA: Automotive Electronics Council, Apr. 2020, p. 61.

[126] Adolf Fick. "Ueber Diffusion." In: *Annalen der Physik* 170.1 (1855), pp. 59–86. ISSN: 1521-3889. DOI: 10.1002/andp.18551700105.

[127] Xuejun Fan. "Moisture Related Reliability in Electronic Packaging." In: *The 58th Electronic Components and Technology Conference (ECTC)*. Lamar University, Texas, USA, May 2008.

[128] Mark D. Placette, Xuejun Fan, Jie-Hua Zhao, and Darvin Edwards. "A Dual Stage Model of Anomalous Moisture Diffusion and Desorption in Epoxy Mold Compounds." In: *2011 12th Intl. Conf. on Thermal, Mechanical & Multi-Physics Simulation and Experiments in Microelectronics and Microsystems*. Apr. 2011, pp. 1/8–8/8. DOI: 10.1109/ESIME.2011.5765824.

[129] H. Shirangi, J. Auersperg, M. Koyuncu, H. Walter, W. H. Muller, and B. Michel. "Characterization of Dual-Stage Moisture Diffusion, Residual Moisture Content and Hygroscopic Swelling of Epoxy Molding Compounds." In: *EuroSimE 2008 - International Conference on Thermal, Mechanical and Multi-Physics Simulation and Experiments in Microelectronics and Micro-Systems*. Apr. 2008, pp. 1–8. DOI: 10.1109/ESIME.2008.4525009.

[130] K. M. B. Jansen, M. F. Zhang, L. J. Ernst, D. K. Vu, and L. Weiss. "Effect of Temperature and Humidity on Moisture Diffusion in an Epoxy Moulding Compound Material." In: *Microelectronics Reliability* 107 (Apr. 2020), p. 113596. ISSN: 0026-2714. DOI: 10.1016/j.microrel.2020.113596.

[131] X. J. Fan, S. W. R. Lee, and Q. Han. "Experimental Investigations and Model Study of Moisture Behaviors in Polymeric Materials." In: *Microelectronics Reliability*. Thermal, Mechanical and Multi-Physics Simulation and Experiments in Micro-Electronics and Micro-Systems (EuroSimE 2008 49.8 (Aug. 2009), pp. 861–871. ISSN: 0026-2714. DOI: 10.1016/j.microrel.2009.03.006.

[132] Derek A. Pratt, Keri A. Tallman, and Ned A. Porter. "Free Radical Oxidation of Polyunsaturated Lipids: New Mechanistic Insights and the Development of Peroxyl Radical Clocks." In: *Accounts of Chemical Research* 44.6 (June 2011), pp. 458–467. ISSN: 0001-4842, 1520-4898. DOI: 10.1021/ar200024c.

[133] Leesa M. Smith, Heather M. Aitken, and Michelle L. Coote. "The Fate of the Peroxyl Radical in Autoxidation: How Does Polymer Degradation Really Occur?" In: *Accounts of Chemical Research* 51.9 (Sept. 2018), pp. 2006–2013. ISSN: 0001-4842, 1520-4898. DOI: 10.1021/acs.accounts.8b00250.

[134] Jon K. West. "Theoretical Analysis of Hydrolysis of Polydimethylsiloxane (PDMS)." In: *Journal of Biomedical Materials Research* 35.4 (1997), pp. 505–511. ISSN: 1097-4636. DOI: 10.1002/(SICI)1097-4636(19970615)35:4<505::AID-JBM10>3.0.CO;2-A.

[135] Moon-Hwan Chang, Diganta Das, P. V. Varde, and Michael Pecht. "Light Emitting Diodes Reliability Review." In: *Microelectronics Reliability*. Reliability of High-Power LED Packaging and Assembly 52.5 (May 2012), pp. 762–782. ISSN: 0026-2714. DOI: 10.1016/j.microrel.2011.07.063.

[136] M. La Grassa, M. Meneghini, C. De Santi, M. Mandurrino, M. Goano, F. Bertazzi, R. Zeisel, B. Galler, G. Meneghesso, and E. Zanoni. "Ageing of InGaN-based LEDs: Effects on Internal Quantum Efficiency and Role of Defects." In: *Microelectronics Reliability*. Proceedings of the 26th European Symposium on Reliability of Electron Devices, Failure Physics and Analysis 55.9 (Aug. 2015), pp. 1775–1778. ISSN: 0026-2714. DOI: 10.1016/j.microrel.2015.06.103.

[137] X. Li and J. J. Coleman. "Time-dependent Study of Low Energy Electron Beam Irradiation of Mg-doped GaN Grown by Metalorganic Chemical Vapor Deposition." In: *Applied Physics Letters* 69.11 (Sept. 1996), pp. 1605–1607. ISSN: 0003-6951. DOI: 10.1063/1.117045.

[138] C. H. Seager, S. M. Myers, A. F. Wright, D. D. Koleske, and A. A. Allerman. "Drift, Diffusion, and Trapping of Hydrogen in p-Type GaN." In: *Journal of Applied Physics* 92.12 (Dec. 2002), pp. 7246–7252. ISSN: 0021-8979. DOI: 10.1063/1.1520719.

[139] A. Sedhain, J. Li, J. Y. Lin, and H. X. Jiang. "Nature of Deep Center Emissions in GaN." In: *Applied Physics Letters* 96.15 (Apr. 2010), p. 151902. ISSN: 0003-6951. DOI: 10.1063/1.3389497.

[140] D. O. Demchenko, I. C. Diallo, and M. A. Reshchikov. "Yellow Luminescence of Gallium Nitride Generated by Carbon Defect Complexes." In: *Physical Review Letters* 110.8 (Feb. 2013), p. 087404. DOI: 10.1103/PhysRevLett.110.087404.

[141] Jörg Neugebauer and Chris G. Van de Walle. "Gallium Vacancies and the Yellow Luminescence in GaN." In: *Applied Physics Letters* 69.4 (July 1996), pp. 503–505. ISSN: 0003-6951. DOI: 10.1063/1.117767.

[142] J. L. Lyons, A. Janotti, and C. G. Van de Walle. "Effects of Carbon on the Electrical and Optical Properties of InN, GaN, and AlN." In: *Physical Review B* 89.3 (Jan. 2014), p. 035204. DOI: 10.1103/PhysRevB.89.035204.

[143] J. L. Lyons, A. Janotti, and C. G. Van de Walle. "Carbon Impurities and the Yellow Luminescence in GaN." In: *Applied Physics Letters* 97.15 (Oct. 2010), p. 152108. ISSN: 0003-6951. DOI: 10.1063/1.3492841.

[144] P. Kamyczek, E. Placzek-Popko, Vl. Kolkovsky, S. Grzanka, and R. Czernecki. "A Deep Acceptor Defect Responsible for the Yellow Luminescence in GaN and AlGaN." In: *Journal of Applied Physics* 111.11 (June 2012), p. 113105. ISSN: 0021-8979. DOI: 10.1063/1.4725484.

[145] M. Auf der Maur, B. Galler, I. Pietzonka, M. Strassburg, H. Lugauer, and A. Di Carlo. "Trap-Assisted Tunneling in InGaN/GaN Single-Quantum-Well Light-Emitting Diodes." In: *Applied Physics Letters* 105.13 (Sept. 2014), p. 133504. ISSN: 0003-6951. DOI: 10.1063/1.4896970.

[146] Marco Mandurrino, Giovanni Verzellesi, Michele Goano, Marco Vallone, Francesco Bertazzi, Giovanni Ghione, Matteo Meneghini, Gaudenzio Meneghesso, and Enrico Zanoni. "Physics-Based Modeling and Experimental Implications of Trap-Assisted Tunneling in InGaN/GaN Light-Emitting Diodes." In: *physica status solidi (a)* 212.5 (2015), pp. 947–953. ISSN: 1862-6319. DOI: 10.1002/pssa.201431743.

[147] Kenji Orita, Matteo Meneghini, Hiroshi Ohno, Nicola Trivellin, Norio Ikedo, Shinichi Takigawa, Masaaki Yuri, Tsuyoshi Tanaka, Enrico Zanoni, and Gaudenzio Meneghesso. "Analysis of Diffusion-Related Gradual Degradation of InGaN-Based Laser Diodes." In: *IEEE Journal of Quantum Electronics* 48.9 (Sept. 2012), pp. 1169–1176. ISSN: 1558-1713. DOI: 10.1109/JQE.2012.2203795.

[148] Hyunsoo Kim, Hyundoek Yang, Chul Huh, Sang-Woo Kim, Seong-Ju Park, and Hyunsang Hwang. "Electromigration-Induced Failure of GaN Multi-Quantum Well Light Emitting Diode." In: *Electronics Letters* 36.10 (May 2000), pp. 908–910. ISSN: 1350-911X. DOI: 10.1049/el:20000657.

[149] Chin-Yuan Hsu, Wen-How Lan, and YewChung Sermon Wu. "Effect of Thermal Annealing of Ni/Au Ohmic Contact on the Leakage Current of GaN Based Light Emitting Diodes." In: *Applied Physics Letters* 83.12 (Sept. 2003), pp. 2447–2449. ISSN: 0003-6951. DOI: 10.1063/1.1601306.

[150] D.L. Barton, J. Zeller, B.S. Phillips, Pei-Chih Chiu, S. Askar, Dong-Seung Lee, M. Osinski, and K.J. Malloy. "Degradation of Blue AlGaN/InGaN/GaN LEDs Subjected to High Current Pulses." In: *Proceedings of 1995 IEEE International Reliability Physics Symposium*. Apr. 1995, pp. 191–199. DOI: 10.1109/RELPHY.1995.513674.

[151] Daniel L. Barton, Marek Osinski, Piotr Perlin, Petr G. Eliseev, and Jinhyun Lee. "Single-Quantum Well InGaN Green Light Emitting Diode Degradation under High Electrical Stress." In: *Microelectronics Reliability* 39.8 (Aug. 1999), pp. 1219–1227. ISSN: 0026-2714. DOI: 10.1016/S0026-2714(99)00010-4.

[152] D.L. Barton and M. Osinski. "Life Tests and Failure Mechanisms of GaN-AlGaN-InGaN Light Emitting Diodes." In: *Conference Proceedings. LEOS'98. 11th Annual Meeting. IEEE Lasers and Electro-Optics Society 1998 Annual Meeting (Cat. No.98CH36243)*. Vol. 2. Dec. 1998, 440–441 vol.2. DOI: 10.1109/LEOS.1998.739803.

[153] A. Sarua, S. Rajasingam, M. Kuball, C. Younes, B. Yavich, and W.n. Wang. "High Temperature Annealing of AlGaN: Stress and Composition Changes." In: *physica status solidi (c)* n/a.1 (2003), pp. 568–571. ISSN: 1610-1642. DOI: 10.1002/pssc.200390115.

[154] G. Meneghesso, S. Levada, E. Zanoni, S. Podda, G. Mura, M. Vanzi, A. Cavallini, A. Castaldini, S. Du, and I. Eliashevich. "Failure Modes and Mechanisms of DC-Aged GaN LEDs." In: *physica status solidi (a)* 194.2 (2002), pp. 389–392. ISSN: 1521-396X. DOI: 10.1002/1521-396X(200212)194:2<389::AID-PSSA389>3.0.CO;2-O.

[155] Adam H. Blake et al. "InGaN/GaN Multiple-Quantum-Well Light-Emitting Diodes Grown on Si(111) Substrates with ZrB2(0001) Buffer Layers." In: *Journal of Applied Physics* 111.3 (Feb. 2012), p. 033107. ISSN: 0021-8979. DOI: 10.1063/1.3684557.

[156] E. Feltin, B. Beaumont, M. Laügt, P. de Mierry, P. Vennéguès, M. Leroux, and P. Gibart. "Crack-Free Thick GaN Layers on Silicon (111) by Metalorganic Vapor Phase Epitaxy." In: *physica status solidi (a)* 188.2 (2001), pp. 531–535. ISSN: 1521-396X. DOI: 10.1002/1521-396X(200112)188:2<531::AID-PSSA531>3.0.CO;2-V.

[157] Yingnan Huang, Jianxun Liu, Xiujian Sun, Xiaoning Zhan, Qian Sun, Hongwei Gao, Meixin Feng, Yu Zhou, and Hui Yang. "High-Quality AlN Grown on Si(111) Substrate by Epitaxial Lateral Overgrowth." In: *Crystals* 13.3 (Mar. 2023), p. 454. ISSN: 2073-4352. DOI: 10.3390/cryst13030454.

[158] Kai Cheng, M. Leys, S. Degroote, M. Germain, and G. Borghs. "High Quality GaN Grown on Silicon(111) Using a SixNy Interlayer by Metal-Organic Vapor Phase Epitaxy." In: *Applied Physics Letters* 92.19 (May 2008), p. 192111. ISSN: 0003-6951. DOI: 10.1063/1.2928224.

[159] JaeWon Lee, Youngjo Tak, Jun-Youn Kim, Hyun-Gi Hong, Suhee Chae, Bokki Min, Hyungsu Jeong, Jinwoo Yoo, Jong-Ryeol Kim, and Youngsoo Park. "Growth of High-Quality InGaN/GaN LED Structures on (111) Si Substrates with Internal Quantum Efficiency Exceeding 50%." In: *Journal of Crystal Growth*. 15th International Conference on Metalorganic Vapor Phase Epitaxy (ICMOVPE-XV) 315.1 (Jan. 2011), pp. 263–266. ISSN: 0022-0248. DOI: 10.1016/j.jcrysgro.2010.08.006.

[160] Kai Cheng, M. Leys, S. Degroote, B. Van Daele, S. Boeykens, J. Derluyn, M. Germain, G. Van Tendeloo, J. Engelen, and G. Borghs. "Flat GaN Epitaxial Layers Grown on Si(111) by Metalorganic Vapor Phase Epitaxy Using Step-Graded AlGaN Intermediate Layers." In: *Journal of Electronic Materials* 35.4 (Apr. 2006), pp. 592–598. ISSN: 1543-186X. DOI: 10.1007/s11664-006-0105-1.

[161] Armin Dadgar, Jürgen Bläsing, Annette Diez, Assadullah Alam, Michael Heuken, and Alois Krost. "Metalorganic Chemical Vapor Phase Epitaxy of Crack-Free GaN on Si (111) Exceeding 1 *M*m in Thickness." In: *Japanese Journal of Applied Physics* 39.11B (Nov. 2000), p. L1183. ISSN: 1347-4065. DOI: 10.1143/JJAP.39.L1183.

[162] A. Strittmatter, A. Krost, M. Straßburg, V. Türck, D. Bimberg, J. Bläsing, and J. Christen. "Low-Pressure Metal Organic Chemical Vapor Deposition of GaN on Silicon(111) Substrates Using an AlAs Nucleation Layer." In: *Applied Physics Letters* 74.9 (Mar. 1999), pp. 1242–1244. ISSN: 0003-6951. DOI: 10.1063/1.123512.

[163] N. P. Kobayashi, J. T. Kobayashi, P. D. Dapkus, W.-J. Choi, A. E. Bond, X. Zhang, and D. H. Rich. "GaN Growth on Si(111) Substrate Using Oxidized AlAs as an Intermediate Layer." In: *Applied Physics Letters* 71.24 (Dec. 1997), pp. 3569–3571. ISSN: 0003-6951. DOI: 10.1063/1.120394.

[164] Lisa Sugiura. "Dislocation Motion in GaN Light-Emitting Devices and Its Effect on Device Lifetime." In: *Journal of Applied Physics* 81.4 (Feb. 1997), pp. 1633–1638. ISSN: 0021-8979. DOI: 10.1063/1.364018.

[165] Guoguang Lu, Shaohua Yang, and Yun Huang. "Analysis on Failure Modes and Mechanisms of LED." In: *2009 8th International Conference on Reliability, Maintainability and Safety*. July 2009, pp. 1237–1241. DOI: 10.1109/ICRMS.2009.5270043.

[166] Lisa Sugiura. "Comparison of Degradation Caused by Dislocation Motion in Compound Semiconductor Light-Emitting Devices." In: *Applied Physics Letters* 70.10 (Mar. 1997), pp. 1317–1319. ISSN: 0003-6951. DOI: 10.1063/1.118523.

[167] X. A. Cao, P. M. Sandvik, S. F. LeBoeuf, and S. D. Arthur. "Defect Generation in InGaN/GaN Light-Emitting Diodes under Forward and Reverse Electrical Stresses." In: *Microelectronics Reliability* 43.12 (Dec. 2003), pp. 1987–1991. ISSN: 0026-2714. DOI: 10.1016/j.microrel.2003.06.001.

[168] G. Meneghesso, S. Levada, R. Pierobon, F. Rampazzo, E. Zanoni, A. Cavallini, A. Castaldini, G. Scamarcio, S. Du, and I. Eliashevich. "Degradation Mechanisms of GaN-based LEDs after Accelerated DC Current Aging." In: *Digest. International Electron Devices Meeting,* Dec. 2002, pp. 103–106. DOI: 10.1109/IEDM.2002.1175789.

[169] Joy Tharian. "Degradation- and Failure Mode Analysis of III-V Nitride Devices." In: *2007 14th International Symposium on the Physical and Failure Analysis of Integrated Circuits*. July 2007, pp. 284–287. DOI: 10.1109/IPFA.2007.4378102.

[170] M. Pavesi, F. Rossi, and E. Zanoni. "Effects of Extreme Dc-Ageing and Electron-Beam Irradiation in InGaN/AlGaN/GaN Light-Emitting Diodes." In: *Semiconductor Science and Technology* 21.2 (Jan. 2006), p. 138. ISSN: 0268-1242. DOI: 10.1088/0268-1242/21/2/006.

[171] Shun-Lien Chuang, A. Ishibashi, S. Kijima, N. Nakayama, M. Ukita, and S. Taniguchi. "Kinetic Model for Degradation of Light-Emitting Diodes." In: *IEEE Journal of Quantum Electronics* 33.6 (June 1997), pp. 970–979. ISSN: 1558-1713. DOI: 10.1109/3.585485.

[172] Takeshi Yanagisawa and Takeshi Kojima. "Long-Term Accelerated Current Operation of White Light-Emitting Diodes." In: *Journal of Luminescence* 114.1 (July 2005), pp. 39–42. ISSN: 0022-2313. DOI: 10.1016/j.jlumin.2004.11.010.

[173] Chang-Chi Pan, Chia-Ming Lee, Jia-Wen Liu, Guan-Ting Chen, and Jen-Inn Chyi. "Luminescence Efficiency of InGaN Multiple-Quantum-Well Ultravioletlight-Emitting Diodes." In: *Applied Physics Letters* 84.25 (June 2004), pp. 5249–5251. ISSN: 0003-6951. DOI: 10.1063/1.1765207.

[174] M. Pavesi, M. Manfredi, G. Salviati, N. Armani, F. Rossi, G. Meneghesso, S. Levada, E. Zanoni, S. Du, and I. Eliashevich. "Optical Evidence of an Electrothermal Degradation of InGaN-based Light-Emitting Diodes during Electrical Stress." In: *Applied Physics Letters* 84.17 (Apr. 2004), pp. 3403–3405. ISSN: 0003-6951. DOI: 10.1063/1.1734682.

[175] Asif Khan, Seongmo Hwang, Jonathan Lowder, Vinod Adivarahan, and Qhalid Fareed. "Reliability Issues in AlGaN Based Deep Ultraviolet Light Emitting Diodes." In: *2009 IEEE International Reliability Physics Symposium*. Apr. 2009, pp. 89–93. DOI: 10.1109/IRPS.2009.5173229.

[176] Osamu Ueda. "Reliability Issues in III–V Compound Semiconductor Devices: Optical Devices and GaAs-based HBTs." In: *Microelectronics Reliability* 39.12 (Dec. 1999), pp. 1839–1855. ISSN: 0026-2714. DOI: 10.1016/S0026-2714(99)00193-6.

[177] A. Uddin, A. C. Wei, and T. G. Andersson. "Study of Degradation Mechanism of Blue Light Emitting Diodes." In: *Thin Solid Films* 483.1 (July 2005), pp. 378–381. ISSN: 0040-6090. DOI: 10.1016/j.tsf.2005.01.018.

[178] M. Pavesi, M. Manfredi, F. Rossi, M. Meneghini, E. Zanoni, U. Zehnder, and U. Strauss. "Temperature Dependence of the Electrical Activity of Localized Defects in InGaN-based Light Emitting Diodes." In: *Applied Physics Letters* 89.4 (July 2006), p. 041917. ISSN: 0003-6951. DOI: 10.1063/1.2240309.

[179] T. Yanagisawa. "The Degradation of GaAlAs Red Light-Emitting Diodes under Continuous and Low-Speed Pulse Operations." In: *Microelectronics Reliability* 38.10 (Oct. 1998), pp. 1627–1630. ISSN: 0026-2714. DOI: 10.1016/S0026-2714(98)00029-8.

[180] T. Hoang, P. LeMinh, J. Holleman, and J. Schmitz. "The Effect of Dislocation Loops on the Light Emission of Silicon LEDs." In: *Proceedings of 35th European Solid-State Device Research Conference, 2005. ESSDERC 2005.* Sept. 2005, pp. 359–362. DOI: 10.1109/ESSDER.2005.1546659.

[181] J. D Wu, C. Y Huang, and C. C Liao. "Fracture Strength Characterization and Failure Analysis of Silicon Dies." In: *Microelectronics Reliability* 43.2 (Feb. 2003), pp. 269–277. ISSN: 0026-2714. DOI: 10.1016/S0026-2714(02)00314-1.

[182] K. S. Kim, M. S. Han, G. M. Yang, C. J. Youn, H. J. Lee, H. K. Cho, and J. Y. Lee. "Codoping Characteristics of Zn with Mg in GaN." In: *Applied Physics Letters* 77.8 (Aug. 2000), pp. 1123–1125. ISSN: 0003-6951. DOI: 10.1063/1.1289494.

[183] K. Köhler, T. Stephan, A. Perona, J. Wiegert, M. Maier, M. Kunzer, and J. Wagner. "Control of the Mg Doping Profile in III-N Light-Emitting Diodes and Its Effect on the Electroluminescence Efficiency." In: *Journal of Applied Physics* 97.10 (May 2005), p. 104914. ISSN: 0021-8979. DOI: 10.1063/1.1901836.

[184] Peter Kozodoy, Steven P. DenBaars, and Umesh K. Mishra. "Depletion Region Effects in Mg-doped GaN." In: *Journal of Applied Physics* 87.2 (Jan. 2000), pp. 770–775. ISSN: 0021-8979. DOI: 10.1063/1.371939.

[185] Qin-Sheng Zhu, H. Nagai, Y. Kawaguchi, K. Hiramatsu, and N. Sawaki. "Effect of Thermal Annealing on Hole Trap Levels in Mg-doped GaN Grown by Metalorganic Vapor Phase Epitaxy." In: *Journal of Vacuum Science & Technology A* 18.1 (Jan. 2000), pp. 261–267. ISSN: 0734-2101. DOI: 10.1116/1.582144.

[186] M. Meneghini, L.R. Trevisanello, S. Levada, G. Meneghesso, G. Tamiazzo, E. Zanoni, T. Zahner, U. Zehnder, V. Harle, and U. Straus. "Failure Mechanisms of Gallium Nitride LEDs Related with Passivation." In: *IEEE InternationalElectron Devices Meeting, 2005. IEDM Technical Digest.* Dec. 2005, 4 pp.–1012. DOI: 10.1109/IEDM.2005.1609534.

[187] G. Meneghesso et al. "Failure Mechanisms of GaN-based LEDs Related with Instabilities in Doping Profile and Deep Levels." In: *2004 IEEE International Reliability Physics Symposium. Proceedings*. Apr. 2004, pp. 474–478. DOI: 10.1109/RELPHY.2004.1315374.

[188] Min-Ki Kwon, Il-Kyu Park, Ja-Yeon Kim, Jeom-Oh Kim, Bongjin Kim, and Seong-Ju Park. "Gradient Doping of Mg in P-Type GaN for High Efficiency InGaN–GaN Ultraviolet Light-Emitting Diode." In: *IEEE Photonics Technology Letters* 19.23 (Dec. 2007), pp. 1880–1882. ISSN: 1941-0174. DOI: 10.1109/LPT.2007.908659.

[189] Oliver Brandt, Hui Yang, Helmar Kostial, and Klaus H. Ploog. "High P-type Conductivity in Cubic GaN/GaAs(113)A by Using Be as the Acceptor and O as the Codopant." In: *Applied Physics Letters* 69.18 (Oct. 1996), pp. 2707–2709. ISSN: 0003-6951. DOI: 10.1063/1.117685.

[190] Xiong Zhang, Soo-Jin Chua, Peng Li, Kok-Boon Chong, and Wen Wang. "Improved Mg-doped GaN Films Grown over a Multilayered Buffer." In: *Applied Physics Letters* 73.13 (Sept. 1998), pp. 1772–1774. ISSN: 0003-6951. DOI: 10.1063/1.122277.

[191] Paola Altieri-Weimar, Arndt Jaeger, Thomas Lutz, Peter Stauss, Klaus Streubel, Klaus Thonke, and Rolf Sauer. "Influence of Doping on the Reliability of AlGaInP LEDs." In: *Journal of Materials Science: Materials in Electronics* 19.1 (Dec. 2008), pp. 338–341. ISSN: 1573-482X. DOI: 10.1007/s10854-008-9575-7.

[192] B. A. Hull, S. E. Mohney, H. S. Venugopalan, and J. C. Ramer. "Influence of Oxygen on the Activation of *p* -Type GaN." In: *Applied Physics Letters* 76.16 (Apr. 2000), pp. 2271–2273. ISSN: 0003-6951, 1077-3118. DOI: 10.1063/1.126318.

[193] Ja-Soon Jang, Seong-Ju Park, and Tae-Yeon Seong. "Metallization Scheme for Highly Low-Resistance, Transparent, and Thermally Stable Ohmic Contacts to p-GaN." In: *Applied Physics Letters* 76.20 (May 2000), pp. 2898–2900. ISSN: 0003-6951. DOI: 10.1063/1.126510.

[194] Shuji Nakamura, Takashi Mukai, Masayuki Senoh Masayuki Senoh, and Naruhito Iwasa Naruhito Iwasa. "Thermal Annealing Effects on P-Type Mg-Doped GaN Films." In: *Japanese Journal of Applied Physics* 31.2B (Feb. 1992), p. L139. ISSN: 1347-4065. DOI: 10.1143/JJAP.31.L139.

[195] Nam Hwang, P.S.R. Naidu, and A. Trigg. "Failure Analysis of Plastic Packaged Optocoupler Light Emitting Diodes." In: *Proceedings of the 5th Electronics Packaging Technology Conference (EPTC 2003)*. Dec. 2003, pp. 346–349. DOI: 10.1109/EPTC.2003.1271543.

[196] Preetpal Singh and Cher Ming Tan. "Degradation Physics of High Power LEDs in Outdoor Environment and the Role of Phosphor in the Degradation Process." In: *Scientific Reports* 6.1 (Apr. 2016), p. 24052. ISSN: 2045-2322. DOI: 10.1038/srep24052.

[197] Bernhard Czerny and Sebastian Schuh. "Fatigue Behavior of Au, Cu and PCC Fine Wire Bond Connections for Power LED Applications." In: *2023 24th International Conference on Thermal, Mechanical and Multi-Physics Simulation and Experiments in Microelectronics and Microsystems (EuroSimE)*. Apr. 2023, pp. 1–5. DOI: 10.1109/EuroSimE56861.2023.10100839.

[198] Yongjun Pan, Fulong Zhu, Xinxin Lin, Fengren Wang, Lang Shi, Yan Kan, Sheng Liu, and Jiajie Fan. "Reliability Prediction of LED Packaging by Fatigue Behavior of Bonding Wire in Power Cycling Accelerated Test." In: *2017 IEEE 19th Electronics Packaging Technology Conference (EPTC)*. Dec. 2017, pp. 1–4. DOI: 10.1109/EPTC.2017.8277431.

[199] Sung-Uk Zhang and Bang Weon Lee. "Fatigue Life Evaluation of Wire Bonds in LED Packages Using Numerical Analysis." In: *Microelectronics Reliability* 54.12 (Dec. 2014), pp. 2853–2859. ISSN: 0026-2714. DOI: 10.1016/j.microrel.2014.07.142.

[200] N. Y. A Shammas. "Present Problems of Power Module Packaging Technology." In: *Microelectronics Reliability* 43.4 (Apr. 2003), pp. 519–527. ISSN: 0026-2714. DOI: 10.1016/S0026-2714(03)00019-2.

[201] Hideo Nakajima. "The Discovery and Acceptance of the Kirkendall Effect: The Result of a Short Research Career." In: *JOM* 49.6 (June 1997), pp. 15–19. ISSN: 1543-1851. DOI: 10.1007/BF02914706.

[202] E. Zakel and H. Reichl. "Au-Sn Bonding Metallurgy of TAB Contacts and Its Influence on the Kirkendall Effect in the Ternary Cu-Au-Sn." In: *IEEE Transactions on Components, Hybrids, and Manufacturing Technology* 16.3 (May 1993), pp. 323–332. ISSN: 1558-3082. DOI: 10.1109/33.232060.

[203] S. Murali, N. Srikanth, and Charles J. Vath. "Effect of Wire Size on the Formation of Intermetallics and Kirkendall Voids on Thermal Aging of Thermosonic Wire Bonds." In: *Materials Letters* 58.25 (Oct. 2004), pp. 3096–3101. ISSN: 0167-577X. DOI: 10.1016/j.matlet.2004.05.070.

[204] Cher Ming Tan and Preetpal Singh. "Time Evolution Degradation Physics in High Power White LEDs Under High Temperature-Humidity Conditions." In: *IEEE Transactions on Device and Materials Reliability* 14.2 (June 2014), pp. 742–750. ISSN: 1558-2574. DOI: 10.1109/TDMR.2014.2318725.

[205] C. D. Breach, Ng Hun Shen, Tee Wai Mun, Teck Kheng Lee, and R. Holliday. "Effects of Moisture on Reliability of Gold and Copper Ball Bonds." In: *2010 12th Electronics Packaging Technology Conference*. Dec. 2010, pp. 44–51. DOI: 10.1109/EPTC.2010.5702603.

[206] C. D. Breach, Tee Wai Mun, Teck Kheng Lee, and R. Holliday. "Moisture Induced Corrosion in Gold and Copper Ball Bonds." In: *2010 34th IEEE/CPMT International Electronic Manufacturing Technology Symposium (IEMT)*. Nov. 2010, pp. 1–11. DOI: 10.1109/IEMT.2010.5746748.

[207] Tim Boettcher et al. "On the Intermetallic Corrosion of Cu-Al Wire Bonds." In: *2010 12th Electronics Packaging Technology Conference*. Singapore: IEEE, Dec. 2010, pp. 585–590. ISBN: 978-1-4244-8560-4 978-1-4244-8562-8. DOI: 10.1109/EPTC.2010.5702706.

[208] Matteo Meneghini, Augusto Tazzoli, Giovanna Mura, Gaudenzio Meneghesso, and Enrico Zanoni. "A Review on the Physical Mechanisms That Limit the Reliability of GaN-Based LEDs." In: *IEEE Transactions on Electron Devices* 57.1 (Jan. 2010), pp. 108–118. ISSN: 1557-9646. DOI: 10.1109/TED.2009.2033649.

[209] Y.K. Su, S.J. Chang, S.C. Wei, Shi-Ming Chen, and Wen-Liang Li. "ESD Engineering of Nitride-Based LEDs." In: *IEEE Transactions on Device and Materials Reliability* 5.2 (June 2005), pp. 277–281. ISSN: 1558-2574. DOI: 10.1109/TDMR.2005.847197.

[210] Matteo Meneghini et al. "A Study of the Failure of GaN-based LEDs Submitted to Reverse-Bias Stress and ESD Events." In: *2010 IEEE International Reliability Physics Symposium*. May 2010, pp. 522–527. DOI: 10.1109/IRPS.2010.5488776.

[211] Sang-Mook Kim, Hwa Sub Oh, Jong Hyeob Baek, Tae-Young Park, and Gun Young Jung. "Negative-Voltage Electrostatic Discharge Characteristics of Blue Light-Emitting Diodes Using an Extended n-Electrode onto Plasma Treated p-GaN." In: *Applied Physics Express* 4.7 (June 2011), p. 072102. ISSN: 1882-0786. DOI: 10.1143/APEX.4.072102.

[212] T.C. Wen, S.J. Chang, C.T. Lee, W.C. Lai, and J.K. Sheu. "Nitride-Based LEDs with Modulation-Doped Al/Sub 0.12/Ga/Sub 0.88/N-GaN Superlattice Structures." In: *IEEE Transactions on Electron Devices* 51.10 (Oct. 2004), pp. 1743–1746. ISSN: 1557-9646. DOI: 10.1109/TED.2004.835985.

[213] G. Meneghesso, A. Chini, A. Maschietto, E. Zanoni, P. Malberti, and M. Ciappa. "Electrostatic Discharge and Electrical Overstress on GaN/InGaN Light Emitting Diodes." In: *2001 Electrical Overstress/Electrostatic Discharge Symposium*. Sept. 2001, pp. 247–252.

[214] C.M. Tsai, J.K. Sheu, P.T. Wang, W.C. Lai, S.C. Shei, S.J. Chang, C.H. Kuo, C.W. Kuo, and Y.K. Su. "High Efficiency and Improved ESD Characteristics of GaN-based LEDs with Naturally Textured Surface Grown by MOCVD." In: *IEEE Photonics Technology Letters* 18.11 (June 2006), pp. 1213–1215. ISSN: 1941-0174. DOI: 10.1109/LPT.2006.875063.

[215] Chuanyu Jia, Cantao Zhong, Tongjun Yu, Zhe Wang, Yuzhen Tong, and Guoyi Zhang. "Improvement of Electrostatic Discharge Characteristics of InGaN/GaN MQWs Light-Emitting Diodes by Inserting an N+-InGaN Electron Injection Layer and a p-InGaN/GaN Hole Injection Layer." In: *Semiconductor Science and Technology* 27.6 (May 2012), p. 065008. ISSN: 0268-1242. DOI: 10.1088/0268-1242/27/6/065008.

[216] Soo-Kun Jeon, Jae-Gab Lee, Eun-Hyun Park, Jin Jang, Jae-Gu Lim, Seo-Kun Kim, and Joong-Seo Park. "The Effect of the Internal Capacitance of InGaN-light Emitting Diode on the Electrostatic Discharge Properties." In: *Applied Physics Letters* 94.13 (Apr. 2009), p. 131106. ISSN: 0003-6951. DOI: 10.1063/1.3114974.

[217] Panpan Li, Hongjian Li, Yongbing Zhao, Junjie Kang, Zhicong Li, Zhiqiang Liu, Xiaoyan Yi, Jinmin Li, and Guohong Wang. "Excellent ESD Resistance Property of InGaN LEDs With Enhanced Internal Capacitance." In: *IEEE Photonics Technology Letters* 27.19 (Oct. 2015), pp. 2004–2006. ISSN: 1941-0174. DOI: 10.1109/LPT.2015.2448418.

[218] Fugen Wu, Wei Zhao, Shaohua Yang, and Chunhua Zhang. "Failure Modes and Failure Analysis of White LEDs." In: *2009 9th International Conference on Electronic Measurement & Instruments*. Aug. 2009, pp. 4–978–4–981. DOI: 10.1109/ICEMI.2009.5274756.

[219] M. Dammann, A. Leuther, F. Benkhelifa, T. Feltgen, and W. Jantz. "Reliability and Degradation Mechanism of AlGaAs/InGaAs and InAlAs/InGaAs HEMTs." In: *physica status solidi (a)* 195.1 (2003), pp. 81–86. ISSN: 1521-396X. DOI: 10.1002/pssa.200306303.

[220] Matteo Meneghini, Lorenzo-Roberto Trevisanello, Ulrich Zehnder, Gaudenzio Meneghesso, and Enrico Zanoni. "Reversible Degradation of Ohmic Contacts on P-GaN for Application in High-Brightness LEDs." In: *IEEE Transactions on Electron Devices* 54.12 (Dec. 2007), pp. 3245–3251. ISSN: 1557-9646. DOI: 10.1109/TED.2007.908900.

[221] Jae Kyoung Mun, Jong-Lam Lee, Haecheon Kim, Byung-Taek Lee, Jae Jin Lee, and Kwang-Eui Pyun. "Degradation Mechanism of GaAs MESFETs." In: *Microelectronics Reliability* 38.1 (Feb. 1998), pp. 171–178. ISSN: 0026-2714. DOI: 10.1016/S0026-2714(97)00067-X.

[222] S.J. Chang, C.H. Chen, Y.K. Su, J.K. Sheu, W.C. Lai, J.M. Tsai, C.H. Liu, and S.C. Chen. "Improved ESD Protection by Combining InGaN-GaN MQW LEDs with GaN Schottky Diodes." In: *IEEE Electron Device Letters* 24.3 (Mar. 2003), pp. 129–131. ISSN: 1558-0563. DOI: 10.1109/LED.2003.809043.

[223] P. Jacob, A. Kunz, and G. Nicoletti. "Reliability and Wearout Characterisation of LEDs." In: *Microelectronics Reliability*. Proceedings of the 17th European Symposium on Reliability of Electron Devices, Failure Physics and Analysis. Wuppertal, Germany 3rd–6th October 2006 46.9 (Sept. 2006), pp. 1711–1714. ISSN: 0026-2714. DOI: 10.1016/j.microrel.2006.07.048.

[224] Donagh O'Mahony, Walter Zimmerman, Sinje Steffen, Just Hilgarth, Pleun Maaskant, Ravin Ginige, Liam Lewis, Benoit Lambert, and Brian Corbett. "Free-Standing Gallium Nitride Schottky Diode Characteristics and Stability in a High-Temperature Environment." In: *Semiconductor Science and Technology* 24.12 (Nov. 2009), p. 125008. ISSN: 0268-1242. DOI: 10.1088/0268-1242/24/12/125008.

[225] Shih-Chang Shei, Jinn-Kong Sheu, and Chien-Fu Shen. "Improved Reliability and ESD Characteristics of Flip-Chip GaN-Based LEDs With Internal Inverse-Parallel Protection Diodes." In: *IEEE Electron Device Letters* 28.5 (May 2007), pp. 346–349. ISSN: 1558-0563. DOI: 10.1109/LED.2007.895428.

[226] G. Meneghesso, S. Levada, E. Zanoni, G. Scamarcio, G. Mura, S. Podda, M. Vanzi, S. Du, and I. Eliashevich. "Reliability of Visible GaN LEDs in Plastic Package." In: *Microelectronics Reliability*. 14th European Symposium on Reliability of Electron Devices, Failure Physics and Analysis 43.9 (Sept. 2003), pp. 1737–1742. ISSN: 0026-2714. DOI: 10.1016/S0026-2714(03)00289-0.

[227] M. Meneghini, L. Trevisanello, C. Sanna, G. Mura, M. Vanzi, G. Meneghesso, and E. Zanoni. "High Temperature Electro-Optical Degradation of InGaN/GaN HBLEDs." In: *Microelectronics Reliability*. 18th European Symposium on Reliability of Electron Devices, Failure Physics and Analysis 47.9 (Sept. 2007), pp. 1625–1629. ISSN: 0026-2714. DOI: 10.1016/j.microrel.2007.07.081.

[228] Longzao Zhou, Bing An, Yiping Wu, and Shunhong Liu. "Analysis of Delamination and Darkening in High Power LED Packaging." In: *2009 16th IEEE International Symposium on the Physical and Failure Analysis of Integrated Circuits*. July 2009, pp. 656–660. DOI: 10.1109/IPFA.2009.5232549.

[229] Lorenzo Trevisanello, Matteo Meneghini, Giovanna Mura, Massimo Vanzi, Maura Pavesi, Gaudenzio Meneghesso, and Enrico Zanoni. "Accelerated Life Test of High Brightness Light Emitting Diodes." In: *IEEE Transactions on Device and Materials Reliability* 8.2 (June 2008), pp. 304–311. ISSN: 1558-2574. DOI: 10.1109/TDMR.2008.919596.

[230] Jianlin Huang, Dušan S. Golubović, Sau Koh, Daoguo Yang, Xiupeng Li, Xuejun Fan, and G. Q. Zhang. "Degradation Mechanisms of Mid-Power White-Light LEDs Under High-Temperature–Humidity Conditions." In: *IEEE Transactions on Device and Materials Reliability* 15.2 (June 2015), pp. 220–228. ISSN: 1558-2574. DOI: 10.1109/TDMR.2015.2418345.

[231] Jianlin Huang, Dušan S. Golubović, Sau Koh, Daoguo Yang, Xiupeng Li, Xuejun Fan, and G. Q. Zhang. "Degradation Modeling of Mid-Power White-Light LEDs by Using Wiener Process." In: *Optics Express* 23.15 (July 2015), A966–A978. ISSN: 1094-4087. DOI: 10.1364/OE.23.00A966.

[232] Hailin Wu, Lin Zhou, Haimei Luo, Wenpeng Xiao, Minggao Cao, Yimin Hu, Gang Jing, and Yan Liu. "Research on Failure Mechanism of the Phosphors and Sealants for White Light Emitting Diode Package." In: *2016 17th International Conference on Electronic Packaging Technology (ICEPT)*. Aug. 2016, pp. 1297–1300. DOI: 10.1109/ICEPT.2016.7583361.

[233] P. McCluskey, K. Mensah, C. O'Connor, F. Lilie, A. Gallo, and J. Fink. "Reliability of Commercial Plastic Encapsulated Microelectronics at Temperatures from 125/Spl Deg/C to 300/Spl Deg/C." In: *HITEN 99. Third European Conference on High Temperature Electronics. (IEEE Cat. No.99EX372)*. July 1999, pp. 17–24. DOI: 10.1109/HITEN.1999.827342.

[234] Patrick McCluskey, Kofi Mensah, Casey O'Connor, and Anthony Gallo. "Reliable Use of Commercial Technology in High Temperature Environments." In: *Microelectronics Reliability*. Reliability of Electron Devices, Failure Physics and Analysis 40.8 (Aug. 2000), pp. 1671–1678. ISSN: 0026-2714. DOI: 10.1016/S0026-2714(00)00188-8.

[235] Wei Chen, Ye Chen, Yixing Cao, Zhen Cui, Xuejun Fan, Guoqi Zhang, and Jiajie Fan. "Sulfur-Rich Ageing Mechanism of Silicone Encapsulant Used in LED Packaging: An Experimental and Molecular Dynamic Simulation Study." In: *Frontiers in Materials* 9 (2022). ISSN: 2296-8016.

[236] G. Mura, G. Cassanelli, F. Fantini, and M. Vanzi. "Sulfur-Contamination of High Power White LED." In: *Microelectronics Reliability*. 19th European Symposium on Reliability of Electron Devices, Failure Physics and Analysis (ESREF 2008) 48.8 (Aug. 2008), pp. 1208–1211. ISSN: 0026-2714. DOI: 10.1016/j.microrel.2008.07.005.

[237] So-Ra Gang, Deokgi Kim, Sang-Mook Kim, Nam Hwang, and Kwang-Cheol Lee. "Improvement in the Moisture Stability of CaS:Eu Phosphor Applied in Light-Emitting Diodes by Titania Surface Coating." In: *Microelectronics Reliability*. SPECIAL ISSUE 23rd EUROPEAN SYMPOSIUM ON THE RELIABILITY OF ELECTRON DEVICES, FAILURE PHYSICS AND ANALYSIS 52.9 (Sept. 2012), pp. 2174–2179. ISSN: 0026-2714. DOI: 10.1016/j.microrel.2012.06.142.

[238] Anjan N. Padmasali and Savitha G. Kini. "A Lifetime Performance Analysis of LED Luminaires Under Real-Operation Profiles." In: *IEEE Transactions on Electron Devices* 67.1 (Jan. 2020), pp. 146–153. ISSN: 1557-9646. DOI: 10.1109/TED.2019.2950467.

[239] Jui Hung Yuan, Tung Han Chuang, and Ju Hui Chuang. "Lumen Maintenance of Ternary Ag-Alloy Wire Bonded LED Package after Reliability Tests." In: *Materials Science Forum* 1003 (July 2020), pp. 275–280. ISSN: 1662-9752. DOI: 10.4028/www.scientific.net/MSF.1003.275.

[240] O.L. Vargas, S.B. Valdez, M.L. Veleva, K.R. Zlatev, W.M. Schorr, and G.J. Terrazas. "The Corrosion of Silver in Indoor Conditions of an Assembly Process in the Microelectronics Industry." In: *Anti-Corrosion Methods and Materials* 56.4 (Jan. 2009), pp. 218–225. ISSN: 0003-5599. DOI: 10.1108/00035590910969347.

[241] J. Farmer, N. Thomas, W. Siekhaus, H. Gregg, A. Erlandson, C. Marshall, E. Honea, S. Payne, T. Parham, and L. Chase. *Atmospheric Tarnishing of Silver-Plated Laser Mirrors*. Tech. rep. UCRL-ID-128599. Lawrence Livermore National Lab. (LLNL), Livermore, CA (United States), Oct. 1997. DOI: 10.2172/574529.

[242] A. Herrmann, S.J.F. Erich, L.G.J. v.d. Ven, W.D. van Driel, M. van Soestbergen, A. Mavinkurve, F. De Buyl, and O.C.G. Adan. "Understanding the Transport Phenomena Leading to Tarnishing of the Reflecting Silver Layer Causing Reduced Light Output of LEDs." In: *2017 18th International Conference on Thermal, Mechanical and Multi-Physics Simulation and Experiments in Microelectronics and Microsystems (EuroSimE)*. Apr. 2017, pp. 1–6. DOI: 10.1109/EuroSimE.2017.7926238.

[243] Chang Jiang Yang, Cheng Hao Liang, and Xia Liu. "Tarnishing of Silver in Environments with Sulphur Contamination." In: *Anti-Corrosion Methods and Materials* 54.1 (Jan. 2007), pp. 21–26. ISSN: 0003-5599. DOI: 10.1108/00035590710717357.

[244] Jun'ichi Sakai, Masataka Omoda, and Yuichi Ishikawa. "Corrosion of Silver by Outgassing from Rubber." In: *Corrosion Science and Technology* 7.2 (2008), pp. 130–133. ISSN: 1598-6462.

[245] C. De Santi, A. Caria, F. Piva, G. Meneghesso, E. Zanoni, and M. Meneghini. "Chapter 7 - Degradation Mechanisms of InGaN Visible LEDs and AlGaN UV LEDs." In: *Reliability of Semiconductor Lasers and Optoelectronic Devices*. Ed. by Robert W. Herrick and Osamu Ueda. Woodhead Publishing Series in Electronic and Optical Materials. Woodhead Publishing, Jan. 2021, pp. 273–312. ISBN: 978-0-12-819254-2. DOI: 10.1016/B978-0-12-819254-2.00001-1.

[246] S. Koh, Willem Van Driel, and G.Q. Zhang. "Degradation of Epoxy Lens Materials in LED Systems." In: *2011 12th Intl. Conf. on Thermal, Mechanical & Multi-Physics Simulation and Experiments in Microelectronics and Microsystems*. Apr. 2011, pp. 1/5–5/5. DOI: 10.1109/ESIME.2011.5765850.

[247] Jan-Chan Huang, Ying-Po Chu, Ming Wei, and Rudolph D. Deanin. "Comparison of Epoxy Resins for Applications in Light-Emitting Diodes." In: *Advances in Polymer Technology* 23.4 (2004), pp. 298–306. ISSN: 1098-2329. DOI: 10.1002/adv.20018.

[248] Hsun-Tien Li, Chia-Wen Hsu, and Kai-Chi Chen. "The Study of Thermal Properties and Thermal Resistant Behaviors of Siloxane-Modified LED Transparent Encapsulant." In: *2007 International Microsystems, Packaging, Assembly and Circuits Technology*. Oct. 2007, pp. 246–249. DOI: 10.1109/IMPACT.2007.4433609.

[249] Eunjin Jung, Min Soo Kim, and Hyunsoo Kim. "Analysis of Contributing Factors for Determining the Reliability Characteristics of GaN-Based White Light-Emitting Diodes With Dual Degradation Kinetics." In: *IEEE Transactions on Electron Devices* 60.1 (Jan. 2013), pp. 186–191. ISSN: 1557-9646. DOI: 10.1109/TED.2012.2226039.

[250] Eduardo Nogueira, Manuel Vázquez, and Carlos Algora. "Accelerated Life Testing in Epoxy Packaged High Luminosity Light Emitting Diodes." In: *Journal of Electronic Packaging* 133.3 (Sept. 2011). ISSN: 1043-7398. DOI: 10.1115/1.4004659.

[251] Danuta Kotnarowska. "Influence of Ultraviolet Radiation and Aggressive Media on Epoxy Coating Degradation." In: *Progress in Organic Coatings* 37.3 (Dec. 1999), pp. 149–159. ISSN: 0300-9440. DOI: 10.1016/S0300-9440(99)00070-3.

[252] Jane L. Down. "The Yellowing of Epoxy Resin Adhesives: Report on Natural Dark Aging." In: *Studies in Conservation* 29.2 (1984), pp. 63–76. ISSN: 0039-3630. DOI: 10.2307/1506076. JSTOR: 1506076.

[253] Jane L. Down. "The Yellowing of Epoxy Resin Adhesives: Report on High-Intensity Light Aging." In: *Studies in Conservation* 31.4 (1986), pp. 159–170. ISSN: 0039-3630. DOI: 10.2307/1506247. JSTOR: 1506247.

[254] Jong Kyu Kim, Hong Luo, Eric Fred Schubert, Jaehee Cho, Cheolsoo Sone, and Yongjo Park. "Strongly Enhanced Phosphor Efficiency in GaInN White Light-Emitting Diodes Using Remote Phosphor Configuration and Diffuse Reflector Cup." In: *Japanese Journal of Applied Physics* 44.5L (May 2005), p. L649. ISSN: 1347-4065. DOI: 10.1143/JJAP.44.L649.

[255] Hong Luo, Jong Kyu Kim, E. Fred Schubert, Jaehee Cho, Cheolsoo Sone, and Yongjo Park. "Analysis of High-Power Packages for Phosphor-Based White-Light-Emitting Diodes." In: *Applied Physics Letters* 86.24 (June 2005), p. 243505. ISSN: 0003-6951. DOI: 10.1063/1.1949282.

[256] Matteo Meneghini, Lorenzo-Roberto Trevisanello, Gaudenzio Meneghesso, and Enrico Zanoni. "A Review on the Reliability of GaN-Based LEDs." In: *IEEE Transactions on Device and Materials Reliability* 8.2 (June 2008), pp. 323–331. ISSN: 1558-2574. DOI: 10.1109/TDMR.2008.921527.

[257] N. Narendran, Y. Gu, J. P. Freyssinier, H. Yu, and L. Deng. "Solid-State Lighting: Failure Analysis of White LEDs." In: *Journal of Crystal Growth*. ICMAT 2003, Symposium H, Compound Semiconductors in Electronic an d Optoelectronic Applications 268.3 (Aug. 2004), pp. 449–456. ISSN: 0022-0248. DOI: 10.1016/j.jcrysgro.2004.04.071.

[258] N. Narendran, Y. Gu, J. P. Freyssinier-Nova, and Y. Zhu. "Extracting Phosphor-Scattered Photons to Improve White LED Efficiency." In: *physica status solidi (a)* 202.6 (2005), R60–R62. ISSN: 1862-6319. DOI: 10.1002/pssa.200510015.

[259] Nguyen T. Tran and Frank G. Shi. "Simulation and Experimental Studies of Phosphor Concentration and Thickness for Phosphor-Based White Light-Emitting-Diodes." In: *2007 International Microsystems, Packaging, Assembly and Circuits Technology*. Oct. 2007, pp. 255–257. DOI: 10.1109/IMPACT.2007.4433611.

[260] Hans de Brouwer, Jos van den Bogerd, and James Hoover. "Color Stability of Polycarbonate for Optical Applications." In: *European Polymer Journal* 71 (Oct. 2015), pp. 558–566. ISSN: 0014-3057. DOI: 10.1016/j.eurpolymj.2015.08.031.

[261] M. Yazdan Mehr, W. D. van Driel, K. M. B. Jansen, P. Deeben, M. Boutelje, and G. Q. Zhang. "Photodegradation of Bisphenol A Polycarbonate under Blue Light Radiation and Its Effect on Optical Properties." In: *Optical Materials* 35.3 (Jan. 2013), pp. 504–508. ISSN: 0925-3467. DOI: 10.1016/j.optmat.2012.10.001.

[262] M. Yazdan Mehr, W. D. van Driel, K. M. B. Jansen, P. Deeben, and G. Q. Zhang. "Lifetime Assessment of Bisphenol-A Polycarbonate (BPA-PC) Plastic Lens, Used in LED-based Products." In: *Microelectronics Reliability* 54.1 (Jan. 2014), pp. 138–142. ISSN: 0026-2714. DOI: 10.1016/j.microrel.2013.09.009.

[263] Moritz Hemmerich, Jörg Meyer, and Frank Walther. "Advanced Test Setup for Accelerated Aging of Plastics by Visible LED Radiation." In: *Materials* 13.19 (Sept. 2020), p. 4261. ISSN: 1996-1944. DOI: 10.3390/ma13194261.

[264] I. B. Rufus, H. Shah, and C. E. Hoyle. "Identification of Fluorescent Products Produced by the Thermal Treatment of Bisphenol-A-based Polycarbonate." In: *Journal of Applied Polymer Science* 51.9 (1994), pp. 1549–1558. ISSN: 1097-4628. DOI: 10.1002/app.1994.070510904.

[265] D. T. Clark and H. S. Munro. "Surface and Bulk Aspects of the Natural and Artificial Photo-Ageing of Bisphenol A Polycarbonate as Revealed by ESCA and Difference UV Spectroscopy." In: *Polymer Degradation and Stability* 8.4 (Jan. 1984), pp. 195–211. ISSN: 0141-3910. DOI: 10.1016/0141-3910(84)90018-1.

[266] A. Davis and J. H. Golden. "Thermal Rearrangement of Diphenyl Carbonate." In: *Journal of the Chemical Society B: Physical Organic* (1968), p. 40. ISSN: 0045-6470. DOI: 10.1039/j29680000040.

[267] I. C. McNeill and A. Rincon. "Degradation Studies of Some Polyesters and Polycarbonates—8. Bisphenol A Polycarbonate." In: *Polymer Degradation and Stability* 31.2 (Jan. 1991), pp. 163–180. ISSN: 0141-3910. DOI: 10.1016/0141-3910(91)90072-Y.

[268] Lieng-Huang Lee. "Mechanisms of Thermal Degradation of Phenolic Condensation Polymers. I. Studies on the Thermal Stability of Polycarbonate." In: *Journal of Polymer Science Part A: General Papers* 2.6 (1964), pp. 2859–2873. ISSN: 1542-6246. DOI: 10.1002/pol.1964.100020635.

[269] Alok Garg, Tejasvi Singhania, Ashutosh Singh, Shilpa Sharma, Sonam Rani, Ananya Neogy, Shri Ram Yadav, Vikas Kumar Sangal, and Neha Garg. "Photocatalytic Degradation of Bisphenol-A Using N, Co Codoped TiO2 Catalyst under Solar Light." In: *Scientific Reports* 9.1 (Jan. 2019), p. 765. ISSN: 2045-2322. DOI: 10.1038/s41598-018-38358-w.

[270] Guangjun Lu, M. Yazdan Mehr, W. D. van Driel, Xuejun Fan, Jiajie Fan, K. M. B. Jansen, and G. Q. Zhang. "Color Shift Investigations for LED Secondary Optical Designs: Comparison between BPA-PC and PMMA." In: *Optical Materials* 45 (July 2015), pp. 37–41. ISSN: 0925-3467. DOI: 10.1016/j.optmat.2015.03.005.

[271] Steven C. Allen and Andrew J. Steckl. "A Nearly Ideal Phosphor-Converted White Light-Emitting Diode." In: *Applied Physics Letters* 92.14 (Apr. 2008), p. 143309. ISSN: 0003-6951. DOI: 10.1063/1.2901378.

[272] R. Baillot, Y. Deshayes, L. Bechou, T. Buffeteau, I. Pianet, C. Armand, F. Voillot, S. Sorieul, and Y. Ousten. "Effects of Silicone Coating Degradation on GaN MQW LEDs Performances Using Physical and Chemical Analyses." In: *Microelectronics Reliability*. 21st European Symposium on the Reliability of Electron Devices, Failure Physics and Analysis 50.9 (Sept. 2010), pp. 1568–1573. ISSN: 0026-2714. DOI: 10.1016/j.microrel.2010.07.056.

[273] Jianlin Huang, Duan S. Golubović, Sau Koh, Daoguo Yang, Xiupeng Li, Xuejun Fan, and G. Q. Zhang. "Rapid Degradation of Mid-Power White-Light LEDs in Saturated Moisture Conditions." In: *IEEE Transactions on Device and Materials Reliability* 15.4 (Dec. 2015), pp. 478–485. ISSN: 1558-2574. DOI: 10.1109/TDMR.2015.2468587.

[274] Xiao Luo, Jiajie Fan, Mengni Zhang, Cheng Qian, Xuejun Fan, and Guoqi Zhang. "Degradation Mechanism Analysis for Phosphor/Silicone Composites Aged under High Temperature and High Humidity Condition." In: *2017 18th International Conference on Electronic Packaging Technology (ICEPT)*. Aug. 2017, pp. 1331–1336. DOI: 10.1109/ICEPT.2017.8046684.

[275] Qin Zhang, Xiu Mu, Kai Wang, Zhiyin Gan, Xiaobing Luo, and Sheng Liu. "Dynamic Mechanical Properties of the Transparent Silicone Resin for High Power LED Packaging." In: *2008 International Conference on Electronic Packaging Technology & High Density Packaging*. July 2008, pp. 1–4. DOI: 10.1109/ICEPT.2008.4607073.

[276] Fan, Wang, Deng, Fan, and Zhang. "High Moisture Accelerated Mechanical Behavior Degradation of Phosphor/Silicone Composites Used in White Light-Emitting Diodes." In: *Polymers* 11.8 (July 2019), p. 1277. ISSN: 2073-4360. DOI: 10.3390/polym11081277.

[277] Agnès Rivaton. "Recent Advances in Bisphenol-A Polycarbonate Photodegradation." In: *Polymer Degradation and Stability* 49.1 (Jan. 1995), pp. 163–179. ISSN: 0141-3910. DOI: 10.1016/0141-3910(95)00069-X.

[278] Saeid Nikafshar, Omid Zabihi, Mojtaba Ahmadi, Abdolreza Mirmohseni, Mojtaba Taseidifar, and Minoo Naebe. "The Effects of UV Light on the Chemical and Mechanical Properties of a Transparent Epoxy-Diamine System in the Presence of an Organic UV Absorber." In: *Materials* 10.2 (Feb. 2017), p. 180. ISSN: 1996-1944. DOI: 10.3390/ma10020180.

[279] Tomer Namrata S., Delor-Jestin Florence, Frezet Lawrence, and Lacoste Jacques. "Oxidation, Chain Scission and Cross-Linking Studies of Polysiloxanes upon Ageings." In: *Open Journal of Organic Polymer Materials* 2012 (Apr. 2012). ISSN: 2164-5752. DOI: 10.4236/ojopm.2012.22003.

[280] Yaël Israëli, Jacques Lacoste, Jacques Cavezzan, and Jacques Lemaire. "Photo-Oxidation of Polydimethylsiloxane Oils Part III—Effect of Dimethylene Groups." In: *Polymer Degradation and Stability* 42.3 (Jan. 1993), pp. 267–279. ISSN: 0141-3910. DOI: 10.1016/0141-3910(93)90223-6.

[281] O. Meszároš, P. Schmidt, J. Pospíšil, and S. Nešpůrek. "Photooxidation of Poly[Methyl(Phenyl)Silylene] and Effect of Photostabilizers." In: *Polymer Degradation and Stability*. Special Issue on Degradation and Stabilisation of Polymers 91.3 (Mar. 2006), pp. 573–578. ISSN: 0141-3910. DOI: 10.1016/j.polymdegradstab.2005.01.059.

[282] Bok Nam Jang and Charles A. Wilkie. "A TGA/FTIR and Mass Spectral Study on the Thermal Degradation of Bisphenol A Polycarbonate." In: *Polymer Degradation and Stability* 86.3 (Dec. 2004), pp. 419–430. ISSN: 0141-3910. DOI: 10.1016/j.polymdegradstab.2004.05.009.

[283] Bok Nam Jang and Charles A. Wilkie. "The Thermal Degradation of Bisphenol A Polycarbonate in Air." In: *Thermochimica Acta* 426.1 (Feb. 2005), pp. 73–84. ISSN: 0040-6031. DOI: 10.1016/j.tca.2004.07.023.

[284] Sabrina Carroccio, Concetto Puglisi, and Giorgio Montaudo. "Mechanisms of Thermal Oxidation of Poly(Bisphenol A Carbonate)." In: *Macromolecules* 35.11 (May 2002), pp. 4297–4305. ISSN: 0024-9297. DOI: 10.1021/ma012077t.

[285] Philippe Banet, Linda Chikh, Thomas Fouet, and Odile Fichet. "Phenyl Effect on Properties Evolution of Silicone Networks under Isothermal and Dynamic High Temperature Aging." In: *Journal of Applied Polymer Science* 139.25 (2022), e52420. ISSN: 1097-4628. DOI: 10.1002/app.52420.

[286] Girish Deshpande and Mary E Rezac. "The Effect of Phenyl Content on the Degradation of Poly(Dimethyl Diphenyl) Siloxane Copolymers." In: *Polymer Degradation and Stability* 74.2 (Jan. 2001), pp. 363–370. ISSN: 0141-3910. DOI: 10.1016/S0141-3910(01)00186-0.

[287] G Camino, S. M Lomakin, and M Lazzari. "Polydimethylsiloxane Thermal Degradation Part 1. Kinetic Aspects." In: *Polymer* 42.6 (Mar. 2001), pp. 2395–2402. ISSN: 0032-3861. DOI: 10.1016/S0032-3861(00)00652-2.

[288] G Camino, S. M Lomakin, and M Lageard. "Thermal Polydimethylsiloxane Degradation. Part 2. The Degradation Mechanisms." In: *Polymer* 43.7 (Mar. 2002), pp. 2011–2015. ISSN: 0032-3861. DOI: 10.1016/S0032-3861(01)00785-6.

[289] S.I. Chan, W.S. Hong, K.T. Kim, Y.G. Yoon, J.H. Han, and J.S. Jang. "Accelerated Life Test of High Power White Light Emitting Diodes Based on Package Failure Mechanisms." In: *Microelectronics Reliability* 51.9-11 (Sept. 2011), pp. 1806–1809. ISSN: 00262714. DOI: 10.1016/j.microrel.2011.07.042.

[290] Xuejun Fan and Cadmus Yuan. "Effect of Temperature Gradient on Moisture Diffusion in High Power Devices and the Applications in LED Packages." In: *2013 IEEE 63rd Electronic Components and Technology Conference*. May 2013, pp. 1466–1470. DOI: 10.1109/ECTC.2013.6575765.

[291] Ibrahim Khalilullah, Talukder Reza, Liangbiao Chen, Mark Placette, A. K. M. Monayem H. Mazumder, Jiang Zhou, Jiajie Fan, Cheng Qian, Guoqi Zhang, and Xuejun Fan. "In-Situ Characterization of Moisture Absorption and Hygroscopic Swelling of Silicone/Phosphor Composite Film and Epoxy Mold Compound in LED Packaging." In: *Microelectronics Reliability* 84 (May 2018), pp. 208–214. ISSN: 0026-2714. DOI: 10.1016/j.microrel.2018.03.025.

[292] Faiz Rahman, Anthony F. George, and Randy Drinkard. "Short- and Long-Term Reliability Studies of Broadband Phosphor-Converted Red, Green, and White Light-Emitting Diodes." In: *IEEE Transactions on Device and Materials Reliability* 16.1 (Mar. 2016), pp. 1–8. ISSN: 1558-2574. DOI: 10.1109/TDMR.2015.2510223.

[293] Cher Ming Tan, B. K. Chen, X. Li, and Sihan Joseph Chen. "Rapid Light Output Degradation of GaN-Based Packaged LED in the Early Stage of Humidity Test." In: *IEEE Transactions on Device and Materials Reliability* 12.1 (Mar. 2012), pp. 44–48. ISSN: 1558-2574. DOI: 10.1109/TDMR.2011.2173346.

[294] Bulong Wu, Xiaobing Luo, and Sheng Liu. "Effect Mechanism of Moisture Diffusion on LED Reliability." In: *3rd Electronics System Integration Technology Conference ESTC*. Berlin, Germany: IEEE, Sept. 2010, pp. 1–5. ISBN: 978-1-4244-8553-6. DOI: 10.1109/ESTC.2010.5642833.

[295] Xiaobing Luo, Bulong Wu, and Sheng Liu. "Effects of Moist Environments on LED Module Reliability." In: *IEEE Transactions on Device and Materials Reliability* 10.2 (June 2010), pp. 182–186. ISSN: 1530-4388, 1558-2574. DOI: 10.1109/TDMR.2009.2038367.

[296] M. B. Neĭman, B. M. Kovarskaya, L. I. Golubenkova, A. S. Strizhkova, I. I. Levantovskaya, and M. S. Akutin. "The Thermal Degradation of Some Epoxy Resins." In: *Journal of Polymer Science* 56.164 (1962), pp. 383–389. ISSN: 1542-6238. DOI: 10.1002/pol.1962.1205616408.

[297] F. J. Arques-Orobon, N. Nuñez, M. Vazquez, C. Segura-Antunez, and V. González-Posadas. "High-Power UV-LED Degradation: Continuous and Cycled Working Condition Influence." In: *Solid-State Electronics* 111 (Sept. 2015), pp. 111–117. ISSN: 0038-1101. DOI: 10.1016/j.sse.2015.05.039.

[298] Alexander Herzog, Simon Benkner, Babak Zandi, Matteo Buffolo, Willem D. Van Driel, Matteo Meneghini, and Tran Quoc Khanh. "Lifetime Prediction of Current-and Temperature-Induced Degradation in Silicone-Encapsulated 365 Nm High-Power Light-Emitting Diodes." In: *IEEE Access* 11 (2023), pp. 19928–19940. ISSN: 2169-3536. DOI: 10.1109/ACCESS.2023.3249478.

[299] Y.C. Hsu, Y.K. Lin, C.C. Tsai, J.H. Kuang, S.B. Huang, H.L. Hu, Y.I. Su, and W.H. Cheng. "Failure Mechanisms Associated with Lens Shape of High-Power LED Modules in Aging Test." In: *LEOS 2007 - IEEE Lasers and Electro-Optics Society Annual Meeting Conference Proceedings*. Oct. 2007, pp. 570–571. DOI: 10.1109/LEOS.2007.4382534.

[300] Banglong Liang, Zili Wang, Cheng Qian, Yi Ren, Bo Sun, Dezhen Yang, Zhou Jing, and Jiajie Fan. "Investigation of Step-Stress Accelerated Degradation Test Strategy for Ultraviolet Light Emitting Diodes." In: *Materials (Basel, Switzerland)* 12.19 (Sept. 2019), p. 3119. ISSN: 1996-1944. DOI: 10.3390/ma12193119.

[301] Mehmet Arik, Anant Setlur, Stanton Weaver, Deborah Haitko, and James Petroski. "Chip to System Levels Thermal Needs and Alternative Thermal Technologies for High Brightness LEDS." In: *Journal of Electronic Packaging* 129.3 (Apr. 2007), pp. 328–338. ISSN: 1043-7398. DOI: 10.1115/1.2753958.

[302] Dongdong Jia, Weiyi Jia, and Yi Jia. "Long Persistent Alkali-Earth Silicate Phosphors Doped with Eu2+,Nd3+." In: *Journal of Applied Physics* 101.2 (Jan. 2007), p. 023520. ISSN: 0021-8979. DOI: 10.1063/1.2409767.

[303] R. Mueller-Mach, G.O. Mueller, M.R. Krames, and T. Trottier. "High-Power Phosphor-Converted Light-Emitting Diodes Based on III-Nitrides." In: *IEEE Journal of Selected Topics in Quantum Electronics* 8.2 (Mar. 2002), pp. 339–345. ISSN: 1558-4542. DOI: 10.1109/2944.999189.

[304] Regina Mueller-Mach, Gerd Mueller, Michael R. Krames, Henning A. Höppe, Florian Stadler, Wolfgang Schnick, Thomas Juestel, and Peter Schmidt. "Highly Efficient All-Nitride Phosphor-Converted White Light Emitting Diode." In: *physica status solidi (a)* 202.9 (2005), pp. 1721–1721. ISSN: 1862-6319. DOI: 10.1002/pssa.200590014.

[305] Yu-Sheng Tang, Shu-Fen Hu, Chun Che Lin, Nitin C. Bagkar, and Ru-Shi Liu. "Thermally Stable Luminescence of KSrPO4:Eu2+ Phosphor for White Light UV Light-Emitting Diodes." In: *Applied Physics Letters* 90.15 (Apr. 2007), p. 151108. ISSN: 0003-6951. DOI: 10.1063/1.2721846.

[306] Chun-Chin Tsai, Jimmy Wang, Ming-Hung Chen, Yi-Cheng Hsu, Ying-Jyun Lin, Chao-Wei Lee, Sheng-Bang Huang, Hung-Lieh Hu, and Wood-Hi Cheng. "Investigation of Ce:YAG Doping Effect on Thermal Aging for High-Power Phosphor-Converted White-Light-Emitting Diodes." In: *IEEE Transactions on Device and Materials Reliability* 9.3 (Sept. 2009), pp. 367–371. ISSN: 1558-2574. DOI: 10.1109/TDMR.2009.2022545.

[307] Rong-Jun Xie, Naoto Hirosaki, Mamoru Mitomo, Kosei Takahashi, and Ken Sakuma. "Highly Efficient White-Light-Emitting Diodes Fabricated with Short-Wavelength Yellow Oxynitride Phosphors." In: *Applied Physics Letters* 88.10 (Mar. 2006), p. 101104. ISSN: 0003-6951. DOI: 10.1063/1.2182067.

[308] Rong-Jun Xie, Naoto Hirosaki, Takayuki Suehiro, Fang-Fang Xu, and Mamoru Mitomo. "A Simple, Efficient Synthetic Route to Sr $_2$ Si $_5$ N $_8$:Eu $^{2+}$ -Based Red Phosphors for White Light-Emitting Diodes." In: *Chemistry of Materials* 18.23 (Nov. 2006), pp. 5578–5583. ISSN: 0897-4756, 1520-5002. DOI: 10.1021/cm061010n.

[309] Rong-Jun Xie, Naoto Hirosaki, Naoki Kimura, Ken Sakuma, and Mamoru Mitomo. "2-Phosphor-Converted White Light-Emitting Diodes Using Oxynitride/Nitride Phosphors." In: *Applied Physics Letters* 90.19 (May 2007), p. 191101. ISSN: 0003-6951. DOI: 10.1063/1.2737375.

[310] R.-J. Xie, N. Hirosaki, K. Sakuma, and N. Kimura. "White Light-Emitting Diodes (LEDs) Using (Oxy)Nitride Phosphors." In: *Journal of Physics D: Applied Physics* 41.14 (July 2008), p. 144013. ISSN: 0022-3727. DOI: 10.1088/0022-3727/41/14/144013.

[311] Masatsugu Oishi, Shohei Shiomi, Takashi Yamamoto, Tomoyuki Ueki, Yoichiro Kai, Shigefusa F. Chichibu, Aiko Takatori, and Kazunobu Kojima. "High Temperature Degradation Mechanism of a Red Phosphor, CaAlSiN3:Eu for Solid-State Lighting." In: *Journal of Applied Physics* 122.11 (Sept. 2017), p. 113104. ISSN: 0021-8979. DOI: 10.1063/1.5003087.

[312] Bi Zhang, Jiang-Wei Zhang, Hao Zhong, Lu-Yuan Hao, Xin Xu, Simeon Agathopoulos, Cheng-Ming Wang, and Liang-Jun Yin. "Enhancement of the Stability of Green-Emitting Ba2SiO4:Eu2+ Phosphor by Hydrophobic Modification." In: *Materials Research Bulletin* 92 (Aug. 2017), pp. 46–51. ISSN: 0025-5408. DOI: 10.1016/j.materresbull.2017.03.057.

[313] Fauzia Iqbal, Sunil Kim, and Hyungsun Kim. "Degradation of Phosphor-in-Glass Encapsulants with Various Phosphor Types for High Power LEDs." In: *Optical Materials* 72 (Oct. 2017), pp. 323–329. ISSN: 0925-3467. DOI: 10.1016/j.optmat.2017.06.024.

[314] Wenxia Li, Zhen Song, Dianpeng Cui, Zhiguo Xia, and Quanlin Liu. "Moisture-Induced Degradation of the Narrow-Band Red-Emitting SrLiAl3N4:Eu2+ Phosphor." In: *Journal of Rare Earths* 36.4 (Apr. 2018), pp. 341–345. ISSN: 10020721. DOI: 10.1016/j.jre.2017.09.010.

[315] Fenfa Yao, Le Wang, Ying Lv, Yixi Zhuang, Tian-Liang Zhou, and Rong-Jun Xie. "Composition-Dependent Thermal Degradation of Red-Emitting (Ca 1-x Sr x)AlSiN 3 :Eu 2+ Phosphors for High Color Rendering White LEDs." In: *Journal of Materials Chemistry C* 6.4 (2018), pp. 890–898. DOI: 10.1039/C7TC04356B.

[316] Chenning Zhang, Tetsuo Uchikoshi, Rong-Jun Xie, Lihong Liu, Yujin Cho, Yoshio Sakka, Naoto Hirosaki, and Takashi Sekiguchi. "Prevention of Thermal- and Moisture-Induced Degradation of the Photoluminescence Properties of the Sr 2 Si 5 N 8 :Eu 2+ Red Phosphor by Thermal Post-Treatment in N 2 –H 2." In: *Physical Chemistry Chemical Physics* 18.18 (2016), pp. 12494–12504. DOI: 10.1039/C6CP01102K.

[317] Jie Zhu, Le Wang, Tianliang Zhou, Yujin Cho, Takayuki Suehiro, Takashi Takeda, Ming Lu, Takashi Sekiguchi, Naoto Hirosaki, and Rong-Jun Xie. "Moisture-Induced Degradation and Its Mechanism of (Sr,Ca)AlSiN 3 :Eu 2+ , a Red-Color-Converter for Solid State Lighting." In: *Journal of Materials Chemistry C* 3.13 (2015), pp. 3181–3188. DOI: 10.1039/C4TC02824D.

[318] Cher Ming Tan, Boon Khai Eric Chen, and Meng Xiong. "Study of Humidity Reliability of High Power LEDs." In: *2010 10th IEEE International Conference on Solid-State and Integrated Circuit Technology*. Nov. 2010, pp. 1592–1595. DOI: 10.1109/ICSICT.2010.5667441.

[319] Jiajie Fan, Mengni Zhang, Xiao Luo, Cheng Qian, Xuejun Fan, Aimin Ji, and Guoqi Zhang. "Phosphor–Silicone Interaction Effects in High Power White Light Emitting Diode Packages." In: *Journal of Materials Science: Materials in Electronics* 28.23 (Dec. 2017), pp. 17557–17569. ISSN: 1573-482X. DOI: 10.1007/s10854-017-7692-x.

[320] Fan Wu, Yiping Wu, Bing An, and Fengshun Wu. "Analysis of Dark Stain on Chip Surface of High-Power LED." In: *2006 7th International Conference on Electronic Packaging Technology*. Aug. 2006, pp. 1–4. DOI: 10.1109/ICEPT.2006.359785.

[321] Yeong-Her Lin, Jiun Pyng You, Yuan-Chang Lin, Nguyen T. Tran, and Frank G. Shi. "Development of High-Performance Optical Silicone for the Packaging of High-Power LEDs." In: *IEEE Transactions on Components and Packaging Technologies* 33.4 (Dec. 2010), pp. 761–766. ISSN: 1521-3331, 1557-9972. DOI: 10.1109/TCAPT.2010.2046488.

[322] Preetpal Singh and Cher Ming Tan. "Uncover the Degradation Science of Silicone Under the Combined Temperature and Humidity Conditions." In: *IEEE Access* 6 (2018), pp. 1302–1311. ISSN: 2169-3536. DOI: 10.1109/ACCESS.2017.2778289.

[323] Jianzheng Hu, Lianqiao Yang, and Moo Whan Shin. "Thermal Effects of Moisture Inducing Delamination in Light-Emitting Diode Packages." In: *56th Electronic Components and Technology Conference 2006*. May 2006, 6 pp.–. DOI: 10.1109/ECTC.2006.1645928.

[324] Xin Li, Xu Chen, and Guo-Quan Lu. "Reliability of High-Power Light Emitting Diode Attached With Different Thermal Interface Materials." In: *Journal of Electronic Packaging* 132.3 (Sept. 2010). ISSN: 1043-7398. DOI: 10.1115/1.4002299.

[325] Cher Ming Tan, Boon Khai Eric Chen, Gan Xu, and Yuanjie Liu. "Analysis of Humidity Effects on the Degradation of High-Power White LEDs." In: *Microelectronics Reliability*. 20th European Symposium on the Reliability of Electron Devices, Failure Physics and Analysis 49.9 (Sept. 2009), pp. 1226–1230. ISSN: 0026-2714. DOI: 10.1016/j.microrel.2009.07.005.

[326] Guangjun Lu, W. D. van Driel, Xuejun Fan, Jiajie Fan, Cheng Qian, and G. Q. Zhang. "Color Shift Acceleration on Mid-Power LED Packages." In: *Microelectronics Reliability* 78 (Nov. 2017), pp. 294–298. ISSN: 0026-2714. DOI: 10.1016/j.microrel.2017.09.014.

[327] Bulong Wu, Xiaobing Luo, Zhili Zhao, and Sheng Liu. "Effect Investigation of Delamination on Optical Output of High Power LEDs." In: *2011 12th International Conference on Electronic Packaging Technology and High Density Packaging*. Aug. 2011, pp. 1–5. DOI: 10.1109/ICEPT.2011.6067013.

[328] Minho Choi, Ki Hyun Kim, Changhun Yun, Dai Hyoung Koo, Sang Bin Song, and Jae Pil Kim. "Direct Correlation between Reliability and pH Changes of Phosphors for White Light-Emitting Diodes." In: *Microelectronics Reliability* 54.12 (Dec. 2014), pp. 2849–2852. ISSN: 0026-2714. DOI: 10.1016/j.microrel.2014.07.141.

[329] Jianlin Huang, Dušan S. Golubović, Sau Koh, Daoguo Yang, Xiupeng Li, Xuejun Fan, and Guo Qi Zhang. "Degradation Mechanisms of Mid-power White-Light LEDs." In: *Solid State Lighting Reliability Part 2: Components to Systems*. Ed. by Willem Dirk van Driel, Xuejun Fan, and Guo Qi Zhang. Solid State Lighting Technology and Application Series. Cham: Springer International Publishing, 2018, pp. 381–432. ISBN: 978-3-319-58175-0. DOI: 10.1007/978-3-319-58175-0_14.

[330] Zhaohui Chen, Zhang Qin, Wang Kai, Luo Xiaobing, and Liu Sheng. "Reliability Test and Failure Analysis of High Power LED Packages." In: *Journal of Semiconductors* 32.1 (Jan. 2011), p. 014007. ISSN: 1674-4926. DOI: 10.1088/1674-4926/32/1/014007.

[331] Shih-Chun Yang, Pang Lin, Chien-Ping Wang, Sheng Bang Huang, Chiu-Ling Chen, Pei-Fang Chiang, An-Tse Lee, and Mu-Tao Chu. "Failure and Degradation Mechanisms of High-Power White Light Emitting Diodes." In: *Microelectronics Reliability*. Thermal, Mechanical and Multi-physics Simulation and Experiments in Micro-Electronics and Micro-Systems (EuroSimE 2009) 50.7 (July 2010), pp. 959–964. ISSN: 0026-2714. DOI: 10.1016/j.microrel.2010.03.007.

[332] Lixia Zhao, Liang Liu, and Peiyue Qi. "Progress of Reliability and Failure Mechanisms for GaN-Based Light-Emitting Diodes." In: *physica status solidi (a)* 219.6 (2022), p. 2100425. ISSN: 1862-6319. DOI: 10.1002/pssa.202100425.

[333] D Raul and K Ghosh. "Performance of Chip-on-Board and Surface-Mounted High-Power LED Luminaires at Different Relative Humidities and Temperatures." In: *Lighting Research & Technology* 51.8 (Dec. 2019), pp. 1249–1262. ISSN: 1477-1535. DOI: 10.1177/1477153518819040.

[334] Jui Hung Yuan and Tung Han Chuang. "Luminous Efficiency of Pd-Doped Ag-Alloy Wire Bonded LED Package after Reliability Tests." In: *Materials Science Forum* 960 (2019), pp. 221–230. ISSN: 1662-9752. DOI: 10.4028/www.scientific.net/MSF.960.221.

[335] Thong Kok Law. "Thermal Management and Humidity Based Prognostics of High-Power LED Packages." PhD thesis. University of Glasgow, 2019.

[336] Anjan N. Padmasali, J. Lokesh, and Savitha G. Kini. "An Experimental Investigation on the Role of LEDs on the Lifetime Performance of Consumer LED Luminaires." In: *IEEE Access* 10 (2022), pp. 131765–131771. ISSN: 2169-3536. DOI: 10.1109/ACCESS.2022.3230474.

[337] Dezhi Zhao, Zhihua Xiong, Cong Chen, and Yunfei Niu. "Comparative Study on the Thermal Performance of Surface-Mounted Devices Light-Emitting Diode Packaging with Poly(1,4-Cyclohexylenedimethylene Terephthalate) and Epoxy Moulding Compound Frames." In: *IET Optoelectronics* 16.1 (2022), pp. 1–9. ISSN: 1751-8776. DOI: 10.1049/ote2.12044.

[338] Lumileds Holding B.V. *LUXEON SunPlus 2835 Line*. https://lumileds.com/products/horticulture-leds/luxeon-sunplus-2835-line/. June 2023.

[339] Redmond Ramin Shamshiri, James W. Jones, Kelly R. Thorp, Desa Ahmad, Hasfalina Che Man, and Sima Taheri. "Review of Optimum Temperature, Humidity, and Vapour Pressure Deficit for Microclimate Evaluation and Control in Greenhouse Cultivation of Tomato: A Review." In: *International Agrophysics* 32.2 (Apr. 2018), pp. 287–302. ISSN: 2300-8725. DOI: 10.1515/intag-2017-0005.

[340] Clemens J.M. Lasance and András Poppe, eds. *Thermal Management for LED Applications*. Vol. 2. Solid State Lighting Technology and Application Series. New York, NY: Springer, 2014. ISBN: 978-1-4614-5090-0 978-1-4614-5091-7. DOI: 10.1007/978-1-4614-5091-7.

[341] Ceren Cengiz, Mohammad Azarifar, and Mehmet Arik. "A Critical Review on the Junction Temperature Measurement of Light Emitting Diodes." In: *Micromachines* 13.10 (Oct. 2022), p. 1615. ISSN: 2072-666X. DOI: 10.3390/mi13101615.

[342] Y. Xi and E. F. Schubert. "Junction–Temperature Measurement in GaN Ultraviolet Light-Emitting Diodes Using Diode Forward Voltage Method." In: *Applied Physics Letters* 85.12 (Sept. 2004), pp. 2163–2165. ISSN: 0003-6951. DOI: 10.1063/1.1795351.

[343] CIE. *CIE 015:2018 Colorimetry, 4th Edition*. Technical Report CIE 015:2018. Vienna, Austria: International Commission on Illumination (CIE), Oct. 2018. DOI: 10.25039/TR.015.2018.

[344] Illuminating Engineering Society. *Projecting Long-Term Chromaticity Coordinate Shift of LED Packages, Arrays, and Modules*. Approved Method ANSI/IES TM-35-19. New York, USA: Illuminating Engineering Society, 2019.

[345] ASTM. *Standard Test Method for Yellowness Index of Plastics*. Tech. rep. ASTM D1925, 70th Edition. ASTM International, 1988, p. 3.

[346] S.-W. Feng, C.-Y. Tsai, Y.-C. Cheng, C.-C. Liao, C.C. Yang, Y.-S. Lin, K.-J. Ma, and J.-I. Chyi. "Phonon–Replica Transitions in InGaN/GaN Quantum Well Structures." In: *Optical and Quantum Electronics* 34.12 (Dec. 2002), pp. 1213–1219. ISSN: 1572-817X. DOI: 10.1023/A:1021382721938.

[347] G. Muziol, M. Hajdel, M. Siekacz, H. Turski, K. Pieniak, A. Bercha, W. Trzeciakowski, R. Kudrawiec, T. Suski, and C. Skierbiszewski. "III-nitride Optoelectronic Devices Containing Wide Quantum Wells—Unexpectedly Efficient Light Sources." In: *Japanese Journal of Applied Physics* 61.SA (Dec. 2021), SA0801. ISSN: 1347-4065. DOI: 10.35848/1347-4065/ac3c1a.

[348] Jaehee Cho, E. Fred Schubert, and Jong Kyu Kim. "Efficiency Droop in Light-Emitting Diodes: Challenges and Countermeasures." In: *Laser & Photonics Reviews* 7.3 (2013), pp. 408–421. ISSN: 1863-8899. DOI: 10.1002/lpor.201200025.

[349] J. Glaab et al. "Degradation of (In)AlGaN-Based UVB LEDs and Migration of Hydrogen." In: *IEEE Photonics Technology Letters* 31.7 (Apr. 2019), pp. 529–532. ISSN: 1941-0174. DOI: 10.1109/LPT.2019.2900156.

[350] Lei Zhang, Yejun Zhu, Wei Wang, Xianghong Bi, Haibin Chen, Karina Leung, Yeqing Wu, and Jingshen Wu. "Study on Ag-Plated Cu Lead Frame and Its Effect to LED Performance Under Thermal Aging." In: *IEEE Transactions on Device and Materials Reliability* 14.4 (Dec. 2014), pp. 1022–1030. ISSN: 1558-2574. DOI: 10.1109/TDMR.2014.2360081.

[351] Yunan Zhou, Weidong Zhuang, Yunsheng Hu, Ronghui Liu, Huibing Xu, Mingyue Chen, Yuanhong Liu, Yanfeng Li, Yaling Zheng, and Guantong Chen. "Cyan-Green Phosphor (Lu2M)(Al4Si)O12:Ce3+ for High-Quality LED Lamp: Tunable Photoluminescence Properties and Enhanced Thermal Stability." In: *Inorganic Chemistry* 58.2 (Jan. 2019), pp. 1492–1500. ISSN: 0020-1669. DOI: 10.1021/acs.inorgchem.8b03017.

[352] Nima Gorjian, Lin Ma, Murthy Mittinty, Prasad Yarlagadda, and Yong Sun. "A Review on Degradation Models in Reliability Analysis." In: *Engineering Asset Lifecycle Management*. Ed. by Dimitris Kiritsis, Christos Emmanouilidis, Andy Koronios, and Joseph Mathew. London: Springer, 2010, pp. 369–384. ISBN: 978-0-85729-320-6. DOI: 10.1007/978-0-85729-320-6_42.

[353] Darshankumar Bhat, Stefan Muench, and Mike Roellig. "Application of Machine Learning Algorithms in Prognostics and Health Monitoring of Electronic Systems: A Review." In: *e-Prime - Advances in Electrical Engineering, Electronics and Energy* 4 (June 2023), p. 100166. ISSN: 2772-6711. DOI: 10.1016/j.prime.2023.100166.

[354] Song Li, Zhiyong Chen, Qiaobin Liu, Wenku Shi, and Kunheng Li. "Modeling and Analysis of Performance Degradation Data for Reliability Assessment: A Review." In: *IEEE Access* 8 (2020), pp. 74648–74678. ISSN: 2169-3536. DOI: 10.1109/ACCESS.2020.2987332.

[355] Rui Kang, Wenjun Gong, and Yunxia Chen. "Model-Driven Degradation Modeling Approaches: Investigation and Review." In: *Chinese Journal of Aeronautics* 33.4 (Apr. 2020), pp. 1137–1153. ISSN: 1000-9361. DOI: 10.1016/j.cja.2019.12.006.

[356] Luis A. Escobar and William Q. Meeker. "A Review of Accelerated Test Models." In: *Statistical Science* 21.4 (Nov. 2006). ISSN: 0883-4237. DOI: 10.1214/088342306000000321. arXiv: 0708.0369 [stat].

[357] Bo Sun, Xiaopeng Jiang, Kam-Chuen Yung, Jiajie Fan, and Michael G. Pecht. "A Review of Prognostic Techniques for High-Power White LEDs." In: *IEEE Transactions on Power Electronics* 32.8 (Aug. 2017), pp. 6338–6362. ISSN: 1941-0107. DOI: 10.1109/TPEL.2016.2618422.

[358] *ANSI/IES TM-21-19: Technical Memorandum: Projecting Long-Term Luminous, Photon, and Radiant Flux Maintenance of LED Light Sources*. Approved Method. New York, USA: Illuminating Engineering Society, 2019.

[359] Georgiy Bobashev, Nicholas G. Baldasaro, Karmann C. Mills, and J. Lynn Davis. "An Efficiency-Decay Model for Lumen Maintenance." In: *IEEE Transactions on Device and Materials Reliability* 16.3 (Sept. 2016), pp. 277–281. ISSN: 1530-4388, 1558-2574. DOI: 10.1109/TDMR.2016.2584926.

[360] Suk Joo Bae, Seong-Joon Kim, Man Soo Kim, Bae Jin Lee, and Chang Wook Kang. "Degradation Analysis of Nano-Contamination in Plasma Display Panels." In: *IEEE Transactions on Reliability* 57.2 (June 2008), pp. 222–229. ISSN: 0018-9529, 1558-1721. DOI: 10.1109/TR.2008.917823.

[361] W.D. van Driel, M. Schuld, B. Jacobs, F. Commissaris, J. van der Eyden, and B. Hamon. "Lumen Maintenance Predictions for LED Packages." In: *Microelectronics Reliability* 62 (July 2016), pp. 39–44. ISSN: 00262714. DOI: 10.1016/j.microrel.2016.03.018.

[362] Vito M. R. Muggeo. "Estimating Regression Models with Unknown Break-Points." In: *Statistics in Medicine* 22.19 (2003), pp. 3055–3071. ISSN: 1097-0258. DOI: 10.1002/sim.1545.

[363] Charlie Pilgrim. "Piecewise-Regression (Aka Segmented Regression) in Python." In: *Journal of Open Source Software* 6.68 (Dec. 2021), p. 3859. ISSN: 2475-9066. DOI: 10.21105/joss.03859.

[364] Svante Arrhenius. "Über die Dissociationswärme und den Einfluss der Temperatur auf den Dissociationsgrad der Elektrolyte." In: *Zeitschrift für Physikalische Chemie* 4U.1 (July 1889), pp. 96–116. ISSN: 2196-7156. DOI: 10.1515/zpch-1889-0408.

[365] J.R. Black. "Electromigration—A Brief Survey and Some Recent Results." In: *IEEE Transactions on Electron Devices* 16.4 (Apr. 1969), pp. 338–347. ISSN: 1557-9646. DOI: 10.1109/T-ED.1969.16754.

[366] Örjan Hallberg and D. Stewart Peck. "Recent Humidity Accelerations, a Base for Testing Standards." In: *Quality and Reliability Engineering International* 7.3 (1991), pp. 169–180. ISSN: 1099-1638. DOI: 10.1002/qre.4680070308.

[367] Henry Eyring. "The Activated Complex in Chemical Reactions." In: *The Journal of Chemical Physics* 3.2 (1935), pp. 107–115. ISSN: 0021-9606. DOI: 10.1063/1.1749604.

[368] Carl Edward Rasmussen and Christopher K. I. Williams. *Gaussian Processes for Machine Learning*. Adaptive Computation and Machine Learning. Cambridge, Mass: MIT Press, 2006. ISBN: 978-0-262-18253-9.

[369] Noel Cressie. "The Origins of Kriging." In: *Mathematical Geology* 22.3 (Apr. 1990), pp. 239–252. ISSN: 1573-8868. DOI: 10.1007/BF00889887.

[370] Hanefi Bayraktar and F. Sezer. Turalioglu. "A Kriging-based Approach for Locating a Sampling Site—in the Assessment of Air Quality." In: *Stochastic Environmental Research and Risk Assessment* 19.4 (Oct. 2005), pp. 301–305. ISSN: 1436-3259. DOI: 10.1007/s00477-005-0234-8.

[371] D. A. Zimmerman et al. "A Comparison of Seven Geostatistically Based Inverse Approaches to Estimate Transmissivities for Modeling Advective Transport by Groundwater Flow." In: *Water Resources Research* 34.6 (1998), pp. 1373–1413. ISSN: 1944-7973. DOI: 10.1029/98WR00003.

[372] Matthew J. Tonkin and Steven P. Larson. "Kriging Water Levels with a Regional-Linear and Point-Logarithmic Drift." In: *Groundwater* 40.2 (2002), pp. 185–193. ISSN: 1745-6584. DOI: 10.1111/j.1745-6584.2002.tb02503.x.

[373] Richard P. Mann, Viktoria Spaiser, Lina Hedman, and David J. T. Sumpter. "Choice Modelling with Gaussian Processes in the Social Sciences: A Case Study of Neighbourhood Choice in Stockholm." In: *PLOS ONE* 13.11 (May 2018), e0206687. ISSN: 1932-6203. DOI: 10.1371/journal.pone.0206687.

[374] Björn R. H. Blomqvist, David J. T. Sumpter, and Richard P. Mann. "Inferring the Dynamics of Rising Radical Right-Wing Party Support Using Gaussian Processes." In: *Philosophical Transactions of the Royal Society A: Mathematical, Physical and Engineering Sciences* 377.2160 (Oct. 2019), p. 20190145. DOI: 10.1098/rsta.2019.0145.

[375] Pham Luu Trung Duong and Nagarajan Raghavan. "Prognostic Health Management for LED with Missing Data: Multi-task Gaussian Process Regression Approach." In: *2018 Prognostics and System Health Management Conference (PHM-Chongqing)*. Oct. 2018, pp. 1182–1187. DOI: 10.1109/PHM-Chongqing.2018.00208.

[376] Pham Luu Trung Duong, Hyunseok Park, and Nagarajan Raghavan. "Application of Multi-Output Gaussian Process Regression for Remaining Useful Life Prediction of Light Emitting Diodes." In: *Microelectronics Reliability* 88–90 (Sept. 2018), pp. 80–84. ISSN: 00262714. DOI: 10.1016/j.microrel.2018.07.106.

[377] Brian P. Weaver, Brian J. Williams, Christine M. Anderson-Cook, and David M. Higdon. "Computational Enhancements to Bayesian Design of Experiments Using Gaussian Processes." In: *Bayesian Analysis* 11.1 (Mar. 2016), pp. 191–213. ISSN: 1936-0975, 1931-6690. DOI: 10.1214/15-BA945.

[378] Tim Voigt, Martin Kohlhase, and Oliver Nelles. "Incremental DoE and Modeling Methodology with Gaussian Process Regression: An Industrially Applicable Approach to Incorporate Expert Knowledge." In: *Mathematics* 9.19 (Jan. 2021), p. 2479. ISSN: 2227-7390. DOI: 10.3390/math9192479.

[379] Zhihua Wang, Qiong Wu, Xiongjian Zhang, Xinlei Wen, Yongbo Zhang, Chengrui Liu, and Huimin Fu. "A Generalized Degradation Model Based on Gaussian Process." In: *Microelectronics Reliability* 85 (June 2018), pp. 207–214. ISSN: 00262714. DOI: 10.1016/j.microrel.2018.05.001.

[380] Sheng Hong and Zheng Zhou. "Application of Gaussian Process Regression for Bearing Degradation Assessment." In: *2012 6th International Conference on New Trends in Information Science, Service Science and Data Mining (ISSDM2012)*. Oct. 2012, pp. 644–648.

[381] Huiwen Deng, Weihao Hu, Di Cao, Weirong Chen, Qi Huang, Zhe Chen, and Frede Blaabjerg. "Degradation Trajectories Prognosis for PEM Fuel Cell Systems Based on Gaussian Process Regression." In: *Energy* 244 (Apr. 2022), p. 122569. ISSN: 0360-5442. DOI: 10.1016/j.energy.2021.122569.

[382] Piyush Tagade, Krishnan S. Hariharan, Sanoop Ramachandran, Ashish Khandelwal, Arunava Naha, Subramanya Mayya Kolake, and Seong Ho Han. "Deep Gaussian Process Regression for Lithium-Ion Battery Health Prognosis and Degradation Mode Diagnosis." In: *Journal of Power Sources* 445 (Jan. 2020), p. 227281. ISSN: 0378-7753. DOI: 10.1016/j.jpowsour.2019.227281.

[383] Vinky Chow, Raphaël C. W. Phan, Anh Cat Le Ngo, Ganesh Krishnasamy, and Siang-Piao Chai. "Data-Driven Photocatalytic Degradation Activity Prediction with Gaussian Process." In: *Process Safety and Environmental Protection* 161 (May 2022), pp. 848–859. ISSN: 0957-5820. DOI: 10.1016/j.psep.2022.03.020.

[384] Adla Ismail, Lotfi Saidi, Mounir Sayadi, and Mohamed Benbouzid. "Gaussian Process Regression Remaining Useful Lifetime Prediction of Thermally Aged Power IGBT." In: *IECON 2019 - 45th Annual Conference of the IEEE Industrial Electronics Society*. Vol. 1. Oct. 2019, pp. 6004–6009. DOI: 10.1109/IECON.2019.8926710.

[385] W. J. Padgett and Meredith A. Tomlinson. "Inference from Accelerated Degradation and Failure Data Based on Gaussian Process Models." In: *Lifetime Data Analysis* 10.2 (June 2004), pp. 191–206. ISSN: 1572-9249. DOI: 10.1023/B:LIDA.0000030203.49001.b6.

[386] S.L.H. Lim, P.L.T. Duong, H. Park, P. Singh, C.M. Tan, and N. Raghavan. "Assessing Multi-Output Gaussian Process Regression for Modeling of Non-Monotonic Degradation Trends of Light Emitting Diodes in Storage." In: *Microelectronics Reliability* 114 (Nov. 2020), p. 113794. ISSN: 00262714. DOI: 10.1016/j.microrel.2020.113794.

[387] Sze Li Harry Lim, Pham Luu Trung Duong, Hyunseok Park, and Nagarajan Raghavan. "Expedient Validation of LED Reliability with Anomaly Detection through Multi-Output Gaussian Process Regression." In: *Microelectronics Reliability*. 33rd European Symposium on Reliability of Electron Devices, Failure Physics and Analysis 138 (Nov. 2022), p. 114624. ISSN: 0026-2714. DOI: 10.1016/j.microrel.2022.114624.

[388] David G. Kleinbaum and Mitchel Klein. *Survival Analysis: A Self-Learning Text*. Statistics for Biology and Health. New York, NY: Springer, 2012. ISBN: 978-1-4419-6645-2 978-1-4419-6646-9. DOI: 10.1007/978-1-4419-6646-9.

[389] T. G. Clark, M. J. Bradburn, S. B. Love, and D. G. Altman. "Survival Analysis Part I: Basic Concepts and First Analyses." In: *British Journal of Cancer* 89.2 (July 2003), pp. 232–238. ISSN: 1532-1827. DOI: 10.1038/sj.bjc.6601118.

[390] Md. Rezaul Karim and M. Ataharul Islam. *Reliability and Survival Analysis*. Singapore: Springer Singapore, 2019. ISBN: 9789811397752 9789811397769. DOI: 10.1007/978-981-13-9776-9.

[391] E. L. Kaplan and Paul Meier. "Nonparametric Estimation from Incomplete Observations." In: *Journal of the American Statistical Association* 53.282 (June 1958), pp. 457–481. ISSN: 0162-1459. DOI: 10.1080/01621459.1958.10501452.

[392] Wayne Nelson. "Theory and Applications of Hazard Plotting for Censored Failure Data." In: *Technometrics* 14.4 (1972), pp. 945–966. ISSN: 0040-1706. DOI: 10.2307/1267144. JSTOR: 1267144.

[393] Odd Aalen. "Nonparametric Inference for a Family of Counting Processes." In: *The Annals of Statistics* 6.4 (July 1978), pp. 701–726. ISSN: 0090-5364, 2168-8966. DOI: 10.1214/aos/1176344247.

[394] D. R. Cox. "Regression Models and Life-Tables." In: *Journal of the Royal Statistical Society. Series B (Methodological)* 34.2 (1972), pp. 187–220. ISSN: 0035-9246. JSTOR: 2985181.

[395] *DIN EN 62717:2019-12: LED Modules for General Lighting - Performance Requirements (IEC 62717:2014, Modified + A1:2015, Modified + A2:2019); German Version EN 62717:2017 + A2:2019*. Standard. Berlin: Beuth Verlag GmbH, 2019, p. 61. DOI: 10.31030/3097033.

[396] Charles R. Harris et al. "Array Programming with NumPy." In: *Nature* 585.7825 (Sept. 2020), pp. 357–362. ISSN: 1476-4687. DOI: 10.1038/s41586-020-2649-2.

[397] Thomas Wiecki et al. *Pymc-Devs/Pymc: V5.6.1*. Zenodo. July 2023. DOI: 10.5281/zenodo.8146216.

[398] Olivier Grisel et al. *Scikit-Learn/Scikit-Learn: Scikit-learn 1.2.2*. Zenodo. Mar. 2023. DOI: 10.5281/zenodo.7711792.

[399] Sebastian Pölsterl. *Scikit-Survival*. Zenodo. June 2023. DOI: 10.5281/zenodo.8025038.

[400] Rainer Storn and Kenneth Price. "Differential Evolution – A Simple and Efficient Heuristic for Global Optimization over Continuous Spaces." In: *Journal of Global Optimization* 11.4 (Dec. 1997), pp. 341–359. ISSN: 1573-2916. DOI: 10.1023/A:1008202821328.

[401] Dong C. Liu and Jorge Nocedal. "On the Limited Memory BFGS Method for Large Scale Optimization." In: *Mathematical Programming* 45.1 (Aug. 1989), pp. 503–528. ISSN: 1436-4646. DOI: 10.1007/BF01589116.

[402] Sham-Tsong Shiue, Hung-Chien Lin, Ting-Ying Shen, and Hsiang-Chun Hseuh. "Humidity and Temperature-Dependence of the Interfacial Shear Strength between the Glass Fiber and Primary Coating in Double-Coated Optical Fibers." In: *Materials Science and Engineering: A* 434.1 (Oct. 2006), pp. 202–206. ISSN: 0921-5093. DOI: 10.1016/j.msea.2006.06.108.

Own Publications

Publications in internationally peer-reviewed journals

Sebastian Babilon, Sebastian Beck, Julian Kunkel, Julian Klabes, Paul Myland, **Simon Benkner** & Tran Quoc Khanh. Measurement of circadian effectiveness in lighting for office applications. *MDPI, Applied Sciences*. **11**, 15:6936 (2021).
DOI: https://doi.org/10.3390/app11156936

Simon Benkner, Sebastian Babilon, Alexander Herzog & Tran Quoc Khanh. Combined Methodology for Accurate Evaluation of Distance and Direction of Chromaticity Shifts in LED Reliability Tests. *IEEE Transactions on Device and Materials Reliability*. **21**, 4, pp. 500-507 (2021).
DOI: https://doi.org/10.1109/TDMR.2021.3109853

Stefan Klir, Fathia Reda, Sebastian Babilon, **Simon Benkner** & Tran Quoc Khanh. Unsupervised Clustering Pipeline to Obtain Diversified Light Spectra for Subject Studies and Correlation Analyses. *MDPI, Applied Sciences*. **11**, 19:9062 (2021).
DOI: https://doi.org/10.3390/app11199062

Simon Benkner, Alexander Herzog, Stefan Klir, Willem D. van Driel & Tran Quoc Khanh. Advancements in Spectral Power Distribution Modeling of Light-Emitting Diodes. *IEEE Access*. **10**, pp. 83612-83619 (2022).
DOI: https://doi.org/10.1109/ACCESS.2022.3197280

Alexander Herzog, Max Wagner, **Simon Benkner**, Babak Zandi, Willem D. van Driel & Tran Quoc Khanh. Long-Term Temperature-Dependent Degradation of 175 W Chip-on-Board LED Modules. *IEEE Transactions on Electron Devices*. **69**, 12, pp. 6830-6836 (2022).
DOI: https://doi.org/10.1109/TED.2022.3214169.

Alexander Herzog, **Simon Benkner**, Babak Zandi, Matteo Buffolo, Willem D. van Driel, Matteo Meneghini & Tran Quoc Khanh. Lifetime prediction of current- and temperature-induced degradation in silicone-encapsulated 365 nm high-power light-emitting diodes. *IEEE Access*. **11**, pp. 19928-19940 (2023).
DOI: https://doi.org/10.1109/ACCESS.2023.3249478.

Alexander Herzog, Paul Myland, Peter Förster, **Simon Benkner**, Babak Zandi, Willem D. van Driel, Sebastian Schöps & Tran Quoc Khanh. Spectral LED degradation modeling using non-negative matrix factorization. *Microelectronics Reliability*. *- Currently under review. ID: MICREL-D-23-00529*

Stefan Klir, Sebastian Babilon, Paul Myland, **Simon Benkner** & Tran Quoc Khanh. Sky-like interior light settings: a preference Study. *Frontiers in Built Environment*. **9**, (2023).
DOI: https://doi.org/10.3389/fbuil.2023.1101534

Other Publications

Stefan Klir, **Simon Benkner** & Tran Quoc Khanh. "Dynamische Leuchtensteuerung als Funktion der Zeit." In: *Licht 9 - Magazin*. **9**, 66-70 (2021).

Conference contributions

Stefan Klir, **Simon Benkner**, Babak Zandi & Tran Quoc Khanh. Der technologische Weg zu smart lighting - von den Leuchten mit Sensorik bis Internet of Things und Machine Learning - Beschreibung der Systemarchitektur. *Licht 2018 - KREATIVE BELEUCHTUNGSLÖSUNGEN 23. Europäischer Lichtkongress*. Swiss, Davos. 09.-12.09.2018.

Simon Benkner, Stefan Klir, William Truong & Tran Quoc Khanh. Sensor array for the analysis of the lighting situation in an intelligent industrial hall. *14. Internationales Forum für den lichttechnischen Nachwuchs*. Germany, Dörnfeld/Ilm. 06.-08.09.2019.

Simon Benkner, Stefan Klir, Alexander Herzog & Tran Quoc Khanh. How data-driven approaches can increase the accuracy of LED reliability predictions. *MikroSystemTechnik Congress 2021*. Germany, Stuttgart-Ludwigsburg. 08.-10.11.2021.

Ferdinand Keil, **Simon Benkner**, Tran Quoc Khanh & Klaus Hofmann. Model-Based Analysis of Accelerated Lifetime Test Data of Off-Line LED Drivers. *34. Workshop Testmethoden und Zuverlässigkeit von Schaltungen und Systemen (TuZ 2022)*. Germany, Bremerhaven. 27.02.-01.03.2022.

Stefan Klir, Sebastian Babilon, Fathia Reda, **Simon Benkner** & Tran Quoc Khanh. Preference Lighting Model: Generalization of lighting preferences for individual users. *2021 Joint Conference - 11th International Conference on Energy Efficiency in Domestic Appliances and Lighting & 17th International Symposium on the Science and Technology of Lighting (EEDAL/LS:17)*. France, Toulouse. 01.-03.06.2022.

Supervised Theses

Betreute Abschlussarbeiten und Seminare

L. Braisz. Entwicklung eines wetterfesten Tageslichtsensors zur richtungsaufgelösten Farbort- und Intensitätsmessung. *Master-Thesis*, Germany: Technical University of Darmstadt, 2017.

S. Kamajou. Entwickeln einer Datenvisualisierung und Auswertung mit zugrundeliegenden Sensordaten aus einer Datenbank. *Bachelor-Thesis*, Germany: Technical University of Darmstadt, 2018.

M. Schmied. Entwicklung und Auswertung eines miniaturisierten Mehrfeld-Präsenzsensors. *Bachelor-Thesis*, Germany: Technical University of Darmstadt, 2018.

D. Bächle. Konzipierung und Aufbau einer Beleuchtungseinheit für widrige Einsatzbedingungen. *Bachelor-Thesis*, Germany: Technical University of Darmstadt, 2019.

P. Dilling. Integration und Charakterisierung eines Moduls zur automatisierten Vermessung von Farbsensoren in einen bestehenden Versuchsstand. *BacBachelor-Thesis*, Germany: Technical University of Darmstadt, 2019.

T. Bölker. Entwicklung und Characterisierung eines automatisierten Messsystems für LED-Module. *Bachelorarbeit*, Germany: Technical University of Darmstadt, 2019.

J. Sokoudjou. Literatur- und Marktrecherche zu aktuell verfügbaren Technologien der Multikanal-Farbsensorik. *Bachelor-Thesis*, Germany: Technical University of Darmstadt, 2019.

D. Krause. Aufbau einer minimalinvasiven Elektronik zur Messung der LED-Vorwärtsspannung auf LED-Modulen. *Bachelor-Thesis*, Germany: Technical University of Darmstadt, 2020.

C. von der Au. Untersuchung des winkelabhängigen Spektralverhaltens von LED-Systemen im Vergleich zu hemisphärisch aufgenommenen Spektren. *Bachelor-Thesis*, Germany: Technical University of Darmstadt, 2020.

M. Sterzik. Charakterisieren und Evaluierung von Sensoren zur Situationserkennung als Internet-of-Things Gerät. *Bachelor-Thesis*, Germany: Technical University of Darmstadt, 2020.

T. Luan. Investigation of Suitability of Dynamic Time Warping for LED Degradation Time Series Classification. *Bachelor-Thesis*, Germany: Technical University of Darmstadt, 2021.

M Peiro. Evaluation moderner statistischer Verfahren zur Modellierung der Degradation von LEDs. *Bachelor-Thesis*, Germany: Technical University of Darmstadt, 2021.

K. van Beek. Moisture Absorption and Desorption of Phosphor-Converted LEDs under WHTOL Conditions. *Master-Thesis*, Germany: Technical University of Darmstadt, 2021.

C. Nounga. Auswirkung der LED-Degradation auf die zirkadiane Wirksamkeit von steuerbaren weißen Beleuchtungssystemen. *Master-Thesis*, Germany: Technical University of Darmstadt, 2022.

D. Müßig. Erzeugung von LED-Spektren in Lebensdaueruntersuchungen mittels probabilistischer Modellierung. *Master-Thesis*, Germany: Technical University of Darmstadt, 2022.

H. Zuo. Development of a Software Framework for the Evaluation of the Lamp Degradation on the Growth Parameters of a Plant. *Master-Thesis*, Germany: Technical University of Darmstadt, 2022.

Y. Chen. Feature Importance in LED Degradation Time Series. *Bachelor-Thesis*, 2022.

T. Bölker. Analyse von Sensordaten und Optimierung der Sensoreinstellungen in realen Beleuchtungssystemen. *Master-Thesis*, Germany: Technical University of Darmstadt, 2022.

Erklärung laut Promotionsordnung

---

§8 Abs. 1 lit. c PromO
Ich versichere hiermit, dass die elektronische Version meiner Dissertation mit der schriftlichen Version übereinstimmt.

§8 Abs. 1 lit. d PromO
Ich versichere hiermit, dass zu einem vorherigen Zeitpunkt noch keine Promotion versucht wurde. In diesem Fall sind nähere Angaben über Zeitpunkt, Hochschule, Dissertationsthema und Ergebnis dieses Versuchs mitzuteilen.

§9 Abs. 1 PromO
Ich versichere hiermit, dass die vorliegende Dissertation selbstständig und nur unter Verwendung der angegebenen Quellen verfasst wurde.

§9 Abs. 2 PromO
Die Arbeit hat bisher noch nicht zur Prüfungszwecken gedient.

Darmstadt, Juni 2023

Simon Benkner

Colophon

This document was typeset using the typographical look-and-feel `classicthesis` developed by André Miede and Ivo Pletikosić. The style was inspired by Robert Bringhurst's seminal book on typography "*The Elements of Typographic Style*". `classicthesis` is available for both LaTeX and LyX:

https://bitbucket.org/amiede/classicthesis/

Happy users of `classicthesis` usually send a real postcard to the author, a collection of postcards received so far is featured here:

http://postcards.miede.de/

Thank you very much for your feedback and contribution.

Final Version as of January 8, 2024 (classicthesis v4.6).